

# K A D A

## Journal of Physics

Vol. 1 (2) December, 2017 ISSN: 2579-1168

A Publication of  
Department of Physics,  
Faculty of Science,  
Kaduna State University, Kaduna.

# KADA JOURNAL OF PHYSICS

*Vol. 1 (2)    December, 2017    ISSN: 2579-1168*

**December, 2017**

All rights reserved: No part of this publication may be reproduced or transmitted in any way or form by any means without the permission and express acknowledgment of the source.

*Published By*  
DEPARTMENT OF PHYSICS, FACULTY OF SCIENCE,  
KADUNA STATE UNIVERSITY,  
P. M. B 2339, KADUNA - NIGERIA.  
Email: [kadajournphys@gmail.com](mailto:kadajournphys@gmail.com)  
[kadajournphys@kasu.edu.ng](mailto:kadajournphys@kasu.edu.ng)

**DEPARTMENT OF PHYSICS,  
FACULTY OF SCIENCE,  
KADUNA STATE UNIVERSITY, KADUNA - NIGERIA**

Editor-in-Chief

**H. O. Aboh**, Ph.D, FNIP

Deputy Editor

**M. S Abubakar**, Ph.D, FNIP

Journal Editorial Committee

**Dr. M. D. Dogara**, MNIP

**Dr. P. M. Gyuk**, MNIP

**Dr. S. G. Abdu**, MNIP

Business Editor

**Mr. Jerry Aba**

Editorial Board Members

**Prof B. J. Kwaha**, FNIP

Department of Physics,  
University of Jos.

**Prof S. B. Elegba**, FNIP

Department of Physics,  
University of Abuja.

**Prof K. M. Lawal**, MNIP

Department of Physics,  
Ahmadu Bello University, Zaria.

**Prof I. Okunade**, MNIP

Centre for Energy Research and Training,  
Ahmadu Bello University, Zaria.

**Prof G. Babaji**, MNIP

Department of Physics,  
Bayero University Kano

**Dr. A. Mayere**

University of Nottingham,  
University Park, Nottingham,  
United Kingdom.

**Introduction:**

Kada Journal of Physics (KJP) is published bi-annually by the Department of Physics, Kaduna State University, Nigeria. The KJP is a peer-review on-line international journal which is aimed at fast but standard publication of cutting edge research in all areas of physics and their applications.

**AUTHOR'S GUIDELINE**

Authors are expected to adhere to the following while submitting their manuscripts for assessment for possible publication in the Kada Journal of Physics.

**FORMAT**

All headings are flush left. The beginning of every paragraph must flush to the left margin. All paragraphs must be blocked and separated with an extra line space between them. All pages must be numbered.

**ARRANGEMENTS**

The contents of the articles must be presented in the following sequence: Title Names(s) of author(s), Abstract, Keywords, Introduction, Materials and Methods, Results, Discussions, Acknowledgments, and References.

**TITLE**

This should be on a separate page and contain the name(s) of the author(s), their addresses and e-mail addresses. In case of more than one author, indicate who correspondences should be addressed to. The title of the paper should, if possible, be short, but must contain enough information to reflect what is contained in the text.

**ABSTRACT**

*This should be in on the same page with the title of the work. The abstract should convey the essential account concisely, in not more than 200 words all in one paragraph.*

**INTRODUCTION**

It is the background information and therefore should include the theory behind the work. The goals of the research or hypothesis explaining clearly what you are investigating and why you choose to investigate it should be comprehensively addressed. The introduction should be motivation for the work.

**MATERIALS AND METHODS**

Procedures and materials used should be

described in sufficient detail to allow repetition of the work. Protocols already described elsewhere can be quoted.

**RESULTS**

Describe the data generated from the experiments using statements, tables and figures. Any data already presented in a table should not be repeated in a figure and vice versa. Also results described in the text must not be repeated in tables and figures again. Present the statistics you calculated, the sample size for the statistical test, and the P-value for the statistics. All tables and figures must be numbered in the order in which they are cited in the text.

**DISCUSSIONS**

Discuss and refer to the results obtained in the experiments and link the results to your original goal or idea. Compare the results obtained to other published studies. Since the objective is to make a contribution to the literature on this particular topic, you are expected to relate your work to the studies already done in this field. If your results are not what you expected, try to explain why they differ.

**ACKNOWLEDGMENT**

Where applicable, acknowledgment(s) should be concise.

**CITATION OF REFERENCES IN THE TEXT**

References by different authors should be arranged chronologically, e.g. (Ado 1965; James 1973; Kelvin 1977). No comma between name and year. References from the same year should be listed alphabetically, e.g. (Ali 1966; Chukwu 1966; Jude 1966) without comma between name and year. When the name of the author and the year of publication do not form part of a sentence, they should be written in parentheses and separated only by a single space without comma, e.g. (Gambo 1931). However, an author's name, and sometimes the year of publication, may form part of a sentence as follows: "Gambo (1931) showed that..." or "In 1931 Gambo published this report..." . In the case of two authors the two names should be linked by an ampersand

(&), E.g. Hassan & Umma (2005). For more than two authors, quote only the name of the first author followed by et al., Typed in italics, e.g. (Aboh, Smith & James (1931) become (Aboh et al. 1931). The quotation of multiple papers published by one author in the same year should be distinguished by the suffixes a, b, c, etc., inserted after the year of publication. For a series of papers, their arrangements should obey ascendant chronological order with each paper separated from the next by a semicolon (Garba 2005; Daniel 2006). If the papers are published the same year, use alphabetical orders (e.g. Daniel 2006; Garba 2006; Haruna 2006). Quotation of papers that are still in the press should be done only for those papers that have actually gone to the press by inserting the words “in press” in the text instead of the year of publication. When an unseen paper is being quoted from another publication, only the latter should be included in the reference list. The example only Garba (2000) would be included in the reference list. Authors must check to ensure accuracy that all references mentions in the text are listed at the end of the paper and vice versa.

#### **LISTING REFERENCES AT THE END OF THE PAPER**

References must be listed out according to the Harvard reference method. When one author has several publications they must be listed out chronologically. When two or more papers have the same author and published in the same year, the letters a, b, c, should be added after the year. When the publication carries the name of an editor and not the author of the article, insert “(Eds.)” between the name and the date of publication. If there is more than one editor, use the abbreviation “(Eds)”. When the reference includes both authors and editors, insert the phrase “edited by” after the title of the book. The title of a journal must be given in full and italicized, using Arabic numerals to indicate the volume number, e.g. *Geophysics*, 7:4-32. When the reference consists of a single page only, just insert a colon before the page number. Papers that are still in press should carry the word “in press”

after the name of the journal, the correct volume and page numbers. Titles of books must be italicized. Use the abbreviation “ed.” for edition and only an Arabic numeral to indicate the volume(s) cited. No page numbers are given for books, e.g. Godwin, A.S. 2006. *Concepts in Physics*, 3rd ed. 1. London; Churchill. When it is only the abstract of an article that had been seen, indicate this as follows: Jonah, T. N. 2005. Rural water development in Nigeria. *Nigerian Journal of Physics*, 2:200-210. Articles and book chapters should be written as follows: King, O. D. 1963. *Briquette making in: Small scale business*, edited by F. Smith & B. Timothy. Kaduna: Nura, B.A. 2003. Groundwater contamination of Narayi village. *Proceedings of the 30th Summit of Science Association of Nigeria*, Abuja, Nigeria 2013: 423-459. Individual articles from Annual Reports should be listed as follows: Esther, S A. A. 2003. Radiation Report of the Nigeria Nuclear Regulatory Agency, Nigeria, for 1999:62. Publications without the name of the author or editor should carry the name of the organization issuing the work, e.g. NNRA 1999. NNRA Year book for 1999. Unpublished theses and dissertations should be listed as follows: Halima, T. H. 2016. *Solar Radiation Effects in Kachia town*, Nigeria. B.Sc. Thesis, Kaduna State University, Kaduna 45 pp. Note that the title of an unpublished work is not italicized. For citations of journals from the web, follow the example below: Abu, M.S. 2005. A new method of digitization. *Science World Journal [on line]* 32-40. Available in <http://www.scienceworldjournal.com> (date and time retrieved).

For articles accessed in the net authors and the date of publication, use the example below: Solar flux over the Equatorial Axis. Retrieved 2nd January, 2016 from [www.cc.geosci.edu](http://www.cc.geosci.edu)

Other relevant information

#### **TABLES**

Each table must be typed using table menu for easy retrieval and editing. It should contain a brief heading with enough information to enable the reader to understand the table

without consulting the text. The approximate positions of all tables must be indicated in the main text. Duplication in the text of information given in the tables must be avoided. They are to be numbered with Roman numerals.

#### **FIGURES**

Illustrations are referred to as figures (abbreviated as "Fig."). The approximate position of all figures must be indicated in the main text. Repetition in the text of information given in the figures must be avoided. They are to be numbered with Arabic numerals. Authors are encouraged to supply the original spreadsheet data used to produce the graph to enable us maintain a uniform look for all graphs in the journal.

#### **PHOTOGRAPHS AND DIAGRAMS**

Production of colour figures are free. They should be saved in JPEG format

#### **PAGE CHARGES**

Twenty Thousand Nigerian Naira (N20,000:00) or US \$100.00 will be charged per article after the paper might have been accepted for publication, while Five thousand

naira (N5,000.00) will be charged for Assessment fee.

Manuscripts that do not comply with the editorial requirements will be returned for amendment before they are considered by the Editorial Committee.

#### **BANKER:**

##### **FCMB**

Kada Journal of Physics

Acct. No. 4358627011

#### **FONT SIZE:**

All text must be in Times Roman with Text Size of 10 and Numbers of pages must not exceed 15 pages per article.

#### ***All Correspondence to:***

**H.O. Aboh**, Ph.D, FNIP

*Editor-in-Chief*

Department of Physics, Kaduna State University, P.M.B. 2339, Kaduna, Kaduna State, Nigeria.

✉ : kadajournphys@gmail.com

copy: kadajournphys@kasu.edu.ng

☎ : +234 813 612 4134, +234 802 334 8334

## IMPROVED SOLAR THERMAL COOKER USING FRESNEL LENS AS CONCENTRATOR

**Auwal Abdulkadir<sup>1\*</sup> and Muhammad Suleiman<sup>2</sup>**

<sup>1, 2</sup>Physics Department, Umaru Musa Yar'adua University, Katsina.  
Email: auwal.abdulkadir@umyu.edu.ng

### ABSTRACT

*Solar cooker is alternative to conventional sources of energy for cooking food like Mud stove, methane cooker, pressure cooker and more. A solar thermal pot using Fresnel lens as radiation concentrator was constructed and the Fresnel lens heat efficiencies were tested and found to be 57.6%. The solar cooker is placed in the sun about one to three hours to take measurements, and the readings were taken and recorded at each interval of 10 minutes. By comparison the highest temperature reached with Fresnel lens in place is about 76.4 degree while without Fresnel lens is 53 degree. Therefore thermal pot with Fresnel lens was proved to be heat efficient than thermal pot without Fresnel lens.*

**Keywords:** *Fresnel lens, Renewable Energy, Solar Pot, Temperature*

### INTRODUCTION

Renewable energy source can ensure suitable development in the community by reducing the dependence on fossil fuel and cutting down of carbon emission, is one of the most important aspect of sustainable development. Solar cooker is another alternative source of energy for cooking which can be driven directly from the sun [1]. Majority of solar cookers presently in used are relatively cheap because they use no fuel and cost nothing to operate. Solar cooker is simple, available, compatible and suited to human environment. Solar Energy is important in many cases as there may be a direct conversion in to electricity by photovoltaic method. Solar cooker will become a dependable energy source without 'new requirement of highly technical specialization for its widespread and safe utilization [1,2].

Concentrators are used sometimes to improve the efficiency of the device in consideration which may be in solar cells or energy harvesters [3-10]. In our case a Fresnel lens was used for this purpose though curved mirrors, aluminium or silver reflecting surfaces that coat the front or back surfaces of

glass or plastic can also be employed. Researchers are now developing cheap polymer films to replace the more expensive glass but here we focus our selves to employ the use of Fresnel rings that will serve as radiation concentrator which may improve the output heat efficiency of the designed solar cooker. In this work we poured 1 litre of water in to our designed pot to test its efficiency and for experimental purposes.

Generally: Fresnel lenses are aspheric and thin lenses, thus, they have the following advantages over the conventional spherical lenses [10- 15].

1. Their aspheric and thin shapes eliminate longitudinal spherical aberration and reduce absorption losses, thus they can be made with very large apertures.
2. In contrast with many of spherical lenses which are biconvex, Fresnel lenses are Plano convex, thus in addition to their aspheric profiles and low f-number leads them to have a strong a symmetric behaviour.
3. The effective focal length is the same

as the back focal length, because the Fresnel lenses are thin lenses, the case of conjugates of focal length and infinity is very negligible.

$$4. \text{ Heat efficiency} = \frac{\text{Output heat}}{\text{Input heat}} \times 100\%$$

Light intensity maximization by Fresnel lens, both parallel and perpendicular to the plane containing the incident, the reflected and the refracted rays depends on reflection and transmission coefficients ( $r_{x,y}$  and  $t_{x,y}$ ) given by the following equations:

$$r_y = \frac{E_r}{E_i} = \frac{n_1 \cos \theta_1 - n_2 \cos \theta_2}{n_1 \cos \theta_1 + n_2 \cos \theta_2} \quad (1)$$

$$t_y = \frac{E_t}{E_i} = \frac{2n_1 \cos \theta_1}{n_1 \cos \theta_1 + n_2 \cos \theta_2} \quad (2)$$

$$r_x = \frac{E_r}{E_i} = \frac{n_2 \cos \theta_1 - n_1 \cos \theta_2}{n_1 \cos \theta_1 + n_2 \cos \theta_2} \quad (3)$$

$$t_x = \frac{E_t}{E_i} = \frac{2n_1 \cos \theta_1}{n_1 \cos \theta_1 + n_2 \cos \theta_2} \quad (4)$$

Equations (1) to (4) are called Fresnel equations. We define the reflectance  $R_{x,y}$  as the fraction of the incident power reflected at the interface by the following equations.

$$R_y = |r_y|^2 = \frac{|n_1 \cos \theta_1 - n_2 \cos \theta_2|^2}{|n_1 \cos \theta_1 + n_2 \cos \theta_2|^2} \quad (5)$$

$$R_x = |r_x|^2 = \frac{|n_2 \cos \theta_1 - n_1 \cos \theta_2|^2}{|n_1 \cos \theta_1 + n_2 \cos \theta_2|^2} \quad (6)$$

Equations (5) and (6) gives the reflectance of the perpendicular and parallel polarized incident ray of light respectively. On the other hand, the transmittance  $T_{x,y}$  can be calculated by the equation below:

$$T_{x,y} = \frac{n_2 \cos \theta_2 |t_{x,y}|^2}{n_1 \cos \theta_1} \quad (7)$$



Fig.1 Linear Fresnel lens

## MATERIALS AND METHOD

### A. Materials

- 50 cm by 30cm ply wood with thickness of 0.008cm
- 47.5 cm by 27.5 cm Aluminum sheet of 0.002 thickness
- 50 cm by 30 cm glass of 0.002cm thickness
- Thermometer
- Glue
- Pot
- Black paint

- ½ inch Nails
- K- thermocouple thermometer
- Linear Fresnel lens
- Irradiance meter
- Scarpole
- bending wire

### B. Method of making the cooker

1. Four 50 cm by 30 cm ply wood with a thickness of 0.008cm, were put together to form a rectangular shape
2. Another ply wood of the same dimension was used to cover the bottom of the



constructed rectangular shape

3. An Aluminum sheet of 47.5 cm by 27.5 cm with thickness of 0.002cm was painted black inside the constructed wooden rectangular shape

4. A glass material with the same dimension as the plywood, with thickness of 0.2mm was

used to cover the top of the constructed rectangular shape.

5. A small hole was made on bottom of the glass so as to insert thermocouple and readings were taken and recorded at each interval of ten minute.



Fig. 2: Solar Thermal Pot using Fresnel lens.

## RESULTS AND DISCUSSIONS

To presents the results there were initial reading recorded as:

1. Stagnant temperature of 27.5 degree Celsius with k thermocouple thermometer at Fresnel lens without load.

2. Ambient temperature is 37.5 degree Celsius with thermometer without load

3. Solar Irradiation without load  $985 \text{ Wm}^{-2}$ , Measured using irrdisance metre.

4. Normal water temperature 31.5 degree Celsius.

5. Mass of water is 1 litre.

6. The experiment was conducted with the fresnel lens on that day.

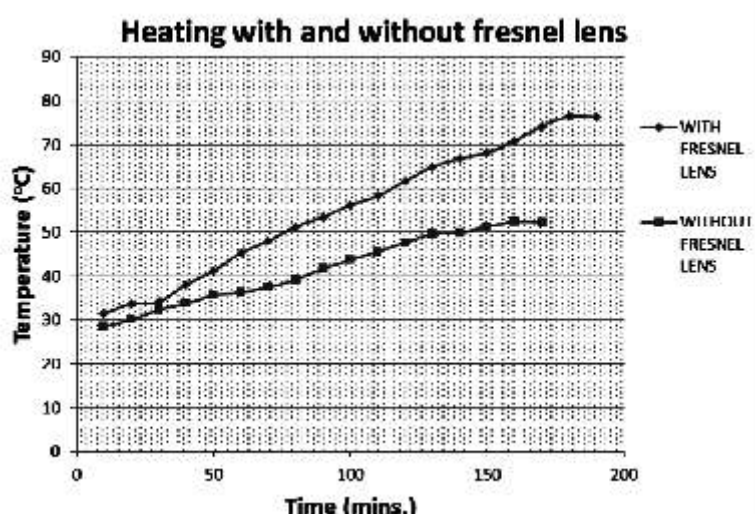


Fig. 3: graph of Temperature against Time for Heating with and without fresnel lens.

The experiment was conducted to observe the temperature variation between different time intervals and determine the highest temperature obtainable using the designed solar cooker. The heat efficiency of Fresnel lens was found to be about 57.7% as compared with the book value. From the graph it is clear that the highest temperature attained in the experiment with Fresnel lens is about 76.4 degree while without Fresnel lens is about 53 degree. It can also be observed that the highest temperature was attained around 12pm to 2pm. The results obtained clearly indicated that the experiment with Fresnel lens gives the highest temperature recorded and is more temperature efficient than without Fresnel lens. In essence by comparison, the experiment with Fresnel lens retained and absorbed more solar energy than without Fresnel lens even though the material used in the construction and the insulating materials as well as the volume remain the same.

## CONCLUSION

A solar thermal pot was constructed using Fresnel lens and the thermal properties, temperature variation and heat efficiency of the Fresnel lens were determined. From results and graph, it is very evident that a solar cooker made from local material was comfortable to tracks the sun. By comparison the highest temperature reached with Fresnel lens is about 76.4 degree while without Fresnel lens is 53 degree. Therefore thermal pot with Fresnel lens is more temperature efficient than thermal pot without Fresnel lens. We can finally conclude that the advantages of solar thermal pot using Fresnel lens are in accordance and comparable to those in some visited available literatures [16-17]:

- (1) Solar cookers use no fuel.
- (2) Reduce environmental damage caused by fuel use.
- (3) Solar cookers have large economic and

environmental benefits by reducing deforestation

- (4) Solar cooker saves cost of fuel.
- (5) Solar cooker use both direct and diffused solar radiation
- (6) Solar cooker are relatively inexpensive.

## Disadvantages of Solar thermal pot using Fresnell lens [16-17]:

1. Solar cooker are less useful in cloudy weather.
2. Many solar cookers take longer to cook food then fuel oven.
3. Solar cookers are affected by strong winds.
- 4 When not use properly the solar cooker may be harmful to the eyes.
5. Solar cookers may require the user to learn special cooking techniques.

## ACKNOWLEDGMENT

This research was conducted at Ibrahim Shehu Shema Centre for Renewable Energy Research Umaru Musa Yar'adua University Katsina Nigeria and as such we may wish to acknowledge their effort in providing a good and safe environment to carry out this work. Author 2 wish to thanks Mr. L Ladan of ISSCERER for his mentoring, guidance and supervising the progress of this work.

## REFERENCES

- American Society for Testing and Materials ( A S T M ) , <http://rredc.nrel.gov/solar/spectra/am1.5/>. Internet Website, 2011. Terrestrial Reference Solar Spectral Irradiance: Air Mass 1.5.
- Ma azu Musa (1994): Design and Construction, and Performance Analysis of Flexible Booster Solar Cooker, published company new delhi. Vol. 6PP 33-93
- B. A. Anićin, V. M. Bobović, and D. M. Davidović, "Fresnel lenses," *Am. J. Phys.* 57, pp.312–316, Apr. 1989.
- R. Leutz and A. Suzuki, *Nonimaging Fresnel*

*Lenses: Design and Performance of Solar Concentrators*, Springer, Berlin, 2001.

A. Davis, "Raytrace assisted analytical formulation of fresnel lens transmission efficiency," in *Novel Optical Systems Design and Optimization*, R. John Koshel and G. Groot Gregory, ed., *Proc. SPIE* 7429, pp. D1–12, Aug. 2009.

A. Davis, K. Levesque, and S. Wilt, "Prism peak rounding in injection molded fresnel lens solar concentrators," in *Diamond Turning and Polymer Optics*, Chris Ghio, ed., *Optifab* TD07, pp. 52(1)–52(3), May. 2011.

E. Jones, T. Oliphant, P. Peterson, *et al.*, "SciPy: Open source scientific tools for Python, [www.scipy.org](http://www.scipy.org)," 2001

M. Born and E. Wolf, *Principles of Optics*, Pergamon Press, Oxford, 6th ed., 1980. See in particular Sec. 1.5.2 "Fresnel Formulae".

E. Hecht and A. Zajac, *Optics*, Addison–Wesley, Reading, Massachusetts, 2nd, 1990. See in particular Sec. 4.3 "The Electromagnetic Approach".

Arise, E. A (1982): Solar Energy Application Industry of Nigeria Solar Energy.

A.O Musa (2010): Unpublished Lecture note Energy and Environment UMYU

Duffie, J.A (1974) "solar energy thermal processor" John Wiley and son London Toronto, Vol. 2 pp22-30

Andrew T. A: 2013 Design and construction of solar cooker over published company academic press, New York

Mishra and Sharma S. P "Performance study of air heated package Bed solar energy collector" Vol No2 pp153-158

Elbart A. M (1983): Handbook of energy technology and economic Kenneth- C.

Brown "solar thermal energy conversion" pp618-634, Wiley-inter science publication

Elfor W. T (1978): Optic of Non imaging concentrators. "Light and solar energy" academic press, New York VOL. 1 PP21-51

Fresnel solar cooker designs - Solar Cooking - Wikia.htm

## SCIENTIFIC REVIEW OF THE IMPACT OF RADIATIONS FROM HOME APPLIANCES ON HUMAN HEALTH

**Bello, A., Gurku, M.U., Emenyonu, V. C.**

Physics of Department, Nasarawa State University, Keffi

Correspondence Email: otranto4sure@yahoo.com

### ABSTRACT

*Electrical Electronic appliances have provided comfort in homes and enabled most activities without much mobility. The safety of radiations from these appliances is a long standing issue thus, while some researchers agree that these radiations are harmful to human health others assert they have no significant effect. The scientific review was to ascertain the effect of non-ionizing radiation from home appliances on human health with the primary aim of establishing causal link with reported physiological observations. Data pooled for the research concentrated on electromagnetic frequencies of home appliances, RF (3kHz – 30GHz) and ELF (50 – 60Hz), physiological observations at threshold limits for researches between 1974 – 2013. Results shows that Electromagnetic Hypersensitivity (EHS) has the highest frequency of physiological occurrence with exposure limits randomly distributed in the data. This stochastic pattern is consistent with the World Health Organization (WHO) statement in 2014 that there is no consensus yet on exposure limits and effects. There was little convergence on cancer also consistent with WHO on its uncertainty. Future problems is determining the build-up factor and cumulative effect of exposure which is consistent with reality.*

**Keywords:** Radiations, Physiological observations, Electromagnetic Frequency, Extremely Low Frequency, Radio frequency

### Introduction:

Radiation can be defined as the process through which energy travels or propagates in the form of waves or particles without the necessary intervention of a material medium. The two types of radiation are ionizing and non-ionizing radiations. Together these two form the electromagnetic spectrum which describes the range of all possible frequencies of electromagnetic radiation. The ionizing part of the spectrum includes the gamma rays, x-rays and the upper part of ultraviolet radiations while the non-ionization part of the spectrum includes some part of the Ultraviolet radiation, Visible Light, Infrared, Microwaves, Radio Frequency (RF) and Extremely Low Frequencies (ELF). Some experts usually lump the Microwaves, RF and the Low frequencies as RF but it is important to note that Electric and Magnetic fields tend to separate at ELF region. This is because in the near field, the power density varies quickly with the distance from the radiating element, making it

unsuitable to define the characteristics of the electromagnetic field in that region. But in the far field the power density is constant and may be used to measure and define exposures in  $\mu\text{W}/\text{cm}^2$ .

The relationship between electric and magnetic fields and the sources that create them (charges and currents) is defined by Maxwell's equations 4 equations. There is an electric field wherever there is an electric charge, but there is only a magnetic field when the electric charge moves, i.e. when there is a flow of electric current. The electric fields are present whether an appliance is on or off, but the magnetic field will disappear as soon as the appliance is turned off. Magnetic field intensity or magnetic excitation (H), is the magnetic field at a point defined by the force exerted on an element of current located at that point (A/m) and its intensity decreases as distance from the source increases. This inverse square relationship is also applicable to electric field.

### Interaction of electromagnetic fields with human tissues

The concept of charges and electromagnetic fields are witnessed within the human body as the fluids in the human body contain charge/ionized particles that are both stationary and circulating. These charges produce electric and magnetic fields making the human body electromagnetic (at a very low level, around 10Hz). Tiny electrical currents existing in human body are due to chemical reactions occurring as part of normal body metabolism but they always drain to earth when there is direct contact through bare foot and minimal direct contact with earth retains EMF in human body. The heart is electrically active due to number of blood vessels with different potential differences while the nerves relay signals by transmitting electric pulses mV range and brain waves in  $\mu\text{V}$ . Collectively, the human body acts like an antenna that absorbs RF and convert them into electric and magnetic fields when we interfere with EMF (Nabeel 2000). Whereas electric fields can be easily shielded or weakened by conducting objects such as buildings, trees, and human skin; the magnetic fields cannot be shielded. Magnetic fields are difficult to shield as they pass through anything that doesn't contain a high degree of iron. This important difference accounts for the fears about EMFs is associated with their magnetic field component and not from the electric fields (Nabeel 2000).

### Concern Regarding Non-Ionization Radiation:

It is an accepted theory that ionizing radiations can strip away an electron leaving an unpaired electron resulting to serious damage to tissues and cells through several mechanisms. It is also accepted that non-ionizing radiation have as much energy to excite the electrons in atoms or molecules but not enough to strip the electrons away hence, generally referred as less harmful.

However, experimental results and scientific

publications are proving that non-ionization radiations from electrical appliances (RF and ELF) are potential sources of health hazards. For instance, according to enwatch.com, an electromagnetic web, Electric heaters produce over 100 mG of radiation that can harm at close range. It was also alleged that it is easy for the person cooking an evening meal using hotplates or oven to be subjected to 5-10 mG for up to an hour which could be fatal. Some studies (Hutter, *et al.*, 2006; Santini, *et al.*, 2002, etc) have shown that there may be an association between some health effects and antennas operating within the microwave frequencies.

In reality, we are daily exposed to these radiations that emanates from home appliances operate within the RF as wireless technology like cordless phones, smart metering systems, wireless baby monitors, wireless doorbells, wireless intercom systems, wireless routers, wireless modems, etc. Others include, kitchen equipment (Stoves, hotplates microwave ovens, serving trays and dishwashers, freezers) Heating equipment (electric blanket, electrically heated carpets and rugs, under-carpet and under-floor, etc), Personal Grooming appliances (Hairdryers, electric shavers, electric toothbrushes, etc) can all produce substantial ELF.

At the moment there is no consensus in the scientific community on the health impacts thus, while some has relegated the effect to tissue heating, others are assert they are carcinogenic, including other sicknesses. Alluding to this problem, the World Health Organization (WHO) has undertaken to conduct a formal risk assessment of all studied health outcomes from RF exposure by 2016 (WHO 2014). They have also advised that public and occupational exposure be limited to the guidelines established by the International Commission for Non-Ionization Radiation Protection (ICNIRP) and Institute of Electrical Electronic Engineers (IEEE). The ICNIRP's reference levels are 500  $\mu\text{T}$  and 10  $\text{kV m}^{-1}$  for

workers and 100  $\mu\text{T}$  and 5  $\text{kV m}^{-1}$  for the public.

### Materials and Methods:

The materials used in this work are books, journals, articles, periodicals, and online materials (over 100 materials) relating to effects of non-ionizing radiations from electrical home appliances such as router, laptop, radio, television set, smart meters, among others from ICNIRP 1998; ICNIRP 2003; ICNIRP 2009a; NIEHS 2002; IARC 2002; WHO 2014; Rapacholi 1998; Blank M, *et. al*, 1997; Behari J 1999; IEEE 2002; NCS 2014; ACS 2014; NASA 2010; among others. Data extracted from the materials covered the threshold limits and physiological observations of experiments on this subject within the period of 1974 – 2013.

The data was segregated into two tables representing exposure from RF home appliances with the corresponding physiological observations and the other

comprising the exposure in the ELF regions with the attendant physiological effects. A statistical approach was adopted to analyze the relationship between exposure and the disease occurrence or physiological observations to reduce the randomness of data by clustering observations with similar physiological outcomes. E.g. physiological outcomes like headaches, insomnia, memory loss, among others that are the characteristics of Electromagnetic Hypersensitivity (EHS) were grouped together as EHS (WHO 2005). Microsoft Excel Programme was used to sort data and obtain the frequency of occurrence of each event to enable the determination of the highest physiological outcomes as associations found consistently are more likely to be causal.

### Results

Based on the results of experiments on ELF & RF of home appliances and the corresponding effects or physiological outcome, clustered from the original data in appendix 1 and II, and processed graphically below.

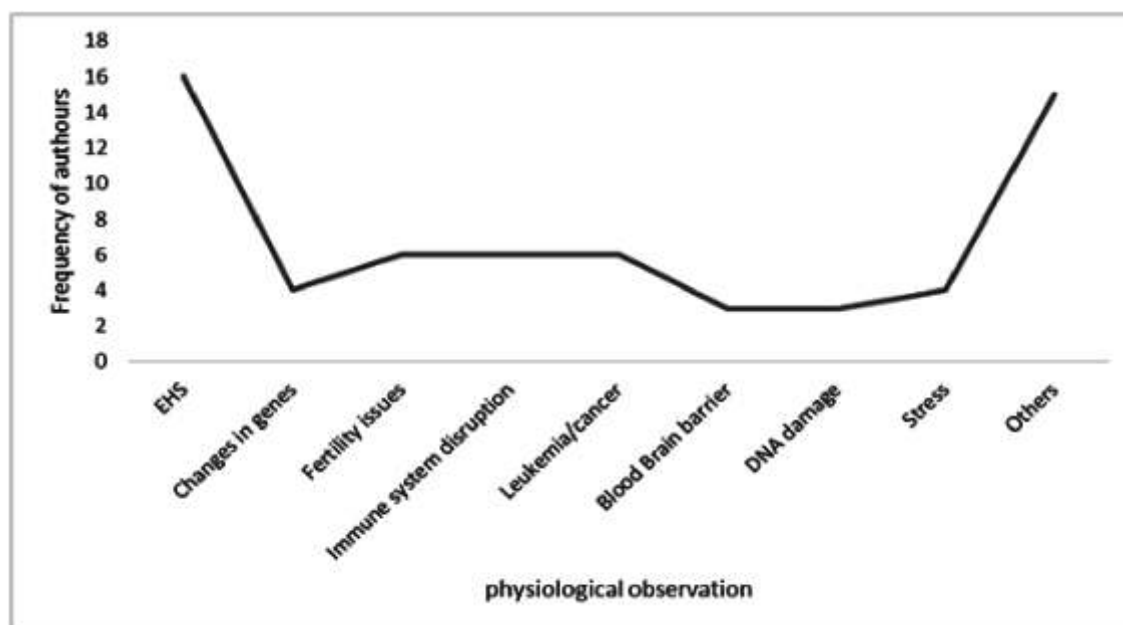


**Figure 1: Line graph showing the frequency of occurrence of physiological observations/effect from the results in Appendix I**

Biomarkers	Frequency of Authors
Oxidative Stress	8
Nitric oxide	2
Reactive Oxygen Species	2
Fertility	2
Free radical production	2
Biomolecule impact	2

ELF (milliTesla)

Research Years

Research Year	ELF (milliTesla)
1995	0.2
1996	0.0056
1997	0.5
2004	5
2005	0
2006	5
2007	1
2008	0.8
2009	7
2010	0.6
2011	2.3
2012	1
2013	0.5
2014	2

---

*Kada Journal of Physics*

### Discussion and Conclusion

In Fig 1. Physiological observations were noted at all thresholds showing a causal link between exposure and biological effect but not all biological effect may be harmful effect. Electromagnetic Hypersensitivity (EHS) has the highest frequency among the physiological observations noted to be randomly distributed in appendix 1, indicating a stochastic convergence which is consistent with the WHO Fact Sheet N° 193, 2014 that there is no consensus yet on exposure limits and effects. Others issues such as immune system disruption, fertility and leukemia/cancer did not enjoy significant frequency also consistent with WHO Fact Sheet N° 193 that RF and ELF may not be carcinogenic. Fig 3. Showed high frequency outcomes on stressors or biomarkers (oxidative stress) with the same effect (insomnia, headaches, anxiety, memory loss/brain fog) as the EHS. It is pertinent to note that most effects were noted at above 0.1mT and 0.5mT recommended limits of the ICNIRP. Sparse scientific activity about RF and ELF (Fig 2 and 4) impacts was recorded in early in 1974 and 1995 respectively but scientific interest set in from the 90s and 2004 respectively. However, the stochastic nature of the physiological distributions indicates

In conclusion, it can be deduced that there is a causal link between exposure and effect but biological effect may not mean harmful effect. EHS may be the likely consequence of exposure to RF and ELF radiations from home appliances. Cancer including Leukemia and other physiological issues like immune system disruption, fertility impacts from exposure may be unlikely. The stochastic nature of the physiological distributions indicates that there is no consensus yet on exposure limits and effects. However much research has so far been conducted in this area and it will continue to elicit interest.

### Recommendations:

There should be more research in this area to establish the physiological effect from

exposure to RF and ELF. However, the research must account for the build-up factor from exposure to variety of sources of ELF or RF and the cumulative exposure which is the reality in most situations. This will enable development of proper guideline standards for public and occupational exposure in view of the surge in wireless technology, electric vehicles, charging stations, electric trains. Understanding these issues will guarantee healthy lives and promote well-being for all, towards the realization of Goal 3, of the Sustainable Development Goals.

### REFERENCES

- Nabeel K. (2000): Electromagnetic Field (EMF) Retrieved 28<sup>th</sup> March, 2017 from [www.Brain101.info/EMF](http://www.Brain101.info/EMF)
- Santini R, Santini P, Danze Jm, Le Ruz P, Seigne N. (2002). Investigation on the health of people living near mobile telephone relay stations: *Pathologie Biologie* [online] 50 (6): 369 -373. Available in [http:// www.journals.Elsevier.com/pathologie-biologie](http://www.journals.Elsevier.com/pathologie-biologie) retrieved 28<sup>th</sup> March, 2017 at 1:00pm
- Hutter HP, Moshhammer H, Wallner P, Kundi M. (2006). Subjective symptoms, sleeping problems, and cognitive performance in subjects living near mobile phone base stations: *Occup Environ Med* [online] 63 (5): 307 - 13 . Available in <http://www.ncbi.nlm.nih.gov> retrieved 29<sup>th</sup> march, 2017
- WHO (2014). Electromagnetic Fields and Public Health: Mobile Phones Fact Sheet No 193: World Health Organization of the United Nations
- WHO (2005). Electromagnetic Fields and Public Health: Electromagnetic Hypersensitivity: World Health organization of the United Nations
- ICNIRP (1998). ICNIRP Guidelines for Limiting Exposure to Time Varying Electric, Magnetic and Electromagnetic Fields (up to 300GHz): International Commission for Non-Ionizing Radiation Protection.
- ICNIRP (2003). ICNIRP Guidelines for



Exposure to Static and Low Frequency Electromagnetic Fields, Biological Effects and Health Consequences (0 – 100KHz) – Review of the Scientific Evidence and Health Consequences. Munich: International Commission for Non-Ionizing Radiation Protection

ICNIRP (2009a). ICNIRP Guidelines for Limiting Exposure to Time Varying Electric, Magnetic and Electromagnetic Fields (up to 300GHz): International Commission for Non-Ionizing Radiation Protection.

IARC (2002). Non-Ionizing Radiation, Part 1: Static and Extremely Low Frequency (ELF) Electric and Magnetic Fields. Volume 80: World Health Organization International Agency for Research on Cancer

Repacholi MH. (1998). Low –Level Exposure to Radiofrequency Electromagnetic Fields: Health Effects and Research Needs. *Bioelectromagnetic Journal* [online] 1-9. Available in <http://onlinelibrary.wiley.com>. Retrieved on 28<sup>th</sup> March, 2017, 3:00pm

ACS (2014). Power lines, Electrical Devices and Extremely Low Frequency Radiation: American Cancer Society

NASA (2011). EMF Interactions with the human body: National Aeronautics and Space Administration (NASA) of the United States.

Blackman CF. (1990). ELF effects on calcium homeostasis. In: Wilson BW, Stevens RG, Anderson LE (eds) *Extremely Low Frequency*

*Electromagnetic Fields: the Question of Cancer*. Battelle Press, Columbus, Ohio, pp 189-208.

Behari, J. (1999). *Biological Effects and Health Implication of Radiofrequency and Microwave*. International Conference on Electromagnetic Interference and Compatibility, New Delhi, India 1999: 449-52.

Blank, M. and Goodman R. (1997). *Do Electromagnetic Fields Interact Directly With DNA?*, *Bioelectromagnetics Journal*; 18 (2):111-15.

Augner C. and Hacker Gw. (2012). Are People Living next to Mobile Phone Base Stations more Strained? Relationship of Health Concerns, Self – estimated distance to base stations and Psychological Parameters. *Indian J. Occcup Environ Med*. 13 (3): 141 – 5.

Bioinitiative (2012). A Rationale for Biologically-Based Public Exposure Standards for Electromagnetic Fields (ELF & RF). Bioinitiative Report 2012. Available in <http://www.bioinitiative.org>. Retrieved on 15<sup>th</sup> December, 2016, 10:00am.

Bioinitiative (2013). *Extremely-Low Frequency EMF Free Radicals Studies* updated March 2014. Bioinitiative Report 2012. Available in <http://www.bioinitiative.org>. Retrieved on 20<sup>th</sup> January, 2016, 12:00noon.

**APPENDIX I**  
**REPORTED BIOLOGICAL EFFECTS FROM RADIOFREQUENCY RADIATION AT LOW-INTENSITY EXPOSURE FROM WIFI (30KB- 300GB) APPLIANCES**

S/NO	RESEARCHER	YEAR	POWER DENSITY	PHYSIOLOGICAL OBSERVATION
1	Belyaev	1997	$10^{-13}$	Changes in genes, problems with chromatin conformation (DNA)
2.	Grundler	1992	$10^{-12}$	Changed growth rates in yeast cells
3.	Belyaev	1997	$10^{-10}$	Changes in genes and chromatin condensation
4.	Behari	2006	0.00034	Chronic exposure to mobile phone pulsed RF significantly reduced sperm count
5.	Velizarov	1999	0.0005	Decreased cell proliferation
6.	Oberfeld	2004	0.0006 – 0.0128	Fatigue, depressive tendency, sleeping disorders, concentration difficulties
7.	Heinrich	2010	0.003 – 0.02	Short term exposure in children caused headache, irritation, concentration difficulties in school
8.	Thomas	2010	0.003 – 0.05	In children and adolescents caused behavioral problems
9.	Mohler	2010	0.005	Chronic exposure caused sleep disturbances
10.	Thomas	2008	0.005 – 0.04	Reported headaches, concentration difficulties
11.	Buchner	2012	0.006 – 0.01	In humans showed increase stress hormones
12.	Navarro	2003	0.01 – 0.11	Caused fatigue, headaches, sleeping disturbances
13.	Hutter	2006	0.01 – 0.05	Reported headache, neurological problems, sleep and concentration problems
14.	Thomas	2008	0.005 – 0.04	Adults exposed reported headache, neurological problems, sleep and concentration problems
15.	Augner	2009	0.015 – 0.21	Reported changes in mental state
16.	Khurana	2010	0.05 – 0.1	Linked to adverse neurological, cardio symptoms and cancer risk
17.	Kundi	2009	0.05 – 0.1	Related to headache, concentration and sleeping problems, fatigue
18.	Otitolaju	2010	0.07 – 0.1	Sperm head abnormalities in mice
19.	Schwartz	1990	0.38	Affected calcium metabolism in heart cells
20.	Akoev	2002	0.8 – 10	Caused emotional behavior changes
21.	Zwamborn	2003	0.13	Decreased cognition and well-being
22.	Kolodynski	1996	0.16	Memory and attention of school children affected

23.	Magras & Zenos	1997	0.168 – 1.053	Irreversible infertility in mice
24.	Hocking	1996	0.2 – 8	Caused a two –fold increase in leukemia
25.	Hocking	2000	0.2 – 8	Decrease survival in children with leukemia
26.	Riddervold	2008	0.21 – 1.28	Adolescents and adults reported increase in headaches
27.	Saunders	1981	0.5	Degeneration of seminiferous epithelium in mice
28.	Avendano	2012	0.5 – 1.0	Decrease in sperm viability within 4hr exposure
29.	Persson	1997	1.0	Pathological leakage of blood brain barrier
30.	Fessenko	1999	1.0	Significant effect on immune function of mice
31.	Novoselova	1999	1.0	Affected function of immune system
32.	Eltiti	2007	1.0	Causes loss of well-being
33.	Dolk	1997	1.3 – 5.7	Associated with doubling of leukemia in adults
34.	Pyrpasopoulou	2004	1.25	Exposure affected kidney development in rats
35.	Nittby	2007	1.5	Reduced memory function in rats
36.	Kesari	2008	2	Induced double strand DNA damage
37.	Wolke	1996	2.5	Affected calcium concentrations in muscles
38.	D' Inzeo	1988	2 – 4	Altered cell membranes
39.	Tattersall	2001	4	Caused changes in the hippocampus (brain memory and learning)
40.	Chiang	1989	4 – 15	Memory impairment, slowed motor skills and retarded learning in children
41.	Boscolo	2001	5	Decrease in immune function
42.	Kwee	2001	5.25	Induce stress response
43.	Dumansky	1974	5 – 10	Impaired nervous system activity
44.	Philips	1998	6	Induce DNA damage in cells
45.	Marinelli	2004	8.75	Caused DNA breaks in leukemia cells
46.	Navakatikian	1994	10	Changes in behavior after 0.5 hour exposure
47.	Richter	2000	10-100	Increased risk in radar operators of
48.	Dutta	1989	12.5	Caused calcium efflux in cells - can affect many critical cell functions
49.	Sarimov	2004	13.5	Affected human lymphocytes - Induced stress response in cells

50.	Mann	1998	20	Increase in serum cortisol (a stress hormone)
51.	Yurekli	2006	28.2	Increased free radical production in rat cells
52.	Veyret	1991	37.5	Immune system effects
53.	Forgacs	2006	45	affected serum testosterone levels in mice
54.	Salford	2003	50	caused a pathological leakage of the blood-brain barrier in 1 hour
55.	Mann	1996	50	18% reduction in sleep (important to memory and learning functions)
56.	Somozy	1991	60	Caused structural changes in cells of mouse embryos
57.	Stankiewicz	2006	60	Pulsed RFR affected immune function in white blood cells
58.	Lebedeva	2000	60	Cortex of the brain was activated by 15 minutes of exposure
59.	Ivaschuk	1999	65	Affected genes related to cancer
60.	Belyaev,	2005	92.5	Caused genetic changes in human white blood cells
61.	Elekes	1996	100	Changes in immune function
62.	Navakaikian	1994	100	A 24.3% drop in testosterone after 6 hours of exposure
63.	Salford	1994	120	A pathological leakage in the blood - brain barrier

**Source: Bioinitiative report, 2012**

**TABLE 1**  
**CLUSTERED TABLE OF DATA OF RADIOFREQUENCY RADIATION FROM WIFI,**  
**WIRELESS HOME APPLIANCES**

<b>HEALTH IMPACT</b>	<b>FREQUENCY (authors)</b>
<b>EHS</b>	<b>16</b>
<b>Changes in genes</b>	<b>4</b>
<b>Fertility issues</b>	<b>6</b>
<b>Immune system disruption</b>	<b>6</b>
<b>Blood Brain Barrier</b>	<b>3</b>
<b>DNA damage</b>	<b>3</b>
<b>Leukemia /Cancer issues</b>	<b>6</b>
<b>Stress induced cases</b>	<b>4</b>
<b>Others</b>	<b>15</b>

**TABLE 2: RECENT STUDIES ON ELF – MAGNETIC FIELDS ON BIOLOGICAL TISSUES**

<b>AUTHOUR</b>	<b>PHYSIOLOGICAL RESPONSE/EFFECT</b>	<b>ELF EMF RANGE (mT)</b>
Akan <i>et al</i> , 2010	Affects bacterial growth and response of immune system to bacterial challenges	1
Akdaz <i>et al.</i> , 2013	Alter protein biomolecules (beta-amyloid protein, protein carbonyl) in rat brain.	0.1, 0.5
Akdag <i>et al.</i> , 2007	Reduce Nitric Oxide (NO) production which impacts on cognitive ability	0.1,0.5
Akdag <i>et al.</i> , 2010	Increases oxidative stress and diminishing antioxidant defense system.	0.1,0.5

Akdaz <i>et al.</i> , 2013	No effect on sperm count & morphology	0.1,0.5
Aken <i>et al.</i> , 2006	Alterations in the germinal epithelium and tunica albuginea of ovaries	1
Ayse <i>et al.</i> , 2006	Increase in differentiation	5
Bawinsm <i>et al.</i> , 1996	- Strong influence on Nitric Oxide (NO) system in brain	0.0056, 0.000056
Bediz <i>et al.</i> , 2006	Increases lipid peroxidation in brain	1
Belova <i>et al.</i> , 2010	Decrease in the rate of reactive oxygen species (ROS) generation by 23%	1
Buczynski <i>et al.</i> , 2005	Protein biomolecules reached highest values, shows platelets sensitivity	1
Buřdak <i>et al.</i> , 2012	- mild oxidative stress and DNA damage inducer.	1
Calota <i>et al.</i> , 2007	- increased the chemiluminescence emission	1
Canseven <i>et al.</i> , 2008	formation of free radicals and behaviour of antioxidant enzymes	1, 2, 3
Cantoni <i>et al.</i> , 1995	does not affect the machinery involved in the repair of DNA lesions in oxidatively injured cells	0.0002 - 0.2
Chu <i>et al.</i> , 2011	- may induce oxidative stress in mouse cerebellum	2.3
Ciejka <i>et al.</i> , 2009	- significant decrease of the organism antioxidant defence - exposure time affects heart rate, plasma antioxidant capacity and the organism defense ability against free radicals.	7
Ciejka <i>et al.</i> , 2011	- affect free radical generation in the brain	7
Cui <i>et al.</i> , 2012	- induced serious oxidative stress in the hippocampus	1
Deng <i>et al.</i> , 2013	- ELF-MF could impact on learning memory and - pro-oxidative function in Kunming mice	2
Ding <i>et al.</i> , 2004	- Cannot induce apoptosis and necrosis	5
Emre <i>et al.</i> , 2011	- increase in the levels of oxidative stress indicators, .	1
Erdal <i>et al.</i> , 2008	ELF-MF exposure may enhance the oxidative stress	1
Falone <i>et al.</i> , 2008	may act as a risk factor for the occurrence of oxidative stress-based nervous system pathologies associated with ageing	0.1
Fiorani <i>et al.</i> , 1997	able to potentiate the cellular damage induced in vitro by oxidizing agents	0.2-0.5
Frahm <i>et al.</i> , 2010	Increased production of reactive oxygen species (ROS)	1.0

Source: Bioinitiative, 2013

## INVESTIGATION OF MACRO AND MICRO ELEMENTAL CONTENT IN BROILER FEED USING NUCLEAR TECHNIQUE

M. S. Anas<sup>\*1</sup>; Y. A. Ahmed<sup>2</sup>; B. Balarabe<sup>1</sup>; N. N. Garba<sup>1</sup>; Aliyu Y<sup>1</sup>.

<sup>1</sup>Physics Department, Ahmadu Bello University, Zaria, NIGERIA

<sup>2</sup>Centre for Energy Research and Training, Ahmadu Bello University, Zaria, NIGERIA

Email: abuumair399@gmail.com

SCIENTIFIC REVIEW OF THE IMPACT OF RADIATIONS FROM HOME APPLIANCES ON HUMAN HEALTH

### ABSTRACT

*This study evaluate the presence and relatively adequacy of macro and micro nutrient content in some selected and commonly sold broiler feed within Kaduna state metropolis Nigeria. Eight (8) different samples (4 starter and 4 finisher) were analyzed using Neutron Activation Analysis (NAA) which has been proven to be non-destructive technique. The result shows that essential macro nutrient such as Mg, Al, K, Ca, Na and Cl were significantly presence in all sample except Mg and Al which were below detection limit (BDL). Micro nutrient such as Fe, CU, Mn, Zn, Co and Cr were virtually presence but Cu is below detection limit (BDL). The result and other related research result within Kaduna state metropolis can be used as a tool to further ensure broiler feed quality control for close monitoring of feed contamination by governments and environmentalist, to avoid toxicity to animals (broiler) as well as human after consumption.*

**Keywords:** Neutron Activation Analysis (NAA); Macro and Micro Elements;

### Introduction:

Mineral elements are divided into two major classes depending on the quantity that is required by the animals (Broiler Chicken). These elements are: Macro-nutrients or major elements, micro-nutrient or trace element. Macro nutrients are nutrient required in large quantity for healthy growth and performance of the animals (Broiler bird) e.g. Calcium (C), Potassium (K), Magnesium (Mg), Chlorine (Cl), Sulphur (S), Phosphorous (P) Sodium (Na) e.t.c. Micro nutrient are required in small quantity for health growth of the animals e.g. Iron (Fe), Copper (Cu), Cromium (Cr), Iodine (I), Manganese (Mn) Selenium (se) Zinc (Zn). Micronutrients also include vitamins which are organic compounds required as nutrient in trace amount. Base on the above description, the nutrient content or requirement should vary from one another. On the bases of physiological structures genetically improved poultry (Broiler), a good knowledge of their nutritional requirement is very important. These nutrient are essential to be in appropriate amount and proportion in the diet of

intensively housed birds, because they have no access to other sources of nutrients. So also, the dietary requirement varies with age body weight and rate of growth of the birds (Broiler). Thus, the requirement of any nutrient may be defined as the amount of that nutrient which must be supplied in the diet to meet the needs of the normal healthy animal given on other wise completely adequate diet in an environment compatible with good health (Anas *et al.* 2015). Such level of nutrient must meet the requirement for maintenance, growth productive and reproductive potential of the animal (NRC, 1994). Also, their deficiency or excess can cause problems to the animals as well as the consumers.

Poultry farming is one of the most important aspects of agriculture with commercial layers and broilers contributing tremendously in meeting the upward protein demand of the increasing population through eggs and meats. Supplementation of some essential metals such as Copper (Cu) Zinc (Zn) and Manganese

(Mn) in chickens' diets is of great importance. Copper prevents anaemia, while Zn and Mn act as catalysts in many enzymatic and hormonal reactions that are related with growth, immunity and skeletal integrity (McDowell, 1992). Supplementation of Cu, Zn and Mn at 8, 40 and 60 ppm ( $\mu\text{g/ml}$ ) respectively was recommended in broiler diets by (NRC 1994) majorly in term of growth.

However, Cu deficiency in birds can lead to rupture of the aorta. Diets deficient in Zn cause retarded growth, shortening and thickening of leg bones and enlargement of the hock joint, poor feathering, anorexia and mortality. Chicks hatched from Zn-deficient hens are weak, while a deficiency of Mn in the diet of chickens is one of the causes of perosis. Nickel is a transition metal with an atomic structure very similar to that of cobalt. Although it is not normally added to chicken diets, but nickel has been detected in liver, kidney and muscle of broilers (Coleman *et al.*, 1992). Evidence of nickel deficiencies in chicks has been reported (NAS, 1980) and dietary nickel levels of 0.1 – 0.3 parts/ $10^6$  or  $\mu\text{g/ml}$  dry weight are considered adequate in poultry diets (Puls, 1988). Heavy metals are ubiquitous and are being released continuously from man-made sources into the aquatic and terrestrial ecosystems, threatening the health of man and animals (Aschner, 2002; Abulude *et al.*, 2006, Abulude *et al.* 2006). They are potentially dangerous due to their toxicity, bioaccumulation and biomagnification abilities when found within living tissue (Kapsimalis *et al.*, 2000), and are stored more quickly than they are excreted. The increase in urbanization, industrialization and agricultural activities have been shown to release heavy metals into the environment (Khalid *et al.*, 2007). In early 2010, there was an incidence of heavy metal poisoning in Zamfara State Nigeria, due to indiscriminate mining by the locals (WWPPR, 2010). In Port-Harcourt and other southern parts of Nigeria, heavy metal contaminations of chicken meat, eggs and other products have been reported

(Okoye *et al.*, 2011; Oforka *et al.*, 2012). Okoye *et al.* 2011 speculated that heavy metals in chicken products could be due to contamination of chicken feeds, the raw materials of which are of various origins. However, little works are available on heavy metal contamination of poultry feed to confirm this speculation and there is no report of such from the study area.

Several studies have shown that high dietary intakes of energy and energy-supplying macronutrients (fat, protein and carbohydrate) may have a positive association with human body. Additionally, fruits and vegetables as sources of dietary fiber, folate, phytoestrogens, vitamin C, selenium, carotenoids, phenols, and flavonoids could protect against the development of colorectal cancer (CRC). Antioxidants are reported to function by trapping free radicals and reactive oxygen molecules at the cellular level, thus acting as a protective mechanism against oxidative damage. Free radicals in the body are generally produced during metabolic processes, such as those involving digestion. For example, iron found in red meat is reported to be a source of free radicals present in the body. Generally, in many households, meals high in fat are usually low in fruits, vegetables and fiber. Therefore, it is unclear if this increase risk in developing CRC is attributable to the high fat intake or the low fruit, vegetable and fiber intake. Free radical-induced lipid peroxidation has been implicated in malignant transformation. The formation of lipid peroxidation products is normally prevented or scavenged by host antioxidants. Low levels of antioxidant nutrients in circulation have been associated with an increased risk of cancer. There are twenty nine elements known which are required by at least one animal species. According to usual division, seven elements are macro-minerals whose requirements or concentrations in organism are expressed by over 100ppm, and 22 elements are micro-minerals in traces whose requirements are



below 100ppm, and even can be expressed in ppb values (Kapsimalis *et al.*, 2000). Of course this classification does not reflect important or less important role of these nutrients, but only necessary quantities in diets or their generally low (or in traces) concentration in tissues. However, in researches relating to mineral nutrition of poultry interest in several minerals is predominant, therefore this study will be focused on several nutrients for which in ordinary diets additional sources are necessary. In this paper a short review of the latest results of calcium, phosphorus and some micro-elements studies which suggest certain practical changes in mineral nutrition of poultry is presented.

### Material and Method

#### Materials

The materials required for the experiment are: Reactor for irradiation, Distil water, HPGe detector, samples for analysis, analytical balance, Glove, Cylinder vials, laboratory agate and mortar, cotton wool, acetone sieve, white papers, forceps spatula, (Oladipo 2003 and Anas *et al.*, 2016)

### Method

In the process of NAA the neutrons interact with the stable isotopes of the target element converting them to radioactive ones. In this research the procedures and steps prepared by Jonah *et al.*, 2005 was adopted for these research and identification of gamma-ray of product radionuclides through their energies and quantitative analysis of their concentrations are achieved using the gamma-ray spectrum analysis software, WINSPAN 2004 in NAA laboratory at Centre for research and training (CERT) Ahmadu Bello University Zaria.

### Result and Discussion

#### Result

Table 3.1 and 3.2 shows list of broiler feeds analyzed for radioactive element, and concentration in part per million (ppm or  $\mu\text{g/g}$ ). The reported uncertainty was calculated mainly from counting statistic and is not normal standard deviation on replicate analyses.

**Table 3.1: Shows the Concentration of Elemental Content in the Broiler Stater Feed with Sample Identification as STA, STB, STC and STD.**

Element	Sample BFA	Sample BFB	Sample BFC	Sample BFD
Mg	21890 $\pm$ 197	61180 $\pm$ 306	32320 $\pm$ 193	BDL
Al	1014 $\pm$ 20	1304 $\pm$ 55	1001 $\pm$ 30	BDL
Cl	1950 $\pm$ 37	2496 $\pm$ 50	1353 $\pm$ 46	14640 $\pm$ 614
Ca	236900 $\pm$ 2132	282200 $\pm$ 2540	169600 $\pm$ 1696	214000 $\pm$ 1562
V	3.59 $\pm$ 0.70	1.60 $\pm$ 0.30	1.00 $\pm$ 0.09	BDL
Cu	BDL	BDL	5.31	BDL
Mn	174 $\pm$ 1	214 $\pm$ 1	139.9 $\pm$ 0.4	24310 $\pm$ 73
Sr	822 $\pm$ 27	607 $\pm$ 12	368 $\pm$ 10	BDL
Na	890 $\pm$ 2	1060 $\pm$ 2	2048 $\pm$ 4	707 $\pm$ 2
K	6381 $\pm$ 121	7814 $\pm$ 125	8794 $\pm$ 158	2584 $\pm$ 90

Table 3.1 continues

Element	Sample BFA	Sample BFB	Sample BFC	Sample BFD
K	6381±121	7814±125	8794±158	2584±90
As	0.06±0.01	0.13±0.02	0.12±0.03	1.42±0.02
Br	1.23±0.05	1.65±0.07	2.28±0.11	0.76±0.06
La	0.93±0.03	1.06±0.04	0.82±0.04	4.41±0.05
Sm	BDL	0.27±0.01	0.23±0.01	1.14±0.01
U	0.032±0.002	0.051±0.003	0.026±0.003	0.047±0.003
Sc	0.21±0.01	0.23±0.01	0.19±0.01	0.81±0.03
Cr	2.11±0.37	2.80±0.43	1.22±0.33	BDL
Fe	1312±67	1493±64	1294±76	23790±214
Co	0.17±0.03	0.08±0.02	0.10±0.02	6.75±0.08
Zn	83.6±4.9	100±5	75.4±4.7	12750±51
Rb	11.9±1.7	14.3±1.8	17.1±1.8	BDL
Ba	101±12	135±18	89.1±11.6	1424±33
Nd	BDL	BDL	BDL	BDL
Eu	BDL	BDL	BDL	0.13±0.03
Yb	BDL	BDL	BDL	BDL
Lu	BDL	BDL	BDL	BDL
Th	0.07±0.02	0.11±0.02	0.09±0.02	0.21±0.03

**Table 3.2: Shows the Concentration of Elemental Content in the Broiler Finisher Feed with Sample Identification as BFA, BFB, BFC and BFD.**

Element	Sample BFA	Sample BFB	Sample BFC	Sample BFD
Mg	21890±197	61180±306	32320±193	BDL
Al	1014±20	1304±55	1001±30	BDL
Cl	1950±37	2496±50	1353±46	14640±614

Table 3.2 continues

Element	Sample BFA	Sample BFB	Sample BFC	Sample BFD
Ca	236900±2132	282200±2540	169600±1696	214000±1562
V	3.59±0.70	1.60±0.30	1.00±0.09	BDL
Cu	BDL	BDL	5.31	BDL
Mn	174±1	214±1	139.9±0.4	24310±73
Sr	822±27	607±12	368±10	BDL
Na	890±2	1060±2	2048±4	707±2
K	6381±121	7814±125	8794±158	2584±90
As	0.06±0.01	0.13±0.02	0.12±0.03	1.42±0.02
Br	1.23±0.05	1.65±0.07	2.28±0.11	0.76±0.06
La	0.93±0.03	1.06±0.04	0.82±0.04	4.41±0.05
Sm	BDL	0.27±0.01	0.23±0.01	1.14±0.01
U	0.032±0.002	0.051±0.003	0.026±0.003	0.047±0.003
Sc	0.21±0.01	0.23±0.01	0.19±0.01	0.81±0.03
Cr	2.11±0.37	2.80±0.43	1.22±0.33	BDL
Fe	1312±67	1493±64	1294±76	23790±214
Co	0.17±0.03	0.08±0.02	0.10±0.02	6.75±0.08
Zn	83.6±4.9	100±5	75.4±4.7	12750±51
Rb	11.9±1.7	14.3±1.8	17.1±1.8	BDL
Ba	101±12	135±18	89.1±11.6	1424±33
Nd	BDL	BDL	BDL	BDL
Eu	BDL	BDL	BDL	0.13±0.03
Yb	BDL	BDL	BDL	BDL
Lu	BDL	BDL	BDL	BDL
Th	0.07±0.02	0.11±0.02	0.09±0.02	0.21±0.03

### Discussion:

The result obtained from the Tables (3.1 & 3.2) above on macro and micro elemental composition of the different feeds (Broiler Starter and Finisher) of four (4) different company were as shown in the tables above. There are 27 elements shown in both tables analyzed by Neutron Activation Analysis (NAA). Some of the elements were found to be detected in all the samples, some below detection limit (BDL) in some and detected in others.

In this analytical result of table 4.1, (Broiler Starter) Mg, Al, Ca, Mn, Na, K, Br, La, Sn, Sc, Co, Zn, Rb and Ba were detected in all the samples. In sample STA; V, Cu, Sr, As, U, Cr, Nd, Jb and Lu were below detection limit (BDL). In sample STB: Cu, As, U, Cr and Lu were below detection Limit. In sample STC; V, Cu, Sr, As, U, Cr, Fe, Nd, Eu, Yb, Lu and Tj were below detection limit. Elements V, Cu, Sr, As, U, Cr, Nd, Eu, Yb, Lu and Th were below detection limit in sample STD. Overall, Cu, As, U, Cr, and Lu found to be below detection limit in all the samples.

It was observed that sample STB in this table has the highest number of detected element of 22, followed by sample STA, STD and STC respectively. These elements are of high significant or importance for the healthy growth and maintenance of the birds (chicks) at early stage (0-4 weeks) and above. Thus are essential and must be provided in a correct proportion. Though some of the elements are of little importance in the feed and animals but essential trace element like; Chromium (Cr) that helps the body to use sugar, protein and fat was below detection limit in all the samples. Iron (Fe) is responsible for the formation of haemoglobin in red blood cells (RBC) and its deficiency leads to anaemia was detected in sample STA, STB, STD and below detection limit in sample STC. Copper (Cu) functions as it catalyses the use of iron and helps for proper respiration in some aerobic organisms was below detection limit in all the samples. Zinc

(Zn) is important and needed for the body's defence (immune) system to properly work and plays role in cells division, growth, wound, healing and breakdown of carbohydrate was detected in all the samples. Manganese (Mn) required in the process of growth and also act as cofactor in some enzymatic reaction was also detected in all the samples.

Elemental concentration between the different samples of some of the important major and trace element was observed. Mg in sample STB>STC>STA>STD, Al in sample STB>STA>STD and >STC. Cl in sample STB>STA>STC and >STD and >STA, K in sample STA>STD>STC and >STB. Mn in sample STC>STB>STD and >STA, Cu and Cr were below detection limit in all samples. Fe in sample STB>STA>STD and below detection limit in sample STC, Zn in sample STA>STB>STC and >STD, Co in sample STB>STA>STD and >STC respectively. Sample were indicated to have the highest major elements concentration and relatively appreciable concentration of trace elements.

In table 4.2, the feed (Broiler Finisher) is fed to the birds above four 94) weeks of age. There were 21 detected elements in sample BFA, 22 in sample BFB, 23 in sample BFC and sample BFD 17 respectively. Unlike table 4.1, the essential major elements were not detected in all the samples. Magnesium (mg) that is required for muscle contraction, utilization of iron and present in teeth and bones was detected in sample BFA, BFB, BFC and below detection limit in sample BFD. Chlorine (Cl) needed for osmotic balance of the cells and transmission of nerve impulses for bone formation and development, blood clotting and normal functioning of the heart, muscles and nervous system was found in all the samples. Sodium (Na) required for nerve impulse transmission and maintenance of osmotic balance of the cells was detected in all the samples and also potassium (K) which its deficiency result to muscle paralysis was

detected in all the samples.

Trace elements take maganese (Mn), Iron (Fe), cobalt (Co) and Zinc (Zn) were found to be detected in all the samples. Copper (Cu) was only detected in sample BFC and below detection limit in BFA, BFB and BFD. Chromium (Cr) was detected in sample BFA, BFB, BFC and below detection limit in sample BFD. Other trace elements such as V, As, Br, La, U, Se, Ba and Th were found to be detected in all the samples. Nd, Yb and Lu were below detection limit in all the sample, while Eu was only detected in sample BFD, Sm in sample BFB, BFC and BFD, Sr in sample BFA, BFB and BFC. As said earlier, some of the elements have little importance in the feed as animals body e.g. Al, but S and P (Sulphur and Phosphorus) have closely related function with calcium and Magnesium. Deficiency of some of these element results to one problem or the other especially those that are essential in young animals known as rickets, weakening of the bones (Osteomalacia) and in large animals Milk fever, Na deficiency leads to muscle cramps, kidney failure, mental apathy and reduced appetite, deficiency in Mg leads to nervous disorder. Trace element like Fe, Cu, and Co deficiency leads to anemia while Mn causes impaired growth, changes in Carbohydrate and lipid metabolism, also interfere with skeletal development.

Concentration of some of the elements between the different feed samples was also observed. Mg in sample BFB, BFC, BFA and below detection limit in sample BFD, Cl in Sample BFD>BFB>BFA and >BFC, Ca in sample BFB>BFA>BFD and >BFC, Na in sample BFC>BFB>BFA and >BFD, K in sample BFC>BFB>BFA and >BFD, V in sample BFA>BFB>BFC and below detection limit in sample BFD, Mn in sample BFD>BFB>BFA and >BFC, Sr, sample BFA>BFB>BFC and below detection limit in BFD, As in sample BFD>BFB>BFA and >BFC, Sm in sample BFD>BFB>BFA and >BFC and below detection limit in A, U in

sample BFB>BFD>BFA and >BFC, Sc in sample BFD>BFC>BFB and >BFA, Cr in sample BFB>BFA>BFC and below detection limit in sample BFD, Fe in sample BFD>BFB>BFA and >BFC, Co in sample BFD>BFA>BFC and >BFB, Zn in sample BFD>BFB>BFA and >BFC, Rb in sample BFC>BFB>BFA and below detection limit in BFD, Ba in sample BFD>BFB>BFA and >BFC and Th in sample BFD>BFB>BFC and >BFA respectively.

Therefore monitoring the concentration of these different elements in these feeds is important, to render the meat from these animals and their byproduct fit for consumption to safeguard public health. This is because ingestion and absorption of these elements in high or above the normal requirement, toxicity would be occurred and leads to failure or malfunction of some certain organs like kidney, liver, pancrease and even death of the animals e.g. Zinc (Zn), Iron (Fe) and Chromium (Cr) in high amount causes toxicity to the animals (Surtipantiet *al.*, 1990 and Okoye *et al.*, 2011).

### Conclusion

In this work, eight (8) different samples of four different companies were bought or purchased from different retailers within Kaduna Metropolis (both starter and finisher) and there elemental composition and concentration was analyzed using neutron activation analysis (NAA). In all the tables, there was appreciable presence of significant number of Micro and Macro elements (Zn, Fe, Cr, Co, Mn, Cu, and Al, Ca, K, Cl, Mg, Na) etc. Though Mg & Al in table 4.2 were below detection limit (BDL) in sample BFD. Trace element like Cu and Cr were below detection limit in all the sample and Fe only in sample STA in table 4.1, then Cr is below detection limit only in sample BFD in table 4.2.

Indeed, the distribution of Zn element in table 4.2 has higher concentration in all the samples and table 4.1 only in sample STA, this shows

Zn is above the permissible limit. Fe has higher concentration also in all the samples in table 4.2 and 4.1 only in sample BFB, therefore there is relatively high level of iron toxicity in table 4.2 (Broiler Finisher) and low in table 4.1 (Broiler starter).

However, the level of other elements in all the samples in table 3.1 and 3.2 were within the tolerance limit. It has been demonstrated that, the method used (Neutron activation analysis NAA) is a non-destructive technique, requires no sample dissolution and it is ideal method for elemental (Micro and Macro element) determination of different broiler feeds.

## References

- Abulude FO, Akinjaagunla YS & Omoniyi A (2006a). An investigation into the effect of vehicular exhaust fumes on the levels of some heavy metals in cows' blood. *Research Journal of Biological Sciences*, **1**(1-4): 9-11.
- Abulude FO, Eluyode SO & Jegede A (2006b). An investigation into the effect of traffic pollution on the levels of some heavy metals in goats' urine samples. *Journal of Animal and Veterinary Advances*, **5**(2): 132-134.
- Aschner M (2002). Neurotoxic mechanism of fish-borne methylmercury. *Environmental Toxicology and Pharmacology*, **12**(2): 101-102.
- Anas, M.S., Ahmed, Y.A., Yusuf (2016): Determination of Trace and Heavy metals in selected Nigeria Broiler Feeds by Neutron Activation Analysis (NAA). *Journal of Nuclear EnSci Power Generate Technology* **5**(3).
- Anas, M.S., Nuhu, A., Yusuf, J.A. (2016): Assessment of Elemental Composition in Selected Nigeria Broiler Feeds Using Neutron Activation Analysis (NAA). *Veterinary Science of Medicine Diagnosis* **5**(3).
- Anas M. S Abdullahi S. Yusuf J. A. Bala B. Salihu Y. B. (2015) Assessment of Toxic elements in selected Nigeria Broiler Feeds using neutron activation analysis (NAA) *Bayero Journal of Pure and Applied Sciences* **8**(2): 166-169.
- Coleman ME, Elder RS & Basu, P (1992). Trace metals in edible tissues of livestock and poultry. *Journal of the Association of Official Analytical Chemists International*, **75**(4): 615-625.
- European Commission; Health and Consumer Protection Directorate - General, Belgium (2003). Opinion of the Scientific Committee on Animal Nutrition on Undesirable Substances in Feed. [http://ec.europa.eu/food/fs/sc/scan/out126\\_bis\\_en.pdf](http://ec.europa.eu/food/fs/sc/scan/out126_bis_en.pdf), retrieved 10-04-2015.
- Falandysz J, Szymczyk-Kobrzynska K, Brzostowski A, Zalewski K & Zasadowski A (2005). Concentrations of heavy metals in the tissue of red deer (*Cervus elaphus*) from the region of Warmia and Mazury, Poland. *Food Additives and Contaminants*, **22**(2): 141-149.
- McDowell LR (1992). *Minerals in Animal and Human Nutrition: Comparative Aspects to Human Nutrition*. Second edition, Academic Press Inc., San Diego, USA. Pp 246-263.
- NAS (National Academy of Sciences) (1980). *Mineral Tolerance of Domestic Animals*, Washington DC, National Academy Press. Pp 1-511.
- NRC (1994). *Nutrient Requirements of Poultry. 9th revised edition*, National Academy of Sciences, Washington, DC. Pp 19-34.
- Oforika NC, Osuji LC & Onwuachu UI (2012). Estimation of dietary intake of cadmium, lead, manganese, zinc and nickel due to consumption of chicken meat by inhabitants of Port-Harcourt Metropolis, Nigeria. *Archives of Applied Science Research*, **4**(1): 675-684.
- Okoye COB, Ibeto CN & Ihedioha JN (2011). Assessment of heavy metals in chicken feeds sold in south eastern Nigeria. *Advances in Applied Science Research*, **2**(3): 63-68.
- Puls R (1988). Mineral levels in animal health: Diagnostic Data, (Second edition.). Sherpa International, Clearbrook, British Columbia, Canada. Pp. 356.
- WWPPR 2010 Six pollutants that jeopardize the health of tens of millions of people. In: *Top Six Toxic Threats*. Blacksmith Institute, Fifth

Avenue New York, NY 10035 US. Pp. 1 – 76.0  
 Kapsimalis B., Palmiro, V. Saueia C., Nisti, M.  
 B (2000): Radiochemical Characterization of  
 Brazilian Phosphogypsum *Journal of  
 Environment Radioactivity* 49:113-122.  
 Kapsimalis R, andsberger S, Ahmed YA (2009)  
 e determination of uranium in food samples  
 by Compton suppression epithermal neutron  
 activation analysis. *Applied Radiation and  
 I s o t o p e s . 6 7 : 2 0 9 7 – 2 0 9 9 .*  
 Khalid N. Rahman S. Ahmad, S., Alli, S.  
 (2007). Trace Metals Determination in

Chicken Eggs. *The Nucleus* 44(1-2)L 39-44 J.I.  
 Gerberding, Toxicological Profile Forzinc,  
 Atlanta Georgia, 2005, Pp. 22 and 23 J.H.  
 Koplan, Atlanta Georgia, 2000a, 26p.  
 Surtipanti, S., Suwirma, S., Yumiarti, S.,  
 YuneMellawati, (1990): Determination of  
 Heavy  
 Metals in Meat, Intestine, Liver, Eggs and  
 Chicken Using Neutron Activation Analysis  
 and Atomic Absorption Spectrometry, Center  
 for the Application of Isotopes Radiation,  
 BATAN.

## A GENERALIZATION OF SCHRODINGER EQUATION FOR PARTICLE MOTION IN THE GRAVITATIONAL FIELD OF HOMOGENOUS SPHERICAL DISTRIBUTION OF MASS

\*<sup>1</sup>Lumbi, L.W.,<sup>1</sup>Nwagbara, O.,<sup>1</sup>Ewa, I. I., <sup>2</sup>Yakubu, N., <sup>3</sup>Nweze, N. O. & <sup>4</sup>Bamikole, J. A.

<sup>1</sup>Department of Physics, Nasarawa State University, Keffi, Nigeria.

<sup>2</sup>Department of Physics, University of Maiduguri, Nigeria.

<sup>3</sup>Department of Mathematical Sciences, Nasarawa State University, Keffi,

<sup>4</sup>Department of Physics, Federal University Lafia, Nigeria.

Email: williamslucas44@gmail.com

### ABSTRACT

*In this article the Riemannian geometry was applied to generalize the well-known Schrodinger's quantum mechanical wave equation for particles of non-zero rest masses in the gravitational field. The results are that the Riemannian quantum mechanical wave equation reduces to  $c^0$  to the well-known Schrodinger's quantum mechanical wave equation and to the order of  $c^{-2}$  it contains additional correction terms which are open up for theoretical development and experimental investigation and applications.*

**Keywords:** *Riemannian Geometry, Schrodinger's Quantum Mechanical Wave Equation, Non - zero Rest Masses and Gravitational Field.*

### Introduction

It is well known that the origin of quantized motion cannot be explained by classical mechanics. The old quantum theory is also inadequate to give a logical explanation for the quantization of certain dynamical quantities in the atomic or subatomic domain.

According to Heisenberg the reason for this failure of the old quantum theory is due to the formulation of the theory on the basis of classical concepts. Heisenberg argued that we should try to develop an atomic mechanics on the basis of quantities which are actually observable in the atomic state, example the energies of the atomic states found by measuring the wavelengths of the spectral lines, intensities of the spectral lines etc. Quantities example the positions or the velocities of the electrons which appear in the old quantum theory cannot be precisely determined because of the uncertainty

principle and hence cannot describe the behavior of atomic systems (Isham *et al.*, 1975; Alvares, 1989).

In 1926 Erwin Schrodinger published an equation which governs the propagation of electron waves. It turned out that Werner Heisenberg had also published a seemingly different theory to explain atomic phenomena. Both the Heisenberg theory and the Schrodinger theory did correctly describe the same phenomena in different presentations. The main distinction between Newtonian (classical) mechanics and quantum (wave) mechanics lies in what they describe as the motion of the particle under the influence of applied force and takes for granted that such quantities as particle position. Its mass, velocity acceleration etc are measurable. Such assumption is completely valid in our day to day experience and Newtonian mechanics provides the correct explanation of the



behavior of moving bodies in the sense that the value it predicts for observation magnitude agree with measured value of these magnitudes. The certainties proclaimed by Newtonian mechanics are illusory and their agreement with experiment is a consequence of the fact that macroscopic bodies are aggregates of microscopic particles and our measurements are the mean of the general behavior. Taken individually, each particle would yield quantum results rather than Newtonian results, thus we only have one set of physical principles that govern our universe, and so far those principles are best described by quantum mechanics (Isham *et al.*, 1975; Alvares, 1989; Ali, 1992; Cathryn, 2000). Schrodinger invention of waves mechanics represent an attempt to overcome some difficulties generated by classical mechanics. The equation also provides a way of generalizing a wave function of a system and how it change dynamically with time. The equation was also successful in describing microscopic particle but is based on the Euclidean geometry and cannot describe particles in the non- relatives region. In this article, the Riemannian geometry was applied to generalize the well - known Schrodinger quantum mechanical wave equation for particles of non - zero rest masses in the gravitational field of static homogeneous spherical massive bodies to obtain additional correction terms which are open up for theoretical development and experimental investigation and applications.

### Theoretical Analysis

According to Newton's dynamical theory of classical mechanics (NDTCM) the classical mechanical energy,  $E$ , and the linear momentum vector,  $p$ , for a particle of nonzero rest mass in a gravitational field is given by (Dirar *et al.*, 1998; Howusu, 2010; Howusu, 2013).

$$E = \frac{1}{2} m_0 u^2 + m_0 f \quad (1)$$

and

$$p = m_0 u \quad (2)$$

where,  $m_0$  is the rest mass,  $u$  is the Euclidean linear speed and  $f$  is the well-known Newtonian gravitational scalar potential exterior to the body for static homogeneous spherical massive bodies

Consequently equation (1) can be expressed in terms of the linear momentum as

$$E = \frac{p^2}{2m_0} + m_0 f \quad (3)$$

According to Bohr's Correspondence and complementary principles if  $\underline{r}$  is the position vector,  $\underline{p}$  is the instantaneous momentum vector of an entity,  $t$  is the time and  $E$  is the instantaneous mechanical energy of an entity, then the corresponding quantum mechanical operator  $\hat{r}$ ,  $\hat{p}$ ,  $t$  and  $\hat{E}$  are given by (Howusu, 2010; Howusu, 2013).

$$\hat{r} = \underline{r} \quad (4)$$

$$\hat{p} = i\hbar \nabla \quad (5)$$

$$\hat{t} = t \quad (6)$$

$$\text{and } \hat{E} = -i\hbar \frac{d}{dt} \quad (7)$$

where,  $i$  is the imaginary unit,  $\hbar$  is the Dirac constant and  $\nabla$  is the Euclidean geometry. It follows from equations (3) subject to (4), (5), (6) and (7) that the quantum mechanical equation is given as

$$i\hbar \frac{d\psi}{dt} = \left( -\frac{\hbar^2}{2m_0} \nabla^2 + m_0 f \right) \psi \quad (8)$$

or more explicitly

$$\hat{E}\psi = H\psi \quad (9)$$

where,  $\psi$  is the mechanical wave function and  $f$  is the Newton's gravitational scalar exterior for static homogeneous spherical massive bodies which is derived based on the Euclidean geometry.

The Riemannian field equation,  $\nabla_R^2$  and gravitational scalar potential,  $f$ , exterior for static homogeneous spherical massive bodies is given explicitly by (Howusu, 2010; Lumbi *et al.*, 2014).

$$\nabla_R^2 = \frac{1}{r^2} \frac{d}{dr} \left[ \left( 1 + \frac{2}{c^2} f \right) r^2 \frac{d}{dr} (x^0, r, \theta, \phi) \right] + \frac{1}{r^2 \sin \theta} \frac{d}{d\theta} \left[ \sin \theta \frac{d}{d\theta} (x^0, r, \theta, \phi) \right] + \frac{1}{r^2 \sin^2 \theta} \frac{d^2}{d\theta^2} (x^0, r, \theta, \phi) - \frac{1}{c^2} \frac{d}{dr} \left[ \left( 1 + \frac{2}{c} f \right)^{-1} \frac{d\psi}{dt} (x^0, r, \theta, \phi) \right] \quad (10)$$

and

$$f = -\frac{Gm_0}{r} \left[ 1 - \frac{Gm_0}{c^2 R} \right] - \frac{G^2 m^2}{c^2 r^2} \quad (11)$$

where,  $G$  is the universal gravitational constant,  $m$  is the mass of the planets,  $r$  is the radial distance from the centre of the sun,  $R$  is radius of the planet and  $r$  is the speed of light in vacuum.

Substituting equations (10) and (11) into (8) and simplifying we obtain

$$\begin{aligned} i\hbar \frac{d}{dt} \psi_R = & \left\{ M_0 c^2 \left[ 1 + \frac{2}{c^2} \left[ -\frac{Gm}{r} \left( 1 - \frac{Gm_0}{c^2 R} \right) - \frac{G^2 m^2}{c^2 r^2} \right] \right]^{\frac{1}{2}} \right. \\ & - \frac{\hbar}{m_0 c^2} \left\{ \frac{1}{r^2} \frac{d}{dr} \left( 1 + \frac{2}{c^2} \right) r^2 \frac{d}{dr} (x^0, r, \theta, \phi) + \right. \\ & \frac{1}{r^2 \sin \theta} \frac{d}{d\theta} \left\{ \sin \theta \frac{d}{d\theta} (x^0, r, \theta, \phi) \right\} + \frac{1}{r^2 \sin^2 \theta} \frac{d^2}{d\theta^2} \\ & (x^0, r, \theta, \phi) - \frac{1}{c^2} \frac{d}{dr} \left[ \left( 1 + \frac{2}{c^2} \right)^{-1} \frac{d}{dt} (x^0, r, \theta, \phi) \right] \left. \right\}^{\frac{1}{2}} \\ & + M_0 \left\{ \left[ 1 + \frac{2}{c^2} \left[ -\frac{Gm}{r} \left( 1 - \frac{Gm_0}{c^2 R} \right) - \frac{G^2 m^2}{c^2 r^2} \right] \right]^{\frac{1}{2}} \left\{ 1 - \frac{\hbar}{m_0 c^2} \left\{ \frac{1}{r^2} \frac{d}{dr} \right. \right. \right. \\ & \left. \left. \left( 1 + \frac{2}{c^2} \right) r^2 \frac{d}{dr} (x^0, r, \theta, \phi) + \frac{1}{r^2 \sin \theta} \frac{d}{d\theta} \left\{ \sin \theta \frac{d}{d\theta} (x^0, r, \theta, \phi) \right\} \right. \right. \right. \\ & \left. \left. \left. + \frac{1}{r^2 \sin^2 \theta} \frac{d^2}{d\theta^2} (x^0, r, \theta, \phi) - \frac{1}{c^2} \frac{d}{dt} \left[ \left( 1 + \frac{2}{c^2} \right)^{-1} \frac{d}{dt} (x^0, r, \theta, \phi) \right] \right\} \right\}^{\frac{1}{2}} \right. \\ & \left. \left. \left. \left. - \frac{Gm}{r} \left( 1 - \frac{Gm_0}{c^2 R} \right) - \frac{G^2 m^2}{c^2 r^2} \right\} + M_0 \left\{ -\frac{Gm_0}{r} \left( 1 - \frac{Gm_0}{c^2 R} \right) - \frac{G^2 m^2}{c^2 r^2} \right\} \right\} \right\} \psi \quad (12) \end{aligned}$$

Equation (12) is the generalized Schrödinger's quantum mechanical wave equation for particles of nonzero rest masses in the gravitational field based on the Riemannian geometry.

## Remarks and Conclusion

We have shown how to generalize the well – known Schrödinger's quantum mechanical wave equation for particles of nonzero rest masses in the gravitational field using a new dynamical approach. It must be noted that to the order of  $c^0$  this equation reduces to the well – known pure Schrödinger's quantum mechanical wave equation which agrees with the well – known equivalence principles in Physics and to the order  $c^2$  it contains additional correction terms which are henceforth opened up for theoretical development and experimental investigation and applications.

## REFERENCES

- Ali, E. 1992. A Generalized Metric of Gravitation. *International Journal of Modern Physics*, Vol. 7 No. 13, Prentice Hall, Pp. 31 - 33
- Alvares, E. 1989. Quantum gravity: Introduction to some Recent Results. *Reviews of Modern Physics*, Vol. 61, No 3, Longman Press. Pp. 561-604
- Cathryn, C. 2000. The Origins of the Quantum Theory. University of Chicago Press, Pp1-14
- Dirar, M. Ali, E. & Sheddah, M.H. 1998. A Generalized Field Cosmology, *Modern Physics letter A*, Vol. 13, No. 37, Thomson Press India Ltd Pp. 3025 - 3031
- Howusu, S.X.K. 2010. Complete Dynamical Theory of Physics, Jos University Press Ltd, Jos Pp. 1-90
- Howusu, S.X.K. 2013. Riemannian Revolution in Physics and Mathematics, Jos University Press Ltd, Jos Pp. 1-200
- Isham, E. J., Penrose, R. & Sciama, D. W. 1975. Introduction to Quantum Gravity. An Oxford Symposium. Oxford University Press, London Pp. 1 - 5
- Lumbi, W.L., Howusu, S.X.K & Liman, M.S. 2014. Generalized Dynamical Gravitational Field Equation for Static Homogeneous Spherical Massive Distribution of Mass. *International Journal of Modern Theoretical Physics* 3(1): 1-12

## ASSESSMENT OF HEAVY METALS CONCENTRATION IN SOIL SAMPLES IN KAKAU DISTRICT, CHIKUN LOCAL GOVERNMENT AREA OF KADUNA STATE

**Galadima S. K; Gyuk P. M; Dogara M. D; Aboh H. O; Kure N.**

Department of Physics Kaduna State University, Kaduna

Email:galadima.sylverster@gmail.com

### ABSTRACT

*This research paper investigated the presence of heavy metals in soil samples from nine selected site in Kaku. A total of nine samples were analyzed at Centre for Energy Research and Training (CERT) Ahmadu Bello University Zaria using Atomic Absorption Spectrometer (AAS). From the result, it was found that Zn has the highest mean concentration 0.053378 mg/l and Cd, Co and Pb have lower concentration with a mean of 0.007256mg/l, 0.012656mg/l and 0.037367mg/l respectively. Ca was found in all samples point to be low, having a mean concentration 0.021867 mg/l which is less than the maximum permissible limits (MPL) recommended by W.H.O of 1.2 to 1.5 mg/l. Hence, the result shows that there were many toxic elements in the sampled area. It is advisable that substances containing heavy metals should not be disposed in farm lands or any dumpsites close to residential areas.*

**Key Words:** Soil, Heavy Metals, Atomic Absorption Spectrometer.

### Introduction:

Man's activity in the environment has led to the pollution of soil mainly by chemical contaminants. Presently in developing countries like Nigeria where studies have shown that there is high level of illiteracy in the country, inadequate awareness on how to eradicate the problem of soil pollution. The presence of heavy metals in soil can affect the quality of food, groundwater, micro-organisms activity, plant growth etc. (Antoaneta et al., 2009). When contaminated soils are later abandoned and then used for agricultural purposes such as farming, animal breeding, herding etc. Plants take in these metals in the process. The fact that they are not bio-degradable (cannot be broken down into smaller parts by bacteria), can have adverse effect on plants. Also these heavy metals have toxic effect on living organisms in the soil when permissible concentration levels are exceeded.

Heavy metals are potential environmental

contaminant with the capability of causing human problems if present in excess in eatable materials. They are given special attention throughout the world due to their toxic effects even at very low concentration (Hardware and Pramod, 2014). Heavy metals are environmental contaminants capable of causing human health problems if excess amount is ingested through food, heavy metals are non biodegradable and persistent, have a long biological half lives and can be bio-accumulated through biological chains. Heavy metal toxicity may occur due to contamination of irrigation water, the application of fertilizer and metal based pesticides, industrial emission, harvesting process, transportation, storage or sale. Crops and vegetables grown in soils contaminated with heavy metals have greater accumulation than those grown in uncontaminated soils. This is because farmlands situated in industrialized areas are prone to pollution by the release of chemicals into the farmlands leading to contamination of plant crops (Bempah et al., 2011).

These heavy metals may adversely affect soil ecology, agricultural production or product quality, and ground water quality, and will ultimately harm to living organism by food chain. These effects are closely related to the biological availability of heavy metals, which in turn are controlled by the metal ion speciation in the soil. Therefore, the determination of free metal ion concentrations in soil solution becomes important. The free metal ion concentration not only depends on the total metal content in soils, but also on the metal species that exist in the soil. (Ene *et al.*, 2009)

### Materials and Methods.

Soil samples were collected randomly in Kaku, Kaso and Kaso Mission in Kakau Districts of Chikun Local Government Area of Kaduna State. Chikun lies within latitude  $10^{\circ}10'37.928''$  to  $10^{\circ}35'59.96''$  and longitude  $007^{\circ}51'57.0''$  to  $007^{\circ}56'49.0''$ . Samples of soil were air-dried, crushed and sieved using 2mm sieve. The samples were kept in a polyethylene bag and labeled accordingly. Samples were stored in a refrigerator at  $4^{\circ}\text{C}$  prior to analysis to inactivate bacteria and prevent any change in volume that may be caused due to evaporation.

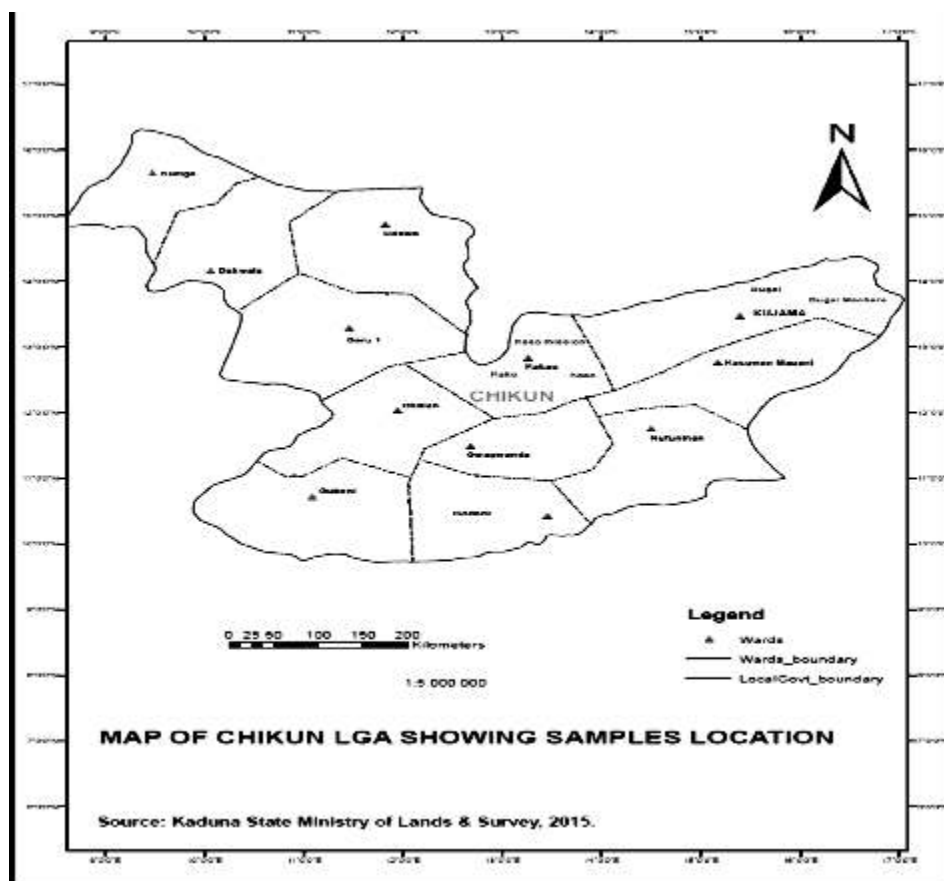


Figure 1: Map of Chikun LGA showing samples location

### Laboratory Analysis:

All reagents used to prepare standard solution were of analytical grade. Glassware was thoroughly washed with detergent and rinsed with distilled water.

### Soil Sample Analysis:

The digestion method by Francek *et al.* (1994) was adopted for the extraction of trace metals in the study. The soil was crushed and 1g was accurately weighted and

digested with 10 ml of 1:1 concentrated  $\text{HNO}_3$ . The mixture was evaporated to near dryness on a hot plate and cooled, and the procedure repeated with 1:1 concentrated  $\text{HCl}$  (15 ml). The extracts were filtered with No. 40 Whatman filter paper and then made up to 100 ml with 2%  $\text{HNO}_3$ .

Digestion was carried out for all the samples. Determination of heavy metals (Cd, Co, Ca, Pb, and Zn) in the soil was performed using the atomic absorption spectrometer (AAS) (200A Model) at the Centre for Energy Research and Training of Ahmadu Bello University, Zaria, Nigeria.

### Results and Discussions

The study was conducted in order to assess the heavy metal contamination of soil samples collected from Kaku, Kaso and Kaso Mission of Kakau District of Kaduna State. Table 1, shows the heavy metals concentration of soil sample collected randomly at various locations on the earth surface.

Soil samples were collected and analysed for heavy metals from each sampling point. A total of nine samples were obtained, three randomly per location on the earth surface and, the results of the analysis is presented in Table 1.

**Table 1: Shows the Concentration of Heavy metals on Soil samples in Kakau District**

Location		Parameter				
		Calcium (Ca) mg/l	Zinc (Zn) mg/l	Lead (Pb) mg/l	Cadmium (Cd) mg/l	Cobalt (Co) mg/l
Kaku	a	0.0153	0.0798	0.0490	0.0014	0.0012
	b	0.0160	0.2548	0.0865	0.0047	0.0845
	c	0.0669	0.3588	-0.0177	0.0024	0.0254
Kaso	a	0.0084	0.0616	0.0427	0.0084	0.0619
	b	0.0367	-0.0097	0.0052	0.0367	-0.0097
	c	0.0061	0.0266	0.1470	0.0061	0.0266
Kaso Mission	a	0.0069	0.0523	0.0042	0.0011	-0.0181
	b	0.0306	0.0040	-0.0052	0.0025	-0.0507
	c	0.0099	-0.3478	0.0448	0.0020	-0.0072

Figure 2 below, shows the mean concentration heavy metal in soil sample in Kaku points a, b and c. From the figure 1, Calcium (Ca) with a mean concentration of 0.032733 is lower than the limit set by WHO at 1.2 to 1.5 mg/l. Depending on age, exposure to high concentration could lead to rickets, tetanus, and osteoporosis. High blood pressure and colon cancer may relate to chronic low intake (naturpsthicmedical.com).

Zinc (Zn) has a mean concentration of 0.231133mg/l which is more than the permissible limit set by WHO of 0.003mg/l. this can lead to decreased growth, loss of taste and smell, sterility, poor wound healing, skin rash, hair loss, heart disease, liver disease, kidney disease, muscle weakness, arthritis,

benign prostatic hyperplasia, infertility, impotence, toxemia of pregnancy, low stomach acid, diabetes, night blindness, cataracts, and immune dysfunction (naturpsthicmedical.com).

Lead (Pb) has a mean concentration of 0.0039267mg/l which is a little higher than the WHO limit of 0.001mg/l. Cadmium also shows a mean concentration of 0.002833mg/l which is lower than the WHO limit set at 0.003mg/l. Cobalt has a mean concentration 0.03733mg/l which is higher than the WHO limit set at 0.006mg/l.

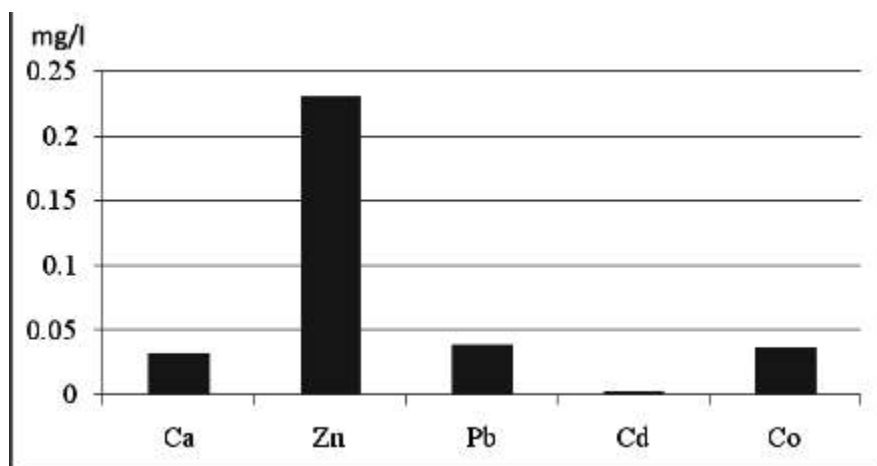


Fig.2: Mean Concentration of Heavy Metals in Soil Samples in Kakau.

Figure 3 shows the mean concentration at points a, b and c in Kaso of Kakau District collected on the surface. Calcium has a mean concentration of 0.07067mg/l which is a little lower than the WHO of 1.2 to 1.5 mg/l depending on age. Zinc has a mean concentration of 0.026167mg/l which is higher than the WHO permissible limit of 0.003mg/l; this can cause any of the conditions mention earlier. Lead on the other hand has a mean concentration 0.064967mg/l which is higher than the limit set by the WHO at 0.001mg/l; its effect can cause any of the following - Microcytic anemia, glycosuria, poor brain function, anorexia, loss of appetite, metallic taste,

insomnia, change in white blood cells. Target organs include the brain, bone, blood, kidneys, and thyroid gland (naturpsthicmedicals.com). Cadmium has a mean concentration of 0.01767mg/l which is lower than the limit set by WHO of 1.2 to 1.5 mg/l and its condition may be any mentioned above. Cadmium has a mean concentration of 0.017062mg/l which is more than the WHO permissible limit of 0.003mg/l and this may cause; Hypotension, hypertension, fatigue, anemia, proteinuria, osteomalacia, nausea, vomiting, diarrhea, emphysema. Target organs are the liver, placenta, kidneys, lungs, brain, and bones (naturpsthicmedicals.com).

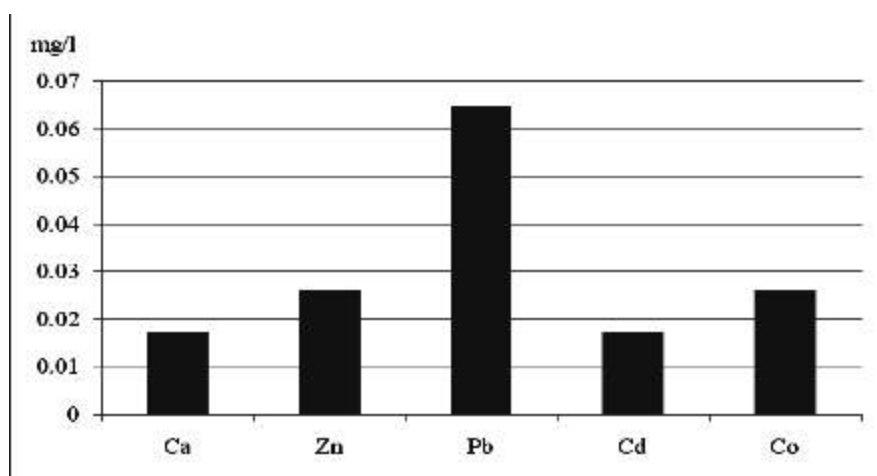
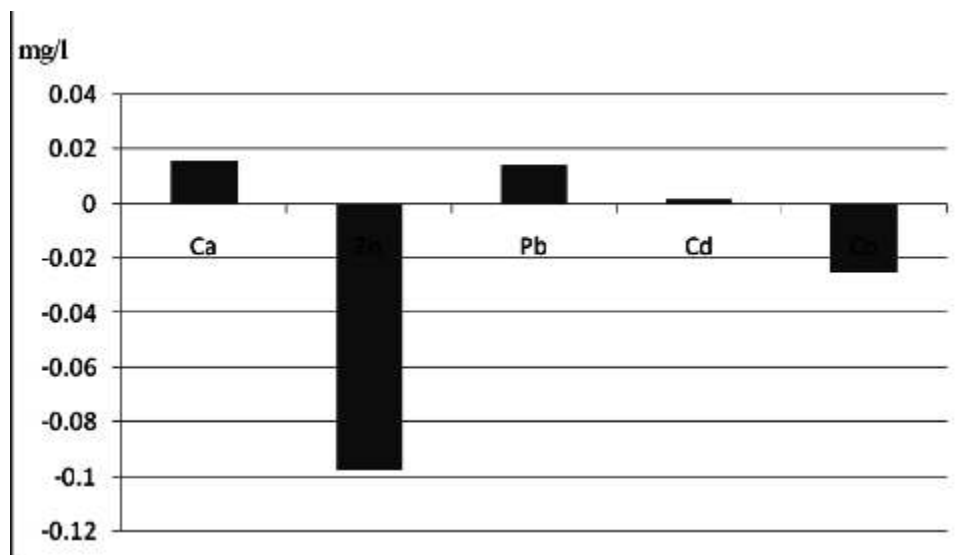


Fig.3: Mean Concentration of Heavy Metals in Soil Samples in Kaso.

Cobalt has a mean concentration 0.026267mg/l which is higher than the WHO limits 0.006mg/l and its effects may be any of this conditions; Anemias may respond to

administration of cobalt chloride. Heart, thyroid, and pancreatic damage result from toxic levels of cobalt. High alcohol use worsens toxicity.



**.4: Concentration of Heavy Metals in Soil Samples in Koso Mission**

From figure 4, Calcium has a mean concentration of 0.0158mg/l, lower than the permissible limits set by WHO of 1.2 to 1.5 mg/l. Zn has a mean concentration of -0.09717mg/l lower than the WHO limits of 0.003mg/l. Pb has a mean concentration of 0.0146mg/l lower than the WHO limit of 0.001mg/l. Cadmium on the other hand has a mean concentration of 0.001867mg/l as against the WHO permissible limit at 0.003mg/l. Cobalt has a mean concentration of -0.02533mg/l against the WHO permissible limit of 0.006mg/l. All the elements analyzed have a lower mean concentration lower than all the limit set by WHO. Its effect may be as already discussed.

### Conclusion

The study has shown that heavy metals pollution of soil is an issue of environmental concern. The results from this study revealed the presence of significant concentrations of Cd, Co, Zn and Pb in soils in Kaku, Kakau district in Kaduna state, Nigeria. Education and legislation on management of pollution in

villages should be intensified to forestall the effects of waste-related problems. The culture of reuse and recycle should be inculcated in the populace and the government should place a ban on the importation of used/damaged electronics into the country. Modern waste disposal facilities should be acquired by relevant authorities and appropriate waste disposal sites be chosen to avoid the injurious effects of indiscriminate disposal of wastes, and residential buildings should be sited farther away from areas of pollution.

### Acknowledgments

We express our sincere gratitude to all the staff members of the Physics Department of Kaduna State University for their guidance and their positive criticism that directed this work. I also wish to express my gratitude to Mr Zakka Marcus of Kaduna State Ministry of Health and Dr W.D Ibrahim of the centre for Energy Research and Training of Ahmadu Bello University, Zaria for allowing us to use their Atomic Absorption Spectroscopy machine for analysis of the samples.

**REFERENCES**

- Antoaneta E, Alina B, Georgescu L (2009): *Determination of heavy metals in soils using XRF Technique*. Rom. J. Phys. 55(7-8):815-820.
- Bempah C. K, Kwofie A.B, Tutu A.O, Denutsui D, Bentil N (2011): *Assessing potential dietary intake of heavy metals in some selected fruits and vegetables from Ghanaian market*. Elitir. Pollut. 39;4921-4926
- Ene A., Popescu I.V, Stihl C, (2009): *Applications of proton-induced X-ray emission technique in materials and environmental science*, Ovidius Univ. Ann. Chem. **20** (1), 35
- Francek M.A., M Aakinmaa B., Pan V. (1994): *Small town lead levels: A case study from the homes of preschoolers in MT-pleasant Michigan*. Environ. Pollut. **1**, 159.
- Hadware D.J and Pramod H.P (2014): *Determination of specific heavy metals in fruit juices using atomic absorption spectroscopy (AAS)*. Int. J. Res. Chem. Environ. 4(3);163-168
- Naturopathicmedicalclinic.com. *Heavy metals and their symptoms*.
- W.H.O (2004): *Guidelines for Drinking Water Quality*. 3rd ed. Geneva, 515: World Health Organization.



## GEOELECTRICAL PROSPECTING FOR FRACTURED BASEMENT AQUIFER IN NORTHERN PORTION OF FUTMINNA'S BOSSO CAMPUS, MINNA, NORTH-CENTRAL NIGERIA

<sup>1,2</sup>C. I. Unuevho, <sup>2a</sup>K. M. Onuoha, <sup>1b</sup>A. N. Amadi, <sup>1c</sup>A. A. Alabi, <sup>3d</sup>J. A. Aderogbin, <sup>4e</sup>E. E. Udensi, <sup>3f</sup>Oshin, O.

1: Department of Geology, Federal University of Technology, Minna

2: Department of Geology, University of Nigeria, Nsukka

3: Department of Earth Sciences, Ajayi Crowther University, Oyo

4: Department of Physics, Federal University of Technology, Minna

?unuevho@gmail.com, a: mosto.onuoha@gmail.com, b: geoamaa76@gmail.com, c: alabiadekola@futminna.edu.ng

d:aaderogbin@gmail.com, e:eeudensi@gmail.com, f:o.oshin@acu.edu.ng

### ABSTRACT

Only one out of three boreholes in the northern portion of FUTMINNA's Bosso Campus is productive. Values of hydrogeophysical parameters characterising fracture column at the productive borehole site were captured from vertical electrical resistivity and spontaneous potential (SP) sounding data. The values were employed to identify other sites with potential for groundwater production in the area. Sounding locations L1, L8, L14, L19 and L20 contain fracture column characterised by 200- 400? m resistivity, -10 to 20mV SP, 1200 - 2400? m<sup>2</sup> transverse unit resistance and 0.05 - 0.1? <sup>-1</sup> longitudinal unit conductance. Boreholes sited at these locations would be productive because the fracture column therein has identical values of hydrogeophysical parameters with the fracture column at the productive borehole site. Sounding locations L14 and L20 were found to be groundwater convergence zones respectively within north-western and eastern portions of the investigated area. The fracture column in the vicinity of sounding location 20 is thickest and more spatially extensive, thereby making the eastern sector the most suitable for drilling productive borehole.

**Keywords:** Fracture column, Groundwater convergence zone.

### Introduction:

Bosso campus of the Federal University of Technology, Minna (FUTMINNA) is sited within the basement complex of north-central Nigeria. A sketch map of the investigated

northern portion of the campus is Fig.1. The investigated portion hosts the FUT Model College, Staff School, Catholic Church, and Interdenominational Chapel.

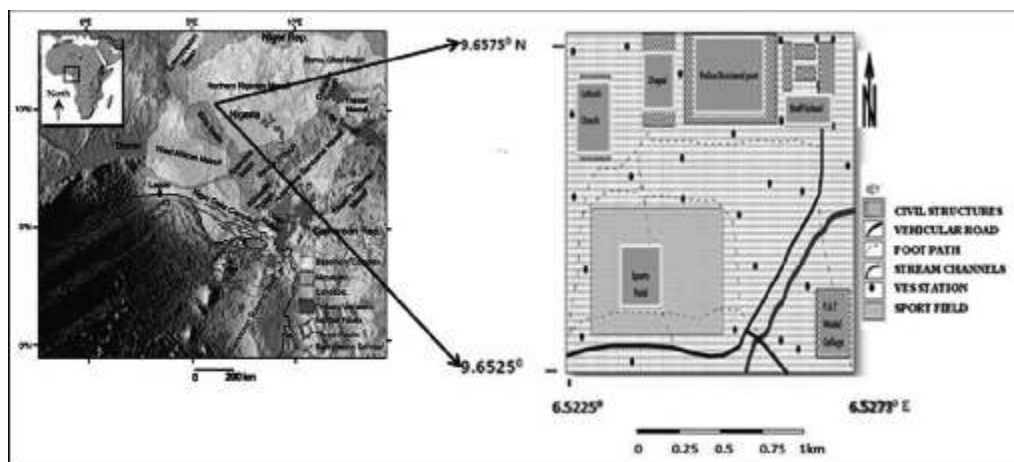


Fig.1: Northern portion of FUTMINNA's Bosso campus

Outcrops of fractured granitic rocks litter the area, and this suggests a very thin regolith. This leaves fractured basement aquifer as the only hope for steady groundwater supply

source in the area. The length of the fractures ranges from 1.0-5.5m, while their width ranges from 0.01-0.1m (Fig.2). The surface fracture density ranges from  $0.9\text{-}2.0\text{m}^{-1}$ .



**Fig.2: A fractured granitic outcrop at Lat. 9.6540°N; Long.6.5235°E**

These fracture parameters suggest the existence of fractured bedrock within the subsurface. Two boreholes in the area have failed to produce water. However, one productive borehole exists in the eastern outskirts of the investigated area. This study attempts to employ the hydrogeophysical parameters of the successful borehole site to identify other sites with potential for groundwater production within the area. The

productive borehole utilises hand operated pump to produce water. This implies it produces water from fractured basement that are shallower than 60m subsurface depth.

During oral discussions, Site –Geologists often reported encountering talc schist in the subsurface while drilling within the vicinity of the area. Outcrops of migmatite-schist complex exist NNE while schist outcrops SE of the area (Fig.3).

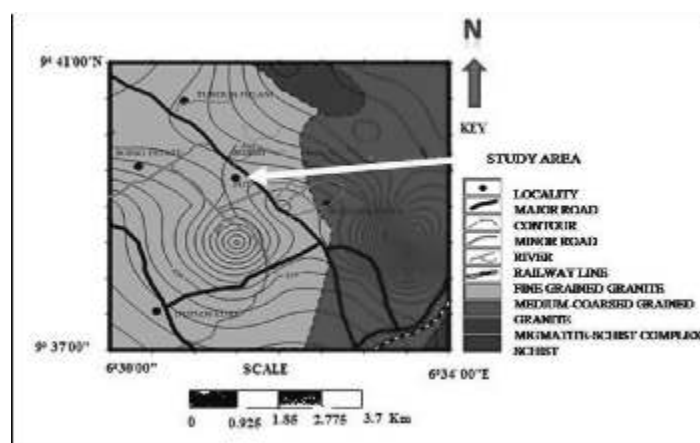


**Fig.3: Geological map of Bosso and environs**

### Materials and Methods:

Campus Omega resistivity meter, *WinResist* forward modelling software and *Suffer 11* contouring software constitute the materials employed in this study. Vertical electrical

resistivity sounding (VES) was carried out with Campus Omega resistivity meter, using the Schlumberger array and maximum current electrode spacing (AB) of 140m. This maximum current electrode spacing is

adequate to enable electrical current penetrate the fresh basement revealed to be shallow by numerous granitic outcrops, and any existing fractured basement revealed to be shallower than 60m depth by the hand-pumped productive borehole. VES was first conducted very close to the productive borehole to ascertain that the resistivity meter is appropriately responsive to subsurface geological conditions. Cumulative resistivity plotting method of Raghunath(2006) was combined with changes from concave to convex curve segments (and vice versa) method of Musset & Khan(2009) to identify approximate number of geoelectric layers, apparent depth to top of each layer and apparent resistivity of each layer. These parameters were used as input data for geoelectric layer modelling performed with *WinResist* forward modelling software. The geoelectric parameters characterising the modelled geoelectric layers constitute true depth to top and base of each layer, layer thickness and layer's true resistivity value. The modelled geoelectric layers constitute

geoelectric section at each VES station, which were interpreted in terms of geological section for the VES stations. Dar Zarrouk parameters (transverse unit resistance,  $T$ ; and longitudinal unit conductance,  $S$ ) were computed for the fractured basement column, using its geoelectric parameters obtained from the geoelectric section as follows (Parasnis 1986; Oladapo *et al.* 2004; Okiongbo & Odubo, 2012):

$$T = \rho_i h_i \text{ -----Equation 1}$$

$$S = \frac{h_i}{\rho_i} \text{ -----Equation 2}$$

where  $\rho_i$  and  $h_i$  are respectively the resistivity and thickness of the fractured column obtained from the modelled geoelectric section.

Suffer 11 contouring software was employed to contour depth to base of fractured basement column, thickness of fractured column, resistivity values as well as  $S$  and  $T$  values of the fractured column. Campus Omega resistivity meter was also employed to measure SP at the AB spacing employed in the resistivity sounding. The SP values were also contoured for the fractured basement.

## Results:

The VES curve in close vicinity (less than a metre offset distance) of the hand-pumped productive borehole is figure 4.

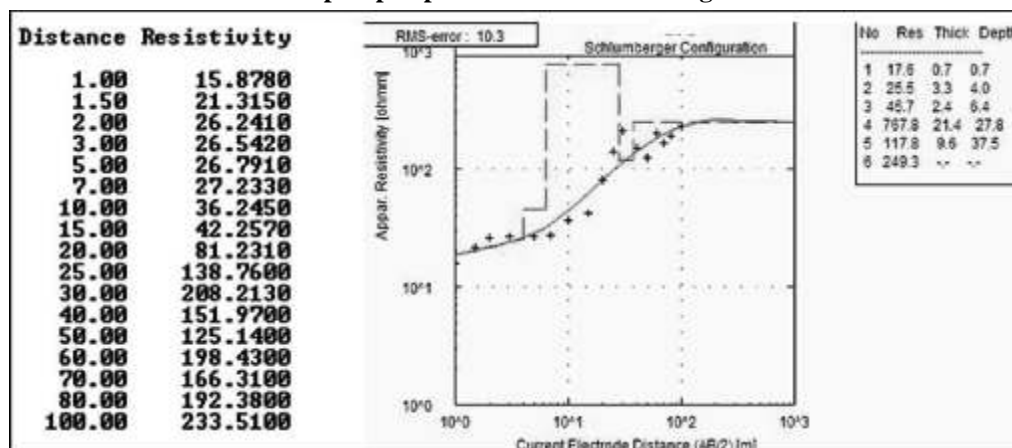


Fig.4: Modelled curve from VES station close to (less than 1m offset distance from) producing hand-pumped borehole

The curve revealed that the first fresh basement surface is about 6m deep. This agrees with the expected implications of observed numerous fresh granitic outcrops. It also revealed the

presence of fractured basement between 37 and 50m depth. This also agrees with the expected significance of observed fractured granitic outcrops. Hand pump drives water

production from the borehole, and this indicates it produces water from fractured basement between 37 and 50m depth, which is captured in its geoelectric section (figure 4). The curve also reveals that the resistivity of the productive interval is less than 300 $\Omega$  m.

The VES curves in the area include A, H, K, KH, HKH, QQH curve types. Of these, the HKH curve type is dominant. Figures 5, 6, 7, 8, 9 and 10 are respective representatives of the A, H, K, KH, HKH, and QQH curve types in the area. The combinations of K with H, and Q with H curve types indicate there exists more than one fresh basement unit in the subsurface.

Drilling has verified this subsurface geological situation in Minna region of North Central Nigerian Basement Complex, where regolith and fresh basement units are drilled through before penetrating fractured basement aquifer unit. The first fresh basement unit is expected to be very shallow in K, KH, and HKH curve types, as indicated by the numerous fresh granitic and fractured granitic outcrops observed in the area. The fractured basement sought for is below the first fresh basement unit, and shallower than 60m depth. Hence maximum electrode spacing of 140m will reveal their presence where they exist.

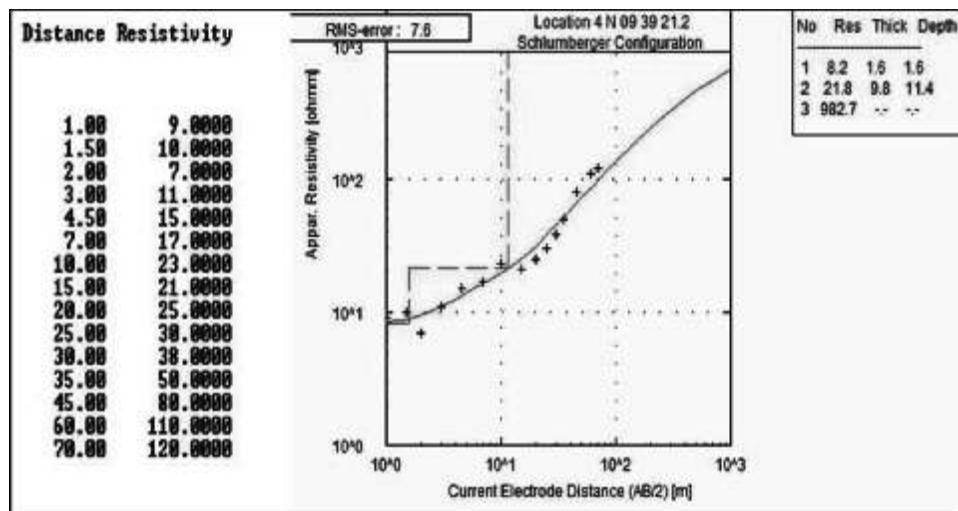


Fig.5: A-type curve in the area

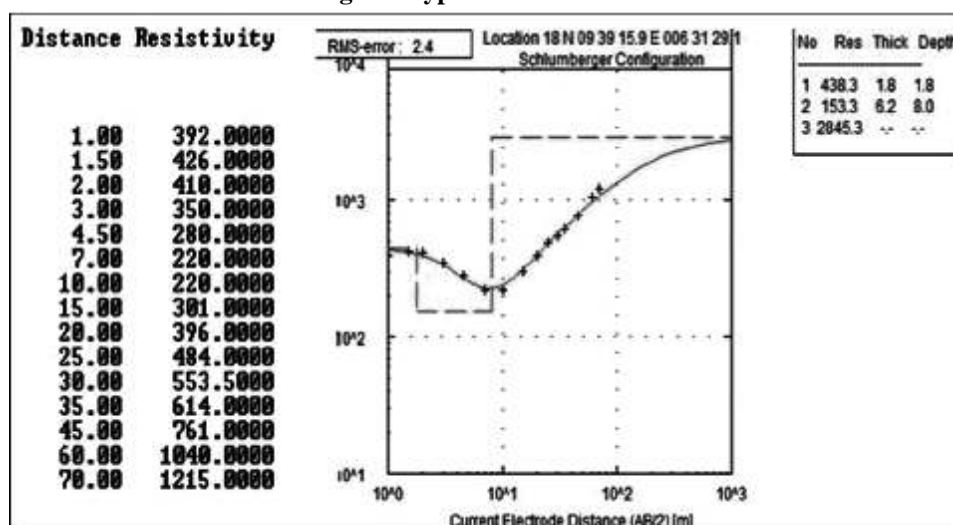


Fig.6: H-type curve in the area

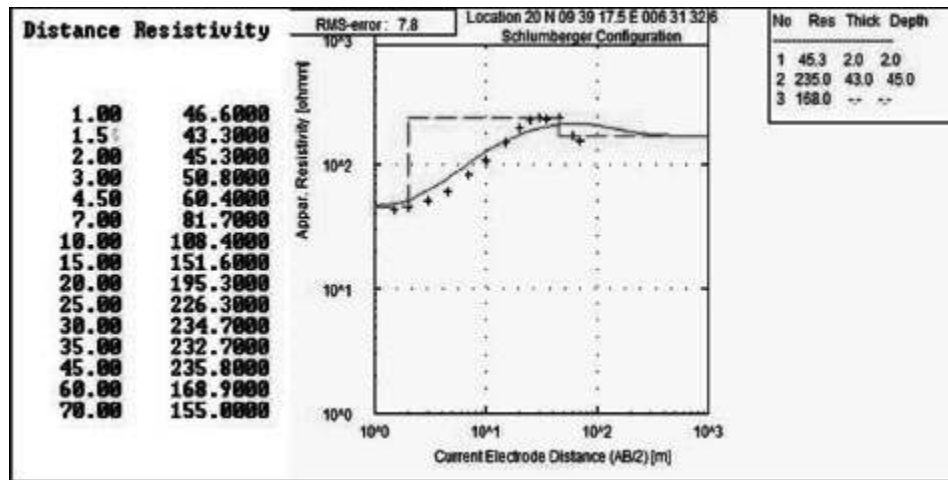


Fig.7: K-type curve in the area

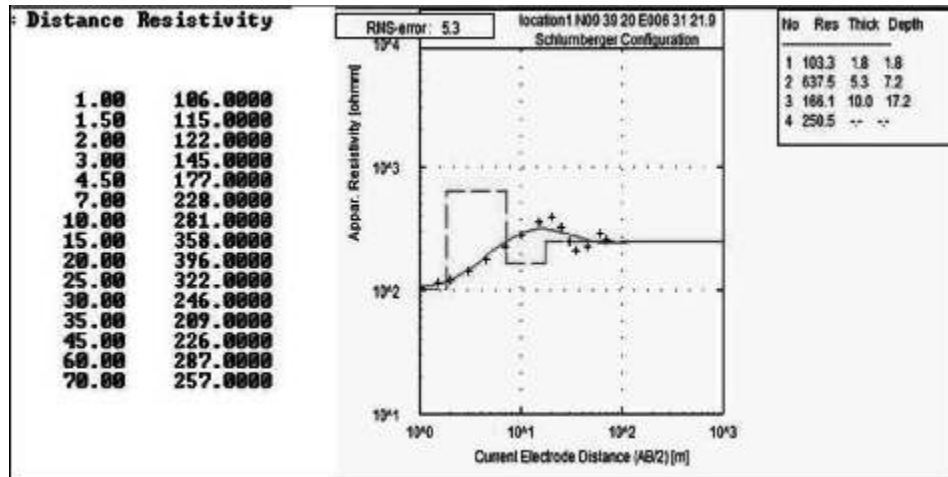


Fig.8:KH-type curve in the area

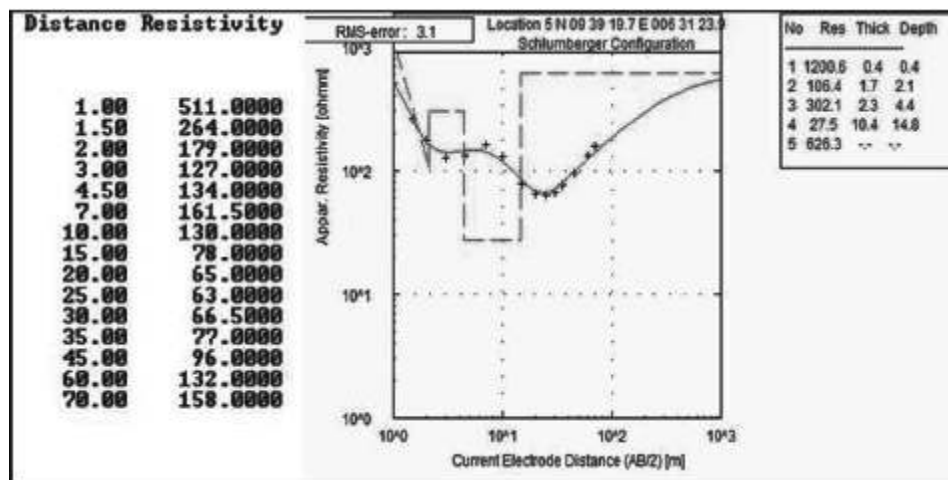


Fig.9: HKH-type curve in the area

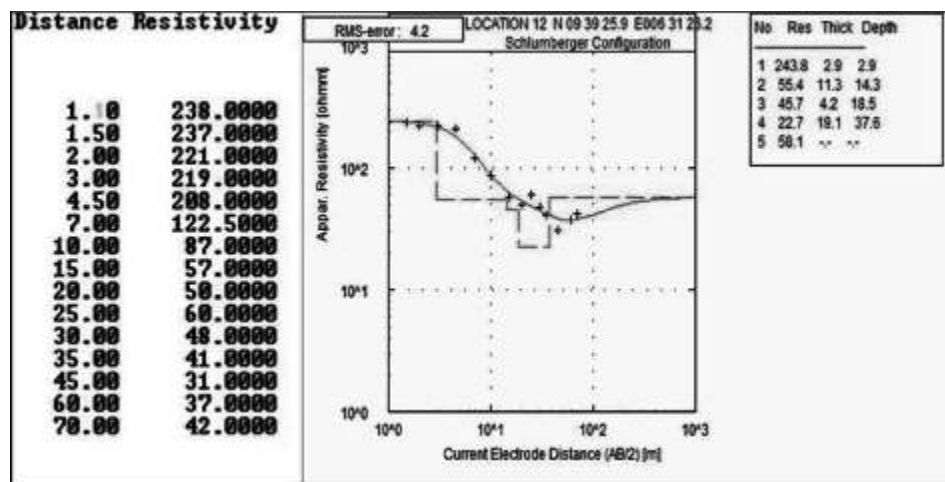


Fig.10: QQH-type curve in the area

**Discusions:**

Location 20 (Fig.7) is apparently the site with highest groundwater potential in the area. Its pattern of resistivity values indicates water-saturated fractures at depth in neighbourhood of

45m. Figure 11 is the modelled VES curve for VES data for location 14, which also appears to possess high groundwater potential because it indicates water bearing fractures between 9 and 14m, and between 18 and 34m depth.

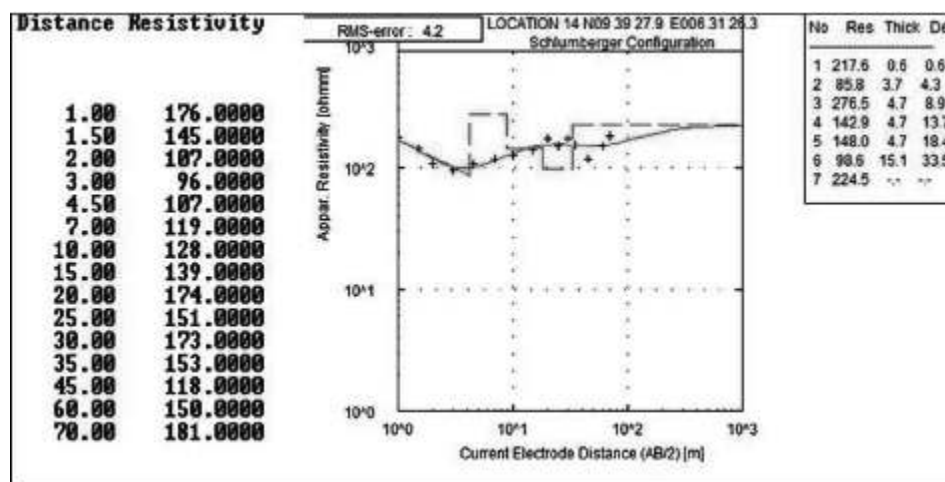


Fig.11: L 14(HKHKH VES curve type)

Figures 12 and 13 are respectively depth to the base map and resistivity map for the fractured basement unit. Fracture bottom at location 20 is deepest (between 28 and 52m) on the eastern portion of the investigated area (Fig.12). This implies that groundwater within fracture zone would flow and converge in the vicinity of location 20, in response to gravity. The resistivity within the groundwater

convergence zone around location 20 is between 200 and 250 $\Omega$  m. The depth range and resistivity value for this location are similar to those of the producing borehole. Locations 1, 8, 12 and 14 (figures 12 and 13) are other locations that are characterised by the attributes of the productive borehole.

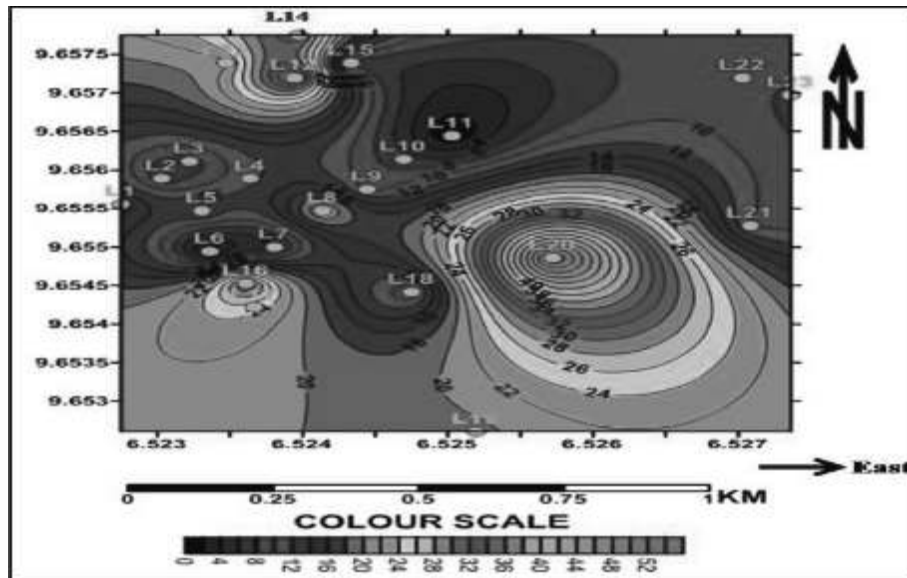


Fig.12: Depth to bottom of fracture column (in metres)

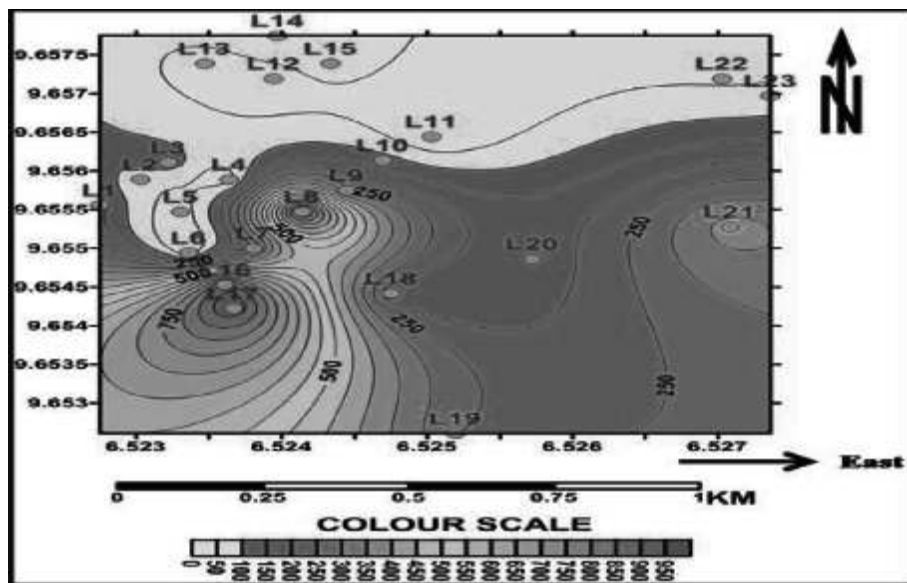


Fig.13: Resistivity variation in fracture column (in ? m)

Figures 14, 15, 16 and 17 are respectively the thickness, SP, T and S maps for the fractured basement interval. Fracture thickness around L20 varies between 6 and 9m (Fig.14) and the SP values vary between -19 and 20mV (Fig.15). T varies from 1200 to 2400  $\Omega \cdot m^2$  (Fig.16) and S varies between 0.05 and 0.1  $\Omega^{-1}$

(Fig.17). These geoelectrical parameters of L20 and its immediate vicinity are identical with those of the productive borehole site, which is characterised by 9.7m fracture thickness, SP values of -7 to 2mV, T value of 1143  $\Omega \cdot m^2$  and S value of 0.8  $\Omega^{-1}$ .

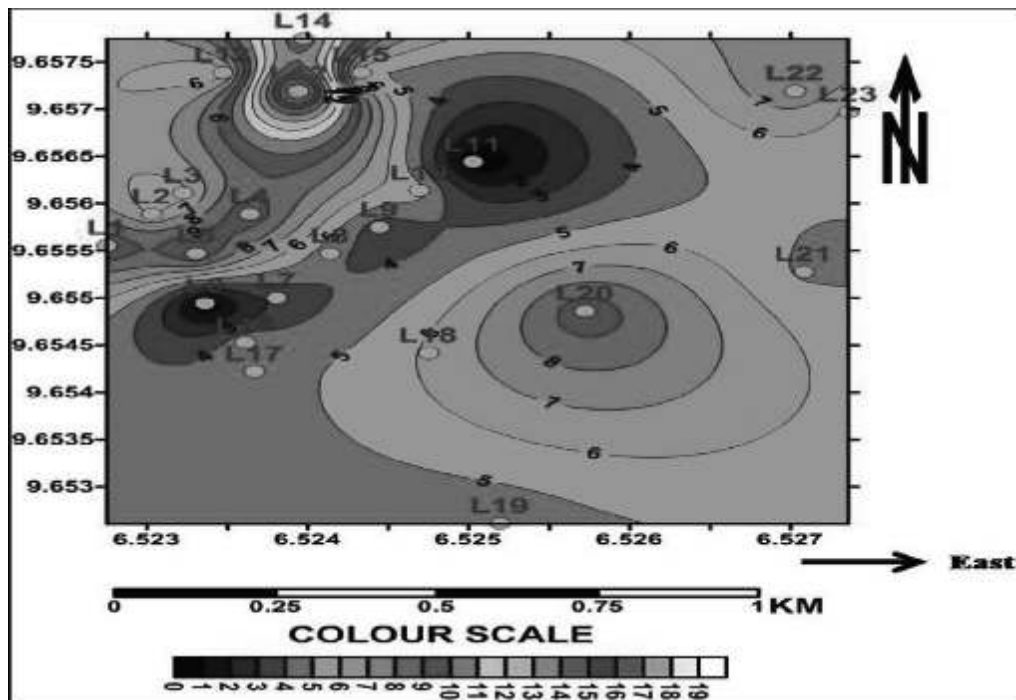


Fig.15: SP values of fracture column (in mV)

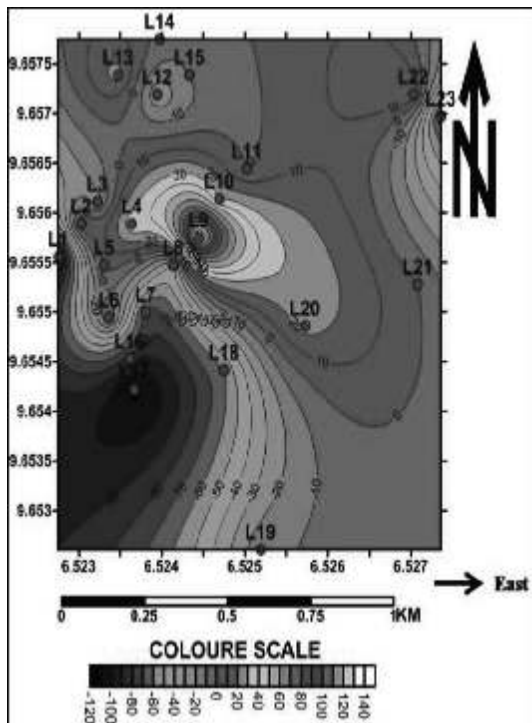
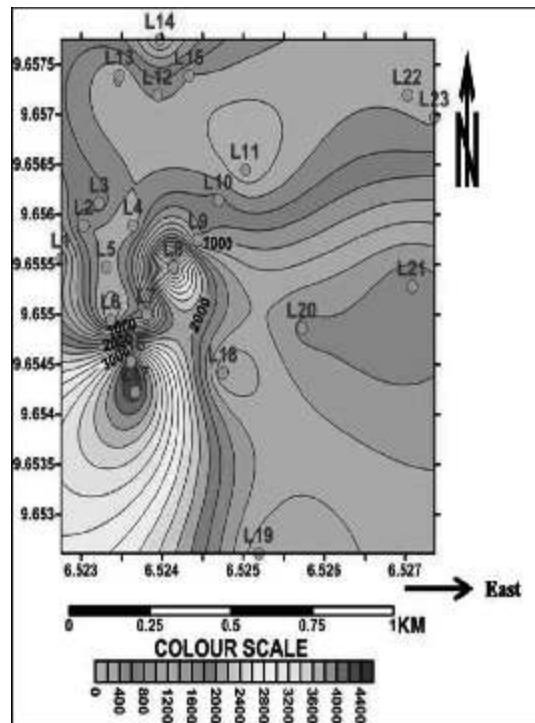
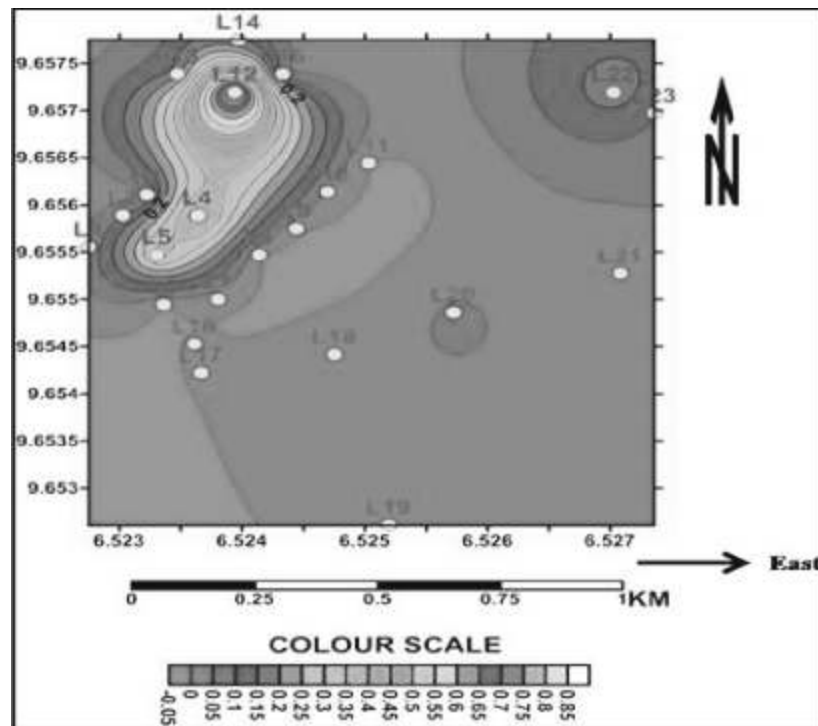


Fig.15: SP values of fracture column (in mV)

Fig.16: T values of fracture column (in ? m<sup>2</sup>)





**Fig.17: S values of fracture column (in  $\Omega^{-1}$ )**

Gravity- induced groundwater convergence zone is expected in the NW portion of the area around L12 and L14, where depth to fracture bottom is between 26 and 34m (Fig.12), fracture thickness is between 11 and 18m (Fig.14) and SP values are between 0 and -10mV (Fig.15). Locations 12, 14 and 19 (like L20) have geoelectrical and Dar Zarrouk parameters that are identical with those of the productive borehole at Latitude 9.656°N and Longitude 6.527°E, about 0.23km north of VESL21.

These locations are markedly different from the location of the failed borehole at latitude 9.6568°N and longitude 6.527°E (about 0.187km NW of L11) in terms of depth to bottom of fracture column, fracture thickness, and fracture column resistivity (except at L12 and L14 where very low resistivity appears attributable to water-filled thick fracture column. The 140m maximum electrode employed in this study is in conformity with Kumar *et al.* (2015), who employed VES with

maximum electrode spacing of 150m to capture water bearing fractures at 46m depth within basement terrain of Osmania University campus at Hyderabad in India. The resistivity values associated with the inferred water-filled fractures in this study are similar to values (between 100 and 300 $\Omega$  m) reported by White *et al.* (1988) to characterise water-filled fractures in Victoria Province of Australia. Dan-Hassan and Olorunfemi (1999) established that all boreholes within groundwater convergence zone are productive within Kaduna town in North Central Nigeria Basement Complex. Ajiroba (2018) found that boreholes in Kaduna region of North Central Nigeria Basement Complex produce water from fractures within groundwater convergence zone, which are characterised by SP values of -10 to +30mv.

The failed borehole is located at a site where fracture thickness is 2m and the depth to bottom of fracture zone is about 4m (Figs.

12, 14, 13). This shallow depth of fracture bottom indicates the failed borehole is located within a divergence zone, from where groundwater flows to the convergence zones in its NW and SE. Groundwater convergence zones are commonly sites for productive boreholes, whereas the divergence zones are sites where boreholes are often unproductive (Olorunfemi & Okhue 1992; Olorunfemi 2009).

### Concluding Remarks:

Vertical electrical sounding and spontaneous data have revealed the presence of subsurface fractured bedrock in the study area. Spatial variation in depth to bottom of the fracture column have revealed a groundwater convergence zone in the eastern sector around L20 and another convergence zone in the NW sector eastern sector around L14. Fracture column in the vicinity of L20 is thickest and most extensive, making the eastern sector most suitable for drilling water wells in the investigated area. Locations 12 and 19 are other sites with good potential for groundwater production. Borehole drilling can now be embarked upon on the basis of the revealed information to produce water for drinking and sanitary purposes at the Model College, Staff School, Catholic Church, and Interdenominational Church.

### References:

- Ajiroba, O.J. 2018. Integrated geological, hydrogeological and geo-electrical exploration for aquifers within kaduna region, Minna sheet 164 SW, North Central Nigeria .B.Tech. Thesis, Federal University of Technology, Minna 127 pp.
- Dan-Hassan, M.A. and Olorunfemi, M.O. 1999. Hydrogeophysical investigation of a basement terrain in the North Central part of Kaduna State, Nigeria. *Journal of mining and geology*, 36(2):189-206.
- Kumar, D.V, Ramadan, G and Jagadish, S.V. 2015. Delineation of groundwater potential zones through electrical resistivity parameter in hard rock terrains, Osmania University campus, Hyderabad, Telangana State, India. *IOSR journal of applied geology and geophysics*, 11:01-10.
- Musset, A.E. and Khan, M.A. 2009. *Looking into the earth: An introduction to geological geophysics*, 1st ed. Cambridge; Cambridge university press.
- Okiongbo, K.S and Odubo, E. 2012. Geoelectric sounding for the determination of aquifer transmissivity in parts of Bayelsa State, South-South Nigeria. *Journal of Water Resource and Protection*, 4: 346-353.
- Oladapo, M.I., Mohammed, M.Z., Adeoye, O.O., and Adetola, B.A. 2004. Geoelectrical investigation of the Ondo State Housing Corporation, Ijapo, Akure, Southwestern Nigeria. *Journal of Mining and Geology*, 40(1): 41-48.
- Olayinka, A.I, Obere, F.O. and David, Jr, L.M 2000. Estimation of longitudinal resistivity from Schlumberger sounding curves. *Journal of Mining and Geology*, 36 (2): 221-229.
- Olorunfemi, M.O. and Okhue, E.T. 1992. Hydrogeologic and geologic significance of a geoelectric survey at Ile-Ife, Nigeria. *Journal of Mining and Geology*, 28:2
- Olorunfemi, M.O. 2009. Groundwater exploration, borehole site selection and optimum drill depth in basement complex terrain. *Water Resources Special Publications Series 1*: 20.
- Paranis, D.S. 1986. *Principles of Applied Geophysics*, 4<sup>th</sup> ed. New York; Chapman and Hall.
- Raghunath, H.M. 2006. *Groundwater*, 3<sup>rd</sup> ed. New Delhi; New Age.
- White, C.C., Houston, J.F.T. and Barker, K.D. 1988. The Victoria Province drought relief project, 1, Geophysical siting of boreholes. *Ground Water*, 26: 309-316

## THE AQUIFER OVERLYING THE BASEMENT COMPLEX IN SOME PARTS OF DAN-HONO, KADUNA, NIGERIA.

M. D. Dogara; H. O. Aboh; J. O. Aloa and K. A. Kogi

Department of Physics, Kaduna State University, Kaduna, Nigeria.

### ABSTRACT

*An electrical resistivity investigation was used to investigate the sub-surface layering in some parts Dan-Hono, Kaduna, with the aim of determining the configuration of the aquifer underlying the region. The result of the interpreted Vertical Electrical Sounding data reveals that the area is underlain by three to five layers. The geologic sections derived from the analyzed geoelectric section suggest that the alluvial deposits of sand, silt and sandy clay as well as the weathered and fractured basement rocks constitute the aquifer in the area. The average thickness of the aquifer was found to be 24m. The resistivity values of the aquifer component range from 20  $\Omega$  m to 650  $\Omega$  m for both sand/silty clay and weathered/fractured basement formations. The zones with relatively high thick weathered layer and possible fractured zones have been successfully identified as potential aquifer zone targets for groundwater development.*

**Keywords:** *Geoelectric Sections, Aquifer zone, Groundwater, Vertical Electrical Soundings*

### Introduction

Water is considered absolutely essential for the sustenance of life. All people irrespective of their development, economics and social condition are entitled to have access to drinking water in good quality and quantities (NWRI, 2011). Approximately 50% of the Nigerian landmass is geologically underlain by crystalline basement rocks. These crystalline rocks have been shown to be potential target for sustainable groundwater supply (Olayinka, 1992). There is a growing concern throughout Nigeria about the contamination of groundwater as a result of geogenic and human activities especially in industrial areas where waste deposit is not properly treated. With the rapid growth in population, urbanization, industrialization and other developmental activities, groundwater resources have become vulnerable to depletion and quality degradation (Payal, 2000).

The area under study lacks detailed geophysical investigations. Most geophysical works carried out around this area are regional in nature or are localized to specific areas. However, most of these works have provided a good background for this research work, thereby providing general information about the geology, hydrogeology and geoelectric

information of the subsurface layer around the study area which are employed as guide in the interpretation of this research work. Aboh (2009), reveals that the sections where the aquifer are thickest and has an averagely low resistivity value are the best areas for the exploitation of underground water. McCurry (1970) has studied the basement geology of Zaria and has concluded that the deeply weathered areas of crystalline basement outcrop constitute the useful aquifers. He has affirmed that the aquifers are variable in extent and thickness ranging from broad areas of deeply weathered to narrow joints and fracture zones. According to NWRI (2011), an estimation of one hundred and three million Nigerians still lack basic sanitation facilities and sixty nine million Nigerians do not have access to improved source of water. This is far larger number than the majority of countries in the developing world and it is a significant portion of the population in Africa. In addition, wide disparities persist across Zones and within States, especially in rural area and urban communities, which aggravate the situation leaving more children and women vulnerable to sickness and poverty. Sanitation receives far less attention than water supply in Nigeria (NWRI, 2011). Most of the water required for domestic and agricultural uses is

sourced from seasonal streams and riverlets which exist in the area as well as from shallow hand-dug wells. These sources most often do not provide the needed good quality supply as they are prone to contamination by human beings and animals (Aboh, 2009). According to Adefila (1975), a survey of 69 boreholes drilled in the Basement Complex rocks of Kaduna State showed that 16 were unproductive, representing 30% failures, while the so-called successes were not encouraging due to low yield. This high rate of unproductive and so, unpromising boreholes have been attributed to the fact that the boreholes were drilled at locations pre-determined by their owners, instead of on the basis of a good hydrogeological/geophysical investigation of the areas concerned. Most dug wells in the rural areas were located by 'common sense' or trial and error rather than by scientific methods due to restricted availability of equipment and operators (Adefila, 1975).

Like in most parts of Africa, Dan-Hono may also face formidable challenges in meeting rising demands of clean water as the available supplies of freshwater are decreasing. This may be due to; extended droughts, population growth and competing demands from a variety of users. Increasing population and its necessities is one of the most important points that have led to the deterioration of surface and subsurface water. Dan-Hono is located in the capital city of Kaduna. Kaduna State is speculated to be a centre of attraction which may soon experience a mass influx of people due to the presence of Kaduna Millennium City. In order to accommodate this expected population expansion, proper geophysical investigation is critical to evaluate the subsurface properties of the study area for groundwater development. These situations therefore make this type of investigation a basic necessity for precise location of geological formations for the siting of productive boreholes. While the government is largely responsible for the provision of social amenities and other infrastructure to her

citizens, this research will provide good information of subsurface properties underlain in the study area in order to adequately guide government in its quest of developing the city.

#### The Location of the Study Area

The study area, Dan-Hono is located in Kaduna, Kaduna State in Central Nigeria and is about 5km away from Kaduna central market and about 2.6 km away from Danbushiya Bridge. It lies on the geographical coordinate of latitude and longitude of  $10^{\circ} 30.47' N$  to  $10^{\circ} 31.08' N$ , and  $007^{\circ} 30.06' E$  to  $007^{\circ} 30.33' E$  respectively. The location covers a total landmass of 400,000 square meters with an average height of 607m (Kaduna, Southeast sheet 144; 1:50,000) above sea level.

#### Geology and Hydrogeology

The study area is capped by layers of indurated laterites. The laterites are sometimes highly consolidated especially at the surface and weathered into lateritic nodules mixed with silty and sandy clays (Isaac et al., 2010). The typical rock types underlying the entire land area of Kaduna State consist of the Precambrian migmatite-gneiss complex, meta-sediments/ meta-volcanics (mostly schists, quartzites, amphibolites and banded iron formations) (Oyawoye, 1970). Most of the areas underlain by the Basement Complex rocks in northern Nigeria consist of a thin discontinuous mantle of weathered rock overlying them. The average thickness of the mantle is about 15m, although depths of about 60m may be encountered. The unweathered bedrock is characterized by rapid grain-size variations from micro to pegmatitic regions but normal sizes are dominant (Isaac, et al., 2010). The study area is drained by both surface water and groundwater. The noticeable streams in the study area include Dan-Hono Stream and Kubai Stream, both drain into river Kaduna. The relief of the area is characterized by undulating plain, gentle slopes, and consists of peneplains with eroded flat tops (Fig. 1).



**Fig. : The Map of the Study Area showing the VES Stations.**

### Materials and Methodology

Electrical resistivity is a geophysical survey method in which an electrical current is injected into the ground to measure the electrical properties of the subsurface (Telford et al., 1990). In this survey, a total of fifty four Vertical Electrical Sounding (VES) points was established at different locations within the study area with maximum spread of 100 meters with an Omega resistivity Terrameter and its accessories using the Schlumberger configuration. This configuration was adopted due to its high signal to noise ratio, its excellent vertical resolution and good depth sensitivity. The soil parameters (resistivities and thicknesses) were used to generate isopach and iso-resistivity maps using *RES1D* (version 1.00.07 Beta) and *Surfer 11* (a computer modeling software) for resistivity curves and contouring respectively. The maps were used to categorize the study area into different aquifer potential zones using different thicknesses and resistivities range obtained.

### Theory of the Schlumberger Technique

The theoretical study of the earth resistivity methods is to consider the case of completely homogenous isotropic medium. The equation which gives the potential due to a single point source of current at surface can be deduced from two basic equations; ohm's law and divergence condition. And the ohm's law is given by:

$$J = \sigma E \quad (1)$$

The potential due to a single point source of current at earth surface is given as:

$$U = \frac{I}{2\pi\sigma r} \quad (2)$$

Where  $\sigma$  = earth resistivity,  $I$  = Current,  $2\pi$  = Constant,  $r$  = Resistance. The current  $I$ , is passed through current electrodes.

The potential difference at a point  $m$  is

$$U_m = \frac{I}{2\pi\sigma} \left[ \frac{1}{r_1} - \frac{1}{r_2} \right] \quad (3)$$

The potential difference at a point  $n$  is

$$U_n = \frac{I}{2\pi\sigma} \left[ \frac{1}{r_3} - \frac{1}{r_4} \right] \quad (4)$$

The difference in potential at  $m$  and  $n$  is given as:

$$\Delta U = U_m - U_n$$

$$U_n = \frac{I}{2\pi\sigma} \left[ \frac{1}{r_3} - \frac{1}{r_4} - \frac{1}{r_3} + \frac{1}{r_4} \right] \quad (5)$$

Hence, the resistivity is given by:

$$\sigma = \frac{\Delta U}{I} \left[ 2 \left\{ \frac{1}{r_3} - \frac{1}{r_4} - \frac{1}{r_3} + \frac{1}{r_4} \right\} \right] \quad (6)$$

$$\text{Let } K = 2 \left\{ \frac{1}{r_3} - \frac{1}{r_4} - \frac{1}{r_3} + \frac{1}{r_4} \right\}$$

Therefore

$$\sigma = KR \quad (7)$$

Where,  $K$  is a Geometric factor and  $R = \frac{\Delta U}{I}$

### The Vertical Electrical Resistivity Interpretation

The data was reduced, and the computed apparent resistivity values were then plotted against their corresponding  $AB/2$  values on log-log graph paper using computer software *Res1D* (version 1.00.07 Beta) developed by Loke (1995), with initial model parameters which gives inversion results. A typical example of such plots is shown in Fig. 2. Special attention is paid to user-friendly interactive interpretation thereby providing low fitting error. The interpreted results were used to generate the final model geoelectric parameters used for the preparation of the geoelectric sections (Fig. 3). The geoelectric

sections were drawn from the interpreted results which shows three-five subsurface layers, however, there are four distinctive

layers as follows: top soil (laterite/sandy/silty clay), quartzite veins/laterite, weathered basement rocks and fractured/fresh basement rocks.

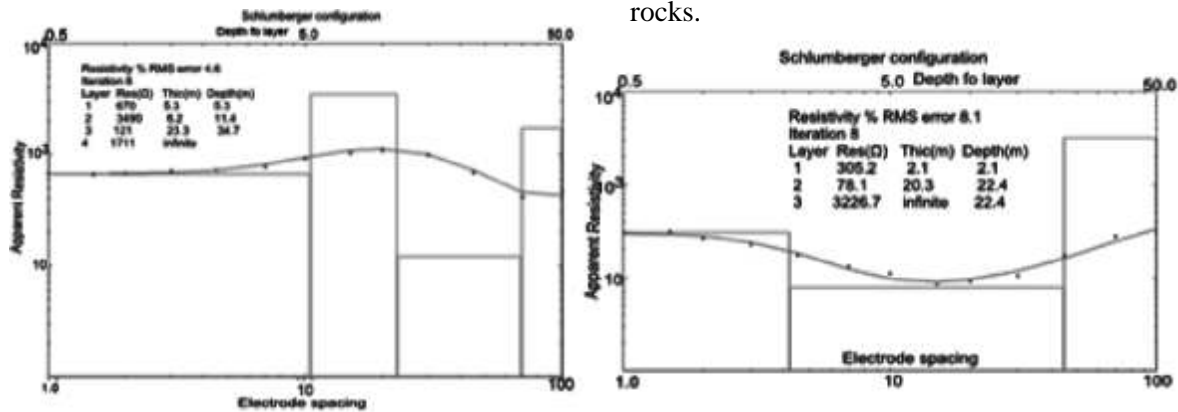


Fig. 2: Typical Resistivity Curves (VES P2/1 and VES P8/6 Respectively)

### Results and Discussion

The geologic sections were constructed using the result of the work after Aboh (2009) and Abdullahi and Udensi (2008). The final model geoelectric parameters were used for the preparation of the geoelectric sections (Fig. 3). The first layer varies from 0.3m – 10m in

thickness and 125? m - 2100? m in resistivity. The derived geologic suggests that the weathered layer varies in composition (silty/sandy clay, clay and sand) with resistivity and thickness values varying from 35 m - 195 m and 11 – 41 m respectively.

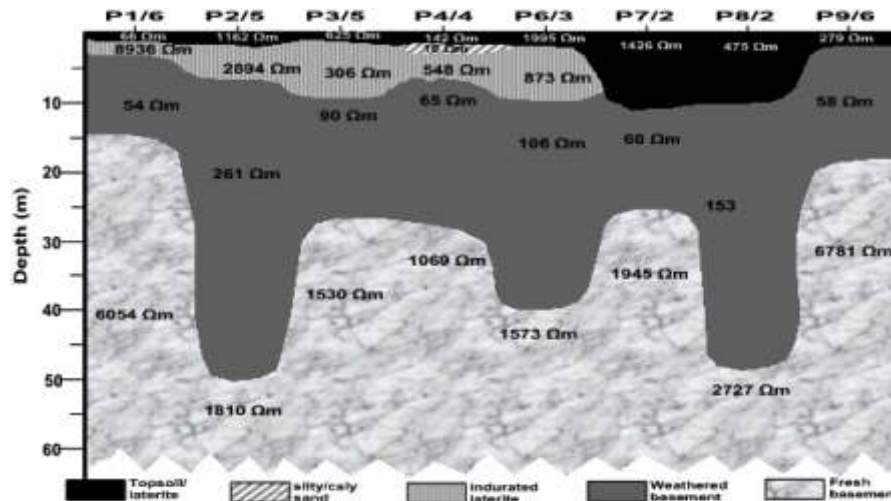


Fig. 3: Geoelectric Section across the Study Area.

Fig. 4 and 5 show the iso-resistivity and isopach map of the weathered basement respectively. The thickest part of the aquifer was found in some section of Northeast, Southwest, upper South south and Northern part of the study area. According to Aboh (2009), the sections where the aquifer are

thickest and has an averagely low resistivity value are the best areas for the exploitation of underground water. With the aquifer thickness (4.0 – 48.0) m, the study area appears good enough for siting of boreholes except some sections of Northern zone at VES location

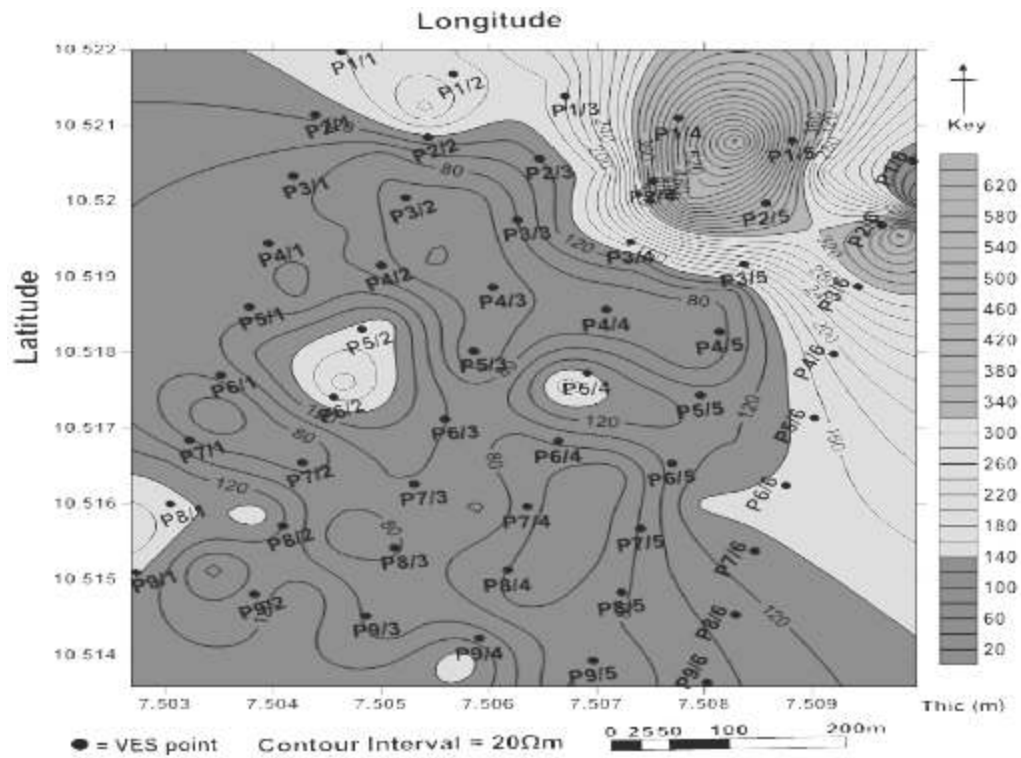


Fig. 4: The Iso-resistivity Map of Weathered Basement Layer

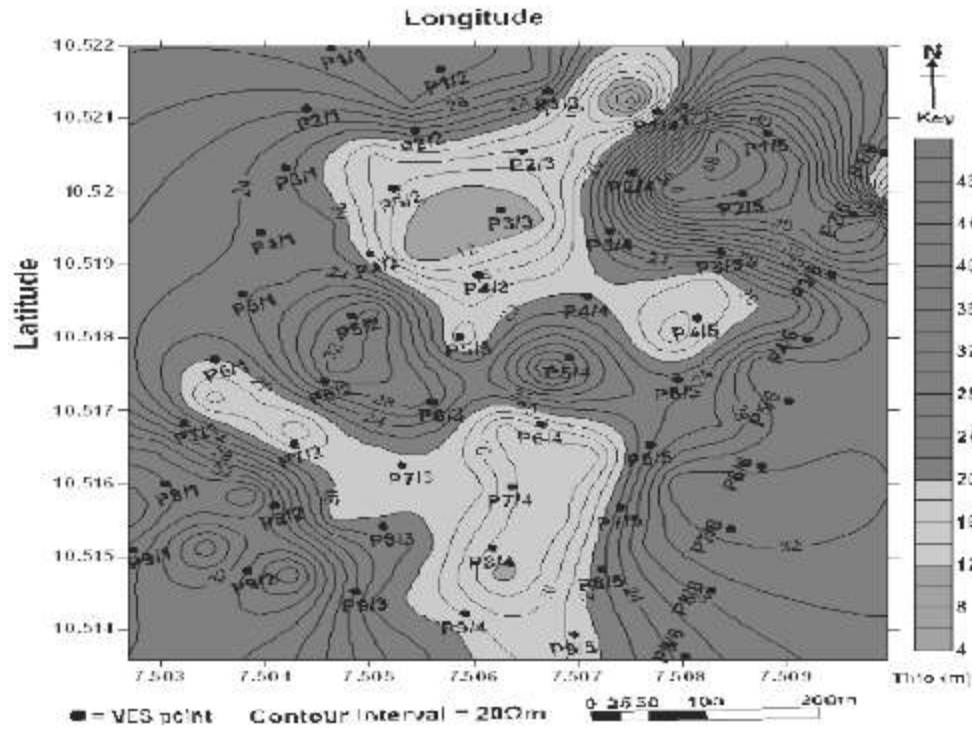


Fig. 5: The Isopach Map of Weathered Basement Layer



Fig. 6 shows the resistivity values of the basement surface obtained in the course of the interpretation which were used to plot the iso-resistivity map of the basement rock underlying the study area. According to Aweto (2012), when the bedrock has relatively low resistivity ( $<750 \text{ m}$ ), this could indicate fracturing and high aquifer potentials. Fig. 6 shows that the study area is underlain by unfractured basement rock mostly at shallow depths. The values of basement resistivity range from  $1000 \text{ m}$  to  $14500 \text{ m}$ . The zones depicted by red are highly resistive ( $>6000 \text{ m}$ ). The rocks in these regions are believed to

be fresh basement and competent. The area with relatively low basement resistivity values ( $<2000 \text{ m}$ ) is also shown on the map. According to Aboh (2002), the rocks in these regions of the study area are less competent probably because they are fractured, faulted or heavily weathered. This could be of great important to underground water development. Fig. 7 shows the depth to the basement (Overburden thickness). The map suggests that the depth to the basement in the study area range from  $14.0 \text{ m}$  to  $56.0 \text{ m}$ . The deepest part (range from  $44\text{m}$  to  $56\text{m}$ ) is the region already suggested for groundwater exploitation in this work.

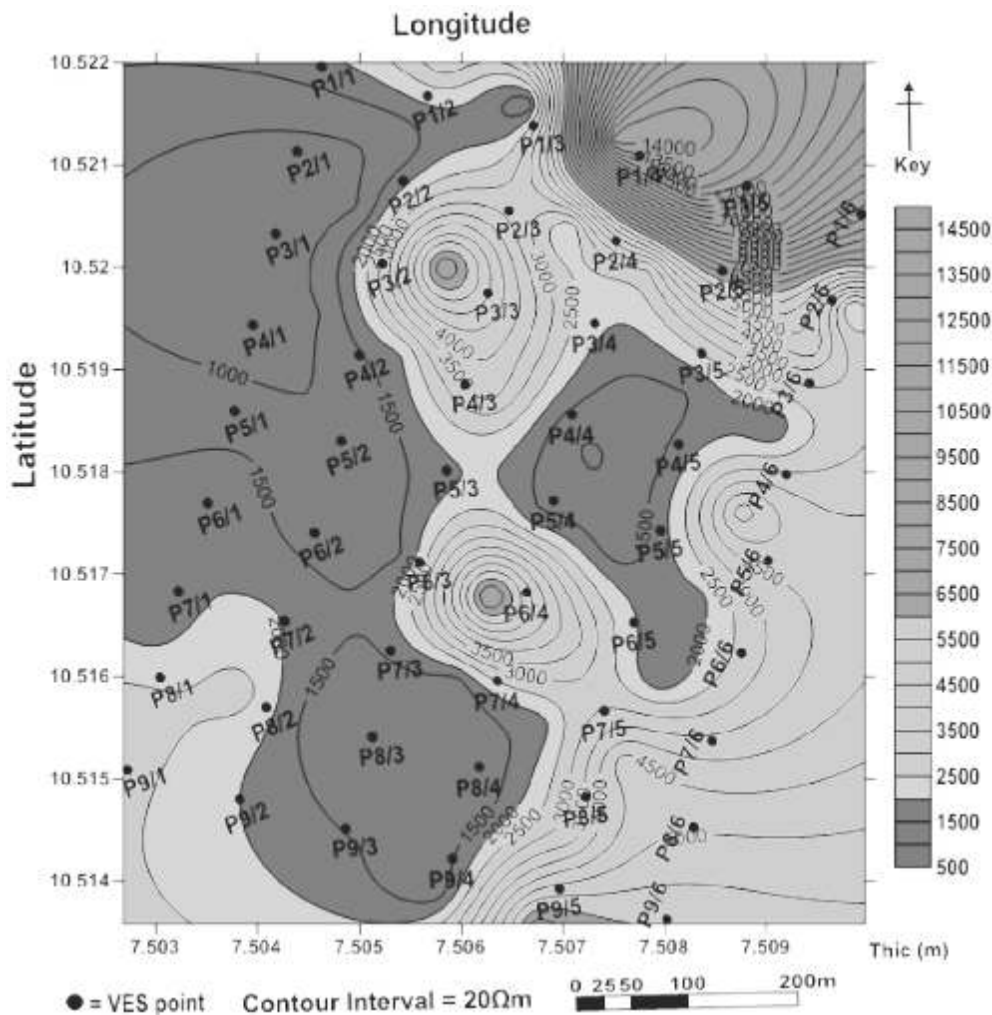


Fig. 6: The Iso-resistivity Map of Basement Rock



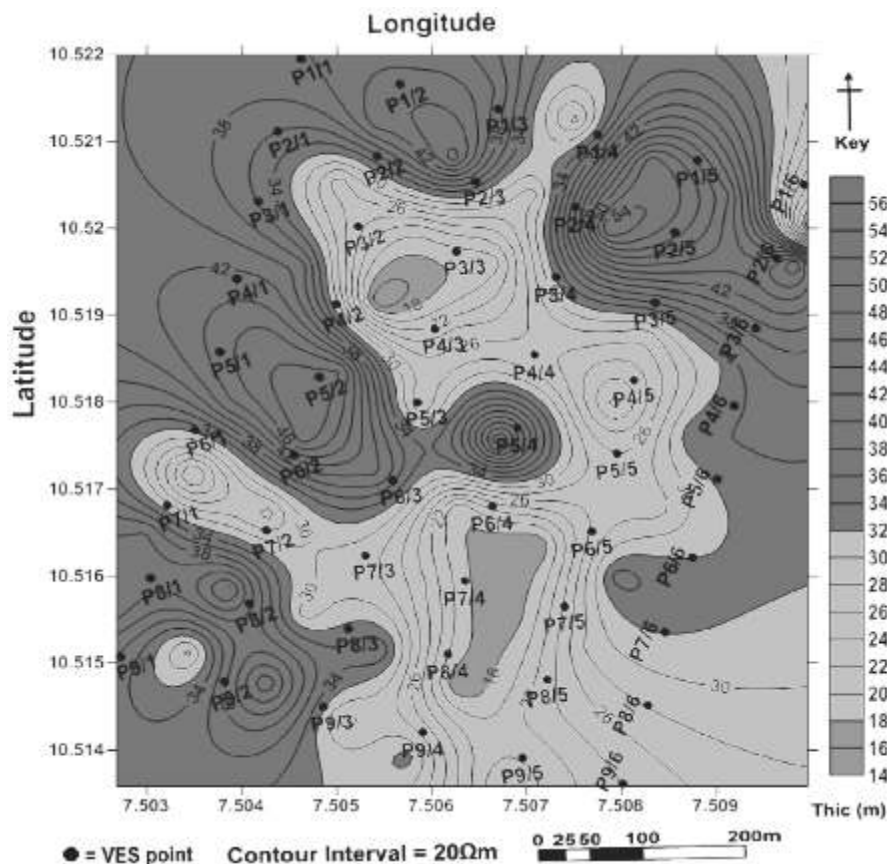


Fig. 7: The Depth to the Basement (Overburden Thickness) Map

#### Evaluation of Aquifer Potential:

Given the average resistivity and thicknesses (150 $\Omega$  m and 24m) values of the aquifer parameters, (Fig. 2, 4, 5, 6 & 7), the study area is highly productive for groundwater exploitation. The aquifer potential of the study area has been classified into high, moderate, relatively moderate aquifer zone depicted by blue, green and red colour respectively. According to Ogundana and Talabi (2014), the combination of overburden materials with the weathered/fractured basement constitutes aquiferous units within the study area although the sand and weathered/fractured basement units are largely responsible for the groundwater potential. Observed thickness and nature of the weathered layer are important parameters suggested for groundwater potential development in this work. Shallow regions (<12m) may be vulnerable to

contamination that may arise from human activities (Aweto, 2012). This means, the study area may be relatively considered protected against contamination from near surface activities such as waste and sewage with overburden thickness extending beyond 15m. According to Olayinka (1992), a borehole should be sited where it can penetrate the maximum possible thickness of the regolith, such that adequate storativity and transmissivity can be guaranteed. As presented in Figs. 2, 4, 5, 6 & 7, such conditions are met in the study. Ogundana and Talabi (2014), noted that the areas with overburden thickness of 15m and above are good for groundwater development depending on the water bearing (aquifer) unit. Based on this information, the study area can be considered largely as a productive zone for groundwater development both in quality and quantity.

## Conclusion

The geoelectric investigation of the study area has revealed that the areas with relatively high thickness of the weathered layer and with appreciably low resistivity values of the weathered and fractured zones are the regions successfully identified as potential targets for siting boreholes in this work. The high thick weathered basement with a relatively low resistivity that covers almost the whole study area is large enough to harbour substantial quantity of water, therefore, this area could be suitable for hand dug wells or boreholes. The dc-resistivity method has proved very successful in the identification and delineation of deep zones of fracturing within the crystalline basement rocks.

## REFERENCES

- Abdullahi, N.K. and Udensi, E. E. (2008). Vertical Electrical Sounding Applied to Hydrogeologic and Engineering Investigations: A Case Study of Kaduna Polytechnic Staff Quarters, Nigeria. *Nigeria journal of Physics*, 20 (1), 175-188
- Aboh H.O. (2001). Detailed regional geophysical investigation of the subsurface terrain in Kaduna Area, Kaduna State. Physics Department, ABU, Zaria. *Unpublished PhD theses*.
- Aboh, H. (2002). *Geotechnical Characterization of Surface Materials in Kaduna Area, Kaduna State*. Zuma Journal of Pure & Applied Science, 4(2).
- Aboh, H. O. (2009). Assessment of the aquifers in some selected villages in Chikun local government area, Kaduna State, Nigeria. *Science World Journal Vol 4 (No 2)* [www.scienceworldjournal.org](http://www.scienceworldjournal.org), 37-42. Retrieved from Kaduna.
- Adefila S.F. (1975). Decline in pressure head of the 'Middle Zone' aquifer of the Chad basin in parts of south-eastern Niger and north-east Nigeria. *Journal of Mining and Geology*, 12(1 & 2);, 23.
- Aweto, K. E. (2012). Aquifer vulnerability assessemtn at Oke-Ila area, Southwestern Nigeria. *Intl. J. Phys. Sci.* 6(33), 7574-7583.
- Isaac, O. O., Jonah, C. A., and Joel, O. A. (2010). *Assessment of Aquifer Characteristics in Relation to Rural Water Supply in Part of Northern Nigeria. Researcher*. 2(3):22-27]
- NWRI, National Water Resource Institute, Kaduna, (2011). *National Assessment of Drinking Water Quality Project Report: NWRI, Kaduna*.
- Ogundana, K. A., & Talabi, A. O. (2014). Geoelectric Characterization of Aquiferous Units and its Implication on Groundwater Potential of Owo, Southwestern Nigeria. *American Journal of Water Resources* 2.2, 37-40.
- Olayinka, A. (1992). Geophysical siting of boreholes in crystalline basement areas of Africa. *Journal Africa Earth Sci. (Middle East)*, 14, 197-207.
- Oyawoye, M. O. (1970). *The Basement Complex of Nigeria*, In: Dessauvage, TFJ and Whiteman, A.J (Eds) *African Geology*. Ibadan: University Press, Ibadan Nigeria.
- Payal, S. (2000). *Deep Trouble: The Hidden Threat of Groundwater Pollution. World Watch Paper #154. ISBN: 1-878071-56-4 pp: 55. ISBN: 1-878071-56-4 pp: 55.*
- Telford, W. M., Geldart, L. P., and Sheriff, E. R. (1990). *Applied geophysics. 2nd Edn*, Cambridge University Press

## INVESTIGATION OF GROUNDWATER POTENTIAL AT KADUNA STATE UNIVERSITY MAIN CAMPUS

**N. K. Abdullahi, A. Ladan, H. Abdulkareem**  
Department of Physics, Kaduna State University

### ABSTRACT

*Geophysical investigation of ground water potential was carried out at Kaduna State University main campus Kaduna State Nigeria which fall within the basement complex of the north western Nigeria. The study area was gridded into 10 profiles having a separation of about 5 m between the profiles. Electrical resistivity method was employed using the 4 electric Schlumberger configuration. Ten vertical electrical sounding (VES) were investigated along the profiles (A-J) with maximum spread of  $AB/2 = 100\text{m}$ . The data collected from each of the VES point was then fed into computer software DCINV and the results shows that the study area is underlain by 4 geologic formations. This formation consists of top soil with resistivity value ranging from 124-ohm-m to 1839-ohm-m and thickness which varies from 0.17m to 5.33m. The second layer which consists of sandy soil has resistivity varying from 39.9-ohm-m to 2695-ohm-m with a thickness varying between 0.26m to 5.59m. Weathered basement which consist of clay, sand and gravels constitute the third layer. This layer has resistivity ranging from 26.1-ohm-m to 30717-ohm-m with maximum thickness of 18.68m. Fractured/fresh basement defines the fourth layer with infinite thickness and resistivity which varies from 420-ohm-m to infinity. Qualitative analysis reveals that the weathered/fractured basement is the aquifer unit in the study area. The VES curve types were diagnostic of three different aquifer types. The weathered layer aquifers were characterized by HA and KH curve types. The weathered/fractured (unconfined) aquifers are characterized by QH and H curve types and the weathered/fractured (confined) aquifers are characterized by HKH type curve. Based on the calculated parameters and considering the materials that constitute the weathered basement layer VES 1,4,7 and 8 were found to be the most promising point for the exploitation of groundwater within the study area.*

### Introduction

Groundwater has become more popular as a source of potable water; it is described as the water found beneath the surface of the earth in underground streams and aquifers. There has been a general assumption in the past that ground water is ever abundant and readily exploitable. Recent studies have shown that new skills and extra effort are necessary needed to determine the optimum location for development of ground water, in order to avoid over exploration which may lead to serious repercussions. It is therefore necessary to employ quick and efficient method for ground water exploration. Ground water and other mineral resources such as hydrocarbons and

solid minerals are of great abundance in Nigeria. The electrical resistivity method has been the most commonly used geophysical tool for groundwater investigation because of its advantage which include simplicity in field technique and data handling procedure. The continual expansion of the Kaduna State University (Kaduna Campus) alongside with increasing staff/student population placed enormous increase in the demand for potable water which demands other alternatives have to be exploited to complement the existing water supply. The aim of this paper is to employ Direct Current Resistivity method using Schlumberger array to investigate ground water potentials in the main campus

behind multipurpose theatre which is adjacent to directorate, academic planning office.

### Theory of D.C Resistivity Technique

The fundamental equation for resistivity survey is derived from Ohm's law (Grant and West, 1965; Dobrin and Savit, 1988) as reported by Nwankwo et al, 2013.

$$= \frac{RA}{L} \quad (1)$$

$$= \frac{RA}{L} \quad (1)$$

$$= \frac{\Delta V}{I} \cdot 2 \quad (2)$$

where  $\Delta V$  is change in voltage and  $r$  is the radius of current electrode's small hemisphere. Since the earth is not homogeneous, equation (2) is used to define an apparent resistivity  $a$  which is the resistivity the earth would have if it were homogeneous (Grant and West, 1965):

$$a = \frac{\Delta V}{I} \cdot 2 \quad (3)$$

where  $2r$  is then defined as a geometrical factor ( $G$ ) fixed for a given electrode configuration.

The Schlumberger configuration was used in this work. The geometric factor  $G$  is thus given as:

$$G = \frac{\left[\left(\frac{AB}{2}\right)^2 - \left(\frac{MN}{2}\right)^2\right]}{2\left(\frac{MN}{2}\right)} \quad (4)$$

### Location and Geological Setting

The study area is located at Kaduna State University (KASU) behind multipurpose theatre which is adjacent to directorate, academic planning office toward the western gate of the university with coordinate that ranges between latitude  $10^\circ 31.072'N$  to  $10^\circ 31.083'N$  and longitude range of  $007^\circ 26.914'E$  to  $007^\circ 26.882'E$ . The elevation of the area was 603m above sea level (Fig 1). Precambrian basement complex rocks underlie the entire area of Kaduna and they consist of migmatite gneiss complex, Meta sediments/meta volcanic (mostly schist, quartzite, amphibolite and banded iron formation, pan African

granitites and calc-alkaline granites, and volcanic of Jurassic age (McCurry, 1976). In the Basement complex, the permeability and storativity of the groundwater system are dependent on structural features such as the extent, and volume of fractures together with thickness of weathering (Eduvie, 1998; Clark, 1985). The relatively high annual rainfall (1270mm) and temperature ( $32^\circ C$ ) in Kaduna, which has resulted in the formation of deep weathered zone in addition to high density of fractures have contributed tremendously to constituting large reservoirs of groundwater, good aquifers and high yields of boreholes (Eduvie, 1998). Geophysical investigation and borehole drilling reports have clearly established two major aquifers. These are the overburden weathered aquifer and the fractured crystalline aquifer (Eduvie, 1998; Dan-Hassan, et al, 1999). Both aquifers at some places are interconnected and form a hydro geological unit of water table surface. The study area has typically savannah climate with distinct wets and dry seasons. The season extends from March/April to October/November and dry season between December and March. Average rainfall for Kaduna is 1053mm (Eduvie, 1998). Rainfall generally reaches its peak in August. Temperature varies between less than  $15^\circ C$  around December/January and  $30^\circ C$  in March/April.

### Materials and Methods

#### Data Acquisition and Interpretation

The electrical resistivity (Vertical Electrical Sounding) method was used for this study. Ten (10) sounding points were investigated. The method involves the passage of electric current (using D.C. or low frequency A.C. current) into the subsurface, through two electrodes (the current electrodes). Resistivity of subsurface layer is determined from ground apparent resistivity is computed from the measurement of current and potential difference between the electrodes pair placed at the surface. The Schlumberger arrangement was employed for this study. The electrode

spread of AB/2 was varied from 1 to a maximum of 100 m. The expected depth of investigation was  $(D) = 0.125 L$ , where  $L = AB$  and AB the current electrode and the potential electrode MN changing correspondingly from 0.3-5m. The measurements were made with Ohmega Resistivity meter units. The field data obtained was analyzed using computer software, IPIWIN (version 3.0.1) developed

by the Geophysical Group, Moscow State University, which gives an automatic interpretation of the apparent resistivity of each VES data. Data were interpreted in terms of Three to five layer structure (Fig. 2). According to Barker et al (1992) a model is considered acceptable at 10% error level. The fit between model response and the field data for the VES points were generally lower than 10% (Table1).



Fig1: Geology map of Nigeria showing the study Area.

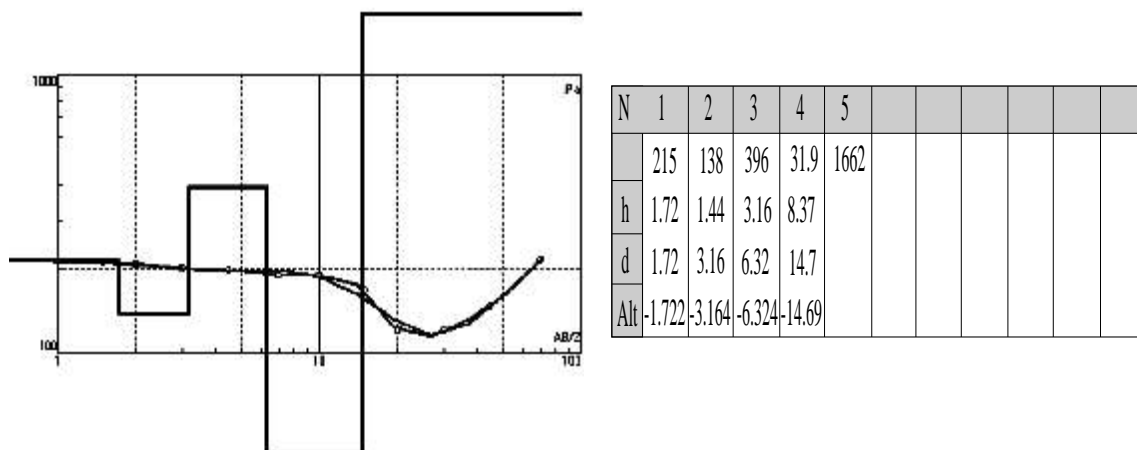


Fig. 2. Typical VES curve and model description

The VES data were subsequently plotted as geo-electric sections (Fig 4) to show the variations of resistivity and thickness values of layers within the depth penetrated in the study area at the indicated VES stations. The interpretation of the VES curves aided by lithological logs from boreholes (Fig. 4) enabled the derivation of maximum of five geologic sections. Qualitative interpretation indicates that the weathered/fractured basement constitutes the main aquifer unit.

### Results and Discussion

The sounding curves of the study area varied from 3 to 5 (Fig 4). Five types of curves were observed (Table 1) in the study area. The KH and H type are the most occurring curves (3 each in number) followed by QH (2 in number), then the HA and HKH with one each. The H-type curve is a common type of curve in the basement crystalline bedrock terrain (Olayinka and Oyedele, 2001). The intermediate layer in the H-curve is usually characterized by low resistivity made of clayey or sandy clay and is often water saturated and highly porous (Oloruntola and Adeyemi, 2014). The HA type consists of the topsoil, clay and weathered basement regolith overlying a Fractured/Fresh basement (Oloruntola and Adeyemi, 2014). Five geologic layers were identified in the study area and they include the lateritic topsoil, clay, sand, weathered bedrock and fresh basement (Fig 4).

BOREHOLE	
Laterite top soil, clayey, brownish (700-900 ohm-m)	15m
Sand, fine, silty, slightly compacted, and light brownish (250-400 ohm-m)	30m
Cuttings of fractured basement rock (300-400 ohm-m)	38m
Fresh basement (300-400 ohm-m)	

Fig. 3. Borehole lithology and interpretation modified from Aboh (2002).

The resistivity of topsoil (Fig4) varies from 118 to 745  $\Omega$ /m. The thickness of topsoil varies from 0.15 to 5.5 m. This layer is of least or no significance as a hydrogeological unit because of its low degree of saturation (Akinlabi et al, 2016; Olorunfemi and Oloruniwo, 1985). The resistivity of the weathered layer varies between 30 and 312  $\Omega$  m and is 0.14 to 61.72m thick. The layer comprises a mixture of clay, sand and gravel. Bedrock resistivity varies between 596  $\Omega$  m and 17478  $\Omega$  m, while depth to the bedrock ranges from 0.4 to 64.8m. The delineated weathered and fractured bedrock columns constituted the aquifer units in the study area. The VES curve types were diagnostic of three different aquifer types. The weathered layer aquifers were characterized by HA and KH curve types. The weathered/fractured (unconfined) aquifers are characterized by QH and H curve types and the weathered/fractured (confined) aquifers are characterized by HKH type curve. The weathered layer aquifer (VES 1, 4, 7 and 8) have thick overburden ranging from 16 m to 65 m and high permeability (sand/gravel materials constitute the weathered layer beneath these VES points) while the weathered/fractured (unconfined) aquifers (VES 3 and 9) have moderate overburden thickness (> 8 m) with high porosity and low permeability (the weathered layer contains high percentage of clay)

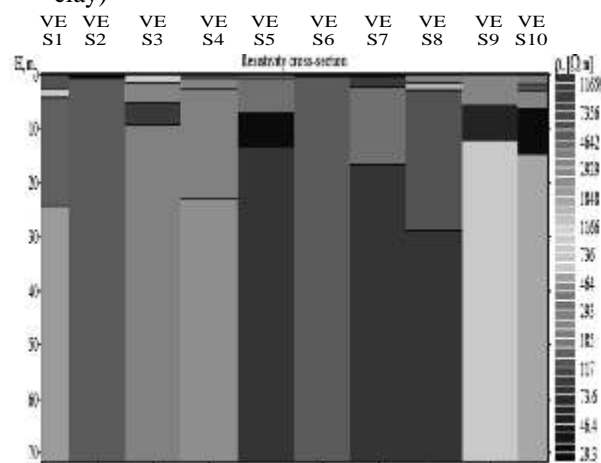


Fig 4 Resistivity cross- sections in the study area

**Table 1. Summary of VES interpreted results in the study area**

VES NO	Layer resistivity 1/ 2/ 3/ 4/ 5 ( m)	Layer thickness $t_1/t_2/t_3/t_4$ / ( m)	curve type	RMS Error (%)	Inferred Lithology
1	118/598/143/1924	2.62/1.56/20.8	KH	4.12	Lateritic topsoil/coarse sand/weathered layer/fresh basement
2	25076/52/5186	0.16/0.45	H $1 > 2 < 3$	8.57	Medium sand/ weathered layer/fresh basement
3	745/438/92/253	1.43/3.69/4.33	QH $1 > 2 > 3 < 4$	0.15	Lateritic topsoil /clayey sand/weathered layer /weathered bedrock
4	225/462/267/2363	0.6/1.97/20.2	KH $1 < 2 > 3 < 4$	0.88	Lateritic topsoil /clayey sand/weathered layer /fresh basement
5	341/306/31/17478	0.7/6.2/6.4	QH $1 > 2 > 3 < 4$	3.87	Lateritic topsoil /clayey sand/weathered layer /fresh basement
6	46991/30/5057	0.6/0.14	H $1 > 2 < 3$	8.79	Medium sand/ weathered layer /fresh basement
7	2369/95/312/5997	0.32/1.94/14.3	HA $1 > 2 < 3 < 4$	6.07	Medium sand/ weathered layer /fresh basement
8	281/1498/133/12006	1.44/1.22/21.9	KH $1 < 2 > 3 < 4$	3.51	Lateritic topsoil/ medium soil/weathered layer /fresh basement
9	456/57/596	5.5/6.6	H $1 > 2 < 3$	0.27	Lateritic topsoil/ weathered basement / fractured bedrock
10	215/138/396/32/1612	1.7/1.4/3.2/8.37	HKH $1 > 2 < 3 > 4 < 5$	3.06	Lateritic topsoil/clayey sand/ sand/ weathered layer /fresh basement

**Conclusion**

The result presented in this work has attempted to define the sub-surface lithology and geo-electrical structure underlying a part of the Kaduna state University, Kaduna, Nigeria. The area is underlain by five layers of different lithological units; the aquifer thickness varies from 14.2 to 21.9 m and the resistivity values of the weathered layer was found to be between 30 ohm-m and 312 ohm-m. VES 1, 4, 7 and 8 were found to be the most promising point for the exploitation of groundwater within the study area. Therefore, the VES points were recommended for siting of groundwater tube.

**REFERENCES**

- Aboh H. O. (2002) Geotechnical characterization of subsurface materials in Kaduna area Kaduna State, Nigeria. *Zuma Journal of Pure & Applied Science*, 4(2):23-33
- Akinlabi, I. A., O. T. Adegoke, and O.R. Bolatan. (2015). "Geophysical Evaluation of Foundation Soils in a Basement Complex Terrain: A Case Study of LAUTECH Campus, Ogbomoso South-western Nigeria". *Pacific Journal of Science and Technology*. 16(1):305-315
- Barker RD, White, CC, Houston JFT (1992). Borehole Siting an African Accelerated Drought

- Relief Project. Hydrogeology of Crystalline Basement Aquifers. In Africa, In E. P. Wright and W. G. Burgess (Eds.), Geological Society of London Special Publication (66:183-201)
- Clark LM. (1985) Groundwater abstraction from the basement complex areas of Africa. Quarterly. Journal of Engineering Geology; 18:25-34.
- Dan-Hassan MA, Olorunfemi MO. Hydro geophysical investigation of a basement terrain in the north-central part of Kaduna State Nigeria. Journal of Mining and Geology. 1999; 35(2):189-205.
- Dobrin, M.B and Savit, C.H. (1988), Introduction to geophysical prospecting. 2nd Ed. London. McGraw-Hill Book Company.
- Eduvie MO. (1998) Groundwater assessment and borehole characteristics, case study from parts of Kaduna Metropolis. Paper Presented at a workshop organized by Kaduna State water board. Nigeria Teachers Institute;
- Grant, F.S and West, G.F. (1965) Interpretation theory in applied geophysics. McGraw-Hill book Company. London.
- IPI2WIN software Moscow State University, Version 3.0; 2003.
- McCurry P. (1976) The Geology of the precambrian to lower paleozoic rocks of Northern Nigeria- A Review in Kogbe, C.A (Editor). Geology of Nigeria. Elizabeth Publication Company, Lagos. Nigeria.; 15-40
- Olayinka, A.I. and A.A. Oyedele. (2001). "Geo-electrical Investigation of Sites along the Proposed Ibadan-Ilorin Dual Carriageway". *Journal Min. and Geol.* 37(2):163-175
- Olorunfemi MO, Oloruniwo, MA (1985). Geoelectric Parameters and Aquifer Characteristics of Some Parts of Southwestern Nigeria. *Geologia Applicante E Idrogeologia*, 20: 99-109
- Oloruntola MO, Adeyemi, GO (2014). Geophysical and Hydro chemical Evaluation of Groundwater Potential and Character of Abeokuta Area Southwestern Nigeria. *Journal of Geography and Geology*, 6(3): 162-177
- Nwankwo, L.I., Olasehinde, P.I. and Osundele, O.E. (2013) Application of Electrical Resistivity Survey for Groundwater Investigation in a Basement Rock Region: A Case Study of Akobo - Ibadan, Nigeria, *Ethiopian Journal of Environmental Studies and Management*, Vol. 6 No.2.pp124-134



## GEOELECTRICAL PROSPECTING FOR WATER-FILLED FRACTURED BASEMENT WITHIN KUNDU, NORTH CENTRAL NIGERIA

<sup>1\*</sup>C.I. Unuevho, <sup>2a</sup>M. Tswako, <sup>3b</sup>K. M. Onuoha, <sup>1c</sup>A. N. Amadi, <sup>4d</sup>E. E. Udensi, <sup>5e</sup>Oshin, O.

1: Department of Geology, Federal University of Technology, Minna

2: Ministry of Water Resources, Minna, Niger State

3: Department of Geology, University of Nigeria, Nsukka

4: Department of Physics, Federal University of Technology, Minna

5: Department of Earth Sciences, Ajayi Crowther University, Oyo

?Email: unuevho@gmail.com, a: tmary2011@gmail.com, b: mosto.onuoha@gmail.com,

c: geoamaa76@gmail.com, d: eeudensi@gmail.com, e: o.oshin@acu.edu.ng

### ABSTRACT

*Three out of six boreholes failed in Kundu, which is a town located within the North Central Nigerian basement complex. Fractures are commonly water filled within topographic depressions along buried basement surfaces, because the depressions are groundwater convergent zones. Thus drilling for potable water supply will be more successful if the boreholes penetrate such fractures. This study was conducted to delineate fracture bearing topographic depressions in Kundu. It was accomplished by integrated stratigraphic and structural interpretation of geoelectrical data, global digital elevation model (GDEM), and exposed lithological units. Hillshade view of the GDEM for Kundu revealed NW-SE displaced major fractures. The dominant lithological units are gneiss and schist. Electrical resistivity, spontaneous potential and induced polarisation data were acquired by Schlumberger sounding, using ABEM SAS 4000 meter. Two groundwater convergence zones were delineated within two confined fracture intervals. The convergence zone associated with the deep fracture interval exists within the central part of the town. The productive boreholes exist within this zone. Drilling more boreholes within the deep convergence zone will increase access to potable water. The shallow convergence zone is a region for productive borehole drilling around the SW of the town, where none has been sited.*

**KEYWORDS:** Basement complex, fractures, topographic depressions

### Introduction:

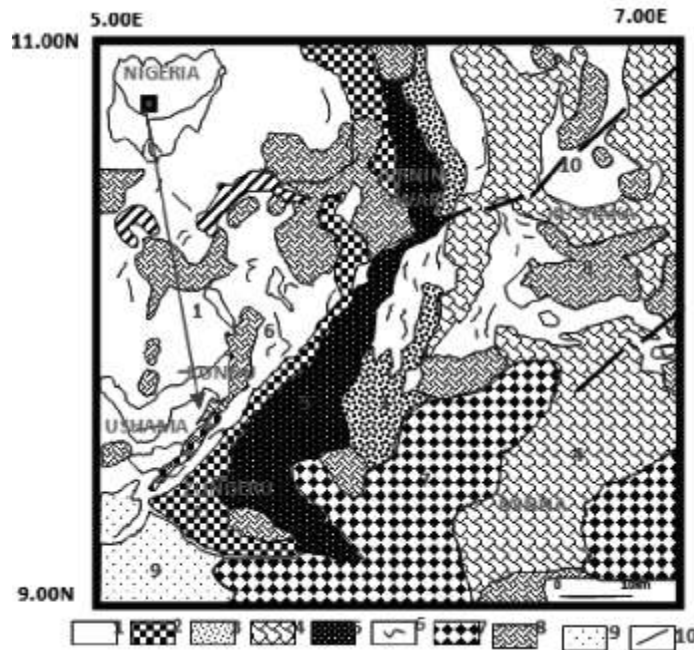
Kundu is a small town within north central Nigerian Basement Complex (figure 1). Groundwater occurrence is localised and difficult to be predicted in basement terrains. This makes locating sites for water borehole drilling very challenging in basement complex areas (Davis & Dewiest 1966). Direct current prospecting has been widely employed in groundwater prospecting in basement areas (Badmus & Olatisu 2012; Ayuk *et al.* 2013; Kumar *et al.* 2014; Ojoina 2014). However, boreholes drilled solely on the basis of resistivity contrast have sometimes failed to produce water. This is probably because similar resistivity anomaly pattern is produced by dry igneous and metamorphic rocks with

conductive mineral impregnations (Unuevho *et al.* 2012).

Out of six boreholes drilled in Kundu, only three are productive. The productive three are inadequate to meet domestic demand for water in the town. Dan-Hassan and Olorunfemi (1999), and Olorunfemi (2009) highlighted that boreholes drilled within groundwater convergence zones in Nigerian basement complex are commonly productive, while those drilled within divergence zones are often dry. By virtue of the foregoing, drilling boreholes to penetrate fractures within groundwater convergence zones should increase potable water supply to adequately

meet domestic water needs in Kundu. Consequently, this study was skewed towards delineating groundwater convergence zones from integrated stratigraphic and structural interpretation of electrical resistivity (ER), spontaneous potential (SP) and induced

polarisation (IP) data, global digital elevation model (GDEM), and exposed lithological units. Such integrated approach has not been previously employed in prospecting for groundwater in Kundu.



Key:

1. Migmatite gneiss (pre-Pan-African)
2. Kyanite and silimanite bearing quartzite
3. Zungeru mylonite
4. Kushaka Formation
5. Birnin Gwari Formation
6. Ushama Schist Formation
7. Foliated Tonalite
8. Late Pan-African granite
9. Cretaceous to Recent sediments
10. Major Fracture.

Figure 1: Study Area within Regional Geological setting (Ajibade, et al. 1989)

### Methodology

Advanced Space Borne Thermal Emission and Reflection Radiometer's Global Digital Elevation Model (ASTER's GDEM) for Kundu was obtained from <https://reverb.echo.nasa.gov>. The elevation model was geo-referenced and processed into hillshade view using ArcMap GIS software. Lineaments were identified and interpreted to represent fractures. The fractures' displacement directions were identified, and the displacement was associated with faulting. Surface lithological mapping of the town and its environs followed. Subsequently, vertical electrical sounding comprising ER, SP and IP were conducted along ten traverses at an average of five stations per traverse. The traverses were oriented along foliation dip direction (SSE) while measurement electrodes

were planted along foliation strike, using Schlumberger electrode geometry. This pattern of data acquisition minimises the influence of lateral lithologic variations that would occur if electrodes are planted in dip direction. The geographical coordinates of the electrical measurement stations were determined using the GPS (Global Positioning System).

Apparent resistivity ( $\rho_a$ ) was calculated from electrical resistance, R, which the equipment (ABEM SAS 4000 device) measured directly using:

$$\rho_a = GR \quad (1)$$

$$G = \frac{(AB)^2 - (MN)^2}{4MN} \quad (2)$$

In equation 1 above,  $G$  represents geometrical factor related to the electrode geometry, while  $AB$  and  $MN$  in equation 2 represent current electrode spacing and potential electrode spacing, respectively. Calculated and cumulative  $\rho_a$  values were plotted against half electrode spacing ( $AB/2$ ) on log-log graph sheets. Cumulative  $\rho_a$  method of Raghunath (2006) was employed to estimate approximate number of geoelectric layers and depth to their respective top. The values obtained were adjusted using measured thickness of top soil and weathered unit at road cutting and other exposed sections. Each geoelectric layer was assigned an approximate  $\rho_a$ . The assigned  $\rho_a$  value marks a distinct discontinuity in the pattern of variation in  $\rho_a$  values within vertically adjacent geoelectric layers. The approximate number of layers, estimated depth to their respective top, and the approximated  $\rho_a$  for each layer, measured  $\rho_a$  and  $AB/2$  data were inputted into *WinResist* (indirect resistivity modelling software) to generate geoelectric sections. Each geoelectric section was subdivided into soil, weathered layer, unconfined fractured basement, shallow confined fractured basement and deep confined fractured basement using distinct discontinuity in the pattern of variation in  $\rho_a$  values. Respective SP and IP value that is representative of the values within a geoelectric layer were chosen for each layer.

The depth to the top of fresh basement surface underlying each confined fractured basement was subtracted from the corresponding station

elevation (obtained using a GPS). This gave the depth of the fresh basement's top with respect to sea level. The depth values were contoured with respect to stations' geographic coordinates (using *suffer11* contouring software) to generate the fresh basement topography. Depressions within the fresh basement topography were identified. Confined fractured basement  $\rho_a$ , thickness, SP and IP values were also contoured. A mosaic map of each confined fractured basement's  $\rho_a$ , SP and IP values, as well as elevation of their underlying fresh basement's top (with respect to sea level) was produced. Basement depression areas that are characterised by both low  $\rho_a$  and 10-20ms IP values within the mosaic map were interpreted to be groundwater convergence zones that possess groundwater saturation attributes. The location map of the existing boreholes in Kundu was produced, and the positions of the productive boreholes were compared with the groundwater convergence zones (Olorunfemi & Okhue 1992; Dan-Hassan & Olorunfemi 1999; Olorunfemi 2009).

## RESULTS

Figure 2 is the hillshade view of the ASTER's GDEM for Kundu and its environs. It revealed major fractures displaced NW-SE by faulting. The geological map produced from surface lithologic mapping is figure 3. It revealed that gneiss; schist, amphibolites and quartzite underlay Kundu and its environs. The gneiss, schist and amphibolite trend NNE, and dip 20 to 60° SSE.

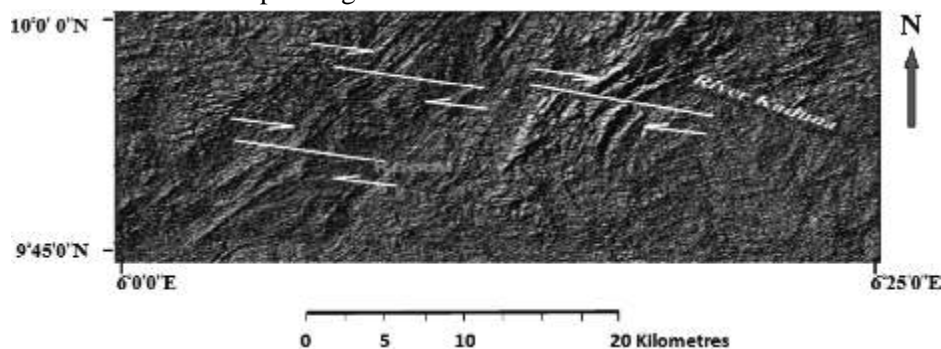
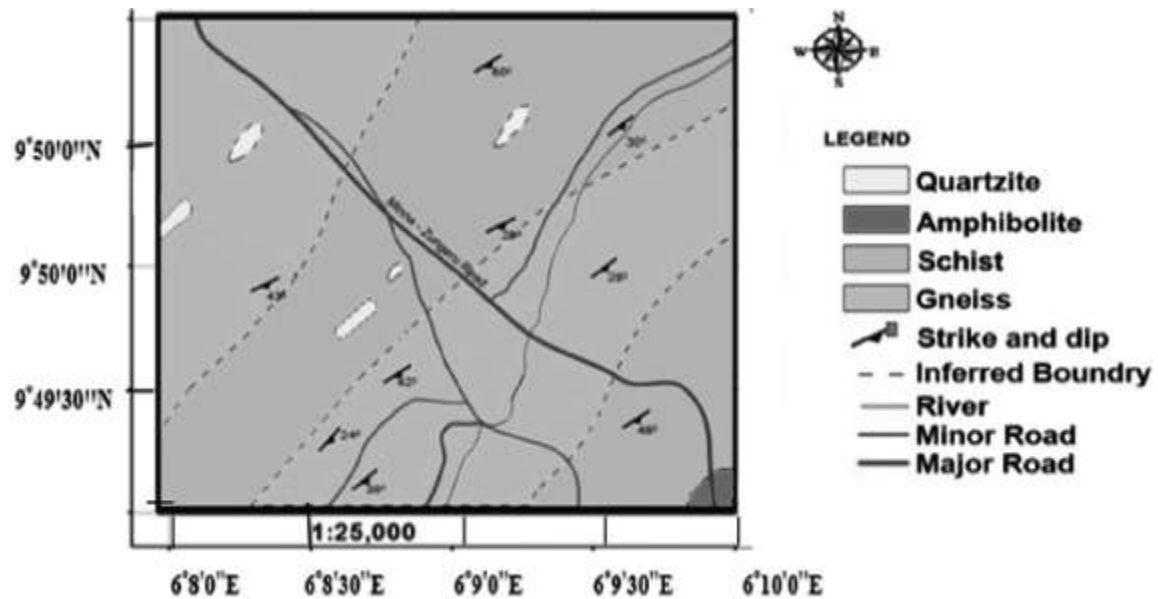


Fig 2: Hillshade topographic image for Kundu and environs



Examples of major surface fractures that indicate polyphase deformation are figures 4, 5 and 6. The surface manifestations of polyphase tectonic deformation in Kundu suggest the existence of different confined fractured basement columns in the subsurface.



Figure 4: Unconfined fractures discharging water into River. Kaduna (N9°50'; E6°10')



Figure 5: Fracture imprints of polyphase tectonic deformation in Kundu's neighbourhood  
N9°49'6.3"; E6°9'7.5"



Figure 6: Unconfined fractures at on schist outcrop at N9°50'; E6°10'

Figure 7 is map of the spatial locations of the sounding stations.

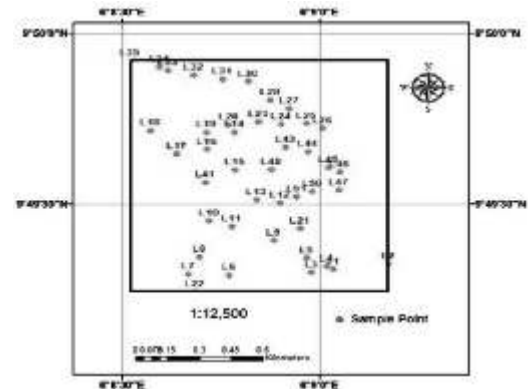


Figure 7: Spatial location of the sounding stations

The apparent resistivity data, modelled resistivity curves and geoelectric layers that are representative of Kundu are presented as figures 8 to 16. The identified curve types and number of geoelectric layers are shown in table1. Q- Type curves were not identified. The captured geoelectric layers, which range from 5 to 10 layers, validate the presence of the confined fractures. The layers represent various combinations of H and K curves. The fractures were distinguished into shallow confined fracture and deep confined fractured

columns. Drilling monitoring in Minna region of North Central Nigerian Basement Complex sometimes indicates penetration of regolith and shallow (or first) fresh basement units before encountering deep fractured basement aquifer unit at depths over 70m. The shallow confined fracture column is sandwiched between the first fresh basement (unweathered and unfractured basement directly underlying the regolith) and second fresh basement (surface of fresh basement that underlay the shallow confined fractured basement

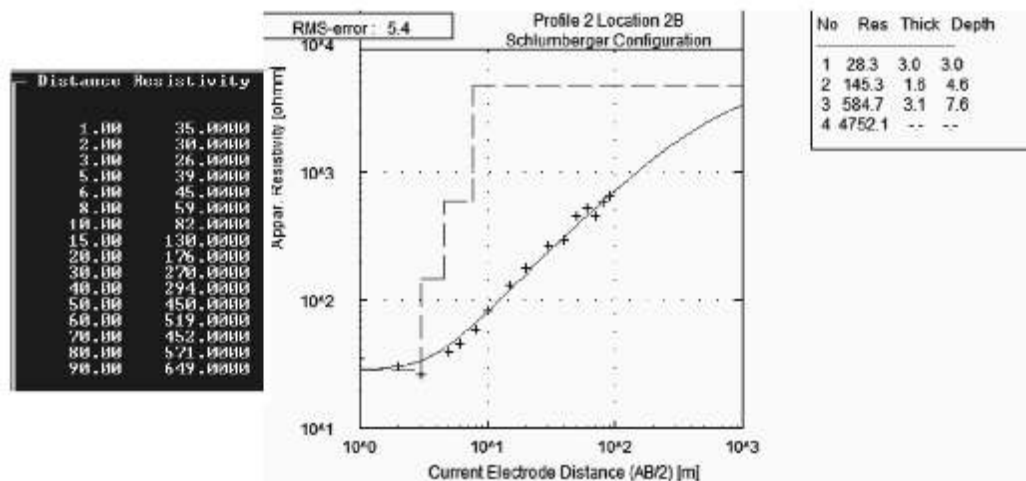


Figure 8: Resistivity sounding data, computer- modelled true resistivity curve and geoelectric Layers at VES 5 station

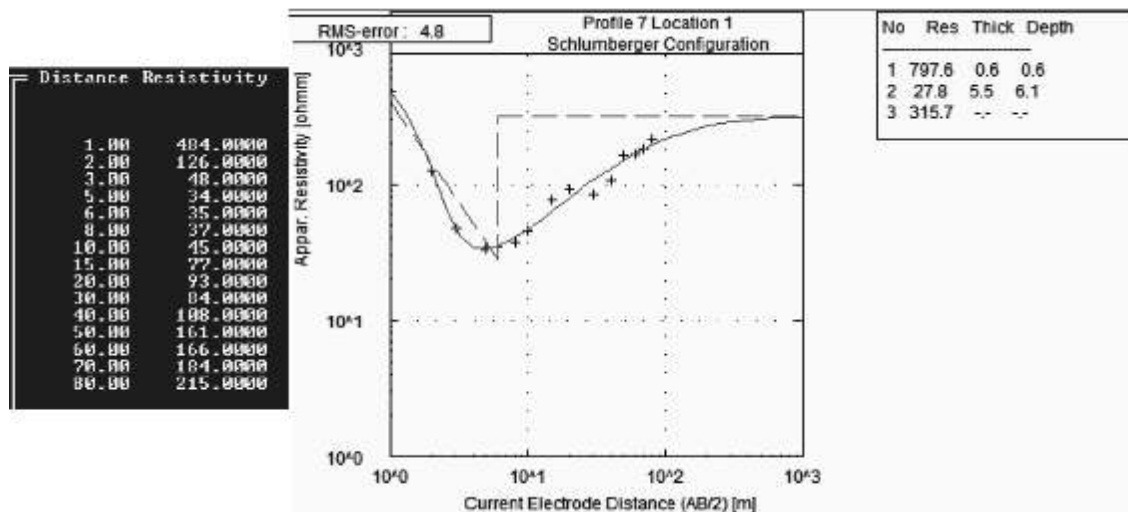


Figure 9: Resistivity sounding data, computer- modelled true resistivity curve and geoelectric Layers at VES 21 station

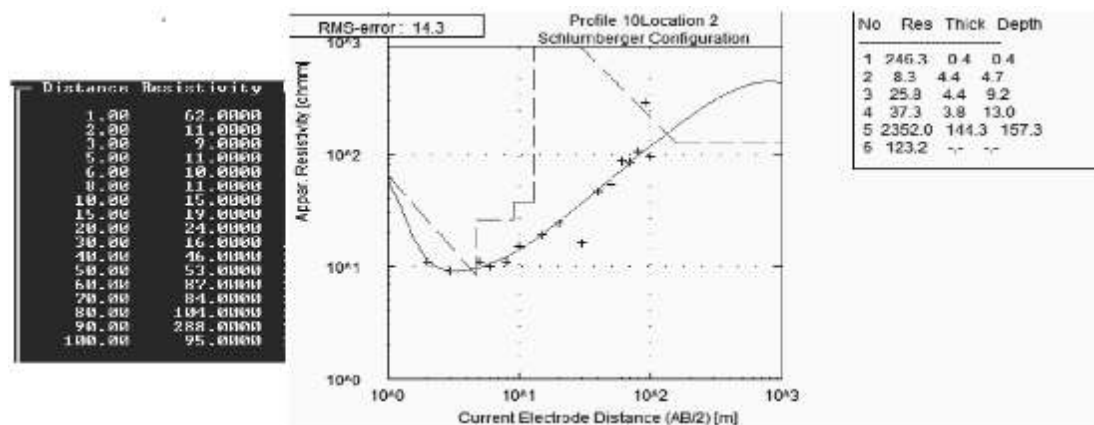


Figure 10: Resistivity sounding data, computer- modelled true resistivity curve and geoelectric Layers at VES 42 station

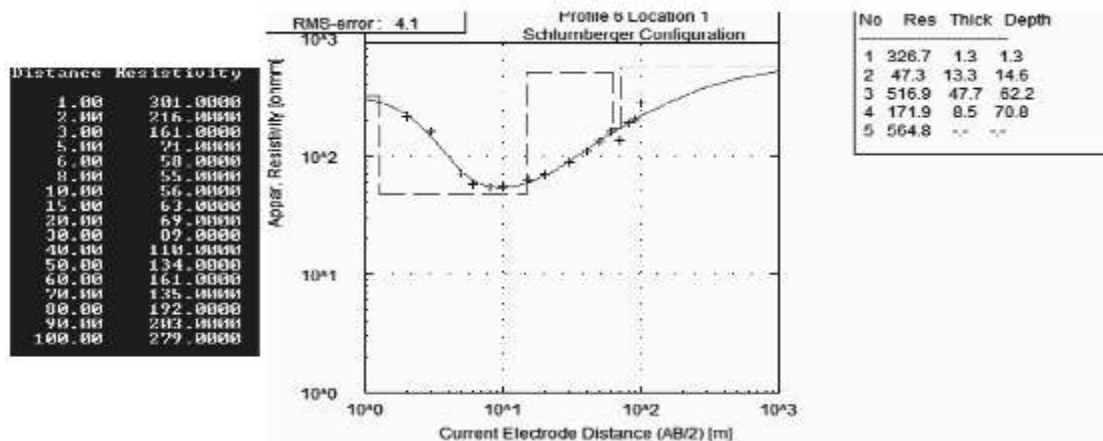


Figure 11: Resistivity sounding data, computer- modelled true resistivity curve and geoelectric Layers at VES 19 station

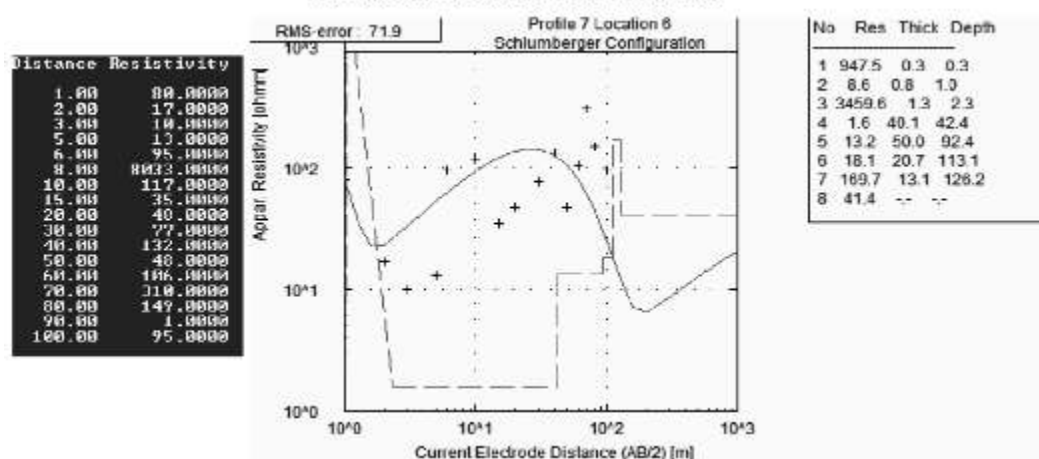


Figure 12: Resistivity sounding data, computer- modelled true resistivity curve and geoelectric Layers at VES 27 station

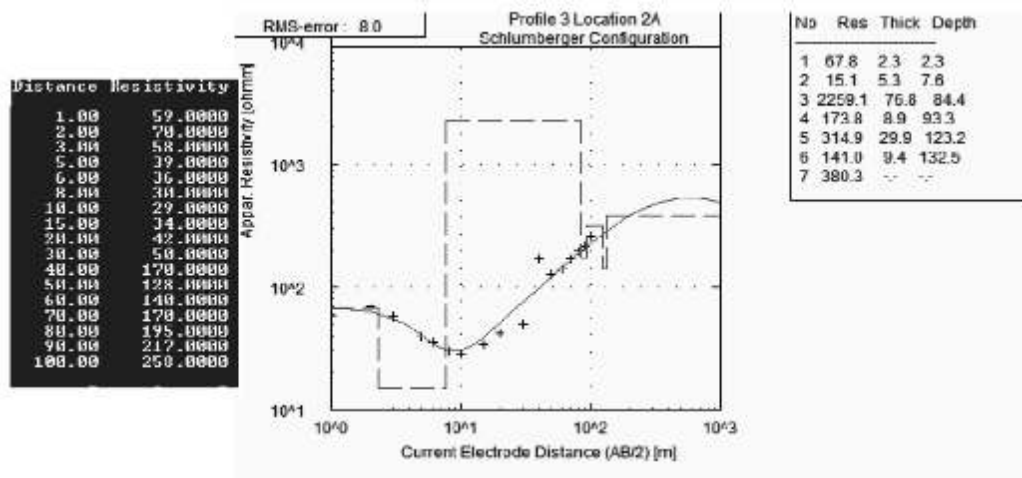


Figure 13: Resistivity sounding data, computer- modelled true resistivity curve and geoelectric Layers at VES 12 station

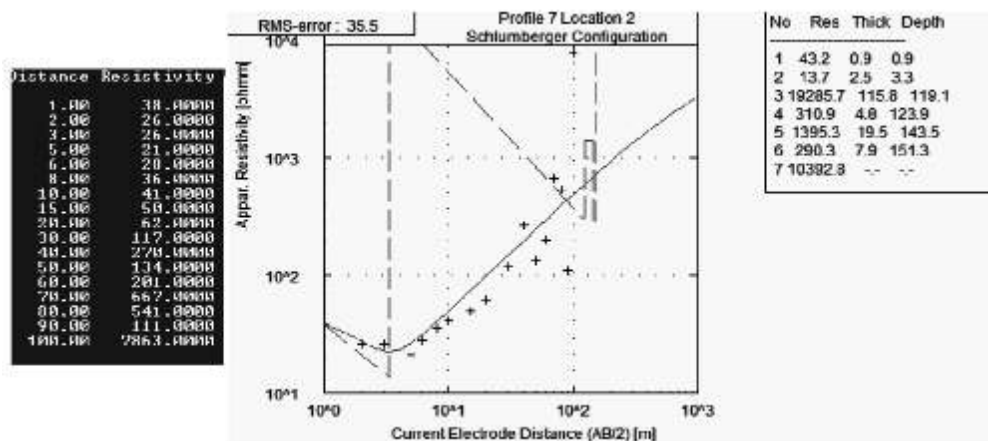


Figure 14: Resistivity sounding data, computer- modelled true resistivity curve and geoelectric Layers at VES 12 station

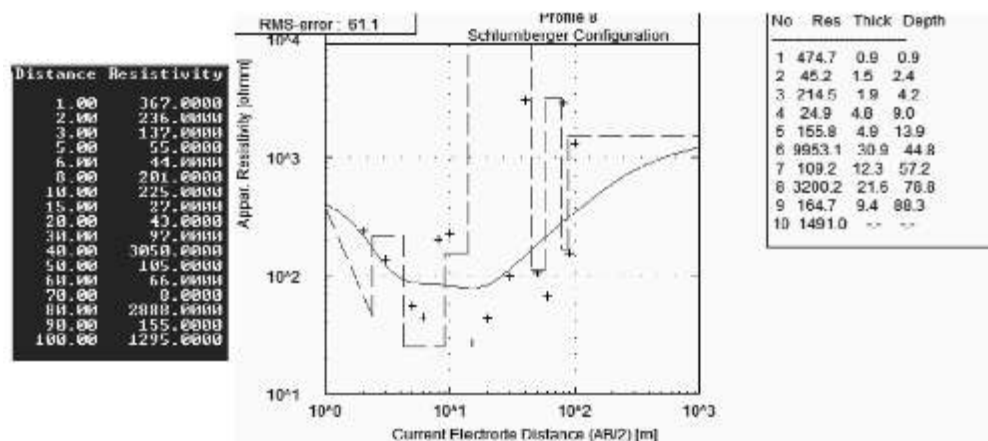
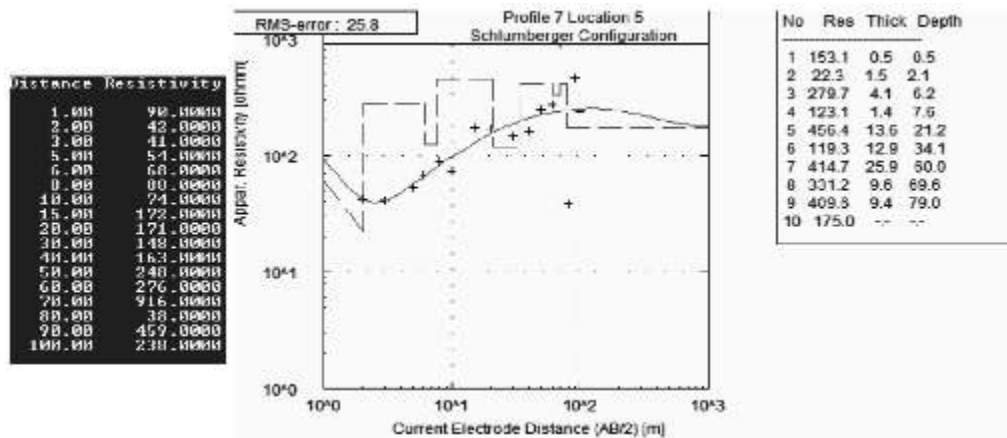


Figure 15: Resistivity sounding data, computer- modelled true resistivity curve and geoelectric Layers at VES 34 station



**Figure 16: Resistivity sounding data, computer-modelled true resistivity curve and geoelectric Layers at VES 26 station**

**TABLE 1: CURVE TYPES AND GEOELECTRIC LAYERS WITHIN KUNDU**

STATION	CURVE TYPE	GEOELECTRIC LAYERS	STATION	CURVE TYPE	GEOELECTRIC LAYERS
VES 5	A	3	VES 12	HKHKH	7
VES 21	H	3	VES 23	HKHKHK	8
VES 42	HK	4	VES 34	KHKHKHK	9
VES 19	HKH	5	VES 26	HKHKHKHK	10
VES 27	HKHAK	7			

Tables 2 and 3 are SP and IP values measured at sounding stations with VES data that are representative values for Kundu. Figures 17, 18, and 19 are respectively the thickness map,

resistivity map and induced polarisation effect map for the shallow confined fracture column. The thickness of this fractured column ranges from 2 to 40m. The resistivity of the column ranges from 300 to 11500? m.

**Table 2: Spontaneous potential values obtained at VES stations 5, 9,12, 15, 21, 23, 26, 34**

AB/2	SP 5 (mv)	SP 9 (mv)	SP 12 (mv)	SP 15 (mv)	SP 21 (mv)	SP 23 (mv)	SP 26 (mv)	SP 34 (mv)
1	35.77	75.46	86.1	9.17	0.113	-0.108	-70.99	49.59
2	36.85	75.1	-79.65	10.32	0.113	- 0.11	-71.53	51.94
3	36.95	72.53	-71.85	11.01	0.107	-0.111	- 69.6	53.5
5	37.21	65.97	-68.64	11.43	0.102	-0.114	-9.515	57.98
6	65.42	81.995	73.275	19.49	86.045	-1.643	6.95	35.4835
8	91.84	-70.17	53:27	- 1.07	98.71	-3.198	16.14	9.695
10	74.21	-29.365	51.565	30.94	83.69	-2.242	18.1905	29.34
15	41.79	-98.06	- 78.3	54.55	77.55	0.536	55.67	-51.84



AB/2	SP 5 (mv)	SP 9 (mv)	SP 12 (mv)	SP 15 (mv)	SP 21 (mv)	SP 23 (mv)	SP 26 (mv)	SP 34 (mv)
20	39.57	-69.86	-86.7	56.14	88.12	2.937	52.67	-54.32
30	39.91	-53.42	-92.34	57	90.61	8.97	57.78	1.101
40	37.11	19.9965	42.6205	28.5035	66.27	65.16	65.54	25.402
50	57.97	0.113	0.138	0.149	32.78	39.28	34.05	0.103
60	66.25	93.05	0.15	0.138	41	40.57	40.76	0.104
70	66.38	77.85	0.159	0.126	44.21	43.83	50.49	0.104
80	33.21	33.435	0.5455	33.068	42.79	22.95	0.801	-0.78
90	0.247	78.51	-80.09	46.62		0.155	0.343	-0.25
100		27.339	-40.74	46.31		27.264	30.614	-14.09

**Table 3: Induced polarisation values obtained at stations IP5, 9, 12, 15, 21, 23, 26, 34**

AB/2	IP 5 (ms)	IP 9 (ms)	IP 12 (ms)	IP 15 (ms)	IP 21 (ms)	IP 23 (ms)	IP 26 (ms)	IP 34 (ms)
1	1.51	0.47	0.64	1.12	1.37	2.45	0.33	0.33
2	1.05	0.79	0.83	0.14	1.91	-1.24	2.59	2.59
3	-3.09	1.4	-2.65	0.58	2.18	1.92	151	151
5	-3.91	0.5	-1.4	-1.9	2.82	-4.68	63.1	63.1
6	-10.735	0.485	0.67	2.395	2.46	83.145	-507	-507
8	-4.74	-0.68	0.63	7.93	1.85	30.7	-378	-378
10	5.84	0.69	1.345	1.463	1.635	73.05	42.5	42.5
15	-0.053	1.25	0.81	1.65	0.96	0.78	-30	-30
20	-3.43	0.069	1.75	-0.057	0.41	0.75	-5.77	-5.77
30	-3.61	0.056	0.26	-1.48	4.14	10.3	-78.3	-78.3
40	-19.815	0.795	1.255	-3.77	2.79	-609	-98.9	-98.9
50	-1.78	0.78	0.73	-1.57	1.36	-4.67	227	227
60	-2.1	0.51	0.45	-2.26	2.3	13.7	17.9	17.9
70	-17.5	0.57	-0.93	-1.36	2.42	-275	-124	-124
80	11.75	0.985	0.545	3.06	2.225	-422.45	-278.5	-278.5
90	-7.65	0.17	-1.37	0.4		-7.58	-147	-147
100		0.3	0.29	6.285		2.84	297.5	297.5

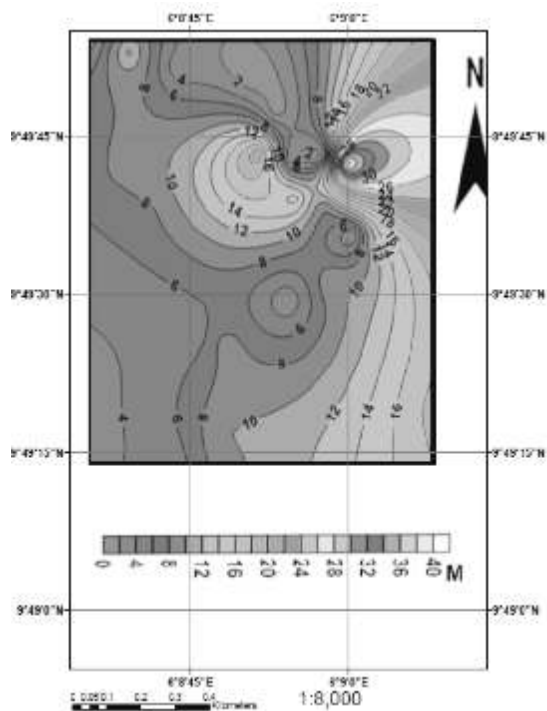


**Figure 17: Thickness map of the first confined fractured basement column**

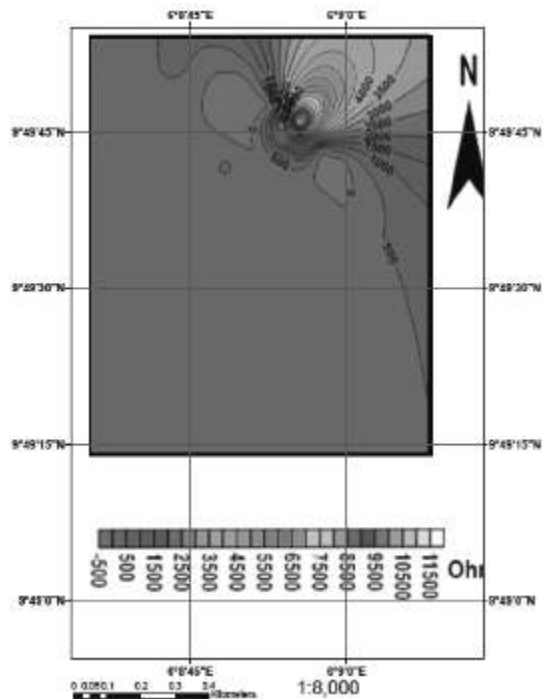


**Figure 18: Resistivity fractured basement column map of the first confined**

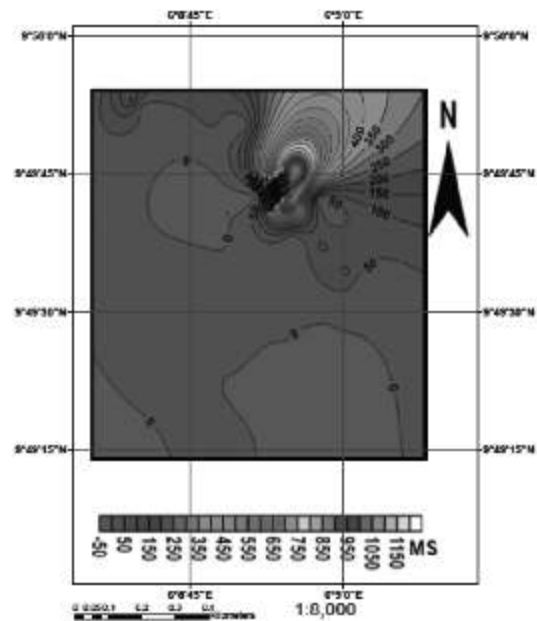


**Figure 19: IP effect map for the first confined fractured bedrock in Kundu**

Figure 20 is the elevation map (with respect to sea level) of the second fresh basement surface, which is the fresh basement surface that underlies the shallow fractured column. The elevation map reveals a topographic depression on its south western portion. This topographic depression is probably a ground water convergence zone within the first confined fractured basement column. The SP map for the shallow confined fractured basement is presented as figure 21.

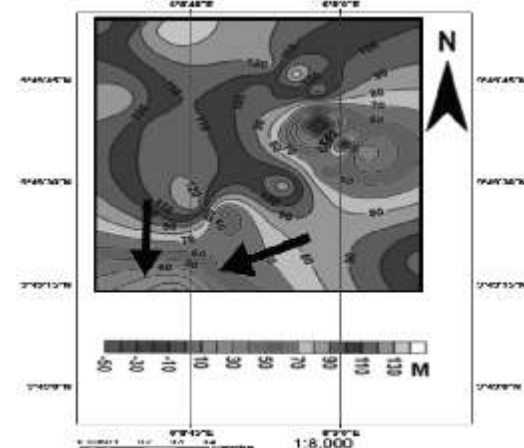


**Figure 20: Elevation map (with respect to sea level) of the second fresh basement surface (surface of fresh basement that underlain the first confined fractured basement column)**

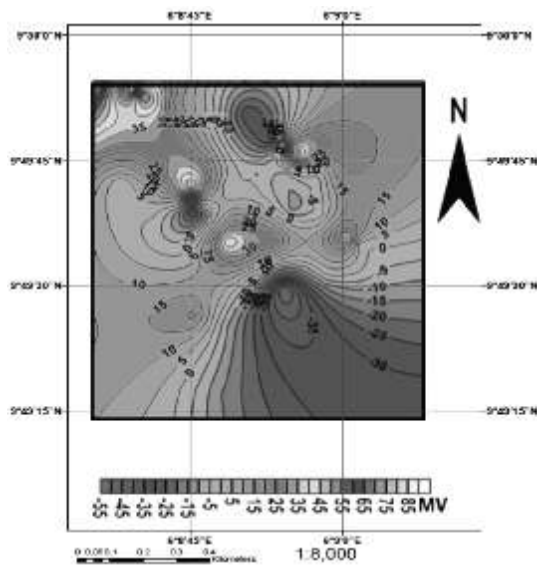


Figure 21: Map of SP values of the first confined fractured basement column

The deep confined fractured basement column is sandwiched between the second fresh basement interval and third fresh basement. Fig 22, 23, and 24 are respectively the thickness map, resistivity map and induced polarisation effect map for the second confined fracture column. The second confined fracture basement column is thickest in the north western portion, where it is 15 to 25m thick. It is 9 to 14m thick in its central portion and thinnest in its eastern part, where it is 2-7m thick (Fig.22). The column's IP effect values range from 0 to 60ms in the central part (Fig.24).

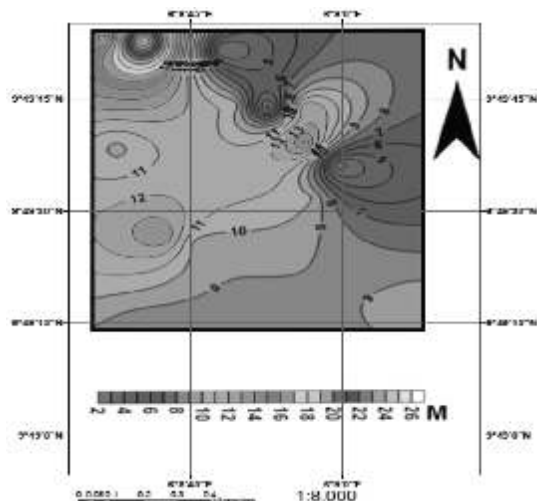


Figure 22: Thickness map for the second confined fractured basement

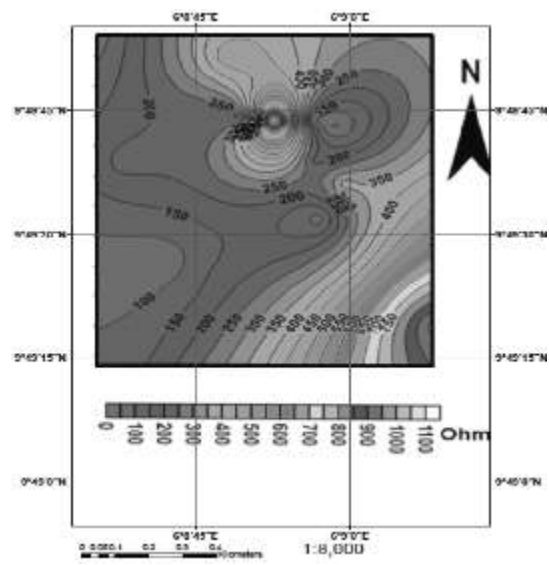


Figure 23: Resistivity map for the second confined fractured basement in Kundu

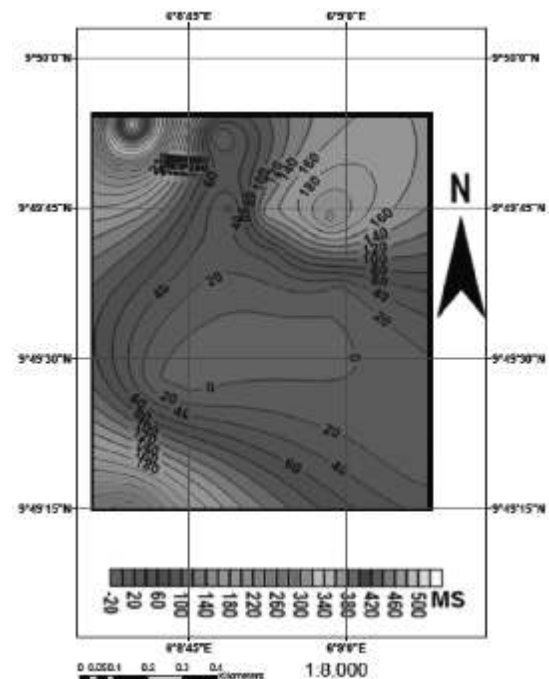


Figure 24: IP effect map for the second confined fractured basement

### Discussion

Figure 25 is the mosaic map that captures area within Kundu where basal surface elevation for shallow confined column is lower than 80m (with respect to sea level), and the column's resistivity, IP and SP values are

respectively lesser than 500  $\Omega$  m, 50ms and +1mv. It reveals the south western part of Kundu where groundwater convergence zone contains water filled fractures. This is defined by Latitudes  $N9^{\circ}49'15''$  to  $N9^{\circ}49'27''$  and Longitudes  $E6^{\circ}8'37''$  to  $E6^{\circ}8'45''$ .

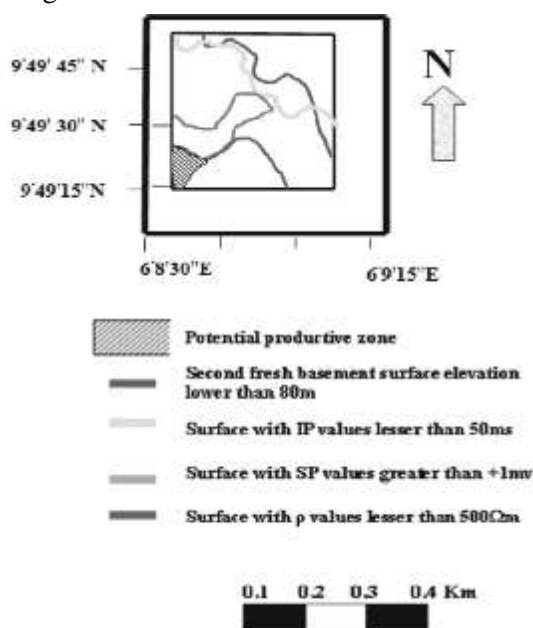


Figure 22: The mosaic map of IP, SP and resistivity values of first (or shallow) confined fractured basement column and elevation of the column's base (the second fresh basement top surface)

The resistivity of the deep fracture column is generally lesser than 300  $\Omega$  m, except in the north central portion where it is up to 1000  $\Omega$  m (Fig.23). This implies that the column is generally characterised by optimal resistivity value that is commonly associated with groundwater occurrence. The column's IP effect values range from 0 to 60ms in the central part (Fig.25). The characterisation of this portion with 0-60ms IP effect and resistivity values of 150 -300  $\Omega$  m indicate presence water filled fractures in the central part of Kundu.

Figures 26 and 27 are respectively the elevation map (with respect to sea level) for the base of the deep fractured basement column (which is also top surface of the third fresh

basement) and SP values map of the second fractured basement column. The deep fracture column occupies a topographic depression in this central part, and thus constitute groundwater convergence zone (Fig.26). The fracture column is associated with +5 to +45mv SP values in this central part (Fig.27). This supports the existence of a topographic depression in the central part of the town

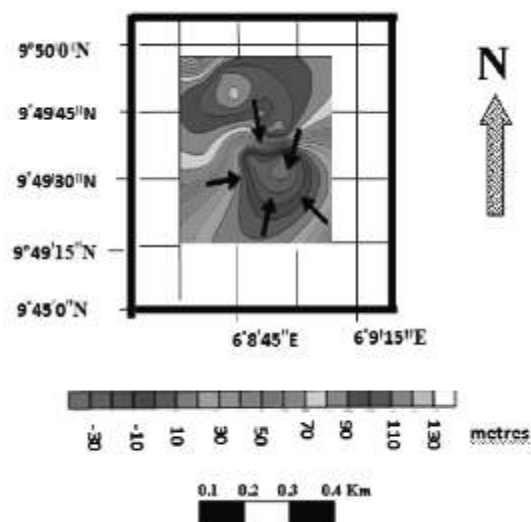


Figure 26: Elevation map for the base of the second confined fractured

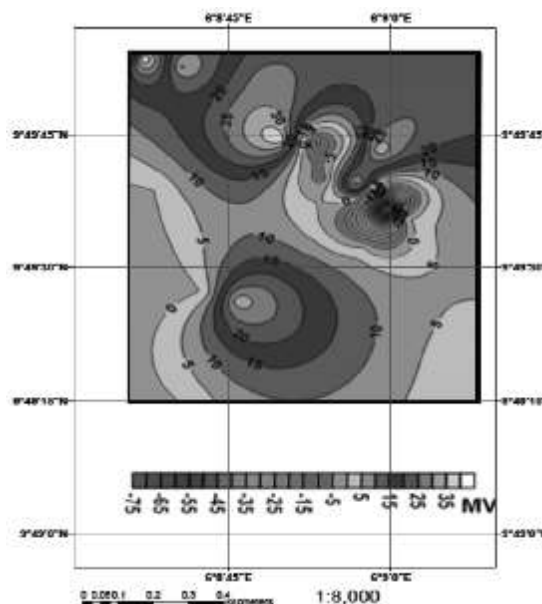
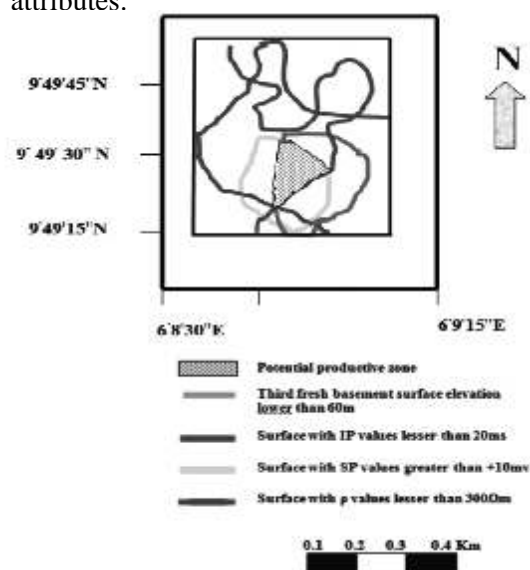


Figure 27: Map of SP values for the second confined fractured basement

Figure 28 is a mosaic map that represents areas where the deep fractured column has a lower than 300m, IP values lower than 20ms, SP values higher than +10mv, and basal surface elevation lower than 90m. The basal surface is the fresh basement surface that directly underlies the fractured column. The shaded part of Fig.28 captures the central part of Kundu where groundwater convergence zone contains fractures with water bearing attributes.



**Figure 28: The mosaic map of IP, SP and resistivity values of first (or shallow) confined fractured basement column and elevation of the column's base (the second fresh basement top surface)**

Figure 29 is the map showing the locations of the existing boreholes in Kundu. It reveals that no borehole has yet been drilled in this part of the town. Thus the convergence zone in south south- west (SSW) of Kundu constitutes a drilling prospect. The productive boreholes (W1, W2 and W6) are located within the shaded portion (Fig.29), where there is high potential for accumulation of producible water. The failed wells (W4, W3) are located on high topographic areas of the elevation map for the base of the deep confined fracture column (Fig.26). Their location on Fig.26 is

defined by Latitudes  $N9^{\circ}49'44.4''$  to  $N9^{\circ}49'58.8''$  and Longitudes  $E 6^{\circ}8'34.8''$  to  $E 6^{\circ}8'56.4''$ . Another failed well (W5) lies outside the convergence zone. Its location coordinates are Latitude  $N 9^{\circ}49'28.4''$  and Longitude  $E 6^{\circ}8'45.6''$  (figures 26, 28 and 29). Thus topographic high zone should be avoided when drilling to tap water from the second confined aquifer. Wells should be drilled within the groundwater convergence zone in this aquifer.

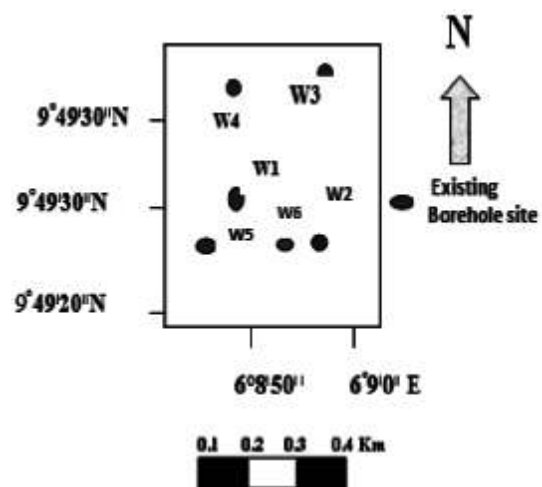


**Figure 29: The Location Map of Boreholes**

### Conclusions

The of H- with K-type curves are geoelectrical imprints of polyphase tectonic deformation driven by multiple orogenic regimes experienced in Kundu and its neighbourhood. Integrated stratigraphic and structural interpretation of ER, SP and IP data has revealed confined shallow and deep fractured basement aquifers within groundwater convergence zones in Kundu. The groundwater convergence zone with shallow aquifer exists in the SW (defined within  $N9^{\circ}49'15''$  to  $N9^{\circ}49'25''$  and  $E 6^{\circ}8'30''$  to  $E 6^{\circ}8'40''$ ) part of the town. It constitutes a drilling prospect since no borehole has yet been drilled to test its groundwater potential. The groundwater convergence zone with deep fractured basement aquifer is located in the central part of the town. The productive boreholes in the town exist within this convergence zone. The failed ones were

drilled in the topographic high zones outside the convergence zone.

### References

- Ajibade, A.C., Woakes, M. and Rahaman, M.A. 1989. Proterozoic Crustal Development in the Pan African Regime of Nigeria. In :Kogbe, C.A. (Ed.) , Geology of Nigeria. Rock View Nig. Ltd., Lagos.
- Ayuk, M.A., Adelusi, A.O., and Adiat, K.A.W. 2013. Evaluation of groundwater potential and aquifer protective capacity assessment at Tutugbua-Olugboyega area, off Ondo road, Akure, SW Nigeria. *International journal of physical sciences*, 8(1): 37-50.
- Badmus, B.S. and Olatisu, O.B. 2012. Geophysical characterisation of basement rocks and groundwater potentials using relectrical sounding data from Odeda quarry site, South –Western Nigeria. *Asian journal of earth sciences*, 5(3):79-87.
- Dan-Hassan, M.A. and Olorunfemi, M.O. 1999. Hydrogeophysical investigation of a basement terrain in the North Central part of Kaduna State, Nigeria. *Journal of mining and geology*, 36(2):189-206.
- Davis, S.W. and De Weist, R.J.M. 1966. *Hydrogeology*, New York: John Wiley and Sons. from resistivity sounding data in parts of Kalmeshwartaluk of Nagpur district, India. *Current science*, 107(7): 1137-1145.
- Ojoina, O.A. 2014. Hydrogeophysical investigation for groundwater in Lokoja metropolis, Kogi State. *Journal of geography and geology*, 6, 1(20): 81-95.
- Olorunfemi, M.O., 2009. *Groundwater exploration, borehole site selection and optimum drill depth in basement complex terrain*: Water resources special publication series.
- Olorunfemi, M.O. and Okhue, E.T. 1992. Hydrogeologic and geologic significance of a geoelectric survey at Ile-Ife, Nigeria. *Journal of Mining and Geology*, 28:2
- Raghunath, H.M. 2006. *Groundwater*, 3<sup>rd</sup> ed. New Delhi; New Age.
- Unuevho, C., Onuoha, K.M. and Alkali Y.B., 2012. Direct current resistivity methods for groundwater prospecting in hardrock terrains: a viable approach to providing sustainable potable water. *Centre for Human Settlements and Urban Development Journal*:1-16.

## APPLICATION OF THE FULL-SCHLUMBERGER ELECTRODE ARRAY FOR GROUNDWATER INVESTIGATION AT THE NIGERIAN COLLEGE OF AVIATION QUARTERS, ZARIA NORTHERN-NIGERIA

**Afuwai Gwazah Cyril**

Department of Physics, Kaduna State University, Kaduna-Nigeria

Email: [cyafuwai@gmail.com](mailto:cyafuwai@gmail.com)

### ABSTRACT

*Geophysical survey using the full-Schlumberger electrode array has been carried out at Nigerian Aviation Quarters, Zaria. The aim was to characterize the site for foundation analysis and to investigate the areas suitable for groundwater exploitation. The work consisted initially of resistivity traversing followed by Vertical electrical sounding (VES) at feasible and anomalous points. The investigation also consisted of geological reconnaissance and hydrological assessment. Terrameter signal averaging system (SAS) model 300 was the instrument used. No booster was used as the expected depth is within the range of penetration of the instrument. A total of 16 vertical electrical sounding was taken at the entire survey area. The VES curves were interpreted using IPI2Win resistivity computer software. The survey area is dominated by mainly four layers, namely: Overburden, Weathered basement, fractured basement and Fresh basement. The overburden consists of laterites, clay and fadama loam. Based on the parameters of the geoelectrical soundings as well as the relevant geologic and hydrogeological information, VES Points 05, 06, 10, 11 and 12 were found to be favourable for borehole development.*

**Keywords:** Groundwater1, Borehole2, Resistivity

### Introduction

This paper assesses the groundwater potentials of Nigerian aviation quarters, Zaria. The climate of the area is made up of two major seasons: Dry season, which usually last from November to February with warm sunshine and hazy harmattan around December and January, and Rainy season which lasts from April to November. Mean monthly temperature range from about 27o to 30o C and the annual precipitation is 1131mm. Groundwater is commonly understood to mean water occupying all the voids within a geologic stratum. This saturated zone is distinguished from an unsaturated zone, where voids are filled with water and air. Water contained in saturated zones is important for engineering works, geologic studies, and water supply developments (Afuwai et al, 2013).

The source of uncontaminated water,

groundwater, is becoming more important for many needs, especially for drinking and Agricultural purposes. Therefore, methods used for locating suitable groundwater aquifers and their hydrological conditions should be more efficient. Recently, geophysical methods – particularly the electrical resistivity methods are playing a satisfactory role in groundwater investigations.

The resistivity of rocks is strongly influenced by the presence of ground water, which acts as an electrolyte. This is especially important in sedimentary rocks containing pore spaces. In metallic ores the resistivity can be very low, but igneous rocks that contain no water can have very high resistivity (Bradley, 1979). The minerals that form the matrix of a rock are generally poorer conductors than groundwater, so the conductivity of a rock increases with the amount of groundwater it contains. This depends on the fraction of the

rock that consists of pore spaces (the porosity) and the fraction of the pore volume that is water filled (the water saturation) Batayneh (2006). The conductivity of the rock is proportional to the conductivity of the groundwater, which is quite variable because it depends on the concentration and type of

dissolved minerals and salts it contains.

The Nigeria college of Aviation, Zaria is located at latitude of  $11^{\circ}09'N$  and at a Longitude of  $7^{\circ}38'E$  in the Sabongari local government area (L.G.A) of Kaduna state, Nigeria (figure 1). The College is accessible mainly through the Zaria-Shika main road



Figure 1. Map of Nigeria showing Zaria.

The study area has dry season (November to April) and wet season (May to October) with rain falling mainly during the wet season with an average annual rainfall of about 109cm (Hore, 1970). The Nigeria college of Aviation, Zaria has been substantially developed over the years; hence it has become imperative for geophysical survey to be carried out to obtain some basic parameters that will aid future development plans in College.

#### Review of Geology and Hydrogeology

The survey area is underlain by crystalline basement rocks. The rocks include different textures of granites, coarse to fine, consisting essentially of biotite, feldspars and quartz. In

most cases the rocks have weathered into reddish micaceous sandy clay to clay materials capped by laterites, (Eduvie, 2003). Generally, only small amount of water can be obtained in the freshly unweathered bedrock below the weathered layers. Groundwater is found mainly in the variable weathered/transition zone and in fractures, joints and cracks of the crystalline basement (Akintorinwa, 2009). Fissure systems in Nigeria rarely extend beyond 50m, as evidenced by the available drilling data (Clark, 1985). The local water table depth is controlled by textural and compositional changes within the regolith vertical profile and the bedrock topography (David et al, 1989).



### Methodology

The method of study includes geophysical investigation using resistivity method and analysis of records on three boreholes located within the quarters. The records include data on geology and parameters determine from pumping test. Not all the boreholes contain enough information for the calculation of such aquifer parameters like transmissivity. In the DC resistivity surveying, using the Schlumberger array (figure2), an electric current is passed into the ground through two outer electrodes (current electrodes), and the resultant potential difference is measured across two inner electrodes (potential electrodes) that are arranged in a straight line, symmetrically about a centre point. The ratio of the potential difference to the current is displayed by the Terrameter as resistance. A geometric factor (G) in metres is calculated as a function of the electrode spacing. The resistance reading obtained by the Terrameter is multiplied by this factor to give an apparent resistivity value. The electrode spacing is progressively increased, keeping the centre point of the electrode array fixed. Schlumberger arrays are relatively sensitive to vertical variations in the subsurface resistivity below the centre of the array but less sensitive to horizontal variations in the subsurface resistivity (Lowrie, 1997). The arrays have moderate depths of investigation and generally strong signal strength which is inversely proportional to the geometric factor used in calculating the apparent resistivity values (Afuwai, 2014). The major limitation of these arrays is the relatively poor horizontal coverage with increased electrode spacing (MacDonald et al, 2002).

A total of sixteen (16) VES Points were sounded.

### Theory of the Resistivity Method

The resistivity surveys use four equi-spaced electrodes in a standard configuration. A low frequency current is applied across the outer electrodes and the voltage measured across the

inner electrodes. Depth probes provide models of vertical variations in ground resistivity using an expanding electrode array offset from a central reference point, (Aboh, 2001). A and B are current electrodes through which current is supplied into the ground, M and N are two potential electrodes to measure the potential differences between the two electrodes and P is the VES station to be sounded. The apparent resistivity is given by  $\rho_a = K (V/I)$  with K a geometric factor which only depends on electrode spacing. The apparent resistivity is the ratio of the potential obtained in-situ with a specific array and a specific injected current by the potential which will be obtained with the same array and current for an homogeneous and isotropic medium of 1 m resistivity (Dobrin, 1976). The apparent resistivity measurements give information about resistivity for a medium whose volume is proportional to the electrode spacing (Koefoed, 1971). Resistivity is affected more by water content and quality than the actual rock material in porous formations. The choice of sounding points was made to cover the adequate areas surrounding the two boreholes at the site so as to achieve the stated objectives. Each point sounded has its azimuth either N-S, E-W, NW-SE or NE-SW (guided by the emplaced structures) also the longitude, latitude and elevation of each VES point was taken so that the profiles can be properly posted on to the survey area.

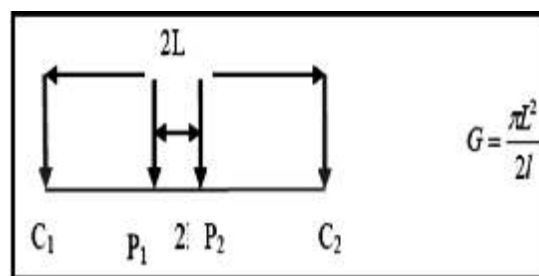


Figure2. The Full-Schlumberger Array

### Results and Discussion

Based on the IPI2Win's method, the field curves were found to be averagely four (4) layers. The resistivity of the layers ranges from 70 to 2000 ohm-m depending on the lithology. These layers can be grouped into top lateritic soil, the sandy clay or clayey sand with intercalation of silts/clays, the weathered regolith transition zone and the fresh basement rock. The drilling results correlates closely with the VES carried out during the survey. The thickness of the overburden in the project area varies depending on the location.

Table 1 shows the interpretation of VES POINT 05, and figure 3 shows typical digitized curve for VES POINT 05. VES Points 05, 06, 10, 11 and 12 have very good groundwater potential.

**Table 1:** Interpretation of VES POINT 05.

N	$\rho$	h	d	AR
1	450	1.61	1.61	-1.611
2	239	2.4	4.01	-4.014
3	100	7.5	11.5	-11.51
4	39.2	31	42.5	-42.52
5	1000			

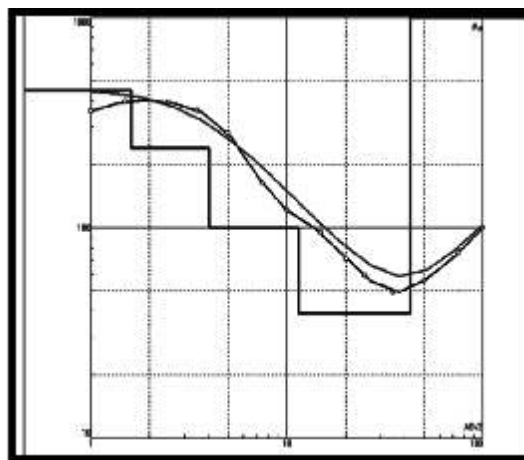
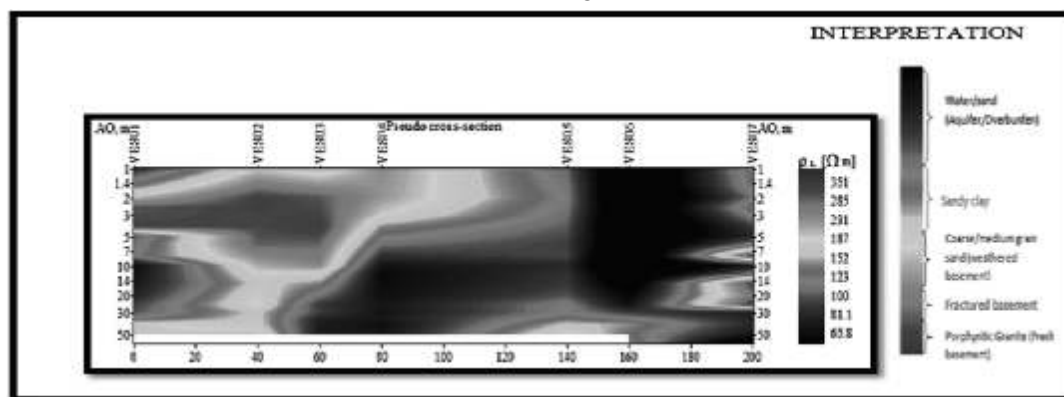


**Figure3.** Typical digitized curve for VES POINT 05.

In figure 3, Apparent resistivity ( $\rho_a$ ) in ohm-metres is plotted against the electrode spacing (AB/2) in metres by the computer software IPI2Win on a log-log scale. The blue colour gives the number of layers, the red colour indicate the synthetic curve while the black colour shows the curve for the field data.

A Profile of length 200m was taken across VES POINTS 01, 02, 03, 04, 05, 06 and 07 to produce a pseudo-section of the subsurface within these VES POINTS. The Pseudo section shows that along the Profile where VES05 and VES06 are located, the area is underlain by an aquifer with thickness of approximately 50m (Figure4). The overburden with a resistivity range of 50-140 $\Omega$  m constitutes of wet brown sand and sandy clay. The weathered basement which is the second layer composed of coarse/medium grain sand.



The interpretation of all the VES points (1 to 16) is given in the table below:

S/N	VES POINTS	AZIMUTH	1	$h_1$	2	$h_2$	3	$h_3$	4	$h_4$	5	$h_5$
1	01	E-W	450	1.61	239	2.4	100	7.5	39.2	31	1000	-
2	02	E-W	151	1.89	1957	1.67	392	74.5	447	-	-	-
3	03	E-W	98.2	2.6	258	6.92	674	14.5	720	-	-	-
4	04	E-W	105	5.54	300	1.67	486	-	-	-	-	-
5	05	E-W	97.9	2.62	133	8.88	432	80.6	527	-	-	-
6	06	E-W	163	0.45	89.1	4.99	316	8.42	373	-	-	-
7	07	E-W	148	2.36	165	1.07	444	21.2	1290	-	-	-
8	08	N-S	90	2.47	208	5.67	462	77.4	576	-	-	-
9	09	N-S	28.4	0.343	197	0.454	38.5	4.14	80.8	-	-	-
10	10	N-S	362	0.684	88.5	3.96	773	-	-	-	-	-
11	11	N-S	208	3.79	82.2	10.6	37.1	14.8	54.9	-	-	-
12	12	N-S	357	0.241	179	1.63	33.5	8.55	54	-	-	-
13	13	N-S	293	4.87	79.4	17	189	-	-	-	-	-
14	14	N-S	266	0.789	204	5.53	44.7	-	-	-	-	-
15	15	E-W	124	0.505	367	0.651	123	8.05	24.7	21.9	4751	-
16	16	E-W	221	0.364	153	6.66	1303	64.7	1676	-	-	-

Where  $h_1$  is the thickness of first layer and  $\rho_1$  is the resistivity of the first layer.

### Conclusion and Recommendation

This study has gone a long way to establish the fact that some parts of the staff quarters of the Nigerian College of Aviation, Zaria contain

reasonable amount of groundwater which if well tapped will go a long way to alleviate the water problem presently going on within the quarters. There is a need for proper

understanding of the groundwater condition of the area, the foundation of which has been laid through this study. This could be achieved by carrying out comprehensive pre-drilling hydrogeological studies for the entire area and all boreholes should be properly designed and properly developed and pump tested. The knowledge of this will reduce borehole failures and low yield currently experienced in some parts of the Zaria area. Based on the parameters of the geoelectrical soundings as well as the relevant geologic and hydrogeological information, VES Points 05, 06, 10, 11 and 12 have been found to have very good groundwater potential.

## References

- Afuwai, G.C. (2013). The Variation in the Depth of Overburden at Different VES Points within Samaru College of Agriculture, A.B.U, Zaria-Nigeria, Using D.C Resistivity Technique. *International Journal of Advances in Science and Technology*. 7(2). Pp44-48. Available online at [www.svpublishers.co.uk/ijast](http://www.svpublishers.co.uk/ijast)
- Afuwai, G.C. and Lawal K.M. (2013). Interpretation of vertical electrical sounding points around two boreholes at Samaru college of agriculture, A.B.U., Zaria-Nigeria. *Scholars Research Library: Archives of Physics Research*. 4(5). Pp49-54. Available online at [www.scholarsresearchlibrary.com](http://www.scholarsresearchlibrary.com).
- Afuwai, G.C. (2014). Geophysical Investigation of Groundwater Potential of Kongo Campus, A.B.U., Zaria-Nigeria. *Ozean Publication: European Journal of Educational Studies*. 7(1), Pp1-7.
- Afuwai, G.C, Lawal, K.M, Sule, P And Ikpokonte, A.E. (2014). Geophysical Investigation Of The Causes Of Borehole Failure In The Crystalline Basement Complex: A Case Study of Kaura Area Of Kaduna State, Nigeria. *Journal of Civil and Environmental Research* (IISTE Publishers). Vol.4, No.23, 2014. Pp 133-138.
- Akintorinwa, O. J. and Adeusi, F. A. (2009). Integration of Geophysical and Geotechnical Investigations for a Proposed Lecture Room Complex at the Federal University of Technology, Akure, SW, Nigeria. *Ozean Journal of Applied Sciences*, 2(1) Pp3-5.
- Batayneh, A. T. (2006). Resistivity tomography as an aid to planning gas-pipeline construction, Risha area, north-east Jordan. *Near Surface Geophysics*, 4, 313–319.
- Bradley, W.B. (1979). Failure of Inclined Boreholes. *Journal of Energy Resources Technology*. 101(4), pp 47-51.
- Clark, L (1985): Groundwater Abstraction From The Basement Complex Area Of Africa. Q.J. Engineering Geology London Vol.18 Pp. 25-34.
- David, L. M. and Ofrey, O. (1989): An in direct method of estimating groundwater Level on Basement complex regoliths. *Water Resources - Journal of Nigeria Association of Hydrogeologists*. Vol. 1, No. 2 pp61-164.
- Offodile, M. E. (1992): An Approach to Groundwater Study and Development in Nigeria, Mecon Services Ltd. Jos. Pp224-227.
- Eduvie, M.O., Olabode, T. and O. O. Yaya (2003): Assessment of groundwater potentials of Abuja environs. 29th WEDC International Conference.
- Lowrie, W. (1997). Fundamental of geophysics. *Cambridge University press*. Location Map Zaria, Sheet102.
- MacDonald, A.M. and Davies, J. (2002) *A Brief Review of Groundwater for Rural Water Supply in Sub-Saharan*

## TILT ANGLE OPTIMIZATION TO MAXIMIZE INCIDENT SOLAR RADIATION ON FLAT PLATE SOLAR COLLECTORS IN ZARIA, NIGERIA

Mohammed Adamu

Department of Physics, Kaduna State University, Kaduna, Nigeria.

E-mail: babanhapsa@gmail.com

### ABSTRACT

*The main objective of the paper is to examine the theoretical aspect of choosing a tilt angle for the solar flat plate collectors facing equator used at Zaria, Nigeria. This will allow collectors to receive the maximum of the incident solar energy. An isotropic model was employed in the computation of total global solar radiation received on tilted collector from data received on the horizontal collector. To determine the optimal tilt angle the inclination angle was varied from 0° to 90° by step of 5°. The analysis showed that the monthly average optimal tilt angle for each month is 60°, 35° and 15° for (January to March), 0° for (April to September) 40°, 55° and 60° for (October to December) respectively.*

**Key words;** Tilt angle, global solar radiation, flat plate solar collectors, Zaria, Nigeria.

### Introduction

Nigeria is among those countries that are characterized with high solar insolation throughout the year, yet facing problems on how to harness this abundant energy. Recent researches Nwofe(2014); Sambo(2015) observed that the climate condition of Nigeria was quite favorable for the implementation of solar thermal and solar power systems. The performance of these systems depends not only on the amount of solar energy captured in an area but also on inclination and orientation of the systems collectors. A number of studies have shown that the best orientation for a collector in the northern hemisphere is the southern direction and for the southern hemisphere is the northern direction but the inclination is changing every time with the position of sun in the sky.

Optimum tilt angle ( $\theta_{opt}$ ) is the inclination angle which flat-plate solar collectors are positioned to the horizontal to capture maximum amount of solar energy (Fig. 1). This angle can be achieved using manual tracking system or automatic tracking system. The automatic tracking systems use energy (usually solar) for

their operation; they are expensive and cannot be applied for solar thermal systems (Ahmad & Tiwari 2009).

This paper examines the theoretical aspects of determining a monthly optimal tilt angle for the solar flat-plate collectors used at Zaria and makes recommendations on how the collected energy can be increased by varying the tilt angle on monthly basis.

### Materials and Methods

According to the literature the total radiation on a tilted surface can be calculated from data of global solar radiation received on horizontal surfaces.

Many researchers have given reviews on how to transform data recorded by horizontal Pyranometers to data that would have been received by tilted surfaces (Ahmad & Tiwari 2009; Armstrong & Hurley 2009; Benghanem 2011; Fawaz *et al.* 2012; Amita & Tiwari 2013; Uba & Sarsah 2013; Ihya *et al.* 2014; Udoakah & Okpura 2015; Berisha *et al.* 2017). Two general models have been proposed; isotropic and anisotropic. The only difference between the two models exists in

the treatment of the diffuse component of the radiation. The assumption generally used for converting the diffuse component value for a horizontal surface to that for a tilted one is that sky radiation is isotropically distributed all times (Amita & Tiwari 2013). However, Amita & Tiwari (2013) stated that this assumption is absolutely wrong because it contradicts experimental and theoretical results. They further suggested that the sky radiation should be treated as anisotropic, particularly due to the strong forward scattering effect of aerosols.



**Fig.1 Tilt angle of a Photovoltaic panel (Abhisheket al. 2012).**

Monthly average daily total radiation on tilted surface ( $H_t$ ) is normally estimated by adding the beam irradiation ( $H_{BT}$ ) the diffused radiation ( $H_{DT}$ ) and the albedo radiation ( $H_R$ ) results. Thus for a surface tilted at a slope angle ( $\gamma$ ) from the horizontal, the incident total radiation is given by

$$H_t = H_{BT} + H_{DT} + H_R \quad (1)$$

Assuming isotropic reflection, the daily ground reflected radiation can be written as (Udoakah & Okpura 2015)

$$H_R = \frac{1}{2} H_{DH} (1 - \cos \gamma) \quad (2)$$

Beam irradiation for the horizontal surface ( $H_{BH}$ ) which is the monthly mean horizontal daily total extraterrestrial solar radiation energy is given by (Amita & Tiwari 2013)

$$H_{BH} = \frac{24}{360} S [1 + 0.033 \cos(\frac{2\pi n}{365})] (\cos \phi \cos \delta \sin \omega_s + \omega_s \sin \phi \sin \delta) \quad (3)$$

Where  $S$  is solar constant ( $4.92 \text{ MJ/m}^2$ ),  $n$  is the day of the year,  $\delta$  is the declination angle which could be estimated for any given day  $n$  using equation (4)

$$\delta = 23.45 + \sin(360(\frac{284+n}{365})) \quad (4)$$

And  $\omega_s$  is the hour angle which is derived from the analysis that the earth rotates one revolution per day corresponding to  $360^\circ$  longitude = 24 hours. This implies that the day length is  $\frac{2\omega_s}{15}$  therefore

$$\omega_s = \cos^{-1}(-\tan \phi \tan \delta) \quad (5)$$

Where  $\phi$  is the latitude of the location, hence the sun rise and sunset angles for a tilted surface  $\omega_s^\gamma$  facing the equator is given by (Amita & Tiwari 2013; Udoakah & Okpura 2015)

$$\omega_s^\gamma = \cos^{-1}(-\tan(\phi - \gamma) \tan \delta) \quad (6)$$

where  $\gamma$  is the tilt angle.

Clearness index  $K_r$  is the ratio of the monthly mean horizontal daily radiation to the monthly mean horizontal daily total extraterrestrial solar irradiation

$$K_r = \frac{H_G}{H_{BH}} \quad (7)$$

$H_G$  is the monthly mean horizontal daily terrestrial solar radiation or the global solar radiation received at the area,  $H_G$  can be referenced from weather station data Nigerian College of Aviation Technology (NCAT) Zaria.

Diffused irradiation ( $H_{DH}$ ) is the monthly average daily value for the diffused irradiation incident on a horizontal surface, which is given by (Uba & Sarsah 2013)

$$H_{DH} = H_G (1.391 - 3.560 K_r + 4.189 K_r^2 - 2.137 K_r^3) \quad (8)$$

For  $\omega_s \leq 81.8^\circ$  and  $0.3 \leq \bar{K}_T \leq 0.8$

$$H_{DH} = H_G (1.311 - 3.022 K_r + 3.427 K_r^2 - 1.821 K_r^3) \quad (9)$$

For  $\omega_s \geq 81.4^\circ$  and  $0.3 \leq \bar{K}_T \leq 0.8$

The diffused radiation received on an inclined surface  $H_{DT}$  is given by

$$H_{DT} = \frac{1}{2} H_{DH} (1 + \cos \theta) \quad (10)$$

The daily beam radiation received on an inclined surface is the irradiation component incident on a horizontal surface on the average day for each month

$$H_B = H_G - H_{DH} \quad (11)$$

The beam received on a tilted collector ( $H_{BT}$ ) is given by (Amita & Tiwari 2013)

$$H_{BT} = H_B \frac{\cos(\theta - \phi) \cos \omega_o \sin \omega_s + \omega_o \sin(\theta - \phi) \sin \omega_s}{\cos \phi \cos \omega_s + \omega_s \sin \phi \sin \omega_s} \quad (12)$$

where

$$R_B = \frac{\cos(\theta - \phi) \cos \omega_o \sin \omega_s + \omega_o \sin(\theta - \phi) \sin \omega_s}{\cos \phi \cos \omega_s + \omega_s \sin \phi \sin \omega_s}$$

and

$$\omega_o = \min(\omega_s, \omega_s^s)$$

The ratio of average diffuse radiation incident on an inclined surface to that on a horizontal surface is given by the relation (Badescu 2002):  $R_D = (3 + \cos(2\theta))/4$

The total radiation on a tilted surface equation (1) can thus be expressed as

$$H_t = H_B R_B + H_{DH} R_D + 1/2 H_G (1 - \cos \theta) \quad (13)$$

where

$$H_{BT} = H_B R_B, H_{DT} = H_{DH} R_D \text{ and } H_R = 1/2 H_G (1 - \cos \theta)$$

A simple mathematical procedure for the estimation of the tilt optimal angle of collector is presented based on the monthly horizontal radiation.

Using equation (1) to (13), total solar radiation received on a tilted surface was calculated for tilt angle 0, 5, 10... 90 degrees for each month of the year. Using Mathcad graphic package graphs were plotted of the total solar radiation ( $H_t$ ) received on tilted surface versus tilt angle ( $\theta$ ) for each month.

Second order polynomial equations were developed to fit the curves. These polynomial equations were differentiated with respect to tilt angle and then equated to zero to obtain the optimum tilt angle ( $\theta_{opt}$ ) corresponding to maximum insolation

The equations (2) to (13) were manipulated into MSEXCEL to calculate the monthly average daily total radiation on a surface facing towards equator as the tilt angle changed from 0° to 90° in steps of 5°. The solar reflectivity ( $\rho$ ) was assumed to be 0.25

### Results and Discussion

The measured monthly mean of daily global solar radiation ( $H_G$ ), the clearness index ( $K_T$ ), and the extraterrestrial solar radiation ( $H_{BH}$ ), global diffuse ( $H_{DH}$ ) and beam radiations ( $H_{BT}$ ) declination ( $\delta$ ) and hour angle ( $\omega_s$ ) at various tilt angles computed from MSEXCEL using equations (1) to (12), the monthly averages over the ten year period (2006 to 2015) of data, processed in preparation for the estimation of the optimum tilt angle are presented in table (I)

Table i. Monthly averages over the ten year period

Months	$H_{BH}$	$H_G$	$H_{DH}$	$H_{BT}$		$\delta$	$K_T$
Jan	30.07	19.16	5.86	13.3	-20.83	84	0.63718
Feb	32.43	20.99	5.5	15.49	-13.28	77	0.64731
March	33.27	22.03	5.51	16.52	-2.55	75	0.66214
Apr	35.55	21.41	6.6	14.81	9.55	78	0.60219
May	34.73	20.08	6.43	13.65	18.84	78	0.57812
June	36.63	18.92	7.54	11.38	23.08	80	0.51649
July	34.97	17.1	6.87	10.23	21.07	78	0.48895
Aug	39.23	15.56	8.37	7.19	13.23	93	0.39662
Sep	36.86	18.68	7.89	10.79	1.91	90	0.50698
Oct	34.63	20.5	6.32	14.18	-9.93	88	0.59188
Nov	31.92	20.74	6.11	14.63	-19.11	86	0.64965
Dec	30.53	19.35	5.97	13.38	-23.10	83	0.63386

Fig. 2 depicted the global, diffuse and beam monthly average radiation on a horizontal surface. It can be seen that the beam

component is more dominant than the diffuse component all the year round thus the main contribution comes from the beam component.

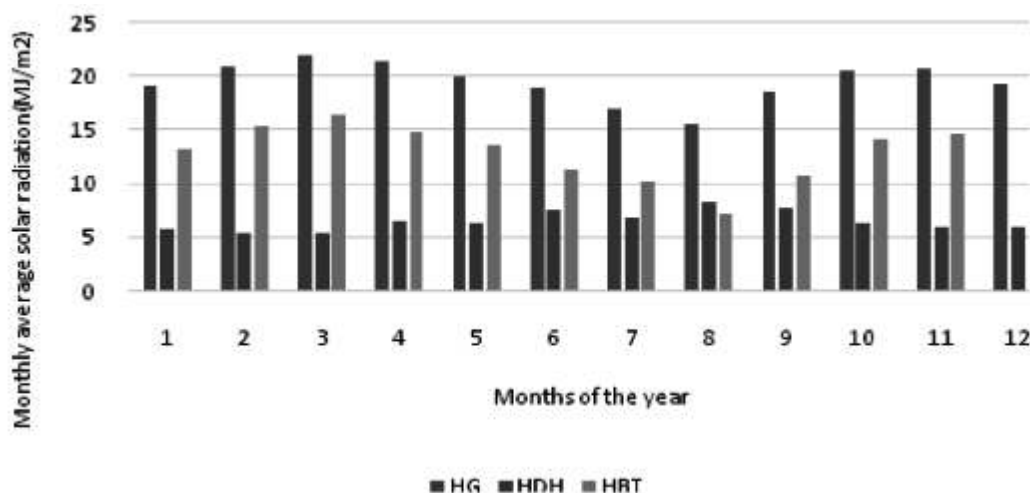
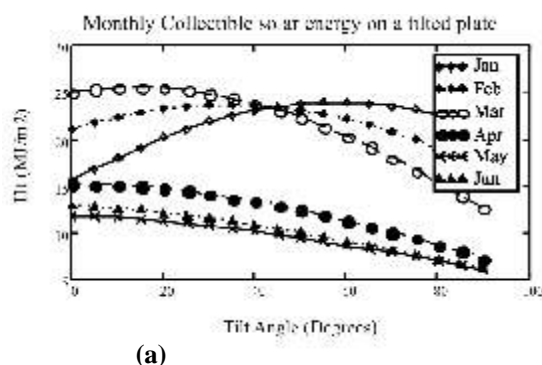
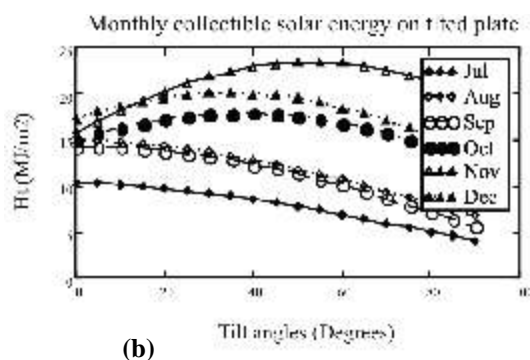


Fig.2 Monthly mean daily global solar radiation ( $H_G$ ), diffuse radiation ( $H_{DH}$ ) and beam radiation ( $H_{BT}$ ) on flat plate collector in Zaria.



(a)



(b)

Fig. 3 (a and b). Monthly average daily total solar radiation on south facing flat plate collector in Zaria for the months of January-June and July-December respectively for different tilt varying from  $0^\circ$  to  $90^\circ$ .



Fig 4. Optimum average tilt angle for each month of the year at Zaria

The graph in Fig. 4 is a plot of the optimal tilt angles of a flat-plate collector against months. In January the optimum tilt angle is  $55^\circ$ . The optimum tilt angle then decreased in February and March to  $25^\circ$  and  $10^\circ$  respectively. These values are so to be expected because during this period, the sun is imagined to be moving towards the latitude of Zaria from the southern hemisphere (i.e., having a decreasing declination). A positive sign indicates that the collector is directed towards the south. This also means that collectors used during this period must have an upward facing component to the direction of the sun. It is clearly seen



from the graph that between the months of April to September, the optimum solar radiation is obtained when the tilt angle is  $0^\circ$ . The values of the optimum tilt angles show an increasing trend from October to December. This is because the sun has just crossed the latitude of the observer and moving towards the south until it has reached its maximum declination in December ( $= -23.10^\circ$ ). This period correspond with the rainy season in Zaria. While between the months of October to march, correspond to the dry season period, the optimum solar radiation is achieved when the tilt angle is  $30^\circ$ ,  $50^\circ$ ,  $60^\circ$ ,  $55^\circ$ ,  $25^\circ$  and  $10^\circ$  respectively.

The mean value of the optimum tilt angle for three periods, January to March, April to September and November to December, were determined. It is required that the collector tilt angle be changed three times a year: January to March( $30^\circ$ ), April to September( $0^\circ$ ) and October to December( $47^\circ$ ). it can be deduced from this that the optimum tilt angle for the period January to March was latitude of the area plus  $20^\circ$ , April to September  $0^\circ$  horizontal position and October to December latitude of the area plus  $36^\circ$ .

The annually mean tilt was calculated by finding the mean value of the tilt angle for all the months of the year. This value was found to be  $19.17^\circ$  which is fixed tilt throughout the year required to give a maximum solar insolation.

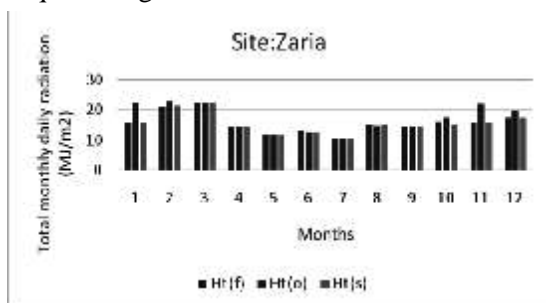


Fig. 5 Total monthly radiation for yearly fixed Ht (f), optimum Ht (o) and seasonally Ht (s) tilt angles

Fig. 5 shows the total monthly daily solar radiation collected for the optimum tilt Ht (o) angles, the seasonal average tilt angles Ht (s) and for the yearly average fixed tilt angles Ht (f). When the monthly optimum tilt angle was used, the yearly collected solar energy was  $206.7 \text{ MJ/m}^2$ . With the seasonally adjusted angle, the yearly collected solar energy was  $186.85 \text{ MJ/m}^2$ . With the yearly average tilt angle, the yearly collected solar energy was  $187.71 \text{ MJ/m}^2$ . Hence the loss of energy when using both the yearly average fixed angle and the seasonal average tilt angle is around 1%.

Every month has its unique optimum tilt angle for the solar collectors. The maximum collected solar energy will be when the optimum tilt is chosen for every month. The results show that the average optimum tilt angle at Zaria for the months of January, February, and March are  $60^\circ$ ,  $35^\circ$ ,  $15^\circ$  respectively and  $0^\circ$  for the months of April to September and  $40^\circ$ ,  $55^\circ$  and  $60^\circ$  for October to December.

For Zaria, the average annual maximum irradiation could be obtained at a tilt angle of about  $19.17^\circ$  which nearly corresponds to the latitude of the study area plus  $8^\circ$ . The gain of energy when using monthly tilted collector is about 9.2% increases as compared with the fixed angle collectors. In conclusion it is recommended to use the monthly tilt angles in many general applications in order to keep the manufacturing and installation of collectors low. For maximum collections of solar energy the collector should be designed such that the angle of tilt can easily be changed at least monthly. Alternatively automatic solar tracking system can be used for solar collectors in industries, satellite etc. where higher precision is needed.

## ACKNOWLEDGEMENTS

The author is grateful to the management of Nigerian College of Aviation Technology (NCAT) Zaria, Nigeria for providing the global solar radiation data for the period of 10 years from 2006 to 2015.

## REFERENCES

- Abhishek, A., Vineet, K. V. & Mishra, S.N. 2012. *Comparative Approach for the Optimization of Tilt angle to receive Maximum Radiation*. International journal of Engineering Research and Technology 5:1-9
- Ahmad, J. M. & Tiwari, G. N. 2009. *Optimization of Tilt Angle for Solar Collector to Receive Maximum Radiation*. The open Renewable Energy Journal 2:19-24.
- Amita, C. & Tiwari, C. 2013. *Optimization of Solar Power by varying Tilt Angle/Slope*. International Journal of Emerging Technology and Advanced Engineering 3:145-150
- Badescu, V.A. 2002. *A new kind of cloudy sky model to compute instantaneous values of diffuse and global irradiance*. Theor Appl Climatol 72: 127-136
- Benghanem, M. 2011. *Optimization of tilt angle for solar panel: case study for Madinah, Saudi Arabia*. [Online] Available from: <http://www.elsevier.com/locate/apenergy> [Accessed 19th January 2018, 13:32pm].
- Bekker, B. 2004. *Methods to extract maximum electrical energy from PV panels on the earth's surface*. University of Stellenbosch.
- Felix, A. U. & Emmanuel, A. S. 2013. *Optimization of tilt angle for solar collectors in Wa, Ghana*. Advanced Applied Science Research 4:108-114
- Ihya, B., Abdellah, M., Rachid, T. & Mohammed, N. B. 2014. *Optimal tilt angles for solar collectors facing south at Fez city (Morocco)*. Journal of Natural Sciences Research 10:120-127
- Nwofe, P. A. 2014. *Need for Energy Efficient Buildings in Nigeria*. International Journal of Energy and Environmental Research. 3:1-9
- Sambo, A. S. 1985. *Empirical Models for the correlation of Global Solar Radiation with Meteorological Data for Northern Nigeria*. Solar and wind Technology 3:219- 221
- Udoakah, Y. N. & Okpura, N. I. 2015. *Determination of optimal tilt angle for maximum solar insolation for PV systems in Enugu-southern Nigeria*. Nigerian journal of technology 34:835- 843

## A STUDY OF GEOTHERMAL ENERGY POTENTIAL OF THE NIGER (BIDA) BASIN AND ADJACENT REGIONS USING GRAVITY AND AEROMAGNETIC DATA.

**Grace A. Mamman<sup>1</sup>, Awajokan E. Ikpokonte<sup>2</sup>, Kola M. Lawal<sup>3</sup>, and L. A. Amed<sup>4</sup>.**

<sup>1</sup>Department of Physics Kaduna State College of Education Gidan Waya <sup>2</sup>Department of Geology Ahmadu Bello University, Zaria, <sup>3,4</sup> Department of Physics Ahmadu Bello University, Zaria.

Email: mamman.grace@yahoo.com, grace2ayuba1@gmail.com)1, awaikpo@yahoo.com

### ABSTRACT

*Gravity and aeromagnetic data covering parts of the Niger (Bida) Basin and its adjacent crystalline Basement Regions including the Confluence area were analyzed for its geothermal energy potential reserves. Results from previous gravity data interpretations show that the Upper Mantle (Moho) is uplifted (Crustal thinning) about 23 km beneath the Niger Basin and the Confluence Area. Geothermal uplift is therefore considered to be generally associated with the crustal thinning and follows with basic intrusives to shallower levels beneath the Basin. The residual gravity result gave maximum sediment thickness (density  $2.54 \text{ kg/m}^3$ ) of about 2 km and a shallow basic body (density  $2.850 \text{ kg/m}^3$ , width 50 km, varied depth extent about 2.22-4.22 km) is probably beneath the Abaji area. While of aeromagnetic data interpretations show that Curie Points Depth (CPD) varies from 12 km to 18 km along the axis of the Basin (where also the en-echelon axial positive gravity anomaly occurs). The magnetic depth to top of thermal anomalous bodies also varies from 0.47 km to 2.2 km while depth to bottom (CPD) varies from 10 km to 12 km beneath the Basin and the adjacent crystalline basement regions. The CPD depths and depths to top of the thermal sources are considered to indicate occurrences of shallow intrabasement with some intrasediment basic intrusive bodies beneath and around the Basin. However, such bodies occurrences at shallower depths are observed to dominate the adjacent crystalline basement regions with higher thermal gradient than observed beneath the basin indicating heat flow towards the marginal sediments of the basin. The Bida (Niger Rift) basin and adjacent region having accessible depths to thermal sources is therefore prospective for detail geothermal (alternative) energy reserve considerable for future generation of electricity to add to the National Grid.*

**Key words:** Gravity, Aeromagnetic, Bida (Niger) Basin, Curie Point Depth (CPD), Geothermal.

### Introduction

Geothermal energy is a clean and sustainable energy source, and is the contained intense heat that continually flows outward from deep within Earth (Nemzer et al., 2009, Megwara et al., 2013 and Sunday, 2015). They added that it is often used nowadays as that part of the earth heat that can, or could, be recovered and exploited by man. It utilizes the earth natural heat by sourcing superheated water found in the earth crust (Abraham, 2014). As the superheated water, moves out to the environment (discharge area), it gets in contact with the surrounding air, and vaporizes (Nemzer et al., 2009). The vapor is then utilized in turning the turbines for the generation of electricity.

### Geothermal Mapping

Geothermal energy sources are easily discovered through a process called geothermal mapping. Saada, (2016), views geothermal mapping as a method of determining the spatial variation in temperature known as the thermal structure of the earth. Akbar & Fathianpour (2016) reported that, the Curie Point Depth (CPD) is of great importance in characterizing (mapping) geothermal resources. Therefore, determination of CPD based on spectrum analysis of magnetic anomaly data can be used to estimate the regional thermal structure of the earth. If the temperature gradient is sufficient enough to provide the required heat

for the development of a geothermal plant, its nature will determine the geothermal plant to build. Tanaka et al. (1999), in a spectral analysis of residual magnetic anomalies determined the bottom of the magnetized crust, to be generally interpreted as the level of the Curie point isotherm. Megwara et al. (2013) also carried out a study of geothermal and radioactive heat across the southern parts of the Bida basin overlapping with this work, using aeromagnetic and radiometric data. Their results show a variation of depths-to-top range, 0.038 to 3.7 km and depths-to-bottom range, 10-15.1 km, with heat flow range, 69.167 to 124.821 mWm<sup>-2</sup>, for shallow magnetic sources. Geothermal research and exploitation works are also carried out in Kenya East Africa Rift system (Tole, 1996).

In this work, a framework for exploration of geothermal resources in parts of the Niger (Bida) Basin and its adjacent crystalline Basement regions including the Confluence area is developed. This is done by mapping out Curie points depths (CPD), geothermal gradient and heat flow from subsurface structures that are magnetic in nature, with the use of aeromagnetic data backed up with deep crustal interpretation of gravity data. Oasis Montaj Soft-wares is applied to analyzing the magnetic data. To meet up with the ongoing 10 National Integrated Power projects (NIPPS) of the Federal Government, according to Sunday, (2015), are thermal plants with some capable of being upgraded to combine circle using steam and thermal chambers to generate significant Mega Watts (MW) of electric Power. Mapping of geothermal reservoirs will be of value to such projects. This study is therefore aimed at mapping out thermal structures within the Bida (Niger) Basin suitable for harnessing geothermal energy that could be exploited to serve as an alternative but sustainable source of energy.

### **Geology of the Area of Study**

The study area, Niger (Bida) Basin and its adjacent crystalline Basement regions

including the Confluence area, occupies 16 standards 1:100,000 Total Intensity Magnetic (TMI) Map sheets and lies within Latitudes 7.5°N to 9.5°N and Longitudes 5.0°E to 7.0°E, as shown in Figure 1.

The Niger Basin otherwise known as the Bida or Nupe Basin is a northwestern-southeast trending intracratonic depression filled with Campano-Maastrichtian sediments extending from Kontagora in the NW to areas slightly beyond Lokoja in the SE. It is underlain by crystalline rocks of the Precambrian to Palaeozoic Basement Complex comprising gneisses, migmatites and rocks of Upper Proterozoic to Cambrian Metasediments. The sediments comprise mainly sandstones, siltstones, and ferruginous sandstones and clays. It merges with Anambra and Sokoto basins in the SE and NW respectively, with few thin unfolded marine types of sediment (Adeleye, 1974). The genesis of the basin sediments may be closely connected with the Santonian orogenic movements of southeastern, Nigeria and the Benue valley, even as it represents in origin, a NW–SE trending embayment, perpendicular to the main axis of the Benue Trough and the Niger Delta Basin.

Ajakaiye (1981) suggested that within the Benue trough are several widely distributed ridge areas which are probably areas of uplifted basement or basic intrusions at depths of 2 km or less; and that the crust beneath the trough is thinner by at least 8 km than beneath the flanking crystalline basement rocks. From their interpretation of the regional anomalies they report an uplift of the mantle which range between 2 km and 5 km, and a corresponding thinning of the crust in the Benue trough.

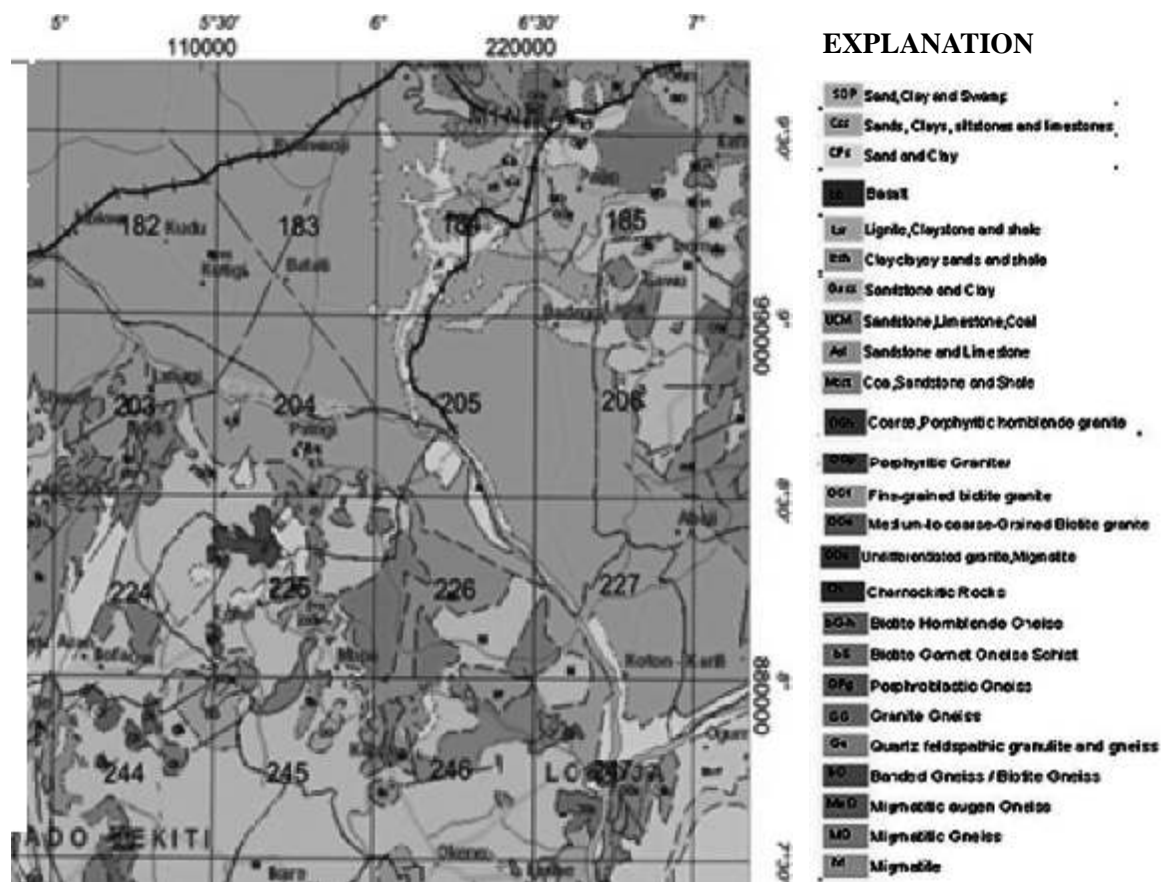


**Figure 1 Geological Map of the Study Area**

Interpretations of Land sat imageries, borehole logs, as well as geophysical data across the entire Mid-Niger Basin suggest that the basin is bounded by a system of linear faults trending northwest-southeast (Kogbe et al., 1983). Gravity studies also confirm central positive anomalies flanked by negative anomalies for the adjacent Benue Trough and typical of rift structures (Ojo, 1984; Ojo and Ajakaiye, 1989 and Ikpokonte, 2009).

Abraham et al., (2014), applied spectra analysis on aeromagnetic data of an area over the Ikogosi warm spring and their results reveal that, the average Curie point depth for the Ikogosi warm spring area is  $15.1 \pm 0.6$  km and centres on the host quartzite rock unit. The computed equivalent depth extent of heat production provides a depth value (14.5 km) which falls within the Curie point depth

margin and could indicate change in mineralogy. Kasidi and Nur, (2014), estimated the CPD, Heat Flow and Geothermal gradient with the use of aeromagnetic Data over Jalingo, North-Eastern Nigeria from, their results of CPD obtained varies between 24 and 28 km, geothermal gradient varies between 21 and  $23^{\circ}\text{C km}^{-1}$ , while the heat flow varies between 53 and  $61 \text{ mWm}^{-2}$ . Bilim et al., (2016) in their study asserts that CPDs have an inverse relationship with the heat-flow so much that regions indicating high heat-flow are associated with shallow CPDs, whereas regions of lower heat-flow are associated with deeper CPDs.

In Curie Point Isotherm studies, it is assumed that the curie temperature of pure magnetite is  $580^{\circ}\text{C}$ . But the general Curie point temperature varies with pressure and mineralogy, at a Curie

point temperature range of 500-600°C (Sa'ada, 2016). Many researchers that worked on the subject matter used 580 °C as a reasonable temperature for the continental crust (Okubo et al., 1985; Tanaka et al., 1999; Abraham et al., 2014; Obande et al., 2014; Sa'ada et al., 2016 and Bilim et al., 2016).

## Materials and Methods

### Aeromagnetic Data

The total intensity aeromagnetic (TMI) data compiled by the Nigeria Geological Survey Agency (NGSA) is obtainable Figure 1. The study area is covered by a high resolution aeromagnetic survey, conducted and published by NGSA of Nigeria from 2005-2010 at a line spacing of 500m and an average terrain clearance of 80m, on the map scale of 1:100,000 series. A total of sixteen (16) sheets were purchased from the NGSA which include sheets 182 - 185, 203 - 206, 224 - 227, 244 - 247, covering the entire study area. High resolution aeromagnetic data are useful for the geologic and geothermal mapping at a variety of scales and enable the estimation of CPD, heat flow and thermal gradient. Other materials include; Oasis Montaj 2010 version, Excel, Suffer 11 and Grapher 8.

### Gravity Methods

The basic theory of gravity survey methods according to Kearey and Brooks (2002) is Newton's law of gravitation, which states that the force of attraction  $F$  between masses  $m_1$  and  $m_2$  whose dimensions are small with respect to the distance between them, is given by

$$F = \frac{m_1 m_2}{r^2} \quad (1)$$

During a gravity survey the gravimeter is read at a base station at a frequency dependent on the drift characteristics of the instrument. At each station, point (P) location, time, elevation distance and gravimeter reading are recorded. The gravity effect of a causative body measured from any point distance  $r$ , away from the Centre of the causative body is given by,

$$gr = \frac{Gm_2}{r^2} = \frac{GV\Delta\rho}{r^2} \quad (2)$$

Where  $\Delta\rho$  is the density contrast of the body with the host rock, and  $V$ , the volume.

The variation of the body geometry and density in the subsurface now depicts the rock types effect on the measurements, thus causing a gravity anomaly. The anomaly of the whole body  $\Delta g$  is then found by summing all such elements which make up the body.

$$\Delta g = \sum \sum \sum G\rho \frac{(z'-z)}{r^2} \partial x' \partial y' \partial z' \quad (3)$$

$\int x', \int y'$  and  $\int z'$  are allowed to approach zero then

$$\Delta g = \iiint \rho \frac{(z'-z)}{r^2} \partial x' \partial y' \partial z' \quad (4)$$

where  $r = \sqrt{(x'-x)^2 + (y'-y)^2 + (z'-z)^2}$

## Methods

### Determination of Curie Point Depth

Tanaka et al., (1999) and Saada, (2016) explained, two different methods that can be used to estimate the depth extent of magnetic sources: The first method focuses on the shape of isolated magnetic anomalies by (Bhattacharyya and Leu, 1975), while the second comprises examining the statistical properties of patterns of magnetic anomalies (Spector and Grant, 1970). Both methods give a relationship between the spectrum of magnetic anomalies and the depth of a magnetic source by transforming the spatial data into the frequency domain. Thus, Spector and Grant (1970) described the basic 2-D spectral analysis method, where they estimated the depth to the top of magnetized rectangular prisms ( $Z_t$ ) from the slope of the log power spectrum. Akbar and Fathianpour, (2016), in their work, optimized the spectral block dimension at the Sabalan geothermal field and its surrounding areas of Iran. They used grid of 37 blocks with different dimensions from  $10 \times 10$  to  $50 \times 50 \text{ km}^2$ , which showed at least 50% overlap with adjacent blocks. Their estimated CPD was in the range of 5 to 21 km. The promising areas had Curie point depths of less than 8.5 km located around

Mountain Sabalan, which encompassing more than 90% of known geothermal resources.

Bhattacharyya and Leu (1975) further calculated the depth of the centroid of the magnetic source bodies ( $Z_0$ ). Okubo et al., (1985) developed the method to estimate the bottom depth of the magnetic bodies ( $Z_b$ ) using the spectral analysis method of Spector & Grant (1970).

To estimate the Curie point (basal) depth  $Z_b$  of

the magnetic source, Tanaka et al., (1999) assumed that the layer of the magnetic source extends infinitely in all horizontal direction. The depth to a magnetic source's horizontal scale, and the magnetization  $M(x,y)$  is a random function of  $x$  and  $y$  (Sa'ada, 2016; Kasidi and Nur, 2014; Tanaka et al., 1999; Bhattacharyya & Lue, 1975; Okubo et al, 1985). Blakely (1995) introduced the

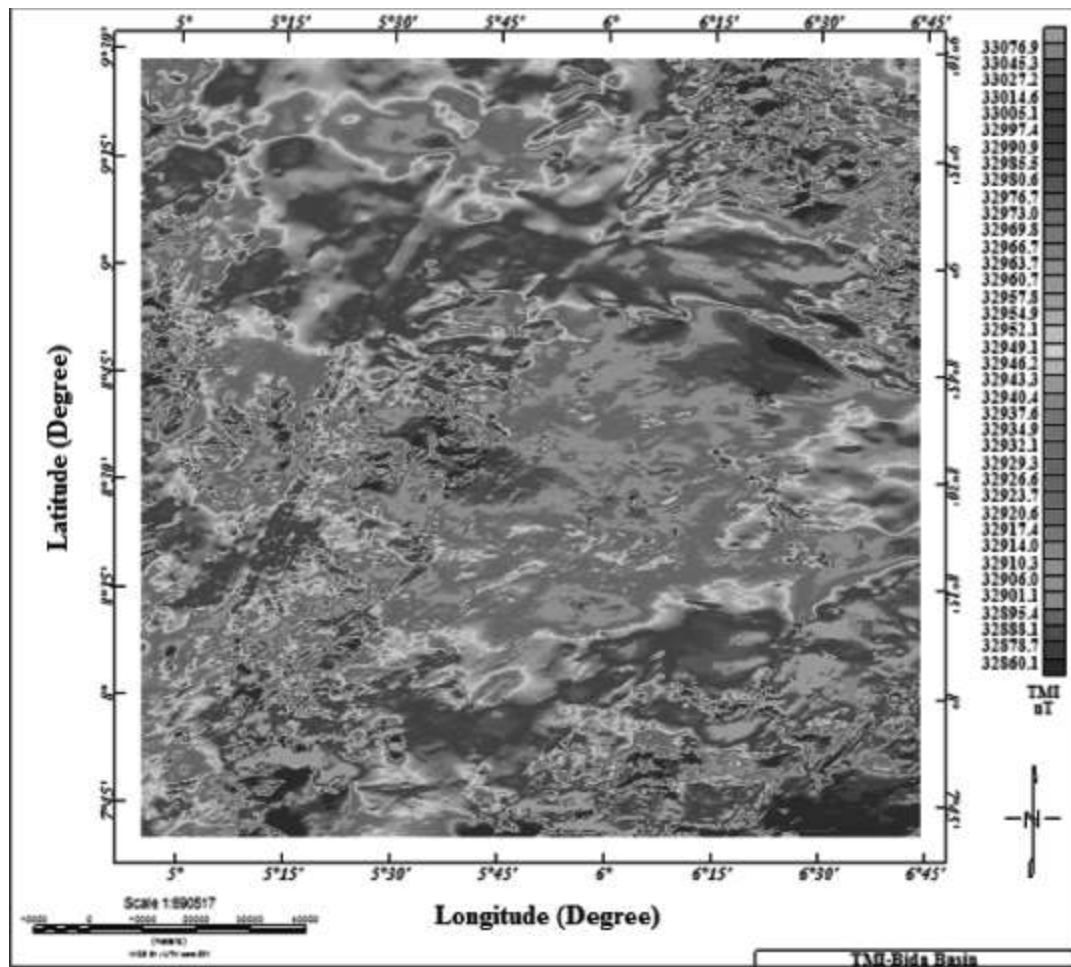


Fig. 2: Total Field Magnetic Intensity (TMI) Map of the Niger (Bida) Basin Study Area.

power density spectra of the total field anomaly data  $P(k)$  as,

$$P(x,y) = P(k_x, k_y) \times F(k_x, k_y) \quad (1)$$

$$= 4\pi^2 C_m^2 |Q_n|^2 |Q_f|^2 e^{-2|k|Z_r} [1 - e^{-|k|(Z_b - Z_t)}]^2$$

Where  $P$ , is the power density spectrum of the magnetization,  $C_m$  is proportionality constant,  $Q_n$  and  $Q_f$  are factors for magnetization and Geomagnetic field direction respectively. While  $Z_b$  and  $Z_t$  are depths to bottom and top of the magnetic source respectively. The equation

can be simplified by noting that all terms except  $|Q_n|^2$  and  $|Q_f|^2$  are radially symmetric. Furthermore, the radial averages of  $Q_n$  and  $Q_f$  are constants. If  $P(x,y)$  is completely random and uncorrelated,  $P(kx,ky)$  is a constant. Hence, the radial average of  $P$  is:

$$P(|k|) = Ae^{-2|k|Z_t} [1 - e^{-|k|(Z_o - Z_t)}]^2 \quad (2)$$

Where  $A$  is a constant and  $k$  is the wave number. Equation (2) can be written as

$$\ln P(|k|)^{\frac{1}{2}} = \ln B - |k|Z_t \quad (3)$$

Where  $B$  is a constant, the upper bound of magnetic source  $Z_t$  could be estimated by fitting a straight line through the high wave number part of the radially power spectrum average power spectrum  $[\ln P(|k|)^{\frac{1}{2}}]$

$$\ln P(|k|)^{\frac{1}{2}} = Ce^{-|k|Z_o} (e^{-|k|Z_t - Z_o} - e^{-|k|Z_b - Z_o}) \quad (4)$$

Where  $C$  is a constant, a long wavelength, equation (4) can be rewritten as

$$P(|k|)^{\frac{1}{2}} = Ce^{-|k|Z_o} (e^{-|k|(Z_t - Z_o)} - e^{-|k|(Z_b - Z_o)}) \quad (5)$$

Where  $2S$  is the thickness of the magnetic source. From equation (5), it can be concluded that

$$\ln \left\{ \frac{P(|k|)^{\frac{1}{2}}}{|k|} \right\} = \ln D - |k|Z_o \quad (6)$$

Then the Basal Depth  $Z_b$  of the magnetic source will be calculated from the equation

$$Z_b = 2Z_o - Z_t \quad (7)$$

Then,  $Z_o$  is the centroid of the magnetic source.  $Z_t$  is the depth to the top of the magnetic source. While  $Z_b$  is the basal depth of the magnetic sources assumed to be the Curie point depth (Bhattacharyya and Lue, 1975; Okubo et al, 1985; Kasidi and Nur, 2014; Sa'ada, 2016). At the basal depth  $Z_b$  Ferromagnetic minerals are converted to paramagnetic minerals due to a temperature of approximately 580°C (=853 K, SI unit) at that depth (Encarta Dictionaries, 2009).

#### Estimating Heat Flow and Thermal gradient

The basic relation for conductive heat transport is Fourier's law. Tanaka et al., (1999),

Abraham et al., (2014), Sa'ada, (2016) showed that any given depth to a thermal isotherm is inversely proportional to the heat flow. In a one-dimensional case under assumptions that the direction of the temperature variation is vertical and the temperature gradient  $\frac{dT}{dz}$  is constant, Fourier's law takes the form

$$q = k \frac{dT}{dz} \quad (8)$$

$q$  is the heat flux measured in units of energy per unit area per unit time, the SI unit being  $W/m^2$ .  $k$  is the coefficient of thermal conductivity which is a measure of how easily heat flows through a material, the SI unit for  $k$  is  $W/m^\circ C$ .

$\frac{dT}{dz}$  is the temperature gradient (the rate of increase of temperature with depth), in order to relate the CPD ( $Z_b$ ) to Curie point temperature, Blim et al., (2016) assumed that the Curie temperature of pure Magnetite 580°C and that Curie point temperature, varies with pressure and mineralogy of rocks. The general accepted value for Curie point temperature in literatures ranges between 500°C - 600°C (Okubo et al., 1985; Tanaka et al., 1999; Bilim et al., 2016; Sa'ada et al 2016) generalized 580°C as a reasonable value for the Curie point temperature. Therefore, the thermal gradient is being calculated as follows

$$\frac{dT}{dz} = \frac{q}{Z_b} = \frac{580^\circ C}{Z_b} \quad (9)$$

The heat flow values are calculated as follows

$$q = k \left( \frac{dT}{dz} \right) = k \frac{580^\circ C}{Z_b} \quad (10)$$

Where  $q$  is the heat flow and  $k$  is the coefficient of thermal conductivity, taken as varies from 2.45 - 2.89  $Wm^{-1}K^{-1}$  with average value, 2.5  $Wm^{-1}K^{-1}$  for basement rocks; and for sedimentary rocks, 1.71 - 2.50  $Wm^{-1}K^{-1}$  with an average value, 1.8  $Wm^{-1}K^{-1}$ .

## RESULTS

### Estimation of CPD

The spectral plots for the sixteen blocks covering Longitudes 5°E to 7° E and Latitudes 7.5°N to 9.5° N was obtained using Oasis Montaj Software (2010). The depth to centroid ( $Z_o$ ) and depth to top ( $Z_t$ ) were estimated from



the plots of  $\ln[(\text{Power})^{1/2} / \text{Wavenumber}]$  against Wavenumber and  $\ln[(\text{Power})^{1/2}]$  against Wavenumber respectively as shown in Figure 3 below. Only four out of the sixteen plots are shown, the remaining plots are in appendix A. The basal depth/CPD was then calculated for each block. These values were used to draw the CPD Map displayed in Figure 4.

#### Estimation of Geothermal Gradient

The geothermal gradient was calculated based on the assumption that rocks are dominated by magnetite which has the Curie point temperature of  $580^\circ\text{C}$ , using equation (9). The computed values were used to draw the Geothermal Gradient Map shown in Figure 5.

#### Estimation of Heat Flow

The heat flow was calculated using the geothermal values with the aid of equation (10) and values used to plot the map shown in Figure 6.

#### Results

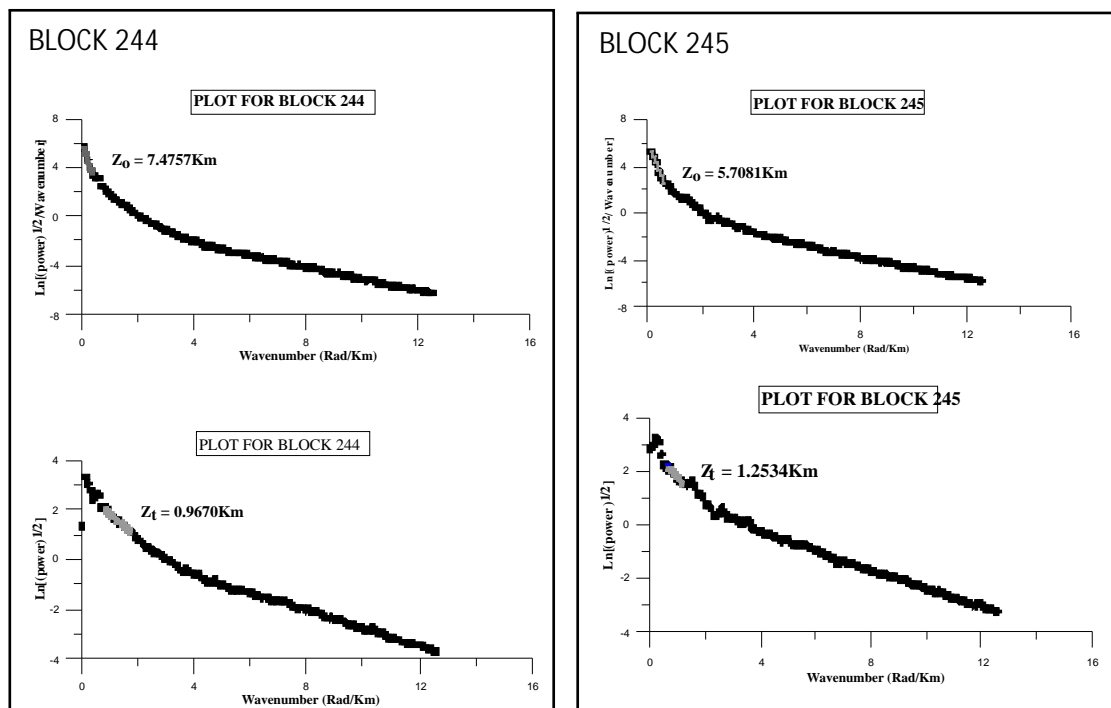
The Curie point depths are estimated using spectral analysis of magnetic anomaly data of the study area, and then compared with the

geology of the area. The Curie point depth estimates the average depth to the bottom of magnetic sources for each block thereby reflect thermal structures of the blocks. This is so since magnetization decreases with increase in temperature. The Curie point depths were used for estimating the geothermal gradient and heat flow. Maps obtained for CPD, geothermal gradient and heat flow were found to be consistent with the observed geological map of the study area. High heat flow values are observed at blocks with low CPD and vice versa and are found on the basement boundaries of the Niger Trough.

#### Curie point Depth

In this research, maximum CPD for deepest source was found to be 17.98 km on block-sheet 18 of 100% sedimentary cover, the minimum CPD is 9.39 km on block-sheet 225 of 100% basement and the mean CPD for the entire study area of 12.82 km.

The heat flow  $q$ , was calculated using the geothermal gradient values with the aid of equation (10). The heat flow values were used to draw the heat flow map shown in Figure 5.



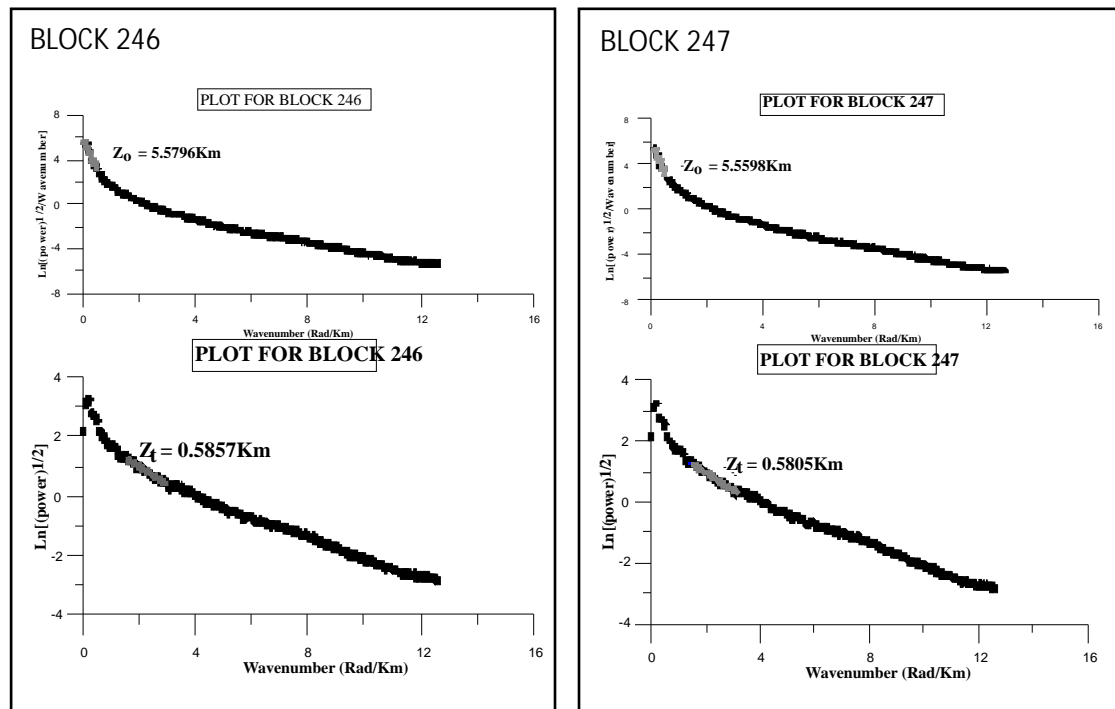


Figure 3: Spectral plots results for the Study Area

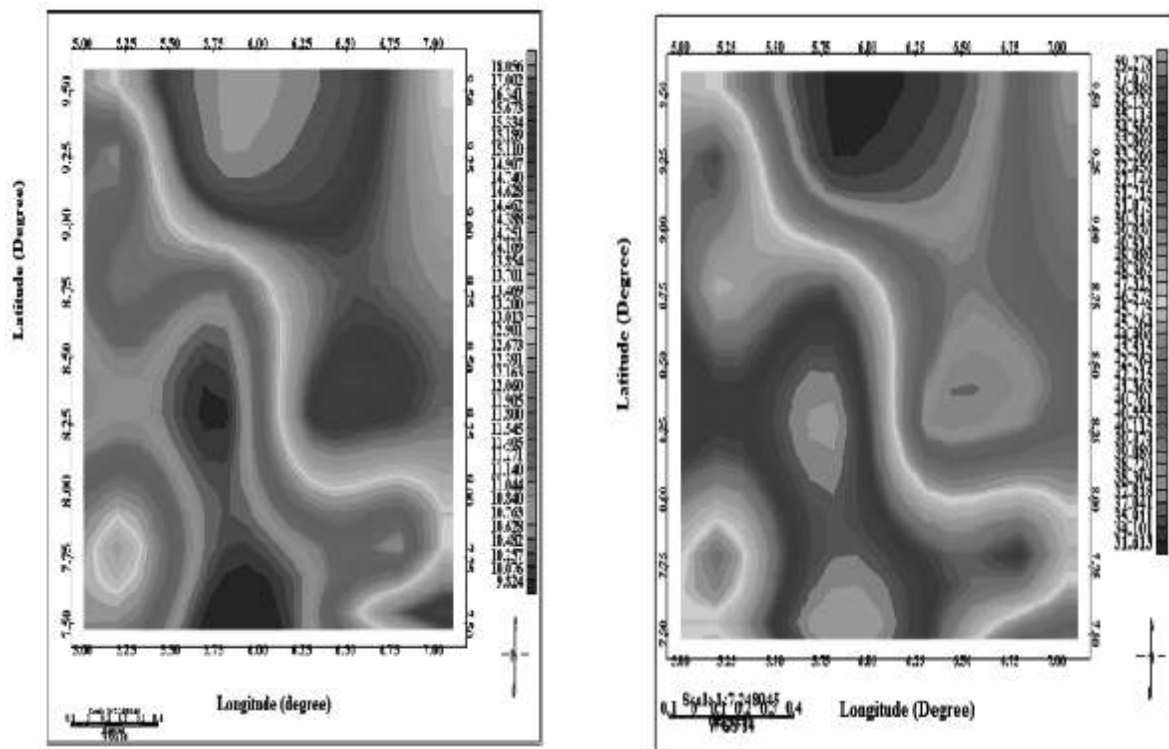


Figure 4 Curie Point Depth Map of the study area Figure 5 Geothermal gradient Map of the study area

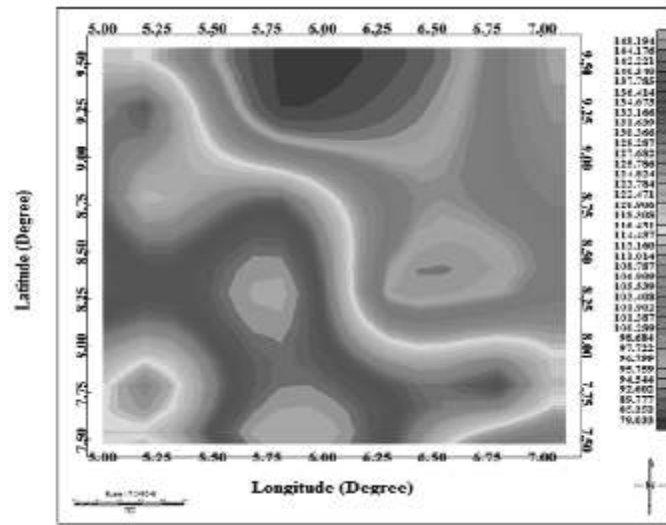


Figure 6. Heat flow Map of the study area

Table 1: Geothermal Data of the 16 Spectral blocks (Topo Sheets) covering the Bida (Niger) Basin Area.

S/N	BLOCKS (Topo Sheets)	$Z_b$ (CPD) (km)	Geothermal gradient ( $^{\circ}\text{Ckm}^{-1}$ )	Residual Geothermal gradient ( $^{\circ}\text{Ckm}^{-1}$ )	$Z_r$ (km)	Heat Flow ( $\text{mWm}^{-2}$ )
1	182(S) MOKWA	10.85	50.97	20.97	1.89	133.64
2	183(S) EGBAKU	17.98	30.76	0.76	2.10	80.64
3	184(S) BIDA	16.54	33.43	3.43	0.72	87.66
4	185(B) PAIKO	12.92	42.80	12.8	0.47	112.22
5	203(S) LAFIAGI	12.41	44.56	14.56	1.38	116.85
6	204(S) PATEGI	10.60	52.17	22.17	0.56	136.81
7	205(S) BARO	13.95	39.64	9.64	1.89	103.96
8	206(S) GULU	14.44	38.30	8.3	2.20	100.03
9	224(B) OSI	10.79	51.25	21.25	1.26	134.44
10	225(B) ISANLU	9.39	58.89	28.89	1.03	154.41
11	226(B) AIYEGUNLE	15.03	36.79	6.79	1.26	96.50
12	227(S) KOTON -KARFI	15.02	36.82	6.82	1.27	96.56
13	244(B) ADO- EKITI	13.98	39.56	9.56	0.97	103.69
14	245(B) IKOLE	10.16	54.43	24.43	1.25	142.68
15	246(B) KABA	10.57	52.32	22.32	0.59	137.14
16	247(S) LOKOJA	10.54	52.47	22.47	0.58	137.58

Note: Geothermal gradient  $^{\circ}\text{Ckm}^{-1}$  is calculated by subtracting average surface-screen temperature of  $27^{\circ}\text{C}$  in the Area for purpose of exploration- depth-rating. An assumed regional background geothermal gradient value of  $30^{\circ}\text{C/km}$  is subtracted from the calculated gradient to obtain the Residual gradient.

## Discussion

Nine blocks out of the sixteen blocks represent the sedimentary basin lying between its basement margins in the study area, with a minimum, maximum and mean CPD of 10.54 km, 17.98 km, and 13.59 km respectively. The basement complex in northern and southern margin parts of the study area consists of seven blocks. The minimum, maximum and mean CPD on the basement are 9.39 km, 14.44 km and 11.75 km respectively, all shallower depths compared to the sediment blocks of the basin.

## Geothermal Gradient

The higher geothermal gradient areas correspond to low CPDs. The minimum is  $32.26^{\circ}\text{Ckm}^{-1}$  and maximum is  $61.76^{\circ}\text{Ckm}^{-1}$ , while the mean value is  $46.88^{\circ}\text{Ckm}^{-1}$  for the study area. This is an indication that the thermal structure is greatest for basement blocks. For the sedimentary basin blocks, the minimum, maximum and mean values are,  $30.76^{\circ}\text{Ckm}^{-1}$ ,  $52.47^{\circ}\text{Ckm}^{-1}$  and  $42.12^{\circ}\text{Ckm}^{-1}$  respectively. While for the basement complex blocks, the minimum, maximum and mean values are,  $40.17^{\circ}\text{Ckm}^{-1}$ ,  $61.76^{\circ}\text{Ckm}^{-1}$  and  $50.58^{\circ}\text{Ckm}^{-1}$ .

Minimum, maximum and mean values for Sedimentary residual geothermal gradient are;  $0.76^{\circ}\text{Ckm}^{-1}$ ,  $22.47^{\circ}\text{Ckm}^{-1}$  and  $12.12^{\circ}\text{Ckm}^{-1}$  respectively. While the minimum, maximum and mean values for Basement residual geothermal gradient are;  $6.79^{\circ}\text{Ckm}^{-1}$ ,  $28.89^{\circ}\text{Ckm}^{-1}$  and  $18.01^{\circ}\text{Ckm}^{-1}$  respectively.

## Heat Flow

Very high heat flow values correspond also with lower CPDs. Minimum, maximum and mean value of heat flow are;  $80.64\text{mWm}^{-2}$ ,  $154\text{mWm}^{-2}$  and  $117.20\text{mWm}^{-2}$  respectively for the study area. For the sedimentary basin, the minimum, maximum and mean values are,  $80.64\text{mWm}^{-2}$ ,  $137.58\text{mWm}^{-2}$  and  $110.46\text{mWm}^{-2}$  respectively. While for the basement complex, the minimum, maximum and mean values are,  $100.43\text{mWm}^{-2}$ ,  $154.40\text{mWm}^{-2}$  and  $126.49\text{mWm}^{-2}$  respectively.

## Origin of the Thermal Uplift and the Gravity Data interpretation

The interpreted magnetic thermal anomalous body sources of this work as obvious from the CDP (bottom depth) ranging from 9.39 to 17.98 km and depth- to- top, 0.47 to 2.1 km (Table 1) indicate shallow crustal basic to ultrabasic sub-basement intrusive sources. The magnetic CDPs of this work are far greater in values than the depths (4-6 km) to sources of a major E-W prominent magnetic anomaly along Longitude  $9^{\circ}$  interpreted by Ojo (1990) in the Basin around Bida in the study area. Ojo (1990) also suggested that the anomaly is probably caused by sub-basement intrusive of high magnetic susceptibility, 0.0478 SI unit and so attribute their origin to basic intrusive, and not from variation of susceptibilities within the basement; but originated as a result of diapiric igneous intrusion through deep fissures associated with materials uplifted from rift origin. Although, the above magnetic depth- to- top of thermally anomalous sub-basement intrusives of this work corresponds well to thickness variations of sediments as interpreted in gravity profile (Ojo and Ajakaiye, 1976; Ikpokonte and Ajayi, 2007), it also indicates top of thermally high surface of bodies of high magnetic susceptibility. This work further considers the broad occurrence of the anomalous body beneath the basin in supports of an origin from deep rift related sources from the gravity interpretation.

Gravity interpretations (Ikpokonte, 1997; Ikpokonte and Ajayi, 2007) of the rift related shallow and deep lithospheric structures in the Lower Niger-Benue is here applied to further throw more light to the origin of the geothermal resources indicated. Figure 6 shows an interpreted gravity profile (AB) of long wavelength residual anomaly across the Lower Niger Basin from a low negative gravity area in the Basement SW of Kaba, through Abaji area (high gravity in the Basin) towards Kwoi area in the NE basement of low negative gravity. The interpretation shows that the Upper Mantle is uplifted to about 23 km

beneath the basin resulting to Crustal thinning in the Lower Niger Basin near the Confluence area. This results to an 11 km short of a normal 34 km crustal thickness under the Continent to the NE and about 30 km thick in the SW towards the continental margin of the Gulf of Guinea. Removal of the interpreted Moho component resulted to obtaining the interpreted component due to shallow crustal structures shown in Fig.7. This interpretation (Fig.7) is one of the several profiles adopted (Ikpokonte, 1997) for explaining the positive high residual and Bouguer anomalies characterizing the axis of the Niger Trough, and the high gradient negative gravity flanking the margins of the trough. Interpretation of the residual anomaly of the AB line figure 8 shows the maximum sediment thickness (density  $2.54 \text{ kg/m}^3$ ) of about 2 km and a shallow basic body (density  $2.850 \text{ kg/m}^3$ , width 50 km, varied depth extent about 2.22-

4.22 km) is probably beneath the Abaji area. Considering the body-width, and its length central along the axis of the basin, it could describe a sheet-like structure of intrabasement mantle-derived origin that could have fissured through an initial NW-SE fault system and emplaced, lost heat to contract, and downwarped. The initial NW-SE megafault system is viewed as a conjugate to the NE-SW Benue megafault system commonly represented in small details on the Pan-African Basement (Ikpokonte, 1997). It is further considered that the geothermal heat content of the uplifted basic Upper Mantle derived materials could have been lost to the shallow granitic crust flanking the basinal margins and transmitted much more than in the water saturated sediments, being flushed by running river in the basin. This is in agreement with the above magnetic thermal results in the basin and its immediate environs (Table 1).

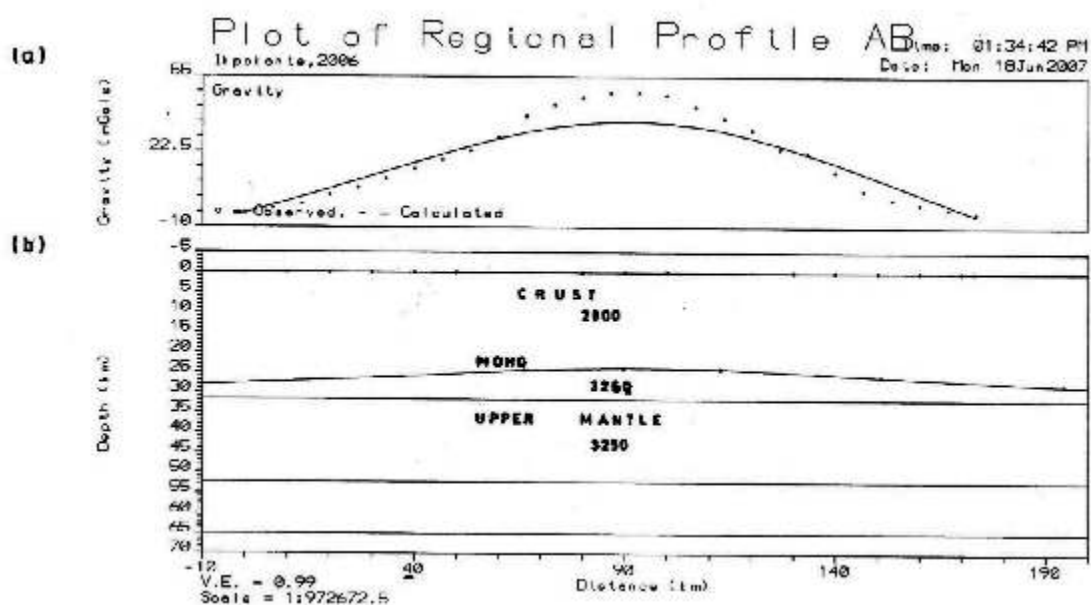


Fig. 7: Two-dimensional model of gravity profile AB-line across the Lower Niger (Bida) Basin a) shows the associated long wavelength anomaly resolution b) shows an interpreted deep lithospheric structure, the Moho. Density units in  $\text{Kg.m}^3$  (after Ikpokonte and Ajaji, 2007). See Fig 8.

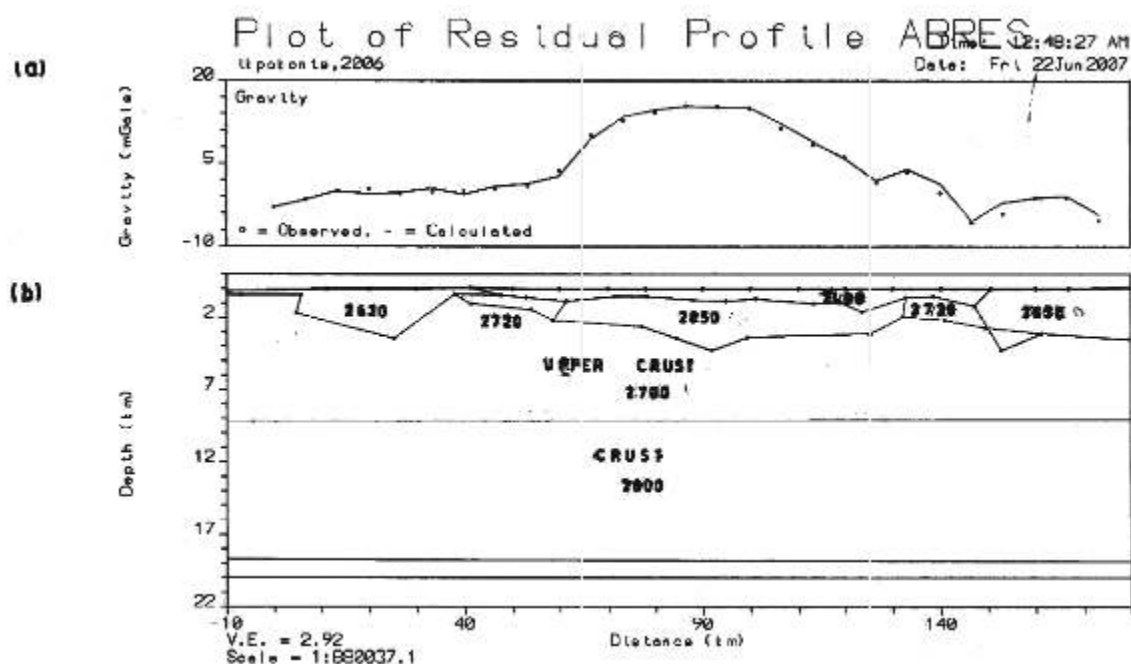


Fig. 8: Two-dimensional model of the residual gravity anomaly along profile AB-line across the Lower Niger (Bida) Basin. a) Shows the plot of the observed and calculated anomaly b) shows an interpreted shallow crustal structure along the profile. Density units in Kg.m<sup>3</sup> (after Ikpokonte and Ajaji, 2007). See Fig. 7.

### Conclusion

In this study, the aim is to estimate the Curie Point Depth (CPD), geothermal gradient and the heat flow values in the Niger (Bida) Basin using Total field magnetic anomaly intensity data (TMI), by applying Spectral analysis method. All results and maps produced correlate with each other. The minimum CPD was found to be 9.34 km at block 225 within the basement complex and the maximum 17.98 km at block 183 within the sedimentary basin. Because the range of CPD values (9.34-17.98 km) falls below the bottom of gravitating body (depth-extent, 2.2-4.22 km) of basic or ultrabasic probably mantle derived material and most probably not far from the Moho surface depth (23-25 km) beneath the basin, it is possible to suggest that the magnetic sources in the study area located at the upper crust are the causative geothermal reservoirs. The deduced geothermal gradient values range from  $30.76^{\circ}\text{Ckm}^{-1}$  to  $58.89^{\circ}\text{Ckm}^{-1}$ , and its residual gradient from 0.76 to  $28.89^{\circ}\text{Ckm}^{-1}$ . The heat flow values vary from  $80.64\text{mWm}^{-2}$  to

$136.81\text{mWm}^{-2}$  in the sediments and from  $87.66\text{mWm}^{-2}$  to  $158.91\text{mWm}^{-2}$  in the Basement flanks of the Basin. Thermal exploration depth to target bodies can be sorted from these results. The probable origin of the thermal bodies of this work therefore depicts sustainability of the resources.

### References

- Abraham, E. M., Lawal, K. M., Ekwe, A. C., Alile, O., Murana, K. A., & Lawal, A. A. (2014). Spectral analysis of aeromagnetic data for geothermal energy investigation of Ikogosi Warm Spring-Ekiti State, southwestern Nigeria. *Geothermal Energy*, 2(1), 1
- Adeleye D.R. (1974) Sedimentology of the fluvial Bida Sandstones (Cretaceous), Nigeria *Sediment Geol* 12:1 – 24
- Ajakaiye, D. E. (1981). Geophysical investigations in the Benue Trough—a review. *Earth Evol. Sci*, 1(2), 110-125.
- Akbar, S., and Fathianpour, N. (2016). Improving the Curie depth estimation through optimizing the spectral block dimensions of the aeromagnetic data in the Sabalan

- geothermal field. *Journal of Applied Geophysics*, 135, 281-287.
- Bhattacharyya, B. K., & Leu, L. K. (1975). Analysis of magnetic anomalies over Yellowstone National Park: Mapping of Curie point isothermal surface for geothermal reconnaissance. *Journal of Geophysical Research*, 80(32), 4461-4465.
- Bilim, F. Akay, T. Aydemir, A. Kosaroglu S. (2016) Curie point depth, heat-flow and radiogenic heat production deduced from the spectral analysis of the aeromagnetic data for geothermal investigation on the Menderes Massif and the Aegean Region, western Turkey. *geothermics* 60 pp 44-57.
- Blakely, R.J., (1995). Potential Theory in Gravity and Magnetic Applications. Cambridge Univ. Press, pp. 307-308
- Ikpokonte, A. E., (1997). Geological and Geophysical Studies of Geotectonic Evolution of the Niger-Benue Confluence Area and Adjacent Regions. Ph D Thesis, Department of Geology, Ahmadu Bello University, Zaria.
- Ikpokonte, A. E. (2009). A continental structural junction: Evidence of shallow crustal discontinuities deduced from the gravity data over the Niger-Benue troughs (confluence) area, Nigeria. *Nigerian Journal of Physics*, 21(1), 27-42.
- Ikpokonte, A.E. and Ajayi, C.O. (2003): A preliminary Interpretation of the Shallow Regional Structures Deduced from Ground Magnetic Data over the Eastern Part of the Lower Benue Trough (Confluence) area, Nigeria.
- Kasidi, S. & Nur, A. (2014). Estimation of Curie Point Depth, Heat Flow and Geothermal Gradient Inferred from Aeromagnetic Data over Jalingo and Environs North-Eastern Nigeria. *International Journal of Science & Emerging Technologies*, 6(6).
- Kogbe, C. A, Ajakaiye DE, Matheis G (1983) Confirmation of rift structure along the Mid Niger Valley, Nigeria. *J Afr Earth Sci* 1 : 127 - 131
- Kwaya, M. Y., Kurowska, E., Alagbe, S. A., Ikpokonte, A. E., & Arabi, A. S. (2013). Evaluation of Depth to Basement Complex and Cenozoic Unconformity from Seismic Profiles and Boreholes in the Nigerian Sector of the Chad Basin. *Journal of Earth Sciences and Geotechnical Engineering*, 3(2), 43-49.
- Megwara, J. U., Udensi, E. E., Olasehinde, P. I., Daniyan, M. A., and Lawal, K. M. (2013). Geothermal and radioactive heat studies of parts of southern Bida basin, Nigeria and the surrounding basement rocks. *International Journal of Basic and Applied Sciences*, 2(1), 125.
- Nemzer, M. L., Carter, A, and Nemzer, K. P., (2009): Geothermal Energy." Microsoft® Encarta® 2009 [DVD]. Redmond, WA: Microsoft Corporation, 2008.
- Nigeria Geological Survey Agency, (2010) Geological Map of the Area of Study Oasis Montaj 2010 version.
- Obande, G. E., Lawal, K. M., & Ahmed, L. A. (2014). Spectral analysis of aeromagnetic data for geothermal investigation of Wikki Warm Spring, north-east Nigeria. *Geothermics*, 50, 85-90.
- Ojo S. B. (1990). Origin of a major aeromagnetic anomaly in the Middle Niger Basin, Nigeria. *Tectonophysics*, 185 (1990) 153-162. Elsevier Science Publishers B.V., Amsterdam.
- Ojo S.B. Ajakaiye, D.E. (1989) Preliminary interpretation of gravity measurements in the Mid-Niger Basin area, Nigeria. In: Kogbe CA (ed) *Geology of Nigeria*, 2nd ed, Elizabethan Publishers, Lagos, pp 347-358
- Okubo, Y., Graf, R. J., Hansen, R. O., Ogawa, K., & Tsu, H. (1985). Curie point depths of the Island of Kyushu and surrounding areas, Japan. *Geophysics*, 50(3), 481-494.
- Saada A. S., (2016) Curie point depth and heat flow from spectral analysis of aeromagnetic data over the northern part of Western Desert, Egypt. *Journal of Applied Geophysics* 134 PP 100-111.
- Spector, A., & Grant, F. S. (1970). Statistical models for interpreting aeromagnetic data. *Geophysics*, 35(2), 293-302.
- Sunday, Echewofun Simon (2015). Renewable: Exploring Geothermal for Electrification. Daily Trust Monday October 26. <http://www.dailytrust.com.ng>.
- Tanaka, A., Okubo, Y., & Matsubayashi, O. (1999). Curie point depth based on spectrum analysis of the magnetic anomaly data in East and Southeast Asia. *Tectonophysics*, 306(3), 461-470.
- Tole, M. P. (1996). Geothermal energy research in Kenya: a review. *Journal of Africa Earth Sciences*, 23(4), 565 - 575.

## QUANTUM MECHANICAL AND ANALYTICAL APPROACH TO BLOCH NMR FLOW EQUATION BASED ON HYPERGEOMETRY FOR ANALYSING TISSUES

Adeyemi O. F \*, Awojoyogbe O. B\* and Nyam G. G

\*Department of Physics ,University of Abuja, Federal Capital Territory Abuja, Nigeria

Department of Physics, Federal University of Technology, Minna, Niger State, Nigeria.

Email: hfog84@yahoo.com

### ABSTRACT

*When an atomic sample is placed in a static magnetic field  $B_0$ , exciting it with a second spatially varying radiofrequency magnetic field  $B_1(x)$  gives information regarding the intrinsic nuclear content, the elastic properties and the environment of the nuclei noninvasively and nondestructively. This makes NMR/ MRI very unique in the studies of biological processes, isolated tissues and cells. In this study, the Bloch NMR flow equation has been solved analytically in terms of hyper geometric functions for molecular characteristics of tissues for medical and biomedical applications. The solutions are used to explore the functional state of tissues to evaluate their health conditions at the molecular level. We developed computational techniques that fundamentally connect the newly obtained MRI parameters to the traditional pulse MRI with the goal of developing Magnetic Resonance Imaging techniques for diagnosis and prognosis at relatively low cost.*

**Keywords:** Bloch NMR flow equation, Magnetic Resonance Imaging, Spatially varying radiofrequency magnetic field  $B_1(x)$ , Hypergeometric functions.

### Introduction

NMR phenomena are also utilized in low-field NMR, NMR spectroscopy and MRI in the Earth's magnetic field (referred to as Earth's field NMR), and in several types of magnetometers. (wikipedia.org, 2015)

Magnetic Resonance Imaging uses a powerful magnetic field along with radio waves (not X-rays) and a computer to produce highly detailed “slice by-slice” pictures of virtually all internal structures of the body. The results enable physicians to examine parts of the body in minute detail and identify disease in ways that are not possible with other techniques. For example, MRI is one of the few imaging tools that can see through bone, making it an excellent tool for examining the brain and other soft tissue. (M. O Dada, et al, 2015 ).

Many of human diseases such as cancer, diabetes, arteriosclerosis and stroke, Alzheimer's disease, AIDS, etc., have all been known to be diseased conditions which take place at quantum (molecular) level. (Allen, S.G. et al. 1997). If we can see exactly what goes on at that level, we may have thorough understanding of their specific causes (or how

they are caused), trace and monitor their progression and get the best cure for them. It is hoped that due to the ability of magnetic resonance to probe right to the fundamental level, we may be able to image human cellular functions and such imaging modalities would definitely help in the understanding of the human diseased conditions. Information gathered from the images can then be added to the present medical database to make it more comprehensive and thus permit the physician to make a more specific diagnosis, prognosis and possibly the appropriate therapy. The basic challenge in this direction is finding the right mathematical frameworks which appropriately describe the processes involved. (Mitchell, J. et al 2008)

Nuclear magnetic resonance (NMR) has been shown to have high sensitivity for detecting intracranial pathology. The high sensitivity of nuclear magnetic resonance (NMR) imaging for detecting intracranial pathology has been reported by several authors [Baliles D. R et al, 1982]. On the basis of the 1971 observation of Damadian [Damadian R, 1971] that both the spin-lattice ( $T_1$ ) and spin-spin ( $T_2$ ) relaxation



times of neoplastic tissue are prolonged, it was hoped that NMR would allow a more precise prediction of tissue characteristics than is possible with computed tomography (CT). The tissue relaxation times of excised tumors have been measured and in vivo measurements have made of tumors in experimental animals [Herfkens R et al, 1981]. A clear overlapping of the values representing tissue relaxation times has been demonstrated between different types of neoplasm and between these and other pathologies.

### Theoretical Computation

We apply a mathematical algorithm to describe in detail the dynamical state of the owing fluid particle starting from the Bloch NMR flow equation

$$\frac{dM_x(t)}{dt} = \frac{M_x(t)}{T_2} \quad (1)$$

$$\frac{dM_y(t)}{dt} = \gamma M_z B_1(x, t) - \frac{M_y(t)}{T_2} \quad (2)$$

$$\frac{dM_z(t)}{dt} = -\gamma M_y B_1(x, t) + \frac{M_0 - M_z}{T_1} \quad (3)$$

Where  $M_x$  and  $M_y$  are transverse magnetization  $M_z$  is the longitudinal magnetization along the x; y and z axis.  $M_0$  is the equilibrium magnetization along z-direction.  $B_1(x)$  is the radio frequency (RF) magnetic field which can be constant.  $T_1$  is the spin-lattice relaxation time;  $T_2$  is the transverse or spin-spin relaxation time and is gyromagnetic ratio of fluid spine.

From equations (2) and (3) we can write

$$V^2 \frac{\partial^2 M_y}{\partial x^2} + 2V \frac{\partial M_y}{\partial x} + V \frac{\partial}{\partial t} \left( \frac{1}{T_1} + \frac{1}{T_2} \right) M_y + \frac{\partial}{\partial t} \left( \frac{1}{T_1} + \frac{1}{T_2} \right) M_y = \gamma B_1^2(x, t) M_y - \gamma B_1(x, t) \frac{M_0}{T_1} \quad (4)$$

Equation (4) is the general NMR Bloch flow equation (Awojoyogbe, 2007).

The time-independent part of (4) is gotten by letting  $\frac{\partial M}{\partial t} = 0$  hence we get

$$V^2 \frac{d^2 M_y}{dx^2} + V \frac{\partial}{\partial x} \left( \frac{1}{T_1} + \frac{1}{T_2} \right) M_y + \frac{1}{T_2} \frac{\partial}{\partial t} M_y + \frac{\partial}{\partial t} \left( \frac{1}{T_1} + \frac{1}{T_2} \right) M_y = \gamma B_1^2(x, t) M_y - \gamma B_1(x, t) \frac{M_0}{T_1} \quad (5)$$

It is convenient to use as dependent variable the departure of the stream function from its classical form. (Awojoyogbe, 2007).

Assuming a solution of (5) as

$$M_y(x, t) = Y(x) \exp^{ix} G(t) e^{lt} \quad (6)$$

$$\text{Where } l = -\frac{1}{2VT_0} \quad (7)$$

$V$  is the instantaneous velocity of the fluid and  $(x)$  is a special function of the transverse magnetization  $M_y$ . When the  $rFB_1(x)$  field is maximum the magnetization  $M_y$  is maximum and  $M_0 = 0$ . At maximum NMR signal (12) become

$$V^2 \frac{d^2 M_y}{dx^2} + V \frac{\partial}{\partial x} \left( \frac{1}{T_1} + \frac{1}{T_2} \right) M_y + \frac{1}{T_2} \frac{\partial}{\partial t} M_y + \frac{\partial}{\partial t} \left( \frac{1}{T_1} + \frac{1}{T_2} \right) M_y = 0 \quad (8)$$

Equation (8) is a time independent Bloch NMR flow equation

From 8 where  $M_y(x, t) = Y(x) \exp^{ix}$  a s a function of position  $(x)$  satisfies

$$\frac{d^2 Y}{dx^2} + \frac{1}{V^2} (\gamma B_1^2(x, t) + T_g - T_R) Y = 0 \quad (9)$$

Where

$$T_R = \frac{1}{4T_0^2}, \frac{1}{T_0} = \frac{1}{T_1} + \frac{1}{T_2} \text{ and } T_g = \frac{1}{T_1 T_2}$$

### NMR Schrodinger Wave Equation

Equation (9) gives the NMR wave equation where  $rFB_1$  is constant but when the  $rFB_1$  field spatially varies with  $x$  (9) become (O.F Adeyemi et al, 2017)

$$\frac{d^2 Y}{dx^2} + \frac{\gamma B_1^2(x)}{V^2} + \frac{T_g - T_R}{V^2} \frac{\partial}{\partial t} Y = 0 \quad (10)$$

$$\frac{d^2 Y}{dx^2} + \frac{\gamma m}{\hbar} (E - E_p(x)) + \frac{T_g - T_R}{V^2} \frac{\partial}{\partial t} Y = 0$$

Here 
$$\frac{g^2 B_1^2(x)}{V^2} = \frac{2m}{\hbar} (E - E_p(x))$$

Where  $E$  and  $E_p(x)$  are the total energy and potential energy of the fluid particle respectively.

$$\frac{d^2 y}{dx^2} + \frac{1}{V^2} \left( \frac{2m}{\hbar^2} EV^2 + T_g - T_R \right) y = \frac{2m}{\hbar^2} E_p(x) \quad (11)$$

Equation 11 is a form of Schrodinger equation in 1 dimension with NMR parameters embedded in it.

The potential in equation (11) is replaced with the Yukawa's potential which is given by

$$E_p(x) = v_0 a \frac{e^{-x/a}}{x} \quad (12)$$

Then we can explicitly write (11) as

$$\frac{d^2 y}{dx^2} + \left( \frac{2m}{\hbar^2} EV^2 + T_g - T_R \right) y = 0 \quad (13)$$

Where  $\frac{2m}{\hbar^2} EV^2$  and  $T_g - T_R$  are constant given as

$$f = \frac{2m_0 a}{\hbar^2} \text{ and } a = \frac{1}{V^2} \left( \frac{2m}{\hbar^2} EV^2 + T_g - T_R \right) \quad (14)$$

The solution to (13) after been subjected to mathematical software called Wolfram Mathematical 9.0 gives a solution in hypergeometric function as (O.F Adeyemi et al, 2017)

$$y(x) = e^{x[i\sqrt{a}]} {}_x F_{(n,b,c)} \quad (15)$$

Where

$$n = 1 + \frac{-4\sqrt{a} - 2(-2\sqrt{a} + f)}{4\sqrt{-a}} = 1 - \frac{f}{2i\sqrt{a}} \quad (15a)$$

$$b = 2 \quad (15b)$$

$$c = 2x\sqrt{-a} = 2x\sqrt{a} \quad (15c)$$

After some mathematical transformation equation (6) becomes (O.F Adeyemi et al, 2017)

$$M_y(x) = \frac{1}{2x\sqrt{a}} G(t) \cos(kx) \quad (16)$$

With Eigen value

$$E = -\frac{m_0^2 a^2}{\hbar^2 (n-1)^2} + \frac{\hbar^2}{2m_0^2} (T_R - T_g) \quad (17)$$

Longitudinal and transverse relaxation (or  $T_1$ -relaxation and  $T_2$ -relaxation) are much slower effects than precession. For biological tissues,  $T_1$  and  $T_2$  vary from hundreds of microseconds to several seconds (see Table (1)). The difference in relaxation times between different tissue types is frequently exploited as a mechanism of generating contrast between different tissues in imaging. For example, bound water tends to have shorter  $T_1$  and  $T_2$  times than free water (i.e. longitudinal magnetization in bound water will recover faster than in free water, and transverse magnetization decay is faster as well).

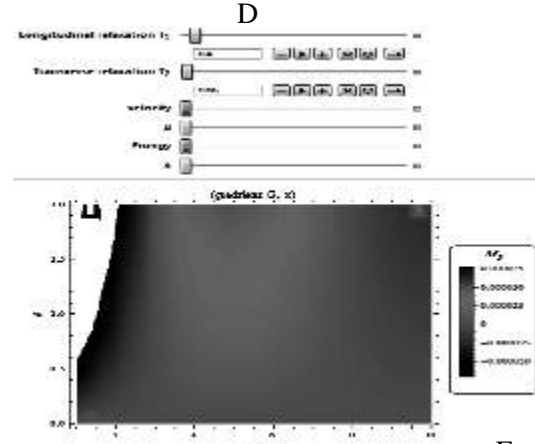
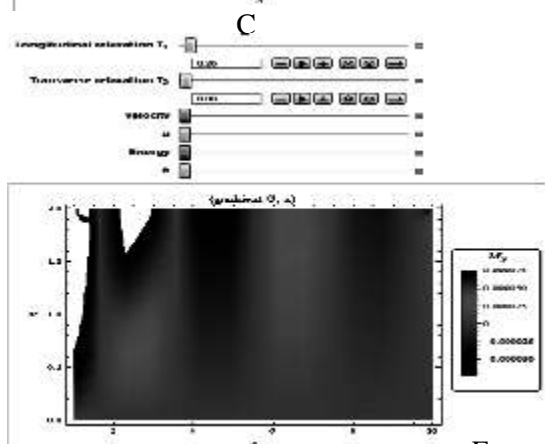
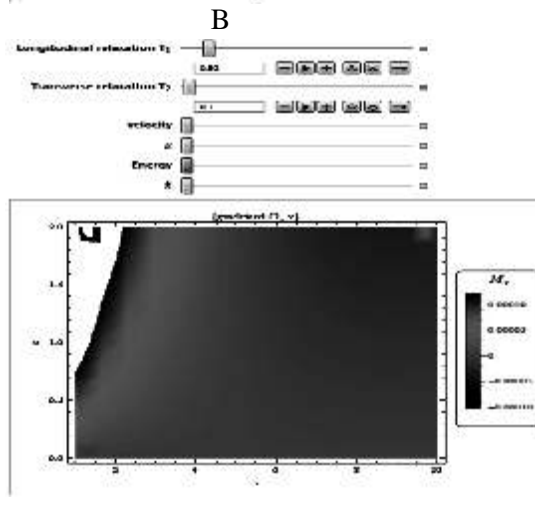
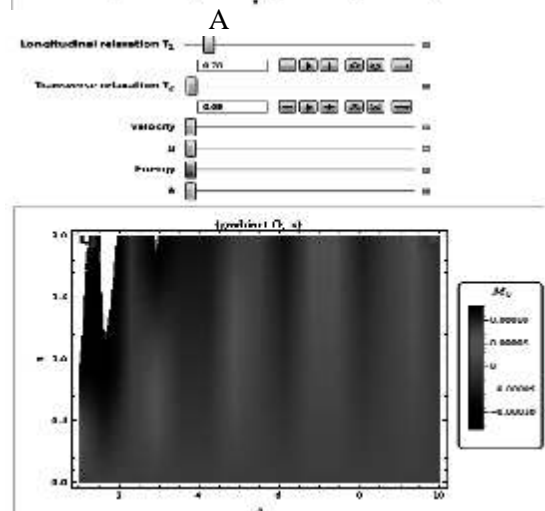
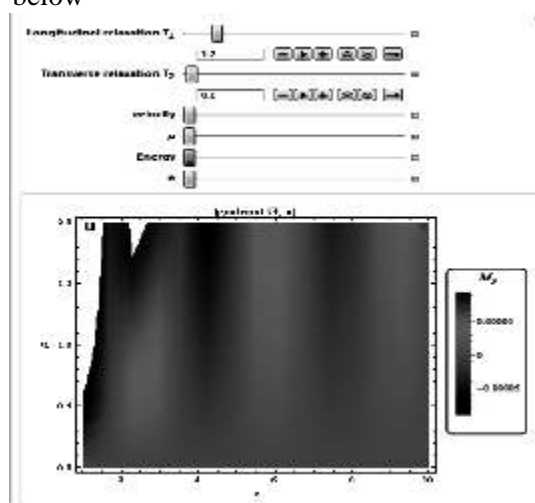
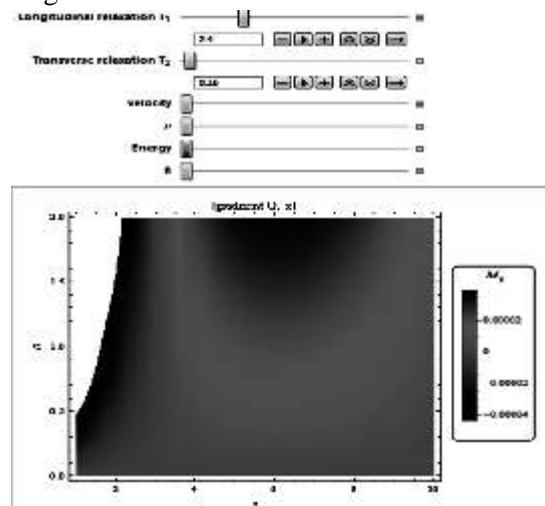
**Table 1. Relaxation Times,  $T_1$  and  $T_2$ , for Different Body Tissues under a 1.5T Magnetic Field Strength, in Milliseconds. (DAVID MORATAL et al, 2006)**

S.NO	TISSUES	$T_1$ (s)	$T_2$ (s)
1	Cerebrospinal Fluid (CSF)	2.4	0.16
2	Blood	1.2	0.1
3	White Matter (WM)	0.78	0.09
4	Grey Matter (GM)	0.92	0.1
5	Fat	0.26	0.08
6	Bone marrow	0.4	0.06
7	Muscle	0.87	0.05
8	Liver	0.5	0.05
9	Pancreas	0.6	0.07

## Result and Discussion

From equation (17) the NMR transverse magnetization of different selected tissues is

simulated using Wolfram Mathematical computer program as shown in the figure below



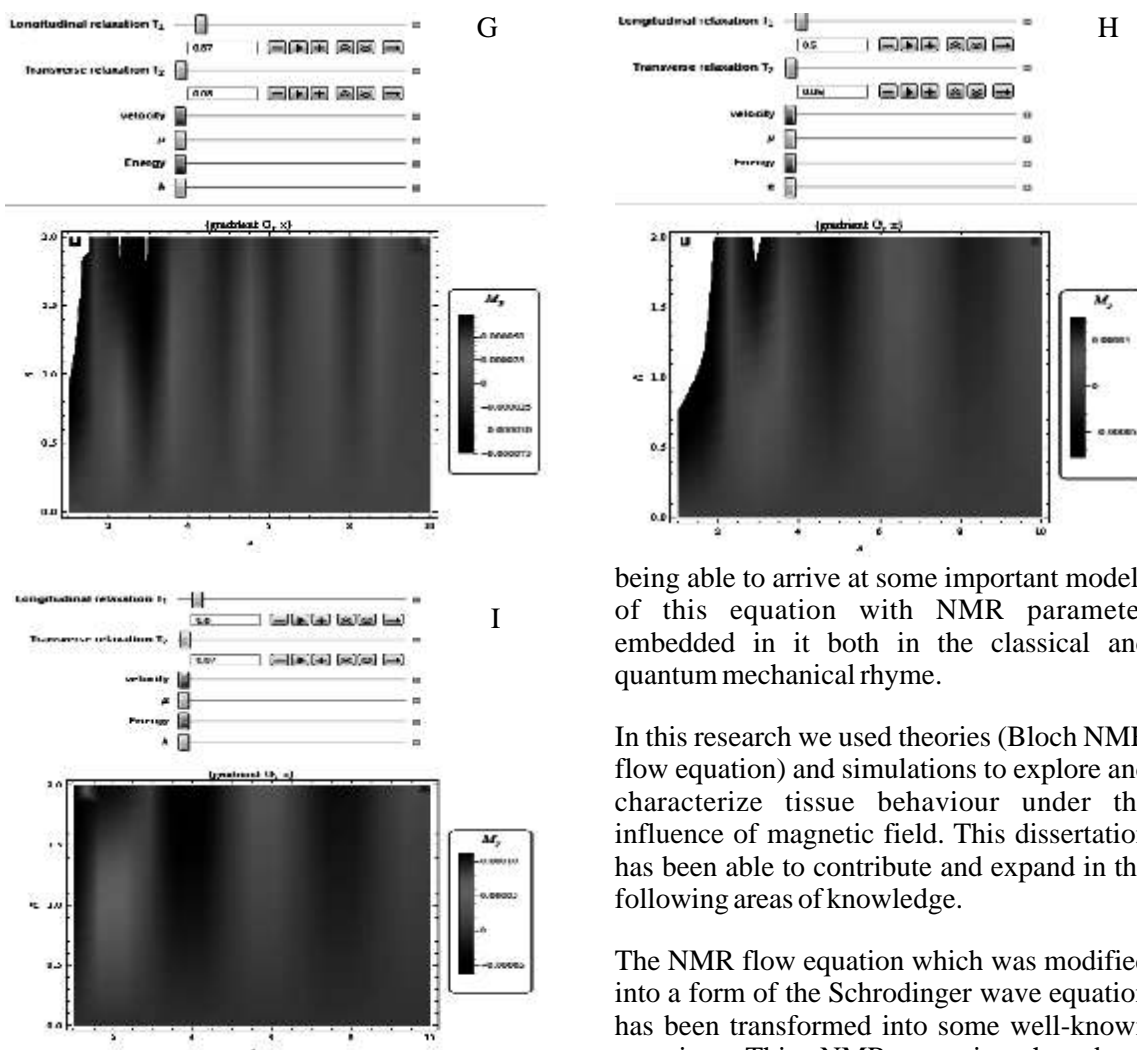


Figure 1: Density maps of transverse magnetization as it varies with  $x$  and gradient for (a) Cerebrospinal Fluid (CSF) (b)(c) white matter (d) gray matter (e) fat (f) bone marrow (g) muscle (h) liver (I) pancreas

Fig 1 shows some contrast in the signal generated from various tissue in the body. This signal can also be used to monitor many more tissue with known  $T_1$  and  $T_2$

### Conclusion

This research has successfully explore the modified Bloch NMR flow equation and has

being able to arrive at some important models of this equation with NMR parameter embedded in it both in the classical and quantum mechanical rhyme.

In this research we used theories (Bloch NMR flow equation) and simulations to explore and characterize tissue behaviour under the influence of magnetic field. This dissertation has been able to contribute and expand in the following areas of knowledge.

The NMR flow equation which was modified into a form of the Schrodinger wave equation has been transformed into some well-known equation. This NMR equation has been transform successfully in equation of Hypergeometric and Bessel equation at various boundary conditions.

The Bloch NMR flow equation has been resolved in the hypergeometric form, for which the signal is model and a computer program was developed to show contrasts between tissues with different  $T_1$  and  $T_2$  when the sizes are just few microns. This is particularly important in diagnosing cancerous cells and tumours with well-known  $T_1$  and  $T_2$ , as well as monitoring patient response after treatment. This study has an edge in the facts that diagnosis/treatment monitoring could be done without the risk

associated with health deterioration due to constant administration of chemotherapeutic drugs.

### Reference

- Allen, S.G.; Stephenson, P.C.L.; Strange, J.H. (1997), "Morphology of porous media studied by nuclear magnetic resonance", *Journal of Chemical Physics* 106 (18): 7802, Bibcode:1997JChPh.106.7802A, doi:10.1063/1.473780
- Awojoyogbe, O. B. (2003). A Mathematical Model of Bloch NMR Equations for Quantitative Analysis of Blood Flow in Blood Vessels with Changing Cross-section II. *Physica A*, (323c), 534-550.
- Awojoyogbe, O. B, Dada, O.M. (2011). Fluid Transport: Theory, Dynamics and Applications (Book Chapter). The Dynamics of NMR Diffusion Equation for the Analysis of Hemodynamic and Metabolic Changes in Biological Tissue. *Nova Science Publication*, USA.
- Awojoyogbe, O.B, Faromika, O.P, Dada, O.M, Boubaker, K., Ojambati (2011) Mathematical Models of Real Geometrical Factors in Restricted Blood Vessels for the Analysis of CAD (Coronary Artery Diseases) Using Legendre, Boubaker and Bessel Polynomials. *Journal of Medical Systems*; 35, 1513-1520.
- Awojoyogbe, O. B. (2007). Solution to Bloch NMR Equations for the Analysis of Hemodynamic Functions of Blood Flow System Using m-Boubaker Polynomials. *Current Applied Physics*, 9, 278-283.
- Cohen, M.H.; Mendelson, K.S. (1982), "Nuclear magnetic relaxation and the internal geometry of sedimentary rocks", *Journal of Applied Physics* 53 (2): 1127, Bibcode:1982JAP...53.1127C, doi:10.1063/1.330526
- Dada, O. M., Awojoyogbe, O. B., & Ukoha, A. C. (2015). A computational analysis for quantitative evaluation of petrol-physical properties of rock fluids based on Bloch NMR diffusion model for porous media. *Journal of Petroleum Science and Engineering*, 127, 137-147
- Damadian R. Tumour detection by nuclear magnetic resonance. *Science* 1971 ;171:1 151-1153
- Mitchell, J.; Webber, J. B. W.; Strange, J. H. (2008), "Nuclear Magnetic Resonance Cryoporometry", *Physics Reports* 461 (1): 1-36, Bibcode:2008PhR...461....1M, doi:10.1016/j.physrep.2008.02.001
- O.F Adeyemi, O.B Awojoyogbe, M. Umar (2017) The generalised nmrschrodinger wave equation

## BULK GERMANIUM OPTICAL PROPERTIES: THE EFFECTS OF EXTINCTION/ABSORPTION COEFFICIENTS AND CRYSTAL MOMENTUM IN THE INFRARED REGION

<sup>a,b</sup>Aliyu Kabiru Isiyaku, Auwal Mustapha Imam<sup>c,d</sup>, Mohammed Isah Kimpa<sup>b,e</sup>, Mustapha Isah<sup>a</sup>, and Thomas Koyah<sup>a</sup>,

<sup>a</sup>Department of Physics, Kaduna State University, Kaduna State, Nigeria.

<sup>b</sup>Department of Physics and Chemistry, Faculty of Applied Sciences and Technology Pagoh Educational Hub, Universiti Tun Hussein Onn Malaysia.

<sup>c</sup>Department of Physics with Electronics, Federal University Birnin Kebbi, Nigeria.

<sup>d</sup>Department of Physics, Universiti Teknologi Malaysia, Johor Bahru

<sup>e</sup>Department of Physics, School of Physical Sciences, Federal University of Technology Minna, Niger State, Nigeria.

mustaphaimamauwal\_GoBack\_GoBack@gmail.com, <sup>a</sup>aikabiru1@gmail.com, Kimpa@futminna.edu.ng, almusty@gmail.com

### ABSTRACT

*Study on the optical behaviours of bulk germanium (Ge) transmitting in infrared (IR) region with respect to parameters such as wavelength and frequency has been an area of interest. Influence of absorption and extinction coefficients and crystal momentum on the optical properties of Ge semiconductor in the IR region were investigated. Developed models and data from existing works on Ge semiconductor were analyzed using a theoretical approach. Optical properties such as absorption and extinction coefficients were found to greatly influence the behavior of Ge semiconducting material, which determines the amount of light absorbed by the materials, most especially in the Infrared region of spectrum. The data and the models used were able to predict the effects on the properties of Ge semiconductor in the IR region.*

**Keywords:** Bulk germanium; infrared region; semiconductor; solid state; quantum confinement

### Introduction

The two outstanding single semiconductor materials of germanium (Ge) and silicon (Si) are proven to be the most considered materials in the field of solid-state device technologies and also nanotechnology in recent years (Frey *et al.*, 2006). In the area of infrared (IR) lens design, these materials are essentials. For window or lens applications in the 1.6-1.8 $\mu$ m spectrum region, Ge semiconductor substrate is mostly used (Koester *et al.*, 2006). Due to its high refractive index, Ge plays part in optical interconnect device if incorporated in Si waveguide for improved silicon photonics devices (Cho *et al.*, 2014). Chromatic aberration in several applications can be avoided if high refractive index and low dispersion bulk materials across different range of temperature are used (Koester *et al.*, 2006). Performance of Si and Ge optical devices transmitting in the infrared region can harness effectively when these materials are cooled to cryogenic temperatures, thereby

improving the signal from the device background radiation (Frey *et al.*, 2006). Nowadays, Ge is used as a component of glass in telecommunications fiber optics; as a polymerization catalyst for polyethylene terephthalate (PET), an IR night vision device and also as a semiconductor substrate in electronic circuitry (Adams, 1990, Koester *et al.*, 2006). Recently, Nanocrystals Si and Ge have been used in photonic devices that emit light in the visible region of the spectrum (Isiyaku & Ghoshal, 2016). This is due to quantum confinement, surface state effects and exciton binding energy (Abdu *et al.*, 2016, Wu & Yang, 2000).

Ge semiconductor material is a lustrous, brittle, hard and greyish white metalloid that is essential in many new-solid state electronic and optical devices with an indirect band gap of 0.66eV and hence does not emit light in the visible range (Isiyaku & Ghoshal, 2016, Aliyu *et al.*, 2016). This semiconductor is obtained in

the form of a single crystal or apolycrystalline material. It is softer than silicon and very much softer than the diamond form of carbon. Polycrystalline Ge is less expensive and is available in larger sizes than mono-crystalline material. Ge crystallizes in the covalently bonded cubic diamond structure from which it melts at 937.4 °C (Audzjonis *et al.*, 2010, Dasgupta and Amitava, 2014). It has an infrared refractive index of 4.00, a room temperature density 5.32 grams per cubic centimeter and radiative recombination coefficient  $6.4 \times 10^{-14} \text{ cm}^3/\text{s}$  for which is stable in air up to 400°C, above which it begins to oxidize (Pearson & Brattain, 1955).

Extinction coefficient ( $k$ ) which is proportional to both absorption coefficient and wavelength is an important parameter for examining the trend of optical and electronic properties of a semiconductor (Harris, 2010). It is an optical property of the semiconductor material that determines how much light is absorbed by the material and is related to the index of refraction (Audzjonis *et al.*, 2010). The excitation range performance at a given wavelength is also estimated by the absorption coefficient which also links to  $k$ , the imaginary part of the index of refraction. This property gives the amount of intensity absorbed per unit length by the material. Optical properties are also related with the increase in crystal momentum for which the wave number decreases. In this work, the effect of the optical absorption coefficient, extinction coefficient and crystal momentum on the optical properties of bulk Ge material with respect to certain varying wavelengths and frequencies are investigated.

### Theory and Methods

The behaviour of electromagnetic radiation depends on its wavelength or energy (i.e. frequency). Higher frequencies indicate shorter wavelengths and vice versa. This interactive electromagnetic radiation exhibit both wave-like and particle-like properties. Here, a theoretical method has been used in

determining the effects of optical absorption, extinction coefficients and crystal momentum of an optical germanium. It provides an important part in examining the optical properties of germanium, especially in the far infrared region of the electromagnetic spectrum.

For a complete one full cycle (one period of a wave), we could say that the wave has moved by one wavelength. Since speed is distance traveled with respect to time spent, and a wave moves a distance of one wavelength in a time of one period, the speed  $v$  is given as,

$$v = \lambda / t \quad (1)$$

If the frequency is given to be;

$$f = 1/t \quad (2)$$

Thus,

$$f = v / \lambda \quad (3)$$

The speed of light in a medium is related to the speed in vacuum by the index of the refraction

$$v = c / n \quad (4)$$

Therefore, Eqn. (2) becomes;

$$f = c / \lambda n \quad (5)$$

Similarly, looking at the Beer Lambert law,

$$I_x = I_{(0)} e^{-ax} \quad (6)$$

where  $I_{(x)}$  indicates the intensity at point  $x$  in the material,  $I_{(0)}$  represents the intensity of light entering the material while  $x$  is number of molecules per centimeter cube.

Optical absorption coefficient ( $\alpha$ ) of a semiconductor material depends mostly on the wavelength of light, causing some wavelength to be absorbed in a medium, while the same medium is transparent to another wavelength. Since the intensity is proportional to the square of the magnitude of the electric field and taking only the first term for the sake of simplicity, we assumed that if the electric field is decreasing with  $e^{-kx}$ , then the intensity of the wave is

decreasing proportionally to  $(e^{-kx})^2 = e^{-2kx}$ . Comparing the expression with Beer Lambert law, we obtain the relationship between the absorption coefficient ( $\alpha$ ) and the extinction coefficient ( $k$ ) as:

$$\alpha = 2kb = 2kw/c = 4\pi k/l \quad (7)$$

Therefore,

$$k = \alpha l / 4\pi \quad (8)$$

where  $k$  and  $\alpha$  are the extinction and absorption coefficients while  $l$  is given as;

$$b = w/c \quad (9)$$

Similarly, the wave number  $k$  as a function of crystal momentum  $P$  of the material is taken as the relation in Equation (10) as reported previously (Harris, 2010).

$$k = P/\hbar \quad (10)$$

Thus,

$$k = 2\pi p/h \quad (11)$$

Equation (3) is used to calculate the frequency of the optical germanium at different wavelengths range 2.5-12 $\mu\text{m}$  for index of refraction values  $n_i$  from the work of Adams (1990). The calculated values of extinction coefficient ( $k$ ) at different absorption coefficient ( $\alpha$ ) and wavelength ( $\lambda$ ) are obtained using Equation (7). Furthermore, wave number  $k$ , dependent momentum  $P$  were calculated with the aid of Equation (10) (Harris, 2010).

## Results and Discussion

Calculated frequencies (Hz) of the bulk germanium in the infra-red region are presented in Table 1. The corresponding frequencies were obtained using equation (3) after careful consideration of the work of Adams (1990).

**Table 1: Infrared wavelength ranges and their corresponding frequencies for decreasing refractive index.**

( $\mu\text{m}$ )	$n$ (refractive index)	$f$ ( $\text{s}^{-1}$ )
2.5	4.0653	$2.95 \times 10^{13}$
3.0	4.0446	$2.47 \times 10^{13}$
4.0	4.0225	$1.86 \times 10^{13}$
5.0	4.0170	$1.49 \times 10^{13}$
6.0	4.0122	$1.25 \times 10^{13}$
7.0	4.0092	$1.07 \times 10^{13}$
8.0	4.0074	$0.94 \times 10^{13}$
9.0	4.0061	$0.83 \times 10^{13}$
10.0	4.0052	$0.75 \times 10^{13}$
11.0	4.0042	$0.63 \times 10^{13}$
12.0	4.0039	$0.62 \times 10^{13}$

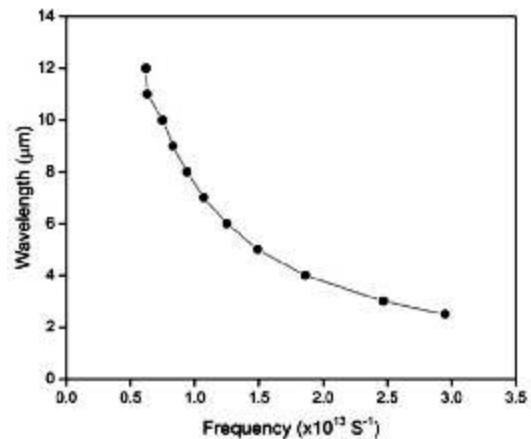


**Fig. 1 Graph of wavelength ( $\lambda$ ) against frequency ( $\text{s}^{-1}$ )**

It is observed that even in infrared region the increase in the wavelength which corresponds to decrease in refractive index lead to decrease in the corresponding frequencies of the optical germanium as shown in Fig. 1. At extreme IR region, the frequencies increases sharply as the wavelength decreases up to long wave IR region, revealing higher energy at range close to visible region. Similarly, the frequencies



decrease as the wavelengths increases toward the microwave IR region indicating a decrease in energy.

Equation (7) is used to calculate the values of extinction coefficient ( $k$ ) at different values of absorption coefficient ( $\alpha$ ) and wavelength ( $\lambda$ ) extracted from the work of Adams (1990) as shown in Table 2.

**Table 2: Calculated extinction coefficient for different absorption coefficient**

$(\text{cm}^{-1})$	$(\mu\text{m})$	$K(\text{c})$
0.0047	2.0	$0.09 \times 10^{-8}$
0.0047	2.5	$0.11 \times 10^{-8}$
0.0047	3.0	$0.15 \times 10^{-8}$
0.0051	4.0	$0.20 \times 10^{-8}$
0.0068	5.0	$0.32 \times 10^{-8}$
0.0107	6.0	$0.59 \times 10^{-8}$
0.0150	7.0	$0.83 \times 10^{-8}$
0.0178	8.0	$1.30 \times 10^{-8}$
0.0215	9.0	$1.70 \times 10^{-8}$
0.029	10.0	$2.58 \times 10^{-8}$

The excitation of electrons in the valence band depends on the absorption coefficient of the material, this extinction coefficient ( $k$ ) parameter provides the framework for testing the number of electrons absorb by the material. This is evidenced in Equation (7), where  $k > 0$  means absorption, while  $k = 0$  means the light travels straight through the material. A plot of absorption coefficient ( $\alpha$ ) against extinction coefficient ( $k$ ) is presented in Fig. 2 using a tabulated data in Table 2. This indicates that the increase in extinction coefficient leads to increase in the corresponding absorption coefficient of an optical germanium in infrared region. This resulted into the optimum emission of IR light region in germanium material. The result shows that even for those photons which have energy above the band gap the absorption coefficient is not constant, but still depends strongly on wavelength.

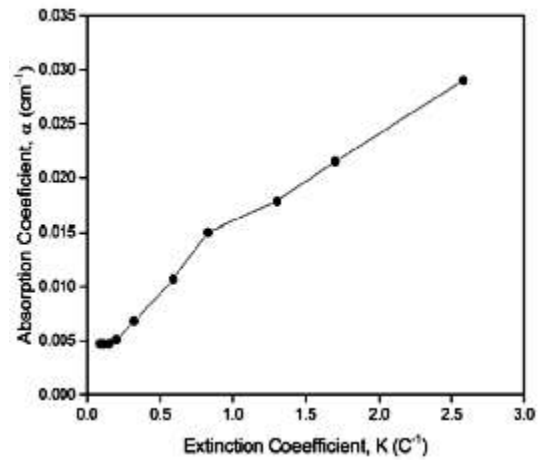


**Fig. 2 Absorption coefficient ( $\alpha$ ) against extinction coefficient ( $k$ ).**

Table 3 gives the calculated values of crystal momentum  $P$ , for a range of wave number from the work of (Harris, 2010), calculated using equation (10). The calculated results were graphically presented in Fig. 3

**Table 3: Calculated crystal momentum for some established values of wave number**

Wavenumber ( $k$ )	Momentum ( $P$ )
$2.208 \times 10^{-28}$	$2.0 \times 10^5$
$1.656 \times 10^{-28}$	$1.5 \times 10^5$
$1.326 \times 10^{-28}$	$1.2 \times 10^5$
$1.104 \times 10^{-28}$	$1.0 \times 10^5$
$0.946 \times 10^{-28}$	$0.9 \times 10^5$
$0.828 \times 10^{-28}$	$0.8 \times 10^5$
$0.736 \times 10^{-28}$	$0.7 \times 10^5$
$0.662 \times 10^{-28}$	$0.6 \times 10^5$
$0.602 \times 10^{-28}$	$0.5 \times 10^5$
$0.552 \times 10^{-28}$	$0.5 \times 10^5$

Phenomena such as the rate of absorption or emission and the distribution of electrons and holes within a solid, the number of available states per unit volume energy are turned by the responses of crystal momentum and wave number. Optical state properties of a semiconductor are affected by the increase in crystal momentum and decrease in wave number. The response of the calculated crystal momentum within the IR region for some existing values of wave number tabulated in Table 3 is plotted in Fig. 3. The bulk germanium crystal momentum greatly enhanced as the wave number decreases.

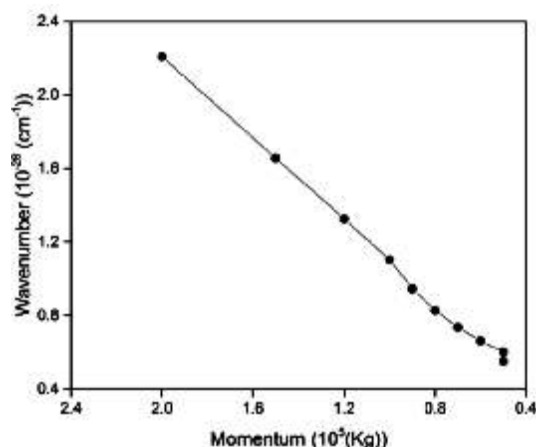


Fig. 3 Absorption coefficient ( ) against extinction coefficient (k).

### Conclusion

The influences of wavelength, frequency and crystal momentum on the optical properties of germanium semiconductor were investigated using some developed models. It is observed that the variable state of wavelengths, the corresponding frequencies and crystal momentum of the optical germanium change exponentially even at the infrared region, thereby affecting the absorption and emitted energy in the same aspect. The effect of extinction coefficient on the absorption rate on the optical germanium is also examined theoretically. Increase in extinction coefficient leads to optimum optical absorption in the infrared region of the Ge material. This shows that the photons with energy above the bandgap depend strongly on the wavelength and have constant absorption coefficient.

### References

- Abdu, Sadiq G, Abbas, Dallatu U, Kabiru, A. I. (2016). A Model Study of the Influence of Temperature on the Photoluminescence of Silicon Nano Crystals. *Journal of Scientific and Engineering Research*, 3, 139–144.
- Adams, J. H. (1990). *Germanium and Germanium Compounds. Metals Handbook*. (10th ed). Ohio: ASM International.
- Audzijonis, A., Altauskas, R., Sereika, R., Igas, L., & Rza, A. (2010). Electronic structure and optical properties of BiSI crystal. *Journal of Physics and Chemistry of Solids*, 71, 884–891.
- Cho, S., Park, J., Kim, H., Sinclair, R., Park, B. G., & Harris, J. S. (2014). Effects of germanium incorporation on optical performances of silicon germanium passive devices for group-IV photonic integrated circuits. *Photonics and Nanostructures - Fundamentals and Applications*, 12, 54–68.
- Frey, B. J., Leviton, D. B., & Madison, T. J. (2006). Temperature dependent refractive index of silicon and germanium. *Proceedings of SPIE - The International Society for Optical Engineering*, 6273 II, 10.
- Harris, T. R. (2010). *Optical Properties of Si, Ge, GAAS, GASB, INAS and INP at Elevated Temperature*. Air Force Institute of Technology.
- Isiyaku, A. K., Ghoshal, S. K. (2016). Photoluminescence spectral features of silicon nanowires. *Jurnal Teknologi*, 78, 153–158.
- Koester, S. J., Schaub, J. D., Dehlinger, G., & Chu, J. O. (2006). Germanium-on-SOI Infrared Detectors for Integrated Photonic Applications. *IEEE Journal of Selected Topics in Quantum Electronics*, 12, 1489–1502.
- Pearson, G. L., & Brattain, W. H. (1955). History of Semiconductor Research. *Proceedings of the IRE*, 43, 1794–1806.
- Wu, Y., & Yang, P. (2000). Germanium nanowire growth via simple vapor transport. *Chemistry of Materials*, 12, 605–607.
- Aliyu I. Kabiru, Musa I. Bala, Isah Mustapha, DallatuAbbaU., & DanlamiAbdulhadi(2016). The Influence of Oscillator Strength on Germanium Nanocrystals. *Bayero Journal of Physics and Mathematical Sciences*. Vol.7, no.1, pp. 89-95.
- Nandita Dasgupta and Amitava Dasgupta (2014). *Semiconductor Devices: Modelling and Technology*, Prentice-Hall of India private limited, New Delhi

## FIRST PRINCIPLE STUDY OF SURFACE AND ELECTRONIC STRUCTURE OF ALUMINA $\gamma$ - $\text{Al}_2\text{O}_3$ (10)

<sup>1</sup>Aminu Abdullahi Yamusa, <sup>2</sup>Alhassan Shuaibu, <sup>3</sup>Salisu Isyaku Kunya and <sup>4</sup>Joshua Adeyemi Owolabi

<sup>1</sup>Department of Physics Federal College of Education Zaria

<sup>2</sup>Department of Physics Kaduna State University

<sup>3</sup>Department of Science Laboratory, Jigawa State Polytechnics

<sup>4</sup>Department of Physics, Nigerian Defence Academy, Kaduna

Email: alhasikara@yahoo.co.uk

### ABSTRACT

Ab-initio calculations based on first principles were carried out on bulk and the (10) surface of  $\gamma$ - $\text{Al}_2\text{O}_3$  in order to study the electronic structures and structural relaxations. The Perdew Burke Ernzerh of exchange-correlation pseudo-potentials as implemented in Quantum ESPRESSO (QE) code was used. The partial and full density of states were obtained, and used to examine the differences between the surface and bulk. An Aluminum vacancy was also created on the surface, and calculations were also carried out on this. The energy of the surface was found to be higher (less negative) than bulk, as expected, and changed from a strong insulator of band gap 5.9488 eV to a conductor. The results show that  $\text{Al}_2\text{O}_3$  is highly ionic, an insulator in bulk and a conductor at the surface.

### Introduction

Considering the technological importance of alumina  $\gamma$ - $\text{Al}_2\text{O}_3$ , it is surprising that the reliable atomic-scale model for the surface structure of the amorphous phase or of the transition alumina has not been explain in details within both experiment and theory. This is partly due to experimental difficulties in preparing uniform surfaces, free of impurities, structural complexity of the bulk phases and the need for details theoretical investigations [1-3]. It has been confirmed that alumina is highly important in many fields of electronics and engineering. It is an insulator, chemically non-reactive, and has a high melting point. Ruby, which is Alumina with a  $\text{Cr}^{3+}$  impurity, is the earliest and most well known laser crystal. Alumina is used in circuit and computer components, as well as micro-abrasives.

Taking into consideration must of the theoretical approaches to modeling alumina used to consider rigid pair potentials which found to be inadequate for the bulk, requiring charge transfer [4] or quadrupolar corrections [5]. But different investigations using the most reliable but computationally demanding density-functional theory (DFT) have concentrated on the (001) and (110) surfaces

of  $\gamma$ - $\text{Al}_2\text{O}_3$ , in applications that the modeled surface can only be as a periodic slab [6-8] or as a cluster [9]. However, some of these suffer from deficiencies in modeling  $\gamma$ - $\text{Al}_2\text{O}_3$  (nonstoichiometry, absence of vacancies or high H concentration) or inadequately representing a surface (insufficient slab area or thickness, frozen atoms). More relevant for the current work on close-packed O surfaces is a periodic DFT study of the hcp-based k- $\text{Al}_2\text{O}_3$  and its close packed (001)-like surfaces [10] significant relaxation of surface Al is discussed in terms of subsurface tetrahedral Al and vacancies.

In this study, we theoretically investigate and predict the surface structure of spinal-based transition alumina,  $\gamma$ - $\text{Al}_2\text{O}_3$ , when fully dehydroxylated. These are compared to a similar surface of  $\gamma$ - $\text{Al}_2\text{O}_3$ . The investigations on the (10) surface of  $\gamma$ - $\text{Al}_2\text{O}_3$  are the subject of this study.

### Computational Method

The  $\gamma$ - $\text{Al}_2\text{O}_3$  unit cell has a hexagonal cell structure, with a rhombohedral primitive cell consisting of 10 atoms. Four of these atoms are Aluminum, six are Oxygen. In this work, we have created a cell of 60 atoms, cleaved at the (10), using an XCysden software [11]. We

have chosen a 60 atom cell in order to have a little interaction between the surfaces. The cell used has a u-vector, which spans the distance from the origin, with length 5.13 Å. The cell is also defined by a v-vector, which is from the origin to another point, its length is 6.99 Å. The vectors u and v are separated by an angle = 84.16°. Both u and v are perpendicular to the vector w. The last vector necessary to describe the cell dimensions is the w-vector, which is from the origin to the last point. After cleaving the plane, a vacuum slab of thickness 10 Angstroms was added. The cut and vacuum slab are made precisely such that there is consistent pattern. The surface is Aluminum terminated, the last layer having four Al atoms. K-point and Energy Cut-off we have used 10×4×4 mesh and 300 eV respectively both in bulk and (10) surfaces. For the exchange correlation functional we have used Perdew Burke Ernzerh (PBE) as implemented in QE [12-13]. The convergence tests for all parameters were done to find optimum settings.

## Results and Discussions

### Surface Structure

When relaxing a surface, atoms nearer to the surfaces are expected to relax with greater displacements than those atoms located in the inside of the cell. This is due to the fact that there are no longer atoms providing electrons to the outer atoms, in order for these outer atoms to feel that their shells are being completed, they sink down into the still "complete" cell. Of course, since there are only discontinuities along the w-direction, relaxations should be chiefly in this direction. The u and v direction displacements are very slight as shown in Fig. 1.

For the (000) surface of Alumina, such behavior was indeed observed. The Aluminum atoms have the greatest relaxations, as they are able to sink downwards into triangle formations of Oxygen atoms below them. Near to the surface, large displacements occur, while in the center of the cell, displacements are so small that the atomic

positions those of bulk Alumina. For the (10) plane, relaxations similar to this are not expected, as there are no "convenient" resting spots for the Aluminum atoms to take. One can also see that there are no triangle formations of Oxygen for the Aluminum atoms to sink into along the w-direction. Results actually show that there are significant relaxations all along the cell length, in not only the w-direction, but in the u and v as well as indicated in Fig. 2.

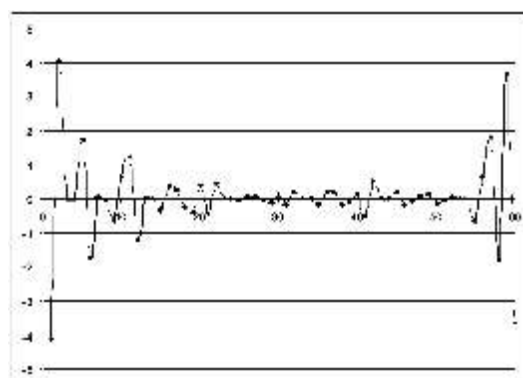


**Fig. 1:** Percent relaxations for Alumina in the u-direction. Notice that the greatest displacements are near to the surfaces. Inside the cell, near to the middle, there is very little relaxation, with the structure being almost bulk.

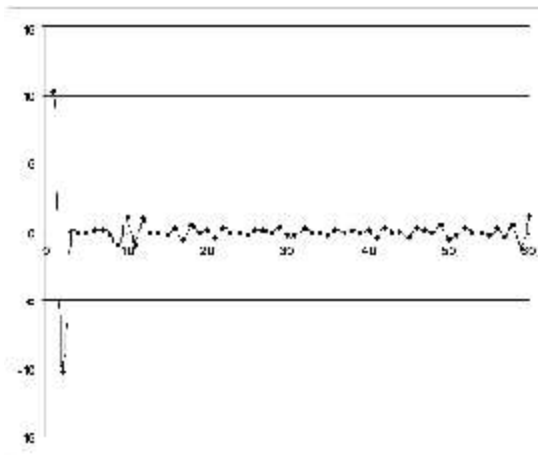


**Fig. 2:** Percent relaxation in Alumina in v-direction. Notice that relaxations near to the surface are greatest. The small relaxations in the center are more apparent here.

## Surface Energy

Table 1: Calculated energies of the bulk, un-relaxed, and relaxed cells

	Bulk	Un-relaxed	Relaxed
Energy (eV)	-2876.0202	-17223.4408	-17229.7369
E/Atom	-287.6020	-287.0573	-287.1622

After obtaining the energies in the table above, the surface formation energy is then obtained as follows. Since the surface energy is the change in energy from bulk to the surface divided by the area of each surface. The energy at the surface (SE) is thus:

$$SE = \frac{(E_{\text{surface}} - N * (E_{\text{bulk} / n}))}{(2 * A)} \quad (1)$$

Where  $N$  the number of atoms in the surface cell,  $n$  is the number of atoms in the bulk cell, and  $A$  is the area of the surface.

The surface area for this system can be found in this manner by using the expression:

$$(u \cdot v) = |u| \cdot |v| \sin \theta = A \quad (2)$$

Hence our calculated surface is found to be 35.67 Å<sup>2</sup> and the calculated surface formation energy for our Alumina is 7.328 J/m<sup>2</sup> which in comparison with other metal oxide surfaces [8-9], this surface energy is quite large. For the surface energy of the relaxed surface, we obtained 5.904 J/m<sup>2</sup> is closer to previous results for a similar surface [9].

## Electronic Structure

### Density of State (DOS)

The density of states for bulk Alumina given in Fig.3 shows that it is plainly a very strong insulator, with a very wide band gap. Most of the valence electrons near the Fermi energy are in the  $p$  states, while most of the states in lower energies in  $s$  states. The states past the Fermi energy consist of a more equal mix of  $s$  and  $p$  states, with  $d$  states not present. After cleaving the surface, adding the vacuum slab, and relaxing the surface, the density of states Fig. 4 shows that the surface is actually a conductor as expected.

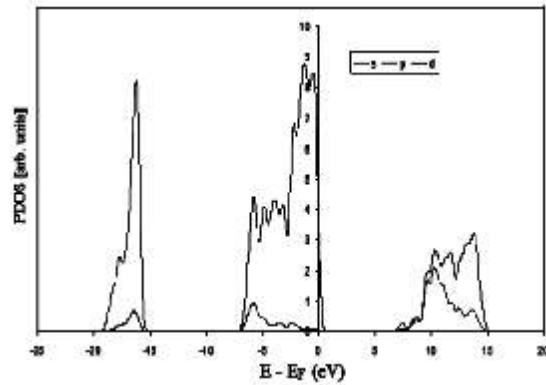


**Fig. 2** Density of states for bulk Alumina. Notice that states from -20 to -15 are chiefly  $s$  states, while states from -10 to 5 are chiefly  $p$  states. States outside the Fermi energy are more balanced between  $s$  and  $p$ , although not filled at zero degrees.

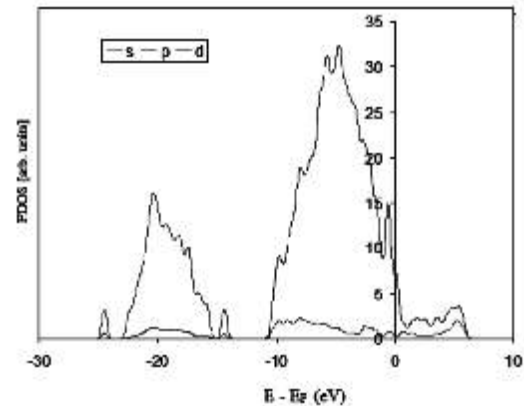


**Fig. 2** Density of states for Alumina relaxed surface. Notice that there is now no Fermi gap, this system has become a conductor. The lower energies are still mostly  $s$  states, and the higher energies are still mostly  $p$  states

### Charge Density Distributions

The charge density analysis option shows how the charge is distributed inside the cell. For a highly ionic system, charge will be localized at certain elements. This means that these

particular elements have more electron negativity, and will attract the free electrons

from the other elements. In an ionic system, these free electrons are drawn completely to the other attractive elements.

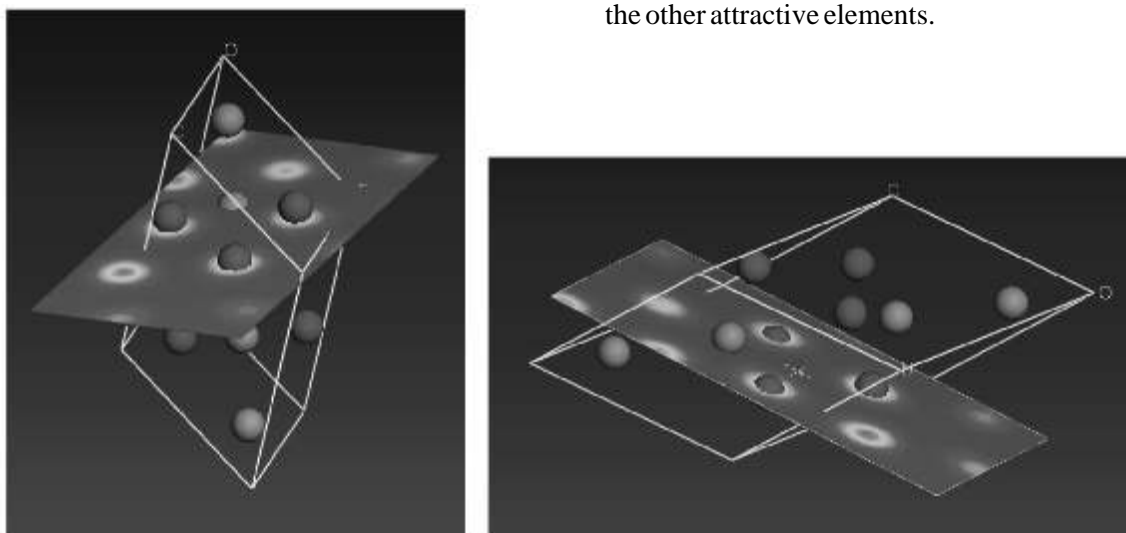


**Fig. 5** Charge density along two different planes in the Alumina bulk primitive cell. Notice that all charge is localized about the red Oxygen atoms. Oxygen is a highly electro-negative, and so makes the bonds of this system ionic

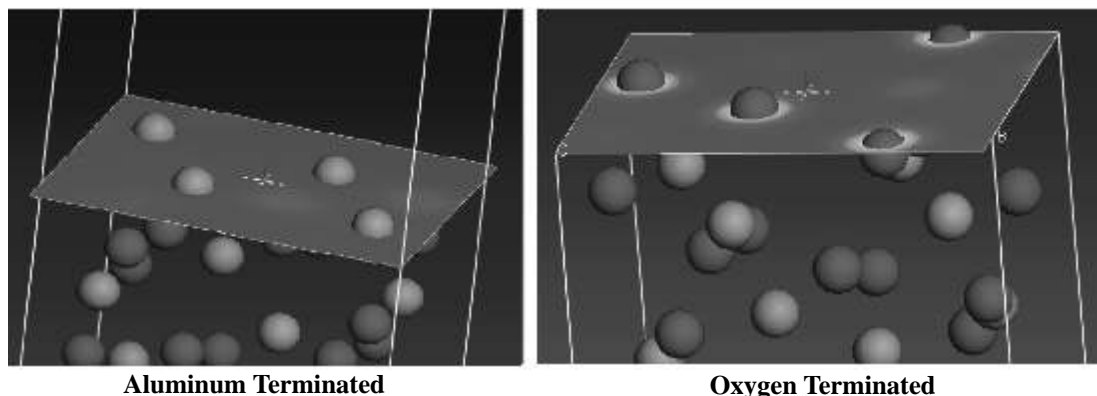


**Fig. 6** Charge density at the two surfaces, notice that the Aluminum terminated surface has only small amounts of charge, due to the Oxygen atoms immediately below the surface. The Oxygen terminated surface shows high charge around the O atoms.

These figures show that there is no change in the behavior of charge between the bulk and surface charge densities. There is still strong charge localization about the highly ionic Oxygen atoms, and still strong charge delocalizations about the Aluminum atoms. Such behavior, again, is the sign of ionic bonds, and an ionic system. The absence of charge at the upper surface and collection of charge at the lower surface may bring rise to an electric field, although this effect has not been

studied in this report.

### Conclusions

In summary, our results show that Alumina is indeed an insulator that changes into a conductor at the ( 10) surface. It has strong ionic bonds, with charge localized at the Oxygen atoms. The high surface energy suggests that this surface is difficult to create experimentally, and there is a strong possibility to fall apart quickly.

## REFERENCES

- Levin, I. and Brandon, D., 1998. Metastable alumina polymorphs: crystal structures and transition sequences. *Journal of the American Ceramic Society*, 81(8), pp.1995-2012.
- Leskelä, M. and Ritala, M., 2002. Atomic layer deposition (ALD): from precursors to thin film structures. *Thin solid films*, 409(1), pp.138-146.
- Paranjpe, A., Gopinath, S., Omstead, T. and Bubber, R., 2001. Atomic layer deposition of  $\text{AlO}_x$  for thin film head gap applications. *Journal of the Electrochemical Society*, 148(9), pp. G465 - G471.
- Streitz, F.H. and Mintmire, J.W., 1999. Energetics of aluminum vacancies in gamma alumina. *Physical Review B*, 60(2), p.773.
- Wilson, M., Exner, M., Huang, Y.M. and Finnis, M.W., 1996. Transferable model for the atomistic simulation of  $\text{Al}_2\text{O}_3$ . *Physical Review B*, 54(22), p.15683.
- Ionescu, A., Allouche, A., Aycard, J.P., Rajzmann, M. and Hutschka, F., 2002. Study of  $\gamma$ -alumina surface reactivity: Adsorption of water and hydrogen sulfide on octahedral aluminum sites. *The Journal of Physical Chemistry B*, 106(36), pp.9359-9366.
- Vijay, A., Mills, G. and Metiu, H., 2002. Structure of the (001) surface of alumina. *The Journal of chemical physics*, 117(9), pp.4509-4516.
- Sohlberg, K., Pennycook, S.J. and Pantelides, S.T., 1999. Explanation of the observed dearth of three-coordinated Al on  $\gamma$ -alumina surfaces. *Journal of the American Chemical Society*, 121(47), pp.10999-11001.
- Maresca, O., Ionescu, A., Allouche, A., Aycard, J.P., Rajzmann, M. and Hutschka, F., 2003. Quantum study of the active sites of the alumina surface (II): QM/MM (LSCF) approach to water, hydrogen disulfide and carbon monoxide adsorption. *Journal of Molecular Structure: THEOCHEM*, 620(2-3), pp.119-128.
- Ruberto, C., Yourdshahyan, Y. and Lundqvist, B.I., 2002. Stability of a flexible polar ionic crystal surface: metastable alumina and one-dimensional surface metallicity. *Physical review letters*, 88(22), p.226101.
- Kokalj, A., 1999. XCrySDen—a new program for displaying crystalline structures and electron densities. *Journal of Molecular Graphics and Modelling*, 17(3-4), pp.176-179.
- Perdew, J.P., Burke, K. and Ernzerhof, M., 1998. Perdew, burke, and ernzerhof reply. *Physical Review Letters*, 80(4), p.891.
- Giannozzi, P., Baroni, S., Bonini, N., Calandra, M., Car, R., Cavazzoni, C., Ceresoli, D., Chiarotti, G.L., Cococcioni, M., Dabo, I. and Dal Corso, A., 2009. QUANTUM ESPRESSO: a modular and open-source software project for quantum simulations of materials. *Journal of physics: Condensed matter*, 21(39), p.395502.

## GEOELECTRIC MAPPING OF SUBSURFACE LAYERS IN A SECTION OF JANRUWA KAMANZO, KADUNA, KADUNA STATE.

**Danjuma, T. T.**  
Department of Physics,  
Bingham University

### ABSTRACT

*Vertical Electrical Sounding (VES) method of Electrical Resistivity was carried out at a section of Janruwa-Kamanzo, Kaduna metropolis, using the Schlumberger array, with maximum electrode separation, AB/2 of 100m on 20 VES stations located on four profiles, having 20m offsets to each other. The survey was carried out with the aim of obtaining information on the subsurface condition. From the derived geoelectric and geologic sections produced it is suggestive that the area is underlain by three to five layers. The first layer has thickness variation from It is suggestive that the area is underlain by three to five layers. The first layer also known as topsoil varies from 0.3 m – 4.7 m in thickness and 63 ? m – 987 ? m in resistivity. This geoelectric derived suggests that the topsoil is highly lateritic in nature. The weathered/fractured basement varies from 3.9 m – 58 m and 73 ? m – 639 ? m respectively. The derived geologic suggests that the weathered layer varies in composition (silty/sandy clay, clay and sand) with an average resistivity and thickness values of 305 m and 17 m respectively. The last layer, which is at infinite thickness, is found to have high resistivity values ranging from 555 m to 3333 m. The observed regions of low resistivity in this layer suggest that the basement rocks may have under fracture and slightly weathered.*

*resistivity and is suggested to consists of materials which are highly lateritic. The weathered/fractured basement varies in depth and resistivity from 3.9 m – 58 m and 73 ? m – 639 ? m respectively. It is the second or third layer in most sections of the study area. The last layer, which is at infinite thickness, is found to have high resistivity values ranging from 1016 m to 3333 m. The observed regions of low resistivity in this layer suggest that the basement rocks may have under fracture and slightly weathered in some of the sections.*

### Introduction

The Kaduna city lies within the area of the Basement Complex of Northern Nigeria. The basement complex includes all rock older than late Proterozoic (Dogara, 1995), and is composed mainly of gneises, migmatites, granites and some extensive areas of Schists, Phyllites and Quartzite. The entire basement has been through at least two tectonometamorphic cycles and consequent metamorphism, magnetization and granitization extensively modified the original rocks, so that they generally occur as relict rafts and xenoliths in migmatites and granites

(McCurry, 1976). The rocks of the area are mostly Precambrian in age and have been subjected to several phases of deformation, the latest being the Pan African Orogeny (Aboh, 2009). During this deformation, the basement produced North-South trending basins of metasediments in the form of synclinoria. Oyawoye (1964), showed that there is structural relationship between this Basement Complex and the rest of the West African basement. This is partly due to the fact that the whole region was involved in a single set of orogenic episode, the Pan African orogeny, which left an imprint of structural similarity



upon the rock units. The actual depth of the weathered zone depends on the length of time in which the rocks have been exposed to surface or near surface conditions and its original minerals. The interface between weathered and unweathered rocks is usually sharp, weathering tends to be particularly well developed along fissure systems, which allow deep percolation of the weathering agent principally oxygenated water. River system can sometimes be guide to fault lines and associated fissure systems because they represent lines of weakness for erosion and weathering (Olabode *et al.*, 1999).

Around the study area, the rock types of the basement, according to Adamu(1991), are medium to coarse grained granite, undifferentiated schist, gneisses, granite gneisses, fine grained biotites and biotites hornblende granite, quartz monzonite, quartz diorite and granodiorites. The superficial deposits, which overlie the basement rocks, act as recharge materials, especially where they are underlain by weathered basement (Eigbefo, 1978). The main aquifer components of the basement complex of Nigeria are weathered and fractured basement (Oluwu, 1967) and water yielding capacities of wells drilled to these components always vary.

This thermotectonic event has virtually obliterated the imprints of earlier events but left its own structural earmarks, which include: filing, fracturing, shearing, granitic emplacement and granitisation. The Migmatite-Gneiss Complex which underlies most of the Kaduna-Zaria area and typifies the area of investigation is characterized by spectacular exposure of well defined Migmatite around Kudenda, Kakau, Sabon Tasha, Kabala East and West areas in Kaduna metropolis. These materials are usually liable to form aquitard and permeable zones to the bedrocks in the country rocks of the area. Associated with the crystalline rocks are the presence of structures like fractures, fissures, veins, joint and such other structural deformations of the basement complex which

controls the flow of ground water and also influence the rate of recharge and discharge of the main aquiferous units (Aboh, 2009). The weathering of the crystalline Basement Complex rocks under tropical condition is well known to produce a sequence of unconsolidated material whose thickness and lateral extent vary extensively. The geology map of the area is as shown in Figure 1.

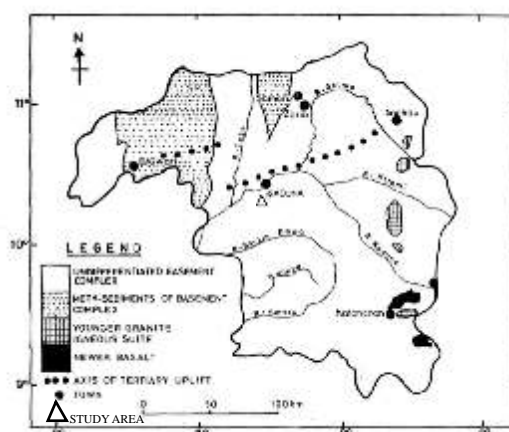


Fig.1: Geological Map of Kaduna State (After Dogara, 1995).

## Materials and Methods

Vertical Electrical Sounding (VES) data were collected on 20 VES points using 4 profiles, each of length 80m. The VES point interval used was 20m. At each VES point, the maximum separation of current electrodes (AB/2) was 100m using the Schlumberger spread.

The arrangement of electrodes in the Schlumberger array which was employed in this work is shown in Fig. 2. A and B represent the current electrodes through which the current was passed into the ground. M and N represent the potential electrodes across which the potential difference caused by the current was measured. The array is as shown in Figure

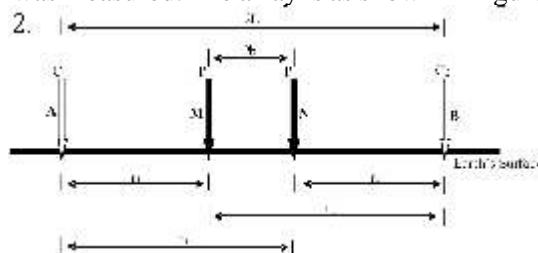


Fig.2: Schlumberger Electrode Array

From Ohm's law, the current  $I$  and the potential  $V$  in a metal conductor at constant temperature are related as follow;

$$V = IR \quad (1)$$

Where  $R$  is the constant of proportionality known as resistance, measured in ohms. The resistance  $R$ , of a conductor is related to its length  $L$  and cross sectional area  $A$ , by

$$R = \frac{\rho L}{A} \quad (2)$$

Where  $\rho$  is the resistivity, and it is a property of the material considered. From (1) and (2),

$$V = \frac{I \rho L}{A} \quad (3)$$

Using the Schlumberger configuration, potential electrodes MN are placed in between the current electrodes AB with a central reference point established. The current electrodes AB are moved outward symmetrically at each successive reading for deeper current penetration and thus deeper probing. The distance between the MN electrodes is increased when the current electrode AB are relatively far apart while maintaining MN being much less than AB (Fig. 2). This is done in order to have measurable potentials and to prevent the voltage from dropping below the reading accuracy of the voltmeter. A potential gradient is measured at M and N when current electrodes located on the surface of the equipotential surface is semi-spherical downward into the ground at each electrode. The surface area will then be  $2\pi L^2$ , where  $L$  is the radius of the sphere.

Thus,

(4)

By deduction then, the potential at M ( $V_M$ ), due to the two current electrodes, is

$$V_M = \frac{I \rho}{2\pi} \left( \frac{1}{r_1} - \frac{1}{r_2} \right) \quad (5)$$

Similarly, the potential at electrode N ( $V_N$ ) is given by

$$V_N = \frac{I \rho}{2\pi} \left( \frac{1}{r_3} - \frac{1}{r_4} \right) \quad (6)$$

Where  $r_1$ ,  $r_2$ ,  $r_3$  and  $r_4$  are shown in fig 2

The potential difference,  $\Delta V$ , across electrodes M and N is  $V_M - V_N$ .

$$\Delta V = V_M - V_N \quad (7)$$

$$\Delta V = \frac{I \rho}{2\pi} \left[ \left( \frac{1}{r_1} - \frac{1}{r_2} \right) - \left( \frac{1}{r_3} - \frac{1}{r_4} \right) \right] \quad (8)$$

$$\Rightarrow \rho = \frac{2\pi \Delta V}{I} \left[ \frac{1}{\left( \frac{1}{r_1} - \frac{1}{r_2} \right) - \left( \frac{1}{r_3} - \frac{1}{r_4} \right)} \right] \quad (9)$$

If the body is inhomogeneous like the study area, apparent resistivity ( $\rho_a$ ) is considered,

$$\rho_a = K \left( \frac{\Delta V}{I} \right) \quad (10)$$

Where  $\rho_a$  is apparent resistivity in ohm-metre, and,

$$K = 2\pi \left[ \frac{1}{\left( \frac{1}{r_1} - \frac{1}{r_2} \right) - \left( \frac{1}{r_3} - \frac{1}{r_4} \right)} \right] \quad (11)$$

$K$  is called the geometric factor whose value depends on the type of electrode array used.

For Schlumberger array, if  $MN = 2b$  and

$$\frac{AB}{2} = L, \text{ then}$$

$$K = \pi \left( \frac{L^2}{2b} - \frac{b}{2} \right) \quad (12)$$

The interpreted data from resistivity curve software were used to prepare the composite goelectric and geologic section along all the four profiles. After the quantitative interpretation, the resulting curves and their final model parameters are presented in Fig. 3 to 6. The goelectric sections reveal the variations of resistivity and thickness values of layers within the study area. Generally, the sections revealed three to five subsurface layers: topsoil/laterite/indurated laterite/quartzite veins, clay/silty/sand, laterite, weathered/fractured layer and the fresh basement as shown in Fig. 3 – 6. These were evaluated from typical rock resistivity values from earlier works carried out near the study area and the ones adopted for this work in Tales 1 and 2 respectively

*Table 1: Typical resistivity values compiled in different basement area in Kaduna State (Dogara, 2005: Jatau E tal., 2013: Aboh, 2001: Aboh, 2009: Abdullahi and Udensi, 2008)*

Soil and Rock Types	Resistivity ( $\Omega$ m)
Topsoil	30 – 270
Silty/sand/clay	40 – 250
Dry sand	500 – 1000
Laterite	200 – 350
Indurated Laterite	450 – 3500
Weathered basement	50 – 350
Fractured basement	400 – 1000
Fresh crystalline basement rock	>1000

*Table 2: Typical Resistivity Values Adopted For this Work*

Soil and Rock Types	Resistivity range
Top layer	63 – 250 $\Omega$ m
Silt/Sandy/clay	217 – 250 $\Omega$ m
Laterite/Indurated laterite	250 – 1800 $\Omega$ m
Weathered Basement	188-340 $\Omega$ m
Fractured Basement	450-1000 $\Omega$ m
Fresh basement	>1000 $\Omega$ m

## Result and Discussion

The geoelectric and geological section describes the electrical properties and lithological formation of a sequence of layered rocks (El-Arabi, 2008). The final model geoelectric parameters across the sections of the study area were used for the preparation of the geoelectric and geologic section for the four profiles (Fig. 3 - 6). Vertical Sounding field curves can be interpreted qualitatively using simple curve shapes, semi-quantitatively with graphical model curves, or quantitatively with computer modelling (Telford, e tal., 1990). In order to investigate the subsurface structural trends in the study area, and to reveal the geoelectric and geologic section of the subsurface formation of the study area, the previous field works has been successfully used to sequence the present work. Thus the geoelectric sections has shown the average variations of resistivity and thickness values of layers within the depth penetrated in the study area at the indicated sections. The geologic sections were constructed using the result of the work after Aboh (2009) and Abdullahi and Udensi (2008). The first layer also known as topsoil varies from 0.3 m – 4.7 m in thickness and 63?  $\Omega$  m – 601?  $\Omega$  m in resistivity. This geoelectric derived suggests that the topsoil is highly lateritic in nature. The weathered/fractured basement varies from 73?  $\Omega$  m – 639?  $\Omega$  m and 3.9m – 58m respectively. The derived geologic suggests that the weathered layer varies in composition (silty/sandy clay, clay and sand) with an average resistivity and thickness values of 305  $\Omega$  m and 17m respectively. The last layer, which is at infinite thickness, is found to have high resistivity values ranging from 1005  $\Omega$  m to 3333  $\Omega$  m. The observed regions of low resistivity in this layer suggest that the basement rocks may have under fracture and slightly weathered.

Generally, the sections revealed three to five subsurface layers which consist of topsoil/laterite/indurated laterite/sandstone, clay/silty/sand, as well as weathered layer and the Fractured/fresh basement rocks.

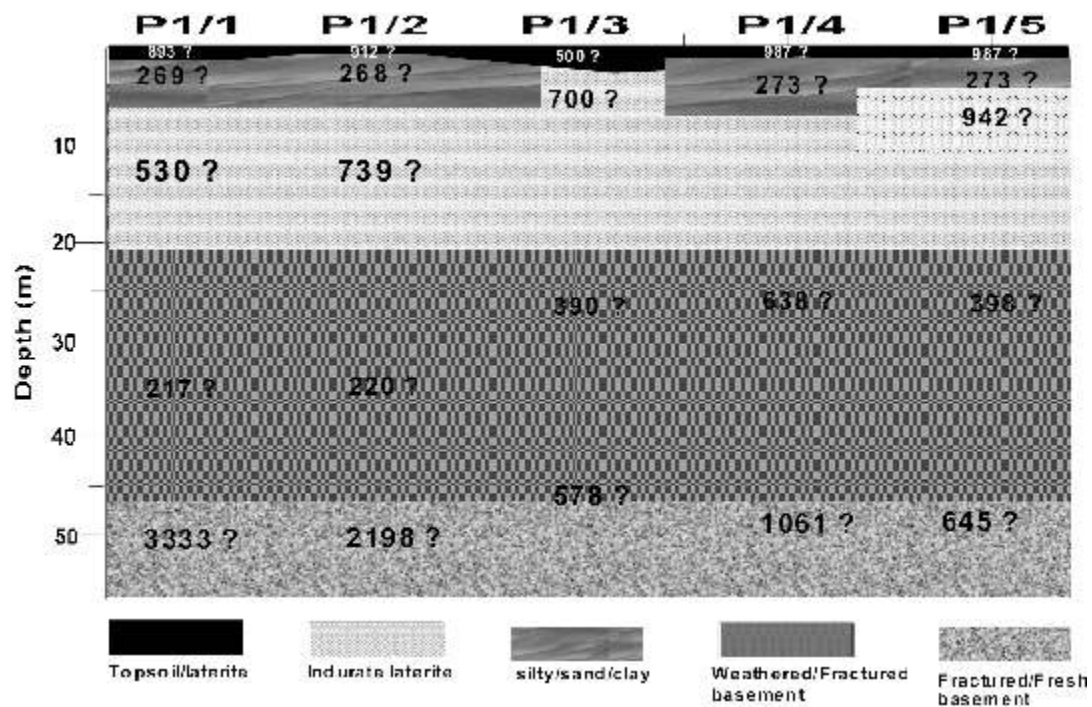


Fig.3: Goelectric/geologic section of profile one (1) across the study area

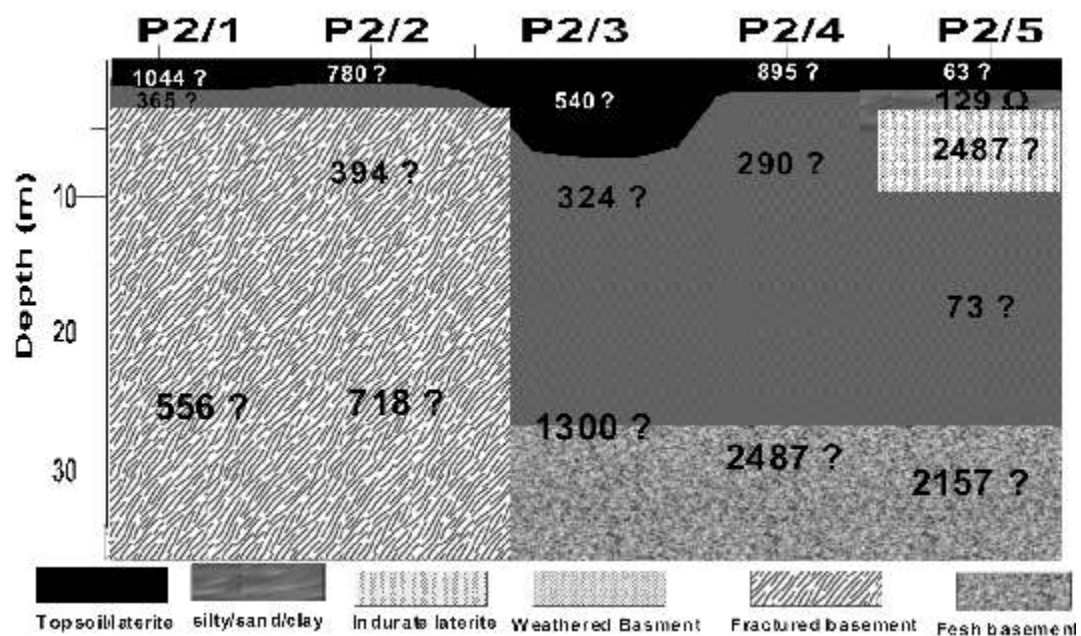


Fig. 4: Goelectric/geologic section of profile two (2) across the study area

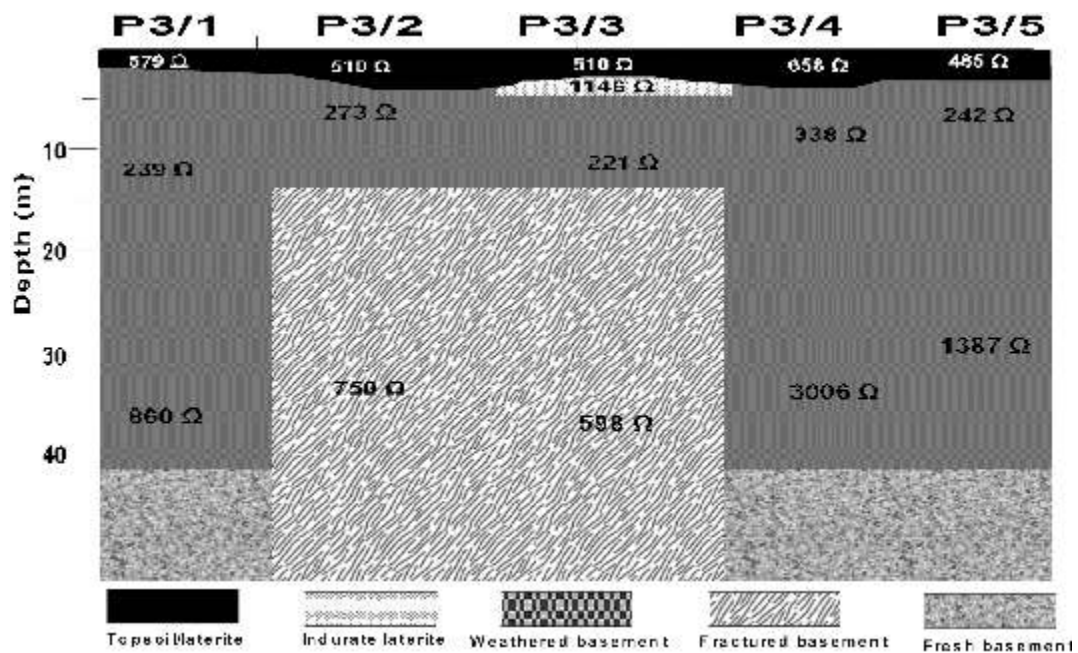


Fig. 5: Geologic/geologic section of profile three (3) across the study area

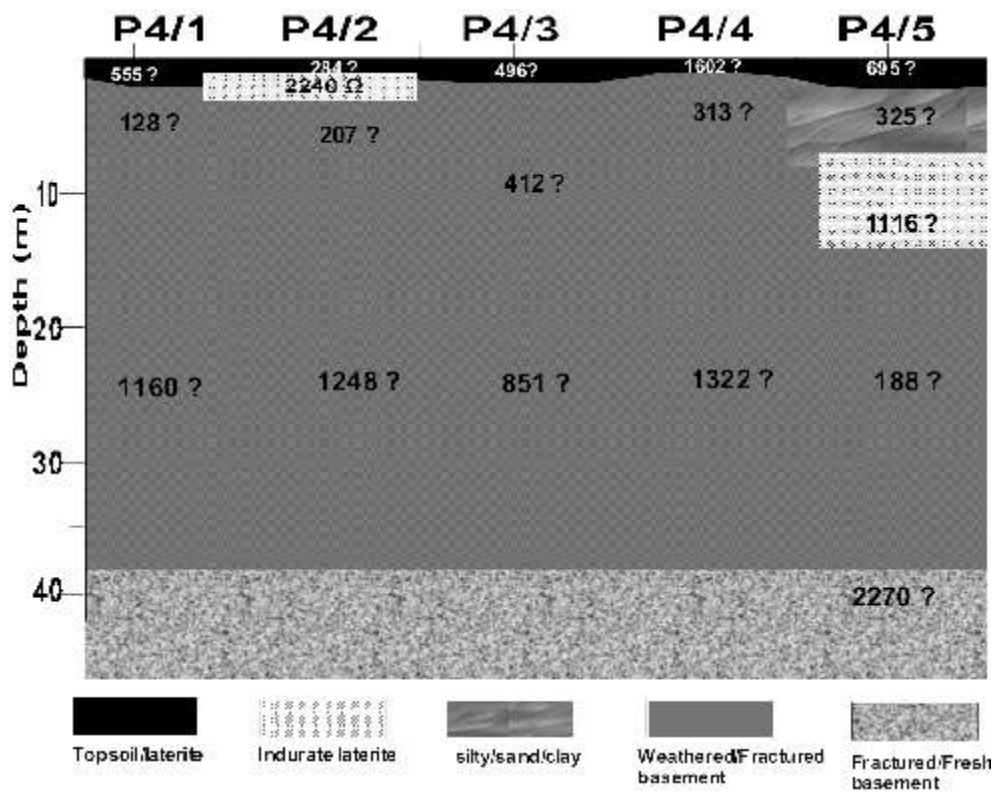


Fig. 6: Geoelectric/geologic section of profile four (4) across the study area

## Conclusion

The interpreted data of Vertical Electrical Sounding (VES) carried out in the study area has revealed three to five subsurface geoelectric layers and geologic sections, namely: topsoil/laterite/ followed by indurated laterite, and weathered basement and fractured/fresh basement rocks. The first layer also known as topsoil varies from 0.3 m – 4.7 m in thickness and 63  $\Omega$  m – 987  $\Omega$  m in resistivity and is thus highly lateritic in nature. The weathered/fractured basement varies from 3.9 m – 58 m and 73  $\Omega$  m – 750  $\Omega$  m respectively and constitutes largely the second layer. The derived geologic suggests that the weathered layer varies in composition (silty/sandy clay, clay and sand). The last layer, which is at infinite thickness, is found to have high resistivity values ranging from 1007  $\Omega$  m to 3333  $\Omega$  m. The observed regions of low resistivity in this layer suggest that the basement rocks may have under fracture and slightly weathered.

The geoelectric and geologic section derived suggests that the weathered basement layer as well as the fractured basement constituted about 43% of the subsurface layers.

## References

- Abdullahi, N. K., and Iheakanwa, A. (2013). "Groundwater Detection in Basement Complex of Noythwestern Nigeria using 2D Electrical Resistivity and Offset Wenner Technique". International Journal of Science and Technology 2 (7).
- Abdullahi, N. K., and Udensi, E. E. (2008). "Vertical Elecrcal Sounding Apllied to Hydrogeologic and Engineering Investigation: A Case Study of Kaduna Polytechnic Staff Quarters, Nigeria". Nigerian Journal of Physics 20 (1).
- Abdullahi, N. K., Udensi, E. E., Iheakanwa, A., and Eletta, B. E. (2014). "Geo-electrical Method Applied to Evaluation of Groundwater Potential and Aquifer Protective Capacity of Overburden Units". British Journal of Applied Science & Technology, 4 (14).
- Aboh, H. O. (2009). "Assessment of the Aquifers in some Selected Villages in Chukun Local Government Area, Kaduna State, Nigeria". Science World Journal, 4.
- Aboh, H. O. (2002). "Geotechnical Characterization of Subsurface Materials in Kaduna Area, Kaduna State, Nigeria". Zuma Journal Of Pure & Applied Science, 4 (2).
- Aboh H.O. (2001). Detailed Regional geophysical Investigation of the Subsurface Terrain in Kaduna Area, Kaduna State. Physics Department, ABU, Zaria. Unpublished PhD theses.
- Aboh, H. O., and Osazuwa, I. B. (2000). "Lithillogical Deductions from a Regional Geoelectric Investigation in Kaduna Area, Kaduna State". Nigerian Journal of Physics, 12.
- Adamu, E. A. (1991). "Source and recharge of groundwater in the basement". Journal of African Earth Sciences 13 (2), 229-234.
- Agbo, C. (2014). "2-D Electrical Resistivity Imaging around the Collapsed Building of Housing Estate at Barnawa-Narayi Junction, Kaduna, Kaduna State". Unpublished M.Sc. Thesis, Department of Physics, Ahmadu Bello University, Zaria.
- Ajibade, L. T., and Okwori, A. (2009). "Developing an Information System for Rurall Water Supply Scheem in Kaduna

State, Nigeria". *Journal of Environmental Science*.

Chendo, I. G., and Obi, N. I. (2015). "Building Collapse in Nigeria: The Causes, Effects, Consequences". *International Journal of Civil Engineering, Construction and Estate Management*, 3 (4).

Dogara, M. D. (1995). "D.C Resistivity Investigation of the Groundwater potential in Romi Chikun Local Government Area Kaduna State Nigeria". Unpublished M.Sc. Thesis, Department of Physics, Ahmadu Bello University, Zaria.

Eigbefo, C. (1978). "Hydrology of Kubani drainage basin, Zaria". Unpublished M.Sc Thesis, Department of Geology, Ahmadu Bello University, Zaria

Ephraim, W. (2016). *Dept. Of Minerals and Petroleum Resources Engineering, Kaduna Polytechnic*. Personal Discussion.

Fadele, S. I., Jatau, B. S., and Goki, N. G. (2013). "Subsurface Structural Characterization of Filatan Area A, Zaria – Kano Road, using the 2D Electrical Resistivity Tomography". *Journal of Earth Sciences and Geotechnical Engineering*, 3 (1).

Fagbenle, O., and Oluwunmi, A. O. (2010). "Building Failure and Collapse in Nigeria: the Influence of the Informal Sector". *Journal of Sustainable Development*, 3 (4).

Haruna, G., Abubakar, I., Rabia, L. B., Saminu, A., Abdullahi, I. and Faustinus, B. (2013). "Climate Change Impact on Sub-Surface Hydrology of Kaduna River Catchment". *Open Journal of Modern Hydrology* 3.

Igboekwe, M. U., Ihekweaba, G., Eke, A. B., and Adama, J. C. (2012). "The Use of Vertical Electrical Sounding (VES) in the

*Evaluation of Erosion in Abia State University, Uturu and Environs*". *The Pacific Journal of Science and Technology*, 13, 509.

Jatau, B. S., Patrick, N. O., Baba, A., and Fadele, S. I. (2013). "The Use of Vertical Electrical Sounding (VES) for Subsurface Geophysical Investigation Around Bomo Area, Kaduna State, Nigeria". *IOSR Journal of Engineering* 3 (1).

Keller, G. V., and Frischnech, F. C. (1979). "Electrical Methods in Geophysical Prospecting". New York: Peramon Press.

Lawal, K. M. (2016). *Dept. Of Physics, Ahmadu Bello University, Zaria*. Personal Discussion.

McCurry, P. (1970). "The Geology of Zaria Sheet 21". Unpublished M.Sc. Thesis, Department of Physics, Ahmadu Bello University, Zaria.

Mohammed, L. N., Aboh, H. O., and Eminike, E. A. (2007). "A Regional Goelectric Investigation for Groundwater Exploration In Minna Area". *Science World Journal* 2 (3).

NGSA. (2016). "Hydrogeological Mapping of Kaduna and its Environs". *Nigerian Geological Survey Agency Report*.

Nwankwoala, H. O., and Warmate, T. (2014). "Subsurface Soil Characterization of a Site for Infrastructural Development Purposes in D/Line, Port Harcourt, Nigeria". *American International Journal of Contemporary Research*, 4 (6).

Oluwu, J. (1967). "Preliminary Investigation of Groundwater Condition in Zaria". GSN Report.

Osele, C. E. (2012). "Application of Electrical Resistivity Method Using

*Vertical Electrical Sounding (VES) for Groundwater Exploration in Onitsha and Environs, Nigeria*". Unpublished M.Sc Thesis, Department of Geological Science, Nnamdi Azikiwe University, Akwa.

Oyawoye, P. O. (1964). "*Geology of Nigerian Basement Complex*". *Journal of Mining and Geology* 1, 110-121.

Paranis, D. S. (1986). "*Principle of Applied Geophysics 4th Edition*". London: Champman and Hall.

Talabi, A. O., and Ayodeji, K. O. (2015). "*Vertical Electrical Resistivity Sounding for Groundwater in Bishini Area of Kaduna State*". *IMPACT: International Journal of Research in Applied, Natural and Social Science* 3 (1).

Telford, W. M., Geldart, L. P., and Sheriff, R. E. (1990). "*Applied Geophysics*". London: Cambridge University Press.